

AD-A124 028

MICRO AND MACRO MECHANICS OF FRACTURE IN CERAMICS(U)  
CALIFORNIA UNIV BERKELEY DEPT OF MATERIALS SCIENCE AND  
ENGINEERING A G EVANS ET AL. 30 OCT 82

1/4

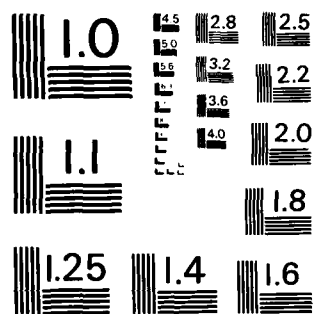
UNCLASSIFIED

NO0014-81-K-0362

F/G 11/2

NL





MICROCOPY RESOLUTION TEST CHART  
NATIONAL BUREAU OF STANDARDS-1963-A

ADA 124025

10

MICRO AND MACRO MECHANICS OF  
FRACTURE IN CERAMICS

Interim Report To  
Office of Naval Research  
Contract No.: N00014-81-K-0362  
January 1, 1982 - December 31, 1982

by

A. G. Evans  
University of California  
Berkeley, California 94720

and

M. Drory, K. T. Faber, J. Hutchinson, G. S. Kino,  
B. T. Khuri-Yakub, J. Lamon, D. B. Marshall, T. Noma,  
H. Ruf, J. W. Tien, T. Uchiyama.

Accession For	
NTIS GRA&I	<input checked="checked" type="checkbox"/>
DTIC TAB	<input type="checkbox"/>
Unannounced	<input type="checkbox"/>
Justification	
By <u>Per Ltr. on file</u>	
Distribution/	
Availability Codes	
Dist	Avail and/or Special
A	



DISTRIBUTION STATEMENT A

Approved for public release  
Distribution Unlimited



SECURITY CLASSIFICATION OF THIS PAGE (When Data Entered)

REPORT DOCUMENTATION PAGE		READ INSTRUCTIONS BEFORE COMPLETING FORM
1. REPORT NUMBER	2. GOVT ACCESSION NO. <b>A124 025</b>	3. RECIPIENT'S CATALOG NUMBER
4. TITLE (and Subtitle) Micro and Macro Mechanics of Fracture in Ceramics		5. TYPE OF REPORT & PERIOD COVERED Interim Report Jan. 1, 1982 - Dec. 31, 1982
		6. PERFORMING ORG. REPORT NUMBER
7. AUTHOR(s) A. G. Evans		8. CONTRACT OR GRANT NUMBER(s) N00014-81-K-0362
9. PERFORMING ORGANIZATION NAME AND ADDRESS Dept. of Materials Science and Mineral Engineering University of California Berkeley, CA 94720		10. PROGRAM ELEMENT, PROJECT, TASK AREA & WORK UNIT NUMBERS
11. CONTROLLING OFFICE NAME AND ADDRESS Office of Naval Research, Code 471 Arlington, VA 22217		12. REPORT DATE October 30, 1982
		13. NUMBER OF PAGES
14. MONITORING AGENCY NAME & ADDRESS (if different from Controlling Office)		15. SECURITY CLASS. (of this report) Unclassified
		15a. DECLASSIFICATION/DOWNGRADING SCHEDULE
16. DISTRIBUTION STATEMENT (of this Report)		
<div style="border: 1px solid black; padding: 5px; text-align: center;"> <b>DISTRIBUTION STATEMENT A</b>            Approved for public release;            Distribution Unlimited         </div>		
17. DISTRIBUTION STATEMENT (of the abstract entered in Block 20, if different from Report)		
<div style="background-color: black; height: 20px; width: 100%;"></div>		
18. SUPPLEMENTARY NOTES		
19. KEY WORDS (Continue on reverse side if necessary and identify by block number)  Ceramics, toughening, surface damage, reliability, thermal shock, NDE, machining.		
20. ABSTRACT (Continue on reverse side if necessary and identify by block number)  The reliability of ceramic materials has been studied by addressing problems concerned with toughness, surface damage and statistics. Toughening effects due to deflecting phases have been studied and shown to yield substantial toughening where rod-shaped phases are used. The surface damage created by machining and implications for NDE have also been addressed, with special emphasis on the role of the residual stresses. Finally, statistical aspects of structural reliability have been studied, both by examining the role of multiple flaw populations on fracture predictability and by quantitatively correlating		

20. thermal shock statistics with mechanical strength distributions.

~~CONFIDENTIAL - SECURITY INFORMATION~~

## INTRODUCTION

Studies of the mechanical properties of ceramics during the current project year have been in three different areas: toughening mechanisms, surface damage and reliability. All of the work is interrelated through the general objective of attaining structural integrity in ceramic components. However, it is convenient to summarize the studies in each area on a separate basis.

### Toughening Mechanisms

The emphasis for the current year has been placed on the quantitative evaluation of the importance of crack deflection to the toughness of polycrystalline single phase and multiphase ceramics. The mechanics of the process has been fully analyzed (paper I) and indicate that the toughness depends only on the volume concentration and shape of the deflecting phase. Particle size and temperature do not affect this toughening mechanism. The maximum toughness is achieved with a rod-shaped deflecting phase of high aspect ratio. The predictions are compared with data obtained for  $\text{Si}_3\text{N}_4$ , a lithium aluminosilicate glass ceramic (paper II) and a monoclinic  $\text{ZrO}_2/\text{ZnO}$  composite (paper III). The presence of deflection toughening is amply confirmed by the experimental measurements and the trends in toughness with volume concentration and shape of the deflecting phase are in accord with prediction. The predicted absence of a size effect is also experimentally confirmed. Additionally, it is interesting to note that transformation toughening does not appear to occur to any significant extent in tetragonal  $\text{ZrO}_2/\text{ZnO}$ .

### Surface Damage

The surface damage studies have emphasized both damage development during machining and the detection of that damage by surface acoustic waves. The machining studies (paper V) have indicated that machining forces exhibit an appreciable dependence on mechanical properties, especially the fracture toughness, elastic modulus and hardness, and some dependence on the thermal properties, thermal conductivity and thermal expansion. Preliminary functional dependencies on these material properties have been established using dimensional analysis techniques. Systematic dependencies on the depth of cut have also been identified.

The strengths of machined specimens have also been subject to study (papers VI and VII). The strengths are influenced both by the machining damage and the residual stress in the plastic layer. Some of these effects have been evaluated by studying the stable growth of cracks beneath the plastic layer, prior to unstable fracture (paper VI). Surface acoustic waves have been utilized for this purpose. Further study of this topic will be required.

An interesting product of the surface damage studies has been the development of a simple technique for measuring the elastic modulus of small specimens, using a Knoop hardness indentation (paper VIII). Specifically, it has been demonstrated that the ratio of the major to minor axis of the Knoop indentation after load removal relates to the ratio of the elastic modulus to hardness of the material. Hence, both modulus and hardness may be ascertained from the indentation.

### Reliability

Statistical issues associated with reliability have been experimentally evaluated from bending tests (paper X) and thermal shock tests (paper XI). Emphasis has been placed on the quantitative use of statistics, recognizing the existence of multiple flaw populations and of multiaxial stresses. It is concluded that size effects can be adequately predicted when the dominant flaw populations have been comprehensively characterized, within the appropriate strength range. Additionally, it has been demonstrated that the thermal shock statistics can be predicted from mechanical strength statistics when fracture in both tests is surface flaw controlled, provided that the heat transfer coefficient has been adequately evaluated. However, similar comparisons for fabrication flaws have yet to be conducted.

## TECHNICAL ARTICLES

### Toughening Mechanisms

- I. K. T. Faber and A. G. Evans, "Crack Deflection Processes: I. Theory."
- II. K. T. Faber and A. G. Evans, "Crack Deflection Processes: II. Experiment."
- III. H. Ruf and A. G. Evans, "Toughening by Monoclinic Zirconia Using a Crack Deflection Mechanism."
- IV. A. G. Evans and J. Hutchinson, "Cleavage Fracture in Mild Steel."

### Surface Damage

- V. T. Uchiyama, D. B. Marshall and A. G. Evans, "Surface Damage in Brittle Solids: Studies of the Development and Influence of Grinding Forces."
- VI. D. B. Marshall, A. G. Evans, B. T. Khuri-Yakub, J. W. Tien and G. S. Kino, "The Nature of Machining Damage."
- VII. D. B. Marshall, "Controlled Flaws in Ceramics: A Comparison of Knoop and Vickers Indentation."
- VIII. D. B. Marshall, T. Noma and A. G. Evans, "A Simple Method for the Determination of Elastic Modulus to Hardness Ratios Using Knoop Indentation Measurements."
- IX. D. B. Marshall, "Delayed Failure in Ceramics."

### Reliability

- X. J. Lamon and A. G. Evans, "The Statistical Analysis of Bending Strengths for Brittle Solids: A Multiaxial Fracture Problem"
- XI. J. Lamon, M. Drory and A. G. Evans, "A Quantitative Study of Thermal Shock Applied to Surface Flaw Populations in Alumina."

TOUGHENING MECHANISMS

CHAPTER I

CRACK DEFLECTION PROCESSES: I. THEORY

by

K. T. Faber and A. G. Evans

Department of Materials Science and Mineral Engineering  
University of California  
Berkeley, CA 94720



Crack Deflection Processes: I, Theory

K. T. Faber and A. G. Evans

Department of Materials Science and Mineral Engineering  
University of California  
Berkeley, CA 94720

ABSTRACT

A fracture mechanics approach has been used to predict fracture toughness increases due to crack deflection around second phase particles. The analysis is based on a determination of the initial twist of the maximum twist of the crack front between particles, which provides the basis for evaluating the deflection-induced reduction in crack driving force. Features found to be important in determining the toughness increase include the volume fraction of second phase, the particle morphology and aspect ratio, and the distribution of interparticle spacing. Predictions are compared with expected surface area increases.

## 1. Introduction

Second phase particles located in the near tip field of a propagating crack perturb the front, causing a reduction in the stress intensity. The reduced stress intensity depends on the character of the particles and the nature of the crack interaction. Two dominant perturbations exist, termed crack bowing and crack deflection. It is essential to discriminate between crack deflection, which produces a non-planar crack, and crack bowing, which produces a non-linear crack front.<sup>1,2,3</sup> Crack bowing originates from resistant second phase particles in the path of a propagating crack. The crack tends to bow between the particles, causing the stress intensity  $K$  along the bowed segment of the crack to decrease (while resulting in a corresponding increase in  $K$  at the particle). The degree of bowing increases until the fracture toughness of the particle is reached, whereupon crack advance ensues. The penetrability (or resistance) of the second phase (related to its fracture toughness, and its volume concentration) determines the extent of crack bowing (discussed in Appendix A), and hence, the toughness increase.

Deflection toughening arises whenever interaction between the crack front and the minor phase produces a non-planar crack, subject to a stress intensity lower than that experienced by the corresponding planar crack. The non-planar crack arises either from residual strains present in the material or from the existence of weakened interfaces. The former derive from elastic modulus and/or thermal expansion mismatch between

the matrix and the particulate phase. The sign of the residual strain determines the direction of deflection.<sup>4</sup> Specifically, a second phase with a greater thermal expansion coefficient or elastic modulus than the matrix produces a tangential compressive strain near the particle/matrix interface and diverts the crack around the particle. Alternately, a second phase with a lower thermal expansion coefficient than the matrix induces tangential tensile strains, causing the crack to deflect toward the particle. However, toughness measurements suggest that the sign and magnitude of the residual strain have no significant influence on the magnitude of crack interaction toughening.<sup>5</sup> Specific effects of residual strain will thus be neglected in the present analysis.

The crack bowing and crack deflection processes (both of which should be insensitive to particle size) undoubtedly occur simultaneously. However, the present treatment is directed toward those materials which toughen primarily by crack deflection processes, rather than by crack bowing. A fracture mechanics approach to crack deflection will be presented, followed by a toughening analysis pertinent to the dominant particle morphologies (spheres, rods and discs). A comparison of experimental observations with the predictions of the analysis and a discussion of the relative roles of bowing and deflection will be presented in a companion paper.<sup>6</sup> Finally, the implications for toughness optimization by means of crack deflection processes will be discussed.

## 2. The Approach

### 2.1 General Considerations

When a crack approaches, or intercepts, a microstructural heterogeneity (in this case, a second phase particle), it will characteristically tilt at an angle,  $\theta$ , out of its original plane, as shown schematically in Figure 1a. The initial tilt angle depends upon the orientation and position of the particle with respect to the advancing crack (as well as the sign of the residual strain developed between the particle and the matrix). Subsequent advance of the crack may result in crack front twist. Specifically, twist of the crack front arises when the orientation of adjacent particles requires the crack to tilt in opposite directions (Figure 1b).

The twisted and tilted cracks are subject to mixed-mode local loading, characterized by the corresponding local stress intensities. The tilted crack has Mode I (opening) and Mode II (sliding) contributions to the stress intensity; while the twisted crack incorporates both Mode I and Mode III (tearing) components. The increase in fracture toughness imparted by deflection of the crack is evaluated from the local stress intensities at the tilted and twisted portions of the crack front. This is achieved by firstly assessing the local stress intensity factors,  $k_1$ ,  $k_2$ , and  $k_3$ , as a function of deflection angle. Crack advance is then assumed governed by the strain energy release rate,  $\mathcal{G}$ , pertinent to each segment of the crack front along its deflected trajectory,

$$E\mathcal{G} = k_1^2 (1-\nu^2) + k_2^2 (1-\nu^2) + k_3^2 (1+\nu), \quad (1)$$

where  $E$  and  $\nu$  are the Young's modulus and Poisson's ratio of the material, respectively. The average,  $\langle \mathcal{G} \rangle$ , across the crack front is then considered to represent the net crack driving force. A comparison of  $\langle \mathcal{G} \rangle$  with the corresponding strain energy release rate for an undeflected crack,  $\mathcal{G}^m$ , provides the present basis for predicting the toughening increment,  $\mathcal{G}_c$ ;

$$\mathcal{G}_c = (\mathcal{G}^m / \langle \mathcal{G} \rangle) \mathcal{G}_c^m. \quad (2)$$

## 2.2 Stress Intensity Factors for Non-Planar Cracks

When the length of the deflected portion of the crack is small with respect to the total crack length, the local stress intensity factors for a tilted crack,  $k_i^t$ , subject to Mode I applied loading are of the form:

$$k_1^t = K_{11}(\theta) K_I \quad (3a)$$

$$k_2^t = K_{21}(\theta) K_I \quad (3b)$$

where  $K_{11}$  and  $K_{21}$  are angular function associated with the tilted crack. First order solutions for  $K_{11}$  and  $K_{21}$  have been presented by Cotterell and Rice<sup>7</sup> as<sup>†</sup>

$$K_{11}(\theta) = \cos^3(\theta/2) \quad (4a)$$

$$K_{21}(\theta) = \sin(\theta/2) \cos^2(\theta/2) \quad (4b)$$

---

<sup>†</sup>It is noteworthy that the functions  $K_{11}$  and  $K_{21}$  are directly analagous to the angular dependence of the normal<sup>21</sup> and shear stresses in the near-tip field (see, for example, Lawn and Wilshaw<sup>8</sup>), and are equivalent to the exact solutions presented by Bilby<sup>9</sup>.

The corresponding stress intensity factors applicable to the twisted crack,  $k_i^T$ , can be expressed as

$$k_1^T = K_{11}(\phi) k_1^t + K_{12}(\phi) k_2^t \quad (5a)$$

$$k_3^T = K_{31}(\phi) k_1^t + K_{32}(\phi) k_2^t \quad (5b)$$

where the angular functions associated with the twisted crack (at angle  $\phi$  with the undeflected crack) are determined by resolving the normal and shear stresses of the tilted crack onto the twist plane. This procedure results in the following angular functions:

$$K_{11}(\phi) = \cos^4(\theta/2) \{2\nu \sin^2 \phi + \cos^2(\theta/2) \cos^2 \phi\} \quad (6a)$$

$$K_{12}(\phi) = \sin^2(\theta/2) \cos^2(\theta/2) \{2\nu \sin^2 \phi + 3 \cos^2(\theta/2) \cos^2 \phi\} \quad (6b)$$

$$K_{31}(\phi) = \cos^4(\theta/2) \{\sin \phi \cos \phi (\cos^2(\theta/2) - 2\nu)\} \quad (6c)$$

$$K_{32}(\phi) = \sin^2(\theta/2) \cos^2(\theta/2) \{\sin \phi \cos \phi (3 \cos^2(\theta/2) - 2\nu)\} \quad (6d)$$

The trends in  $K_{ij}$  are illustrated in Figure 2 for the case  $\theta = \phi$ , pertinent to spherical particles. The accuracy of the  $K_{ij}(\phi)$  solutions is presently unknown.

### 3. Analysis

Analysis of crack deflection may be treated sequentially. Initially, upon interception of a particle, the crack is forced to tilt out of the plane normal to the applied stress. Continued propagation around the particle results in crack front twist.<sup>†</sup> The twist angle increases and tends toward a maximum as the crack circumvents the particle. The ratio of the lengths of the tilted to the twisted crack decreases as the twist develops, resulting in contributions to the toughening from both the twist and tilt components. In order to evaluate the toughening, it is necessary to ascertain which portion of the deflection (the initial tilting or the subsequent maximum twisting) results in the lower crack driving force, and consequently the greater toughening. Particle morphology effects are incorporated into the analysis by investigating the three dominant morphologies; the sphere, the rod and the disc.

#### 3.1 Initial Deflection by Tilt

The crack tilt angle upon interception of a spherical particle decreases or remains constant as the crack extends around the particle, forming hemispherical or conical fracture morphologies. For rod- or disc-shaped particles, the tilt angle remains constant throughout crack advance. Thus, for all three morphologies the initial angle of crack deflection dictates the maximum tilt-induced toughening.

The average driving force on a crack tilted by an array of second phase particles can be determined by firstly assuming that the second phase exhibits spatial and alignment randomness throughout the material.

---

<sup>†</sup>Development of crack twist occurs when the tilt around adjacent particles occurs in opposite directions ( $\text{sign}_{\theta_1} = -\text{sign}_{\theta_2}$ ).

Given this assumption, simple probabilistics can be used to characterize the crack trajectory.

The analytic procedure will be presented in detail for a sphere. The analogous results for disc- and rod-shaped particles may be evaluated using the same approach, by incorporating appropriate stereological relations obtained from Fullman.<sup>10</sup> Consider a number,  $N_V$ , of spheres, radius  $r$ , contained per unit volume. The total crack front length that intercepts spheres between  $\theta$  and  $\theta + d\theta$ , denoted here as  $D(\theta)$ , is the product of the probability that a propagating crack will intersect a sphere at angles between  $\theta$  and  $\theta + d\theta$  ( $P = 2rsin\theta d\theta$ ) with the projected interception length ( $2rsin\theta$ ):

$$D(\theta) = 4N_V r^2 \sin^2 \theta d\theta. \quad (7)$$

Integrating  $D(\theta)$  over all  $\theta$  provides the total intercepted crack front length,  $N_V \pi r^2$ . The ratio of  $D(\theta)$  to the total intercepted length (which determines the fraction of the crack front which tilts between  $\theta$  and  $\theta + d\theta$ ) can be used as the stress intensity factor weighting function. Weighting functions,  $F(\theta)$ , for the three morphologies are as follows:

$$F(\theta)_{\text{sphere}} = (4/\pi) \sin^2 \theta d\theta \quad (8a)$$

$$F(\theta)_{\text{disc}} = (4/\pi) \sin^2 \theta d\theta \quad (8b)$$

$$F(\theta)_{\text{rod}} \approx (1.55 + 1.10\theta - 2.42\theta^2 + 1.78\theta^3) \sin\theta \cos\theta d\theta \quad (8c)$$



The result for rod-shaped particles is an approximation obtained by regression analysis, pertinent to length/radius ratios in the range 5 to 25.

Combining Eqs. (1), (3) and (8) and integrating over all possible tilt angles gives the net driving force on the tilted crack. For spherical particles, the relative driving force is given by

$$\langle \mathcal{G} \rangle_{\text{sphere}}^t / \mathcal{G}_{\infty} = (4/\pi) \int_0^{\pi/2} \sin^2 \theta [(\kappa_1^t)^2 + (\kappa_2^t)^2] d\theta, \quad (9)$$

where  $\kappa_i = k_i/K_I$ .  $\langle \mathcal{G} \rangle^t$  prescribes the strain energy release rate only for that portion of the crack front which tilts. To characterize the entire crack front at initial tilt  $\langle \mathcal{G} \rangle^t$  must be qualified by the fraction of the crack length intercepted (and superposed on the driving force that derives from the remaining undeflected portion of the crack). The fraction of crack length which tilts is a product of the number of intersections per unit length ( $0.75 V_f/r$ ) and the average projected line length ( $4\pi/r$ ). The resultant toughening increment, derived directly from the driving forces (cf. Eq. (2)), is given by

$$(\mathcal{G}_c^t)_{\text{sphere}} = (1 + 0.87V_f) \mathcal{G}_c^m \quad (10a)$$

Equivalent results for rod- and disc-shaped particles are

$$(\mathcal{G}_c^t)_{\text{rod}} \approx (1 + V_f(0.6 + 0.007 (H/r) - 0.0001 (H/r)^2)) \mathcal{G}_c^m \quad (10b)$$

$$(\mathcal{G}_c^t)_{\text{disc}} = (1 + 0.56 V_f(r/t)) \mathcal{G}_c^m \quad (10c)$$

where  $(H/r)$  relates the rod length  $H$  to its radius,  $r$ , and  $(r/t)$  is the ratio of the disc radius,  $r$ , to its thickness,  $t$ . The toughening increment due to initial crack tilt is plotted as a function of aspect

ratio ( $R = H/2r$  or  $2r/t$ ) in Figure 3.

For disc-shaped particles of high aspect ratio, tilt of the crack front can act as a considerable source of toughening. However, neither the sphere nor the rod derive appreciable toughening from the initial tilting process. Moreover, the aspect ratio of the rods has little effect on  $\mathcal{G}^t$ . This is evident from the schematic in Figure 4. Changes in aspect ratio, for a constant volume fraction of rods, exert a minimal influence on the fraction of the crack front which intercepts the particles and subsequently, tilts. However, it is readily apparent that the amount of twisted crack will be greatly influenced by the aspect ratio of the rods. The twist contribution should thus dominate the rod-induced toughness.

### 3.2 Subsequent Twist/Tilt

The spatial location and orientation of adjacent particles determines whether the inter-particle crack front will tilt or twist. If adjacent particles produce tilt angles of opposite sign, twist of the crack front will result. Alternately, tilt angles of like sign at adjacent particles cause the entire crack front to tilt. Thus, to evaluate the toughening increment, all possible particle configurations must be considered. Initially, conditions of constant interparticle spacing are analyzed for each particle morphology. This analysis will be followed by an illustrative analysis of variable interparticle spacings pertinent to spherical particles.

#### 3.2.1 Two Particle Interactions at Constant Spacing

##### 3.2.1.1 Spherical Particles

The average twist angle is determined by the mean center-to-center nearest neighboring distance,  $\Delta$ , between particles for randomly arranged

spheres of radius  $r$ , <sup>12</sup>

$$\frac{\Delta}{r} = \frac{e^{8V_f}}{V_f^{1/3}} \int_{8V_f}^{\infty} x^{1/3} e^{-x} dx . \quad (11)$$

where  $V_f$  is the volume fraction of spheres. This spacing dictates the maximum twist angle for a given volume fraction and particle size, as shown schematically in Figure 5. The maximum occurs when the particles are nearly co-planar with the crack, as given by

$$\phi_{\max} = \sin^{-1}(2r/\Delta) . \quad (12)$$

Note that the maximum twist angle (on substitution of Eq. (11)) is exclusively dependent on the volume fraction.

Integrating over all configurations (the limits of which are shown schematically in Figure 5), the net driving force due to twist, for a uniform distribution of twist angles between 0 and  $\phi_{\max}$ , becomes

$$\frac{\langle \mathcal{G} \rangle^T}{\mathcal{G}^{\infty}} = \frac{1}{\phi_{\max}} \int_0^{\phi_{\max}} \left\{ \left( \frac{1}{\phi} \int_0^{\phi} \kappa_1^T d\phi \right)^2 + \left( \frac{1}{\phi} \int_0^{\phi} \kappa_3^T d\phi \right)^2 \right\} d\phi \quad (13)$$

The inner integrals are necessary since the influence of the tilted crack on the twist plane is a maximum at the tilt-twist interface and approaches zero at the center of the twist front.

The toughening increment is computed by synthesizing the tilt and twist components. This is achieved by assuming that the maximum in the toughening for each configuration is accomplished when the crack undergoes maximum twist. Each component is then modified by the amount of crack front subject to twist and tilt. (For derivation of the twist and tilt

fractions, see Appendix A). The average  $\mathcal{G}$  becomes

$$\begin{aligned} \frac{\langle \mathcal{G} \rangle}{\mathcal{G}^\infty} &= \frac{1}{\phi_{\max}} \int_0^{\phi_{\max}} \frac{\sin \phi}{\sin \phi + \cot \phi} [(\kappa_1^t)^2 + (\kappa_2^t)^2] d\phi + \\ &\quad \frac{1}{\phi_{\max}} \int_0^{\phi_{\max}} \frac{\cot \phi}{\sin \phi + \cot \phi} \left[ \left( \frac{1}{\phi} \int_0^\phi \kappa_1^T d\phi \right)^2 + \left( \frac{1}{\phi} \int_0^\phi \kappa_3^T d\phi \right)^2 \right] d\phi \end{aligned} \quad (14)$$

The first term on the right hand side of the equation refers to the fraction of crack front that undergoes tilt at the particle; while the second term refers to the corresponding crack front between particles. In addition  $\langle \mathcal{G} \rangle$  must now be modified by the increased length of the crack front. Incorporation of the corrected length leads to

$$\begin{aligned} \frac{\langle \mathcal{G} \rangle}{\mathcal{G}^\infty} &= \frac{1}{\phi_{\max}} \int_0^{\phi_{\max}} \frac{\sin \phi}{\sin \phi + \cot \phi} [(\kappa_1^t)^2 + (\kappa_2^t)^2] d\phi + \\ &\quad \frac{1}{\phi_{\max}} \int_0^{\phi_{\max}} \frac{\cot \phi \cos \phi}{\sin^2 \phi + \cot \phi} \left[ \left( \frac{1}{\phi} \int_0^\phi \kappa_1^T d\phi \right)^2 + \left( \frac{1}{\phi} \int_0^\phi \kappa_3^T d\phi \right)^2 \right] d\phi \end{aligned} \quad (15)$$

The resultant toughening increment obtained from Eqs (15) and (2) is plotted in Figure 6 for spheres of uniform spacing.

The preceding analysis neglects configurations wherein  $\theta_1$  and  $\theta_2$  are of like sign. Account of such occurrences could be incorporated by presuming that they occur along one-half of the crack front, and by recognizing that crack deflection in this circumstance involves a simple tilt morphology, which may be described by the probabilistic values developed in Section 3.1. However, the relative tendencies for the

intervening crack front to either tilt or remain planar (and bow between the spheres) are not known. Both will exert some influence on the tilt component of the toughening, but can not be predicted from the present analysis.

### 3.2.1.2 Rod-Shaped Particles

Analysis of the twist of the crack front around rod-shaped particles is a more formidable problem, because of difficulties in describing the rod orientation with respect to the crack front and to adjacent rods. Consider the schematic of Figure 7. The effective angle of the tilt (denoted by  $\lambda$ ) is defined by the orientation of the rod with respect to the direction of crack propagation. Hence if  $\mu$  is the angle between the normal from the rod tip to the crack plane and the x-axis (parallel to the direction of propagation), the effective tilt angle is described by

$$\lambda = \tan^{-1}(\tan\theta/\cos\mu) \quad (16)$$

A schematic representation of the twist of a crack between two adjacent rods, shown schematically in Figure 8, indicates that the twist angle,  $\phi$ , is denoted by

$$\phi = \tan^{-1} \left\{ \frac{\alpha \sin\theta_1 + (1-\beta) \sin\theta_2}{\Delta'} \right\}, \quad (17)$$

where

$$\Delta' = \left\{ \left( \frac{\Delta}{H} - \alpha \cos\theta_1 \sin\mu_1 + (1-\beta) \cos\theta_2 \sin\mu_2 \right)^2 + \left( \alpha \cos\theta_1 \cos\mu_1 - (1-\beta) \cos\theta_2 \cos\mu_2 \right)^2 \right\}^{1/2} \quad (18)$$

and  $\alpha$  and  $\beta$  are the relative locations at which the crack plane intercepts the rods.

The best available approximation for the interparticle spacing between randomly arranged rod-shaped particles is that given by Bansal and Ardell<sup>12</sup> for the center-to-center nearest neighbor spacing between finite parallel cylinders:

$$\frac{\Delta}{r} \approx \frac{e^{4V_f}}{V_f^{1/2}} \int_{4V_f}^{\infty} x^{1/2} e^{-x} dx. \quad (19)$$

Substitution of Eqs. (18) and (19) into Eq. (17) indicates that the twist of the crack front is influenced not only by the volume fraction of rods but also by the ratio of the rod length to radius. In addition, it is noted that certain orientations and spatial positions result in a twist angle greater than  $\sim \pi/2$ . Under these conditions crack closure occurs and the local stress intensity,  $k_i$ , must be set equal to zero.

Analytically tractable solutions for  $k_i$ , based on the preceding analysis, are contingent upon imposition of the simplification that the influence of the tilted crack on the twist crack front be expressed in terms of an average tilt angle  $\langle \lambda \rangle$ ;

$$\langle \lambda \rangle = \frac{(\alpha/2)\lambda_1 \sin \theta_1 + ((1-\beta)/2)\lambda_2 \sin \theta_2}{\alpha \sin \theta_1 + (1-\beta) \sin \theta_2} \quad (20)$$

Replacing  $\theta$  by  $\langle \lambda \rangle$  in Eqs. (5) and (6) and integrating over all possible configurations, the strain energy release rate due to twist of the crack front can then be written, for  $\phi < \pi/2$ , as

$$\frac{\langle \mathcal{G} \rangle^T}{\mathcal{G}^\infty} = \frac{4}{\pi^4} \int_{-\pi/2}^{\pi/2} \int_{-\pi/2}^{\pi/2} \int_0^1 \int_0^1 \int_{-\pi/2}^0 \int_0^{\pi/2} \left[ \cos^4(\langle \lambda \rangle / 2) \{ 2\nu \sin^2 \phi + \right. \\ \left. \cos^2 \phi \cos^2(\langle \lambda \rangle / 2) (1 + 2 \sin^2(\langle \lambda \rangle / 2)) \}^2 + \{ \sin \phi \cos \phi (\cos^2(\langle \lambda \rangle / 2) - 2\nu) + \right. \\ \left. \sin^2(\langle \lambda \rangle / 2) (3 \cos^2(\langle \lambda \rangle / 2) - 2\nu)^2 \right] d\theta_1 d\theta_2 d\alpha d\beta d\mu_1 d\mu_2 \quad (21)$$

The preceding equation may be solved using a recursive Gaussian quadrature method.<sup>13</sup>

For  $\theta_1$  and  $\theta_2$  of like-sign, the resultant tilted crack, occurring along one-half of the crack front, has a net driving force (from Eqs. (1), (3) and (4);

$$\frac{\langle \mathcal{G} \rangle^t}{\mathcal{G}^\infty} = \frac{4}{\pi^4} \int_{-\pi/2}^{\pi/2} \int_{-\pi/2}^{\pi/2} \int_0^1 \int_0^1 \int_0^{\pi/2} \int_0^{\pi/2} \cos^4(\bar{\lambda} / 2) d\theta_1 d\theta_2 d\alpha d\beta d\mu_1 d\mu_2, \quad (22)$$

where  $\bar{\lambda} (=1/2[\tan^{-1}(\tan \theta_1 / \cos \mu_1) + \tan^{-1}(\tan \theta_2 / \cos \mu_2)])$  is the average tilt angle across the tilted plane.\*

Normalizing with respect to the length of the undeflected crack, the total strain energy release rate in the presence of rods becomes

$$\langle \mathcal{G} \rangle_{\text{rod}} = \eta/2 \langle \mathcal{G} \rangle^T + \xi/2 \langle \mathcal{G} \rangle^t \quad (23)$$

where  $\eta$  and  $\xi$  are the ratios of the undeflected to deflected crack front lengths and can be expressed as

<sup>†</sup>The integration limits are not all encompassing. In the computer analysis of Eq. (21), the integrand is set equal to zero for any  $\phi \geq \pi/2$ .

\*It is interesting to note that there is little variation (<10%) in  $\langle \mathcal{G} \rangle^t / \mathcal{G}^\infty$  for volume fractions between 0.01 and 0.40 (for a given aspect ratio).

$$\eta = \frac{[(\Delta/H) - \alpha \cos \theta_1 \sin \mu_1 + (1-\beta) \cos \theta_2 \sin \mu_2]}{[(\Delta')^2 + (\alpha \sin \theta_1 + (1-\beta) \sin \theta_2)^2]^{1/2}} \quad (24)$$

and

$$\xi = \frac{[(\Delta/H) - \alpha \cos \theta_1 \sin \mu_1 + (1-\beta) \cos \theta_2 \sin \mu_2]}{[(\Delta')^2 + (\alpha \sin \theta_1 - (1-\beta) \sin \theta_2)^2]^{1/2}} \quad (25)$$

Since both  $\eta$  and  $\xi$  are functions of the spatial variables,  $\theta$ ,  $\mu$ ,  $\alpha$  and  $\beta$ , they must be included in the integrals in Eqs: (21) and (22).

The toughening increment derived from Eq. (23) by numerical integration is plotted in Figure 9 for three aspect ratios. It is instructive to note that the toughening increment becomes volume fraction invariant above  $\sim 0.2$ . The influence of aspect ratio,  $R$ , tends to an asymptotic limit at large values of  $R$ , such that the maximum toughening induced by rod-shaped particles approaches  $\sim 4$ .

### 3.2.1.3 Disc Shaped Particles

Crack deflection toughening by disc-shaped particles can be analyzed by minimal modification to the analysis of toughening by rod-shaped particles presented in the preceding section. Noting that the effective tilt angle  $\lambda \equiv \theta$ , by virtue of the particle geometry (cf. Figure 10), the average tilt angle  $\langle \lambda \rangle$  (equivalent to Eq. (20) for the rod) can be expressed as

$$\langle \lambda \rangle = \frac{(\alpha/2) \theta_1 \sin \theta_1 + ((1-\beta)/2) \theta_2 \sin \theta_2}{\alpha \sin \theta_1 + (1-\beta) \sin \theta_2} \quad (26)$$



The interparticle spacing,  $\Delta$ , in the absence of a rigorous solution for the center-to-center nearest neighbor spacing, is approximated by the point-to-point spacing through the volume<sup>12</sup>,  $\langle \Delta \rangle$ ,

$$\langle \Delta \rangle \sim N_V^{-1/3} . \quad (27)$$

Employing this relation, an association between the relative dimensional ratios of the rod,  $(\Delta/H)$ , and the disc  $(\Delta/2r)$  can be established;

$$\frac{\langle \Delta \rangle_{\text{rod}}/H}{\langle \Delta \rangle_{\text{disc}}/2r} = \frac{(r_{\text{rod}}/H)^{2/3}}{2(t/r_{\text{disc}})^{1/3}} . \quad (28)$$

This relation permits an approximate computation of  $\langle \mathcal{G} \rangle$  for discs, using the same expressions derived for rods.

The resultant toughening is plotted in Figure 11 and compared to the toughening derived from initial tilt. It is noted that, although initial tilting induces significant toughening, the major toughening, as in the case of spheres and rods, again derives from crack front twist.

### 3.2.2 Two Particle Interactions With Variable Interparticle Spacing

Incorporating a standard normal distribution of interparticle spacings into Eq. (14) results in a modified strain energy release rate,

$$\frac{\langle \mathcal{G} \rangle}{\mathcal{G}_\infty} = \frac{1}{\sqrt{2\pi}} \left[ \int_{-z_0}^3 e^{-z^2/2} (\mathcal{G}^T(z) + \mathcal{G}^t(z)) dz + (\mathcal{G}^T(z_0) + \mathcal{G}^t(z_0)) \int_{-3}^{-z_0} e^{-z^2/2} dz \right] . \quad (29)$$

where  $z = [x - (\Delta/r)]/\sigma$ , and  $z_0$  defines the interparticle spacing below which particle contact occurs,  $z_0 = (2-(\Delta/r))/\sigma$  (the second term on the right-hand side represents the fraction of contiguous particles). Predictions of toughness afforded by crack deflection around spheres are plotted in Fig. 6, for spheres with and without a spacing distribution. The toughness becomes insensitive to the value of the standard deviation for  $\sigma > 0.40 (\Delta/r)$ . Incorporation of the distribution function increases the toughness by  $\sim 40\%$ . The toughness becomes insensitive to the value of the standard deviation for  $\sigma \geq 0.40 (\Delta/r)$ . This result is contrary to the intuitive rationale that the best mechanical properties are expected to coincide with the best dispersion of second phase particles, and consequently, the lowest standard deviation. However, contacting spheres, which result in twist angles of  $\pi/2$ , minimize the crack driving force, and exert a more pronounced effect than spheres separated by spacings  $> \Delta$ . It is interesting to note here that in the similar problem of dislocation motion, it is the largest spacing between obstacles which controls the dislocation motion; whereas the smallest spacings between obstacles appears to determine the crack propagation behavior.

### 3.3 Surface Area Approximation

Surface area increases are regarded as a lower bound estimate of the toughening increment. It would be expedient, then, to compare this lower bound,  $\mathcal{G}^S$ , with the toughness calculated using the stress intensity approach.

The fracture surface morphology induced by deflection around spherical particles can be modelled as an array of cones with heights ranging from

0 to  $r$ , the sphere radius. The toughness increase associated with this surface area can be estimated as,

$$\frac{(\mathcal{G}_c^s)_{\text{sphere}}}{\mathcal{G}_c^m} = \frac{1}{2} \left[ 1 + \frac{\sqrt{(\Delta/2)^2 + r^2}}{\Delta/2} \right]. \quad (30)$$

This relation is plotted versus volume fraction in Figure 6 where it is compared with the deflection calculations. The stress intensity prediction substantially exceeds the surface area lower bound. The excess energy presumably results in phonon release.

Similar calculations can be accomplished for rod-shaped particles by assuming that the fracture morphology comprises cones (height, 0 to  $H$ ) for the twisted crack front and 'tents' (height, 0 to  $H$ ) for the tilted crack. The resultant toughness due to the additional surface area can be described\* by

$$\frac{(\mathcal{G}_c^s)_{\text{rod}}}{\mathcal{G}_c^m} = \frac{2}{\pi \Delta} \int_0^{\pi/2} \sqrt{\left(\frac{\Delta}{2}\right)^2 + \left(\frac{H}{2r} r \sin \theta\right)^2} d\theta + \frac{1}{\pi} \int_0^{\pi/2} \sec \theta d\theta. \quad (31)$$

Comparing the surface area calculations with the stress intensity predictions in Figure 12 again demonstrates the significant difference in the two calculations.†

\*The second term in Eq. (31), deriving from the tilted crack surface, is treated as a constant (evaluated at  $\pi/\Delta$ ). Recall that in Eq. (22) there is little variation in the corresponding term,  $\langle \mathcal{G} \rangle^t$ , derived from the fracture mechanics analysis.

†At high volume fractions and at large aspect ratios, the values of toughening from the fracture mechanics predictions and the surface area approximation converge. This is probably due to neglect of particle-particle contact in the surface area treatment.

### 3.4 Deflection Profiles

In addition to the toughness predictions formulated in Section 3.2, it is of interest (to facilitate comparison with experimental observations<sup>6</sup>) to examine the projection of the deflected crack. To predict the crack front profile, the frequency of twist angles,  $\phi$ , and tilt angles,  $\lambda$ , must be calculated for all  $\phi$  and  $\lambda$ . For rod-like and disc-like morphologies, the density function of  $\phi$  and  $\lambda$  cannot be solved analytically. However, estimated densities can be computed using an iteration process with random numbers substituted for  $\theta_1$ ,  $\theta_2$ ,  $\mu_1$ ,  $\mu_2$ ,  $\alpha$  and  $\beta$  in Eqs. (17) and (20). By summing the resultant deflection angles in designated intervals, an estimate of the frequency distribution is provided. As an example, frequency distributions for twist angles of rods ( $V_f = 0.2$ ) with three aspect ratios are plotted in Figure 13. The predictions demonstrate the significant influence of the aspect ratio on the distribution of twist angles, revealing the expected higher average angles at larger aspect ratios.

The instantaneous crack front, however, will not experience the maximum twist, but will sample deflections at all stages. This effect is incorporated by first, qualifying  $\alpha$  and  $\beta$  (refer to Figure 8) with a random variable between 0 and 1 (designated as  $\omega$ ) to account for the linear progression of the crack front from its interception with the particles ( $\omega = 0$ ) to the point of maximum twist ( $\omega = 1$ ). Thus the average twist angle,  $\hat{\phi}$ , for rods intercepted by a normal plane (of Eq. (17)) would be

$$\hat{\phi} = \tan^{-1} \left[ \frac{\alpha \omega \sin \theta_1 + (1-\beta) \omega \sin \theta_2}{\Delta''} \right] \quad (32)$$

$$\text{where } \Delta'' = \left\{ \left( \frac{\Delta}{H} - \alpha \omega \cos \theta_1 \sin \mu_1 + (1-\beta) \omega \cos \theta_2 \sin \mu_2 \right)^2 + \left( \alpha \omega \cos \theta_1 \cos \mu_1 - (1-\beta) \omega \cos \theta_2 \cos \mu_2 \right)^2 \right\}^{1/2}$$

Then, the summed frequencies are further qualified by the probability,  $\mathcal{P}$ , that the normal plane will intersect a given angle. For rods,

$$\mathcal{P} \cong [\alpha \cos \theta_1 \cos \mu_1 + (1-\beta) \cos \theta_2 \cos \mu_2] / 2 \quad (33a)$$

while for discs,

$$\mathcal{P} \cong [\alpha' \cos \theta_1 \cos \mu_1 + (1-\beta)' \cos \theta_2 \cos \mu_2] / 2 \quad (33b)$$

where  $\alpha' = 1/(2\pi)[2 \cos^{-1}(1-2\alpha) - \sin(2 \cos^{-1}(1-2\alpha))]$   
and  $(1-\beta)' = 1/(2\pi)[2 \cos^{-1}(1-2\beta) - \sin(2 \cos^{-1}(1-2\beta))]$ .

A similar procedure is used to determine the distribution of average tilt angles,  $\hat{\lambda}$ . For either rods or discs, the average tilt angle intercepted by the normal plane is

$$\hat{\lambda} = \tan^{-1} \left[ \frac{\alpha \omega \sin \theta_1 + (1-\beta) \omega \sin \theta_2}{\Delta''} \right] \quad (34)$$

The number of occurrences for a particular  $\hat{\lambda}$  is again modified by  $\mathcal{P}$  in Eq. (33). Smoothed frequency curves for three aspect ratios of rods ( $V_f = 0.2$ ) are plotted in Figure 14. As the aspect ratio increases, the shift to higher twist angles is evident. The tilt angle frequency monotonically decreases from  $0^\circ$ , with a greater proportion of small tilt angles existing for less elongated rods. These plots should provide a basis for comparisons with experimentally determined deflections.

#### 4. IMPLICATIONS AND CONCLUSIONS

A prediction of the increase in toughness due to crack deflection is formulated, based upon a fracture mechanics approach. The model demonstrates the diminution of the driving force at the tip of a tilted and/or twisted crack. As evident from the outset, the toughness predictions are invariant with particle size. Clearly, the increase in toughness only depends on particle shape and the volume fraction of second phase. The most effective morphology for deflecting propagating cracks is the rod of high aspect ratio, which can account for four fold increases in fracture toughness. The toughening arises primarily from twist of the crack front between particle configurations which cause a crack to twist at angles  $\geq \pi/2$ , as indicated by deflection profiles. Less effective in toughening are disc-shaped particles and spheres, respectively. The fracture toughness, regardless of morphology, is determined by twist of the crack front at its most severe configuration, rather than the initial tilt of the crack front. Only for the case of disc-shaped particles does the initial titling of the crack front provide significant toughening; however, the twist component still overrides the tilt-derived toughening.

Additional important features of the deflection analysis include the appearance of asymptotic toughening for the three morphologies at volume fractions in excess of 0.2. It is also noted that a significant influence on the toughening by spherical particles is exerted by the interparticle spacing distribution; greater toughening is afforded when spheres are nearly contacting such that twist angles approach  $\pi/2$ .

These predictions provide the basis for design of a high toughness two-phase ceramic materials. The ideal second phase, in addition to maintaining chemical compatibility, should be present in amounts of 0.10 to 0.20 volume percent. Greater amounts may diminish the toughness increase due to overlapping particles. Particles with high aspect ratios are most suitable for maximum toughening especially particles with rod-shaped morphologies.

#### Acknowledgements

The research of K. T. Faber was sponsored by The Carborundum Company, Niagara Falls, N.Y., and of A. G. Evans by ONR (Contract No. 00014-81-K-0362). Computational assistance was provided by M. D. Drory.

REFERENCES

1. F. F. Lange, Phil. Mag., 22, 983 (1970).
2. A. G. Evans, Phil. Mag., 26, 1327 (1972).
3. D. J. Green, P. S. Nicholson and J. D. Embury, J. Mat. Sci. 14, 1657-1661 (1979).
4. D. B. Binns, Science of Ceramics (ed. G. H. Stewart), Academic Press, London, 1962, p. 315.
5. K. T. Faber, A. G. Evans and M. D. Drory, in Fracture Mechanics of Ceramics (ed. R. C. Bradt, A. G. Evans, D. P. H. Hasselman and F. F. Lange), Vol. 5-6. Plenum Press, New York, 1982 in press.
6. K. T. Faber and A. G. Evans, to be published.
7. B. Cotterell and J. R. Rice, Int. J. Frac. 16 [2] 155-159 (1980).
8. B. R. Lawn and T. R. Wilshaw, Fracture of Brittle Solids, Cambridge University Press, Cambridge, 1975, p. 53.
9. B. A. Bilby, G. E. Cardew and I. C. Howard, Proc. 4th Int. Conf. on Frac. (ed. D. M. R. Taplin), Vol. 3, Univ. of Waterloo Press, Waterloo, 1977, p. 197.
10. R. L. Fullman, Trans. AIME, 197, 447 (1953).
11. C. W. Corti, P. Cotterill, and G. A. Fitzpatrick, Int. Metall. Rev., 19, 77 (1974).
12. P. P. Bansal and A. J. Ardell, Metallography, 5, 97 (1972).
13. H. Lipps, Recursive Gaussian Quadrature for Multi-Dimensional Integrals (RGAUSS), CERN Program.
14. S. Chandrasekhar, Rev. Mod. Phys. 15, 1 (1943).
15. D. J. Green, submitted to Communications of the American Ceramic Society.
16. F. F. Lange, J. Amer. Ceram. Soc. 54 [12] 614 (1971).



Appendix A

Fracture Toughness Increases From Crack Bowing as Related to Obstacle  
Shape, Volume Concentration and Penetrability

Green<sup>15</sup> proposed a simple expression to correlate fracture toughness data attributed to crack bowing, and hence, to infer an effective obstacle penetrability. The expression, based on curve fitting the numerical expressions by Evans<sup>2</sup> and Green et al.<sup>3</sup>, is of the form

$$\frac{\sigma_A}{\sigma_c} = \sum_{n=0}^{n=7} A_n \left( \frac{r'}{C} \right)^n \quad (A1)$$

where  $\sigma_A$  is the stress needed to propagate a crack through a series of obstacles,  $\sigma_c$  the fracture stress when no obstacles are present,  $r'$  is some function of the obstacle half-dimension,  $r_0$ , and can be modified to account for obstacle penetrability. From the above expression, the penetrability-spacing ratio ( $r'/c$ ) can be related to the fracture toughness by

$$\left( \frac{\sigma_A}{\sigma_c} \right) = \frac{E_o}{E_o - r_0} = \left( \frac{K_c}{K_c^o} \right) \quad (A2)$$

where the matrix properties are denoted by the subscript (or superscript) o. The nearest neighbor obstacle spacing,  $C$ , may also be a function of obstacle strength. Strong particles should bow cracks between nearest neighbor particles (where  $2C = N_A^{-1/2} - 2r_0$  and  $N_A$  is the number of particles per unit area of fracture surface); whereas the spacing between weak obstacles, which do not cause significant bowing of the crack front, can be best described by the mean free path. Incorporating these effects,

Green<sup>15</sup> demonstrated that data on glass-alumina composites, studied by Lange<sup>16</sup>, are consistent with an obstacle strength,  $r'/r_0 = 0.64$ , but that the strength increases with increasing particle size.

The crack bowing theory is clearly not predictive at its present level of development. In addition to Green's analysis, two additional features require consideration. First, the operative interparticle spacing,  $C$ , can exhibit a multitude of possibilities, as discussed in a review by Corti et al.<sup>11</sup> The pertinent interparticle spacing should be consistent with the nature of the property-controlling phenomenon (e.g. mean free path vis-a-vis nearest neighbor spacing). For example, Figure 15 presents a comparison between Green's prediction for crack bowing between "strong" obstacles, (where the spacing,  $2C = N_A^{-1/2} - 2r_0$ ) and the more precise prediction also based on nearest neighbor spacing,<sup>12</sup>

$$\frac{2C}{r_0} = \frac{1}{3\pi V_f} \int_0^{6V_f} \frac{\Gamma(1/2, x) e^x dx}{(6V_f - x)^{1/2}} \quad (A3)$$

where  $\Gamma(1/2, x)$  is the incomplete gamma function. Second, obstacle morphology is likely to have a significant effect on the magnitude of crack bowing. The effective value of the obstacle size,  $r_0$ , will be highly sensitive to the orientation of angular obstacles with respect to the crack front. Modifications to Green's results are plotted in Figure 16. It can be seen that rods or discs of low aspect ratio,  $R$ , can reduce the effectiveness of crack bowing, while high aspect ratio particles enhance bowing. For weak obstacles, the magnitudes of the morphology effects are reduced, but similar trends are followed.

Applications of the above crack bowing solutions to experimental data assumes that toughening increases are due, in total, to crack bowing. In order to differentiate the fractional toughening attributed to crack bowing, an independent measure of the obstacle penetrability is necessary (in lieu of empirically determining penetrability from fitting toughness measurements to the bowing theory). Material parameters which might influence the obstacle penetrability are the ratio of the matrix to obstacle toughness and the strength and coherency of the obstacle-matrix interface.

Appendix B

Determination of Tilt and Twist Fractions

Referring to Figure 17, let  $x$  be the segment of the crack front undergoing tilt and let  $y$  be the twist segment. From trigometric relations, the fraction of tilt and twist can be written as

$$x_{\text{frac}} = \frac{r \sin \phi}{r \sin \phi + r \cos \phi / \sin \phi} = \frac{\sin \phi}{\sin \phi + \cot \phi} \quad (\text{B1})$$

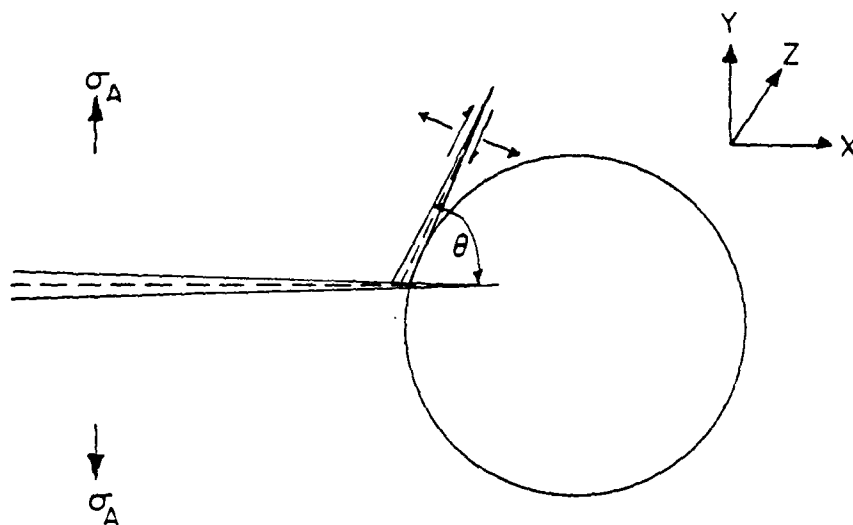
$$y_{\text{frac}} = \frac{r \cos \phi / \sin \phi}{r \sin \phi + r \cos \phi / \sin \phi} = \frac{\cot \phi}{\sin \phi + \cot \phi} \quad (\text{B2})$$

In comparing these fractions to the undeflected crack front of unit length, it can be observed from Figure 17 that there is no increase in the crack front length of the tilted fraction,  $x_{\text{frac}}$ . However, the ratio of the undeflected segment  $y'$  to the twisted segment,  $y$ , can be expressed as

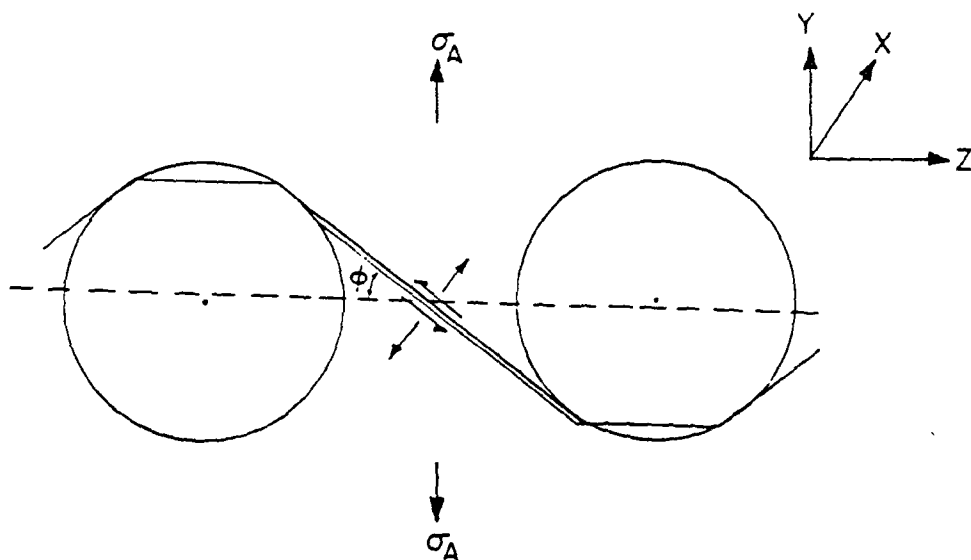
$$y'/y = \cos \phi . \quad (\text{B3})$$

- Figure 1. Schematics of typical crack deflection: a) tilt, and b) twist of the crack front.
- Figure 2. Angular functions (a)  $K_{11}$  and  $K_{21}$  vs. tilt angle,  $\theta$ , used to modify the applied stress intensity  $K_I$  and (b)  $K_{11}$ ,  $K_{12}$ ,  $K_{31}$  and  $K_{32}$  vs. twist angle,  $\phi = \theta$ , used to modify the local stress intensity factors,  $k_1$  and  $k_2$ .
- Figure 3. Normalized toughening increment for initial tilt of a crack vs. aspect ratio for three particle morphologies.
- Figure 4. Schematic of twist of a crack around rods of two aspect ratios,  $R$ , at constant volume fraction.
- Figure 5. Schematics of two spheres whose centers are separated by a distance,  $\Delta$ , demonstrating a) minimum twist and b) maximum twist, the limits over which the net crack driving force is calculated (Eqs. 13-15).
- Figure 6. Relative toughness predictions from crack deflection model for spherical particles including the effect of a distribution in interparticle spacing. Predictions are compared to the relative toughness due to surface area increase.
- Figure 7. Schematic of a rod-shaped particle tilted at angle,  $\theta$ , with the x-z plane and rotated by angle,  $\mu$ , to the direction of crack propagation (parallel to the x-axis). The angle,  $\lambda$ , defines the tilt angle.
- Figure 8. Schematic of twist of a crack between two adjacent rod-shaped particles whose centers (in the x-z plane) are separated by a distance,  $\Delta$ .

- Figure 9. Relative toughness predictions from crack deflection model for rod-shaped particles of three aspect ratios.
- Figure 10. Schematic of adjacent disc-shaped particles whose centers are separated by a distance,  $\Delta$ . Discs are tilted at angles,  $\theta_1$  and  $\theta_2$ , with respect to the x-z plane, and are offset by angles,  $\mu_1$  and  $\mu_2$ , with the direction of crack propagation (parallel to the x-axis).
- Figure 11. Relative toughness predictions for initial tilt and for maximum twist based on crack deflection model for disc-shaped particles of two aspect ratios.
- Figure 12. Relative toughness predictions compared with surface area approximations for rod-shaped particles of two aspect ratios.
- Figure 13. Frequency distribution for maximum twist angles for rods of three aspect ratios present in volume fractions of 0.2.
- Figure 14. Frequency distributions for average twist and tilt angles intercepted by a normal plane for rods of three aspect ratios, present in volume fractions of 0.2.
- Figure 15. Toughness predictions for crack bowing between "strong" obstacles, calculated using two interparticle spacings.
- Figure 16. Toughness predictions for crack bowing between spheres (Ref. 15), discs and rods.
- Figure 17. Schematic of twist and tilt fractions of crack front at maximum twist between two spheres.



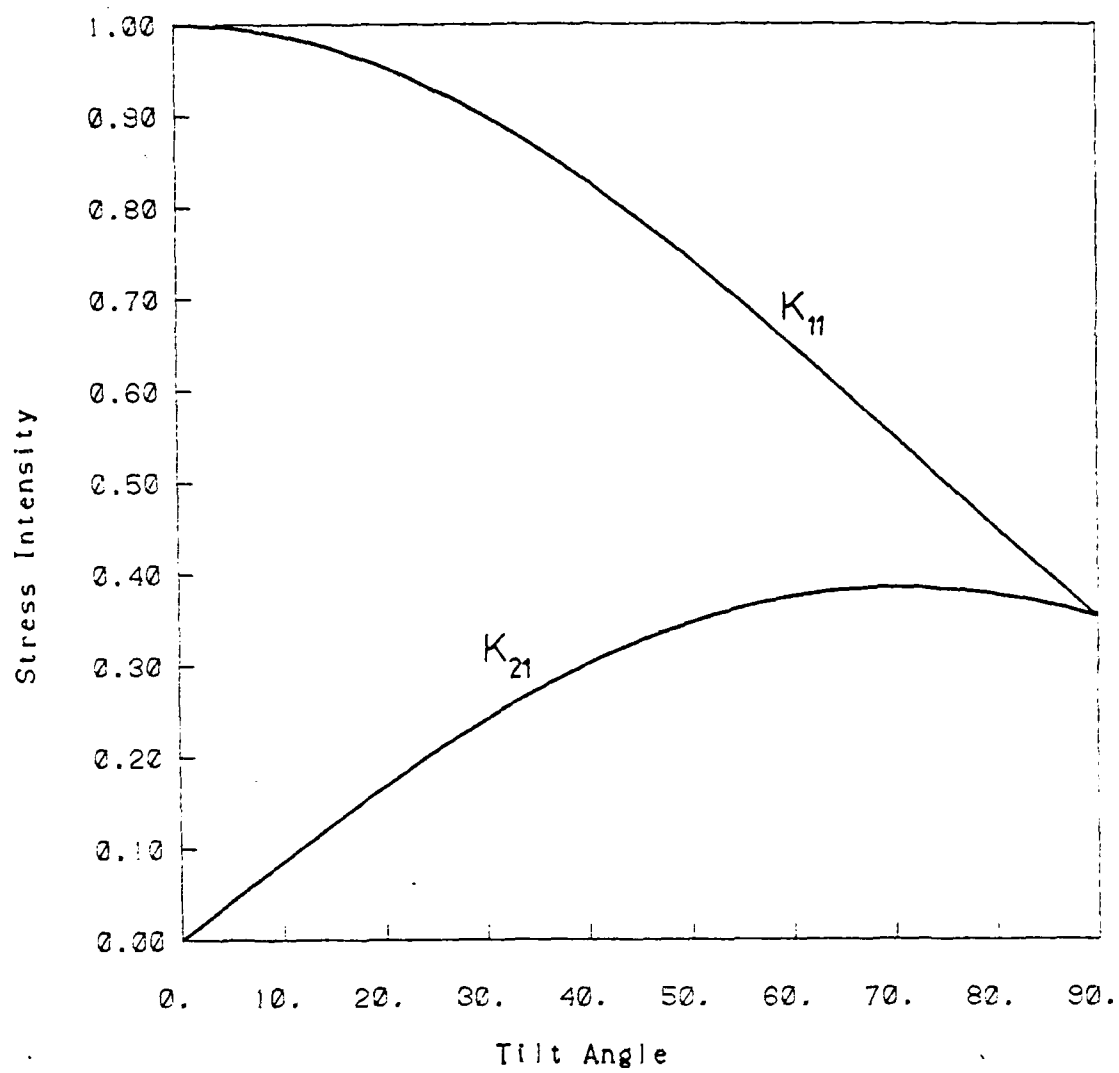
a) CRACK TILTED AT ANGLE  $\theta$  ABOUT Z AXIS



b) CRACK TWISTED AT ANGLE  $\phi$  ABOUT X AXIS

XBL 817-6062

Fig. 1



XBL 818-11476

Fig. 2a



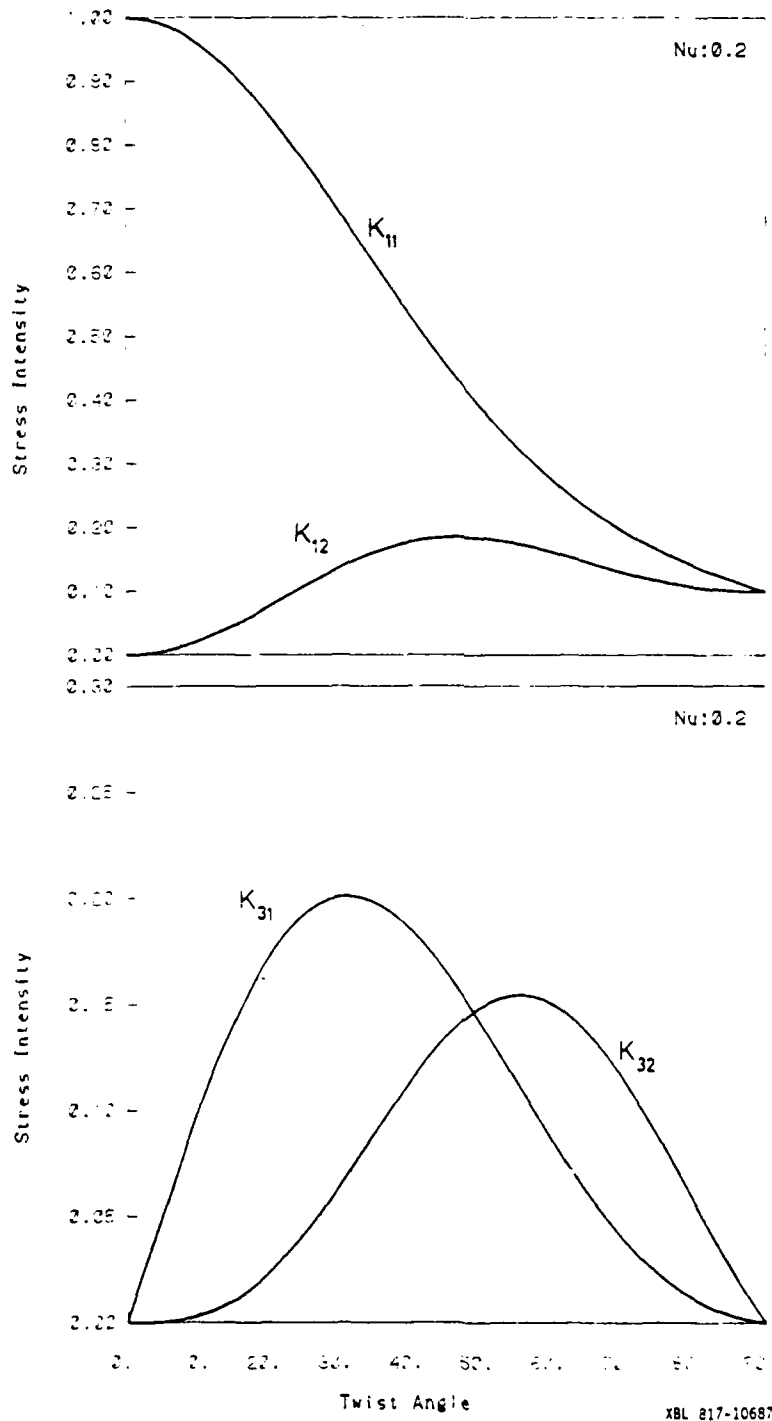
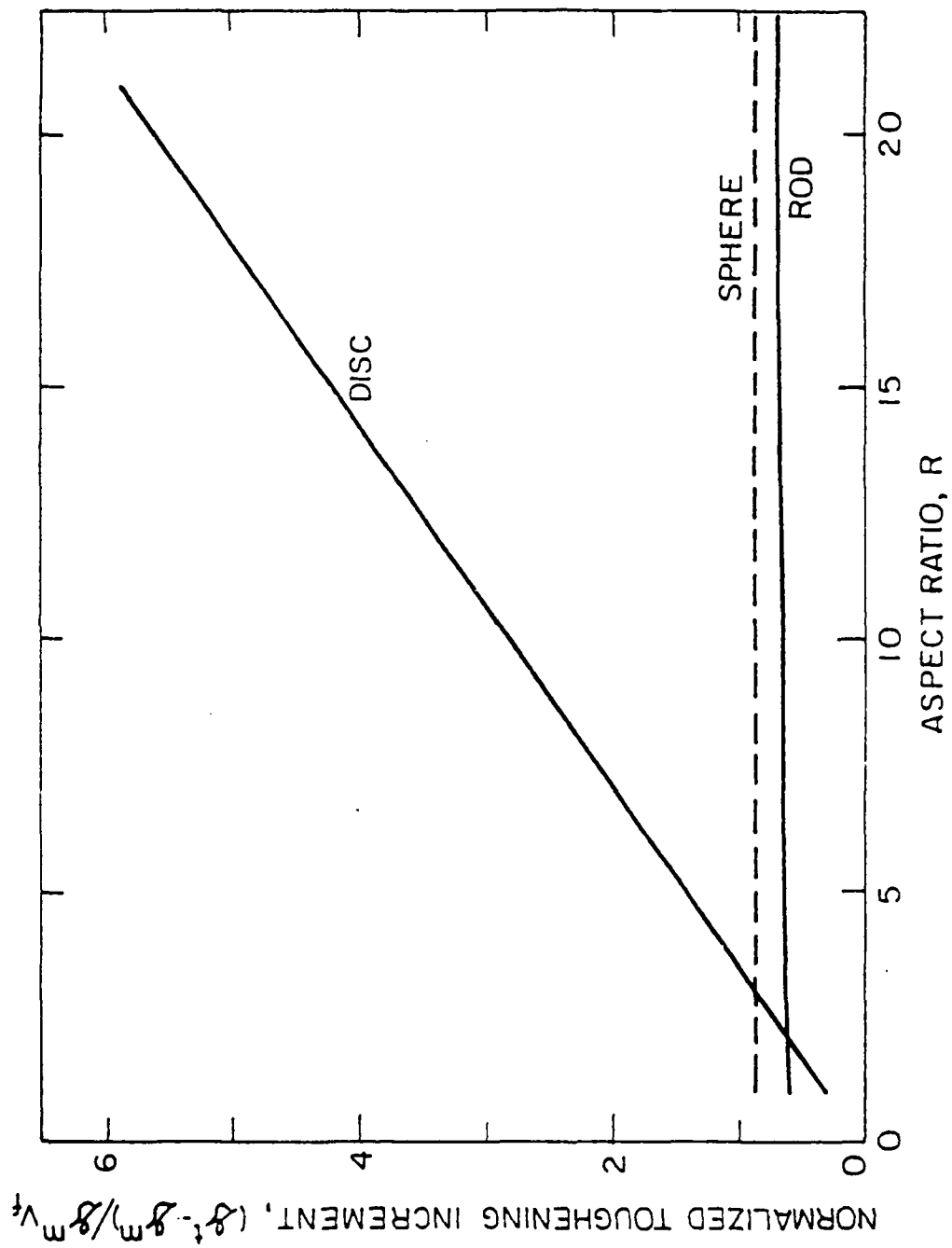
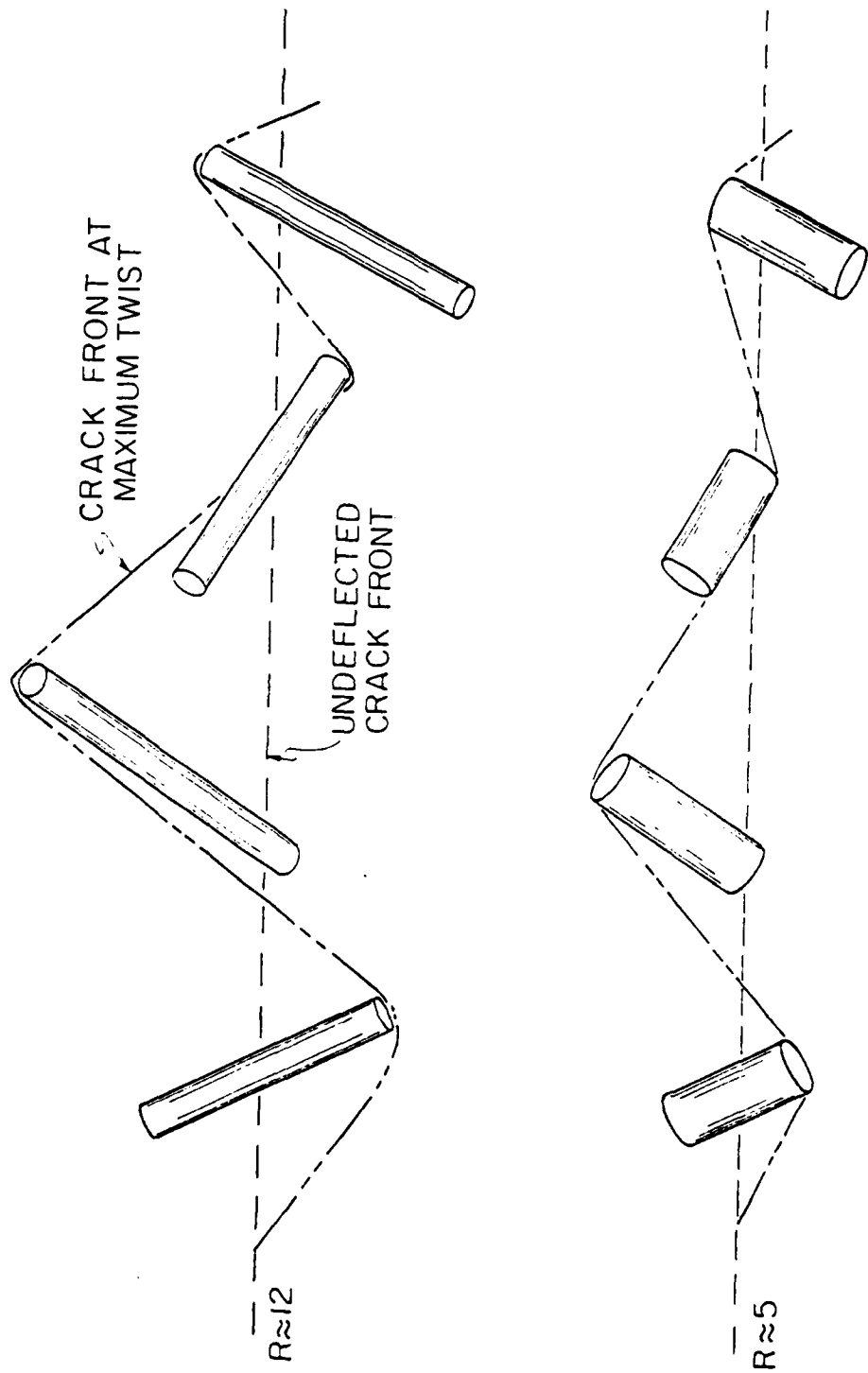


Fig. 2b



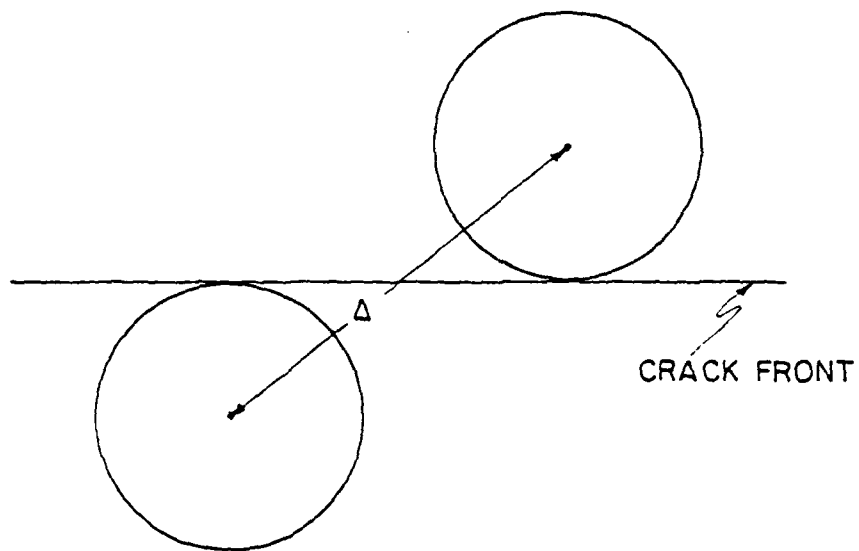
XBL 823-5480

Fig. 3

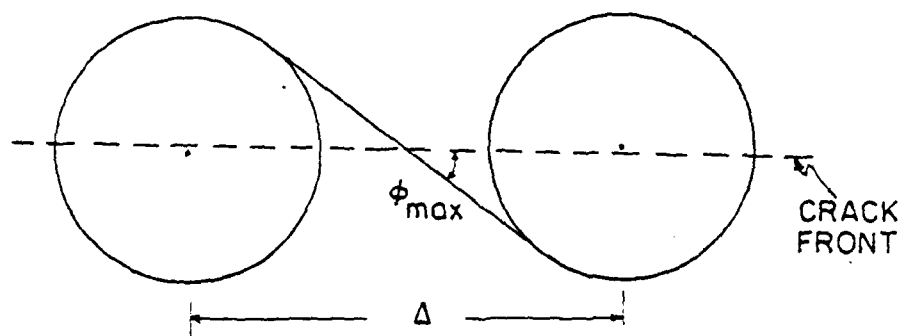


XBL 823-5486

Fig. 4



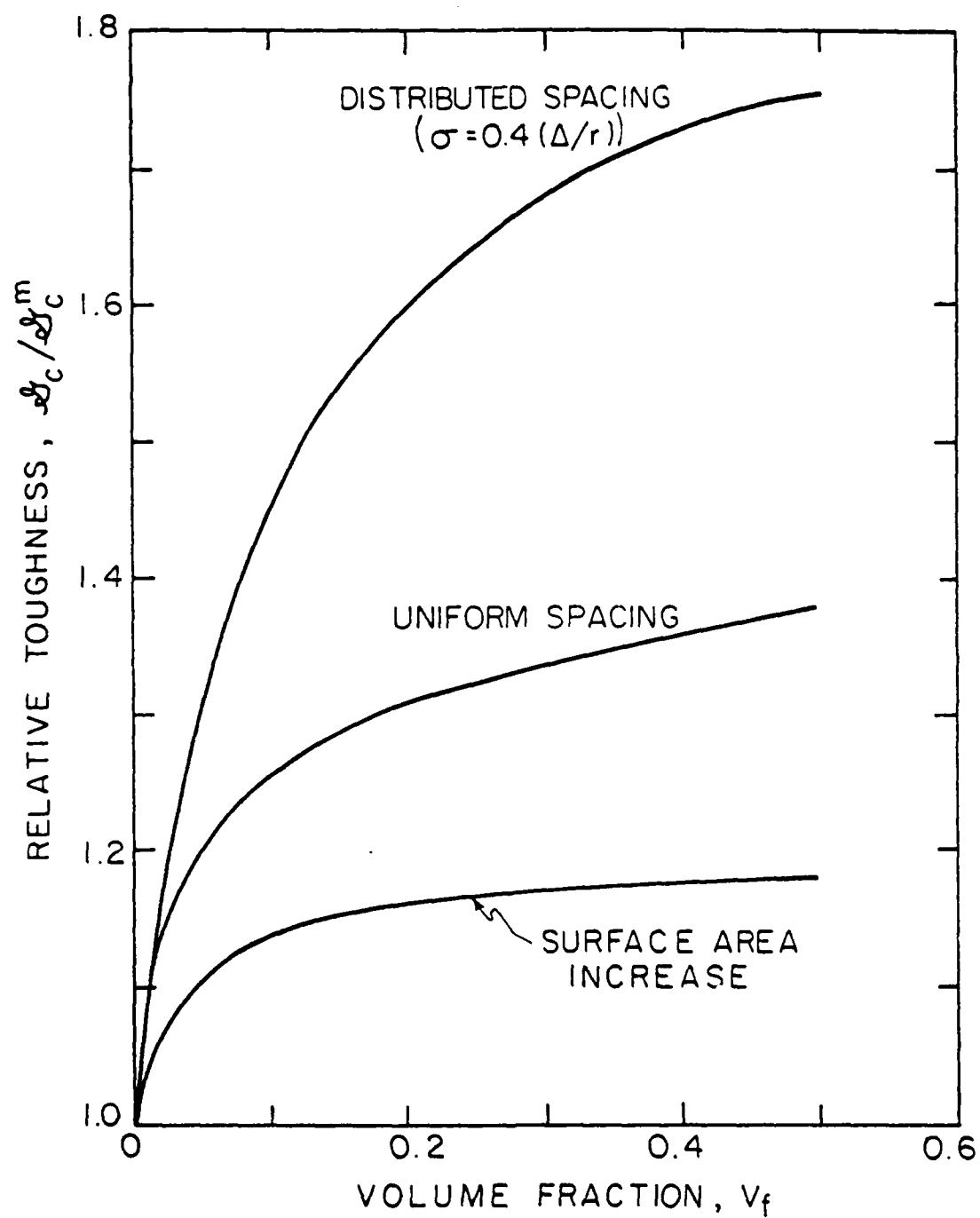
a)  $\phi = 0$  FOR GIVEN NEAREST NEIGHBOR  
CENTER-TO-CENTER DISTANCE,  $\Delta$



b)  $\phi = \phi_{\max}$  FOR GIVEN NEAREST NEIGHBOR  
CENTER-TO-CENTER DISTANCE,  $\Delta$

XBL 817-6063

Fig. 5

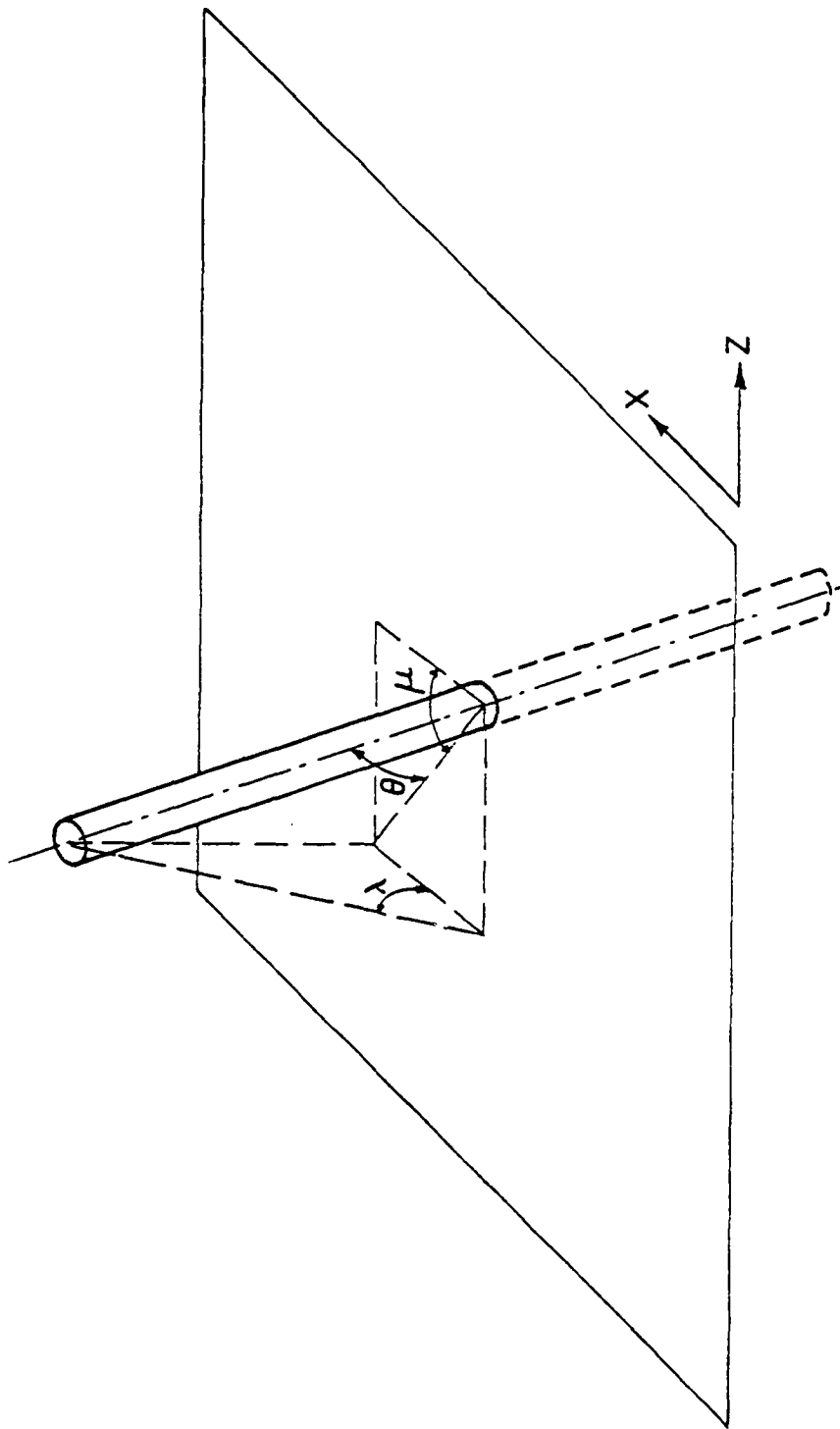


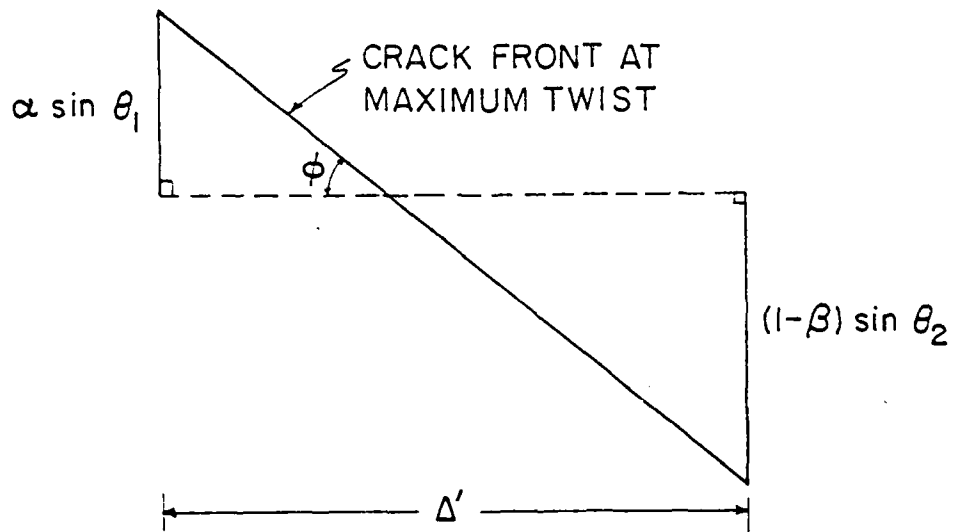
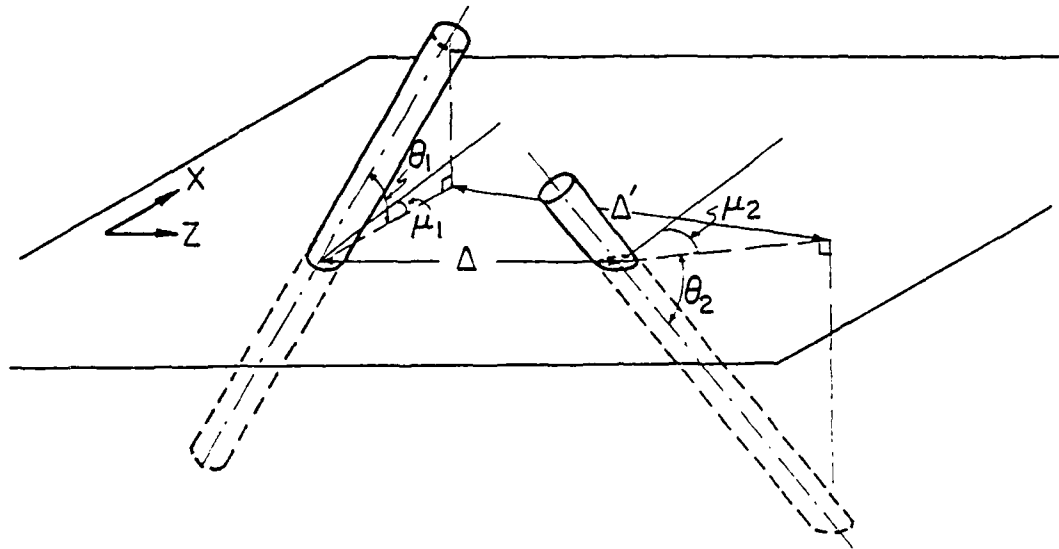
XBL825-5789

Fig. 6

XBL 8111-12856

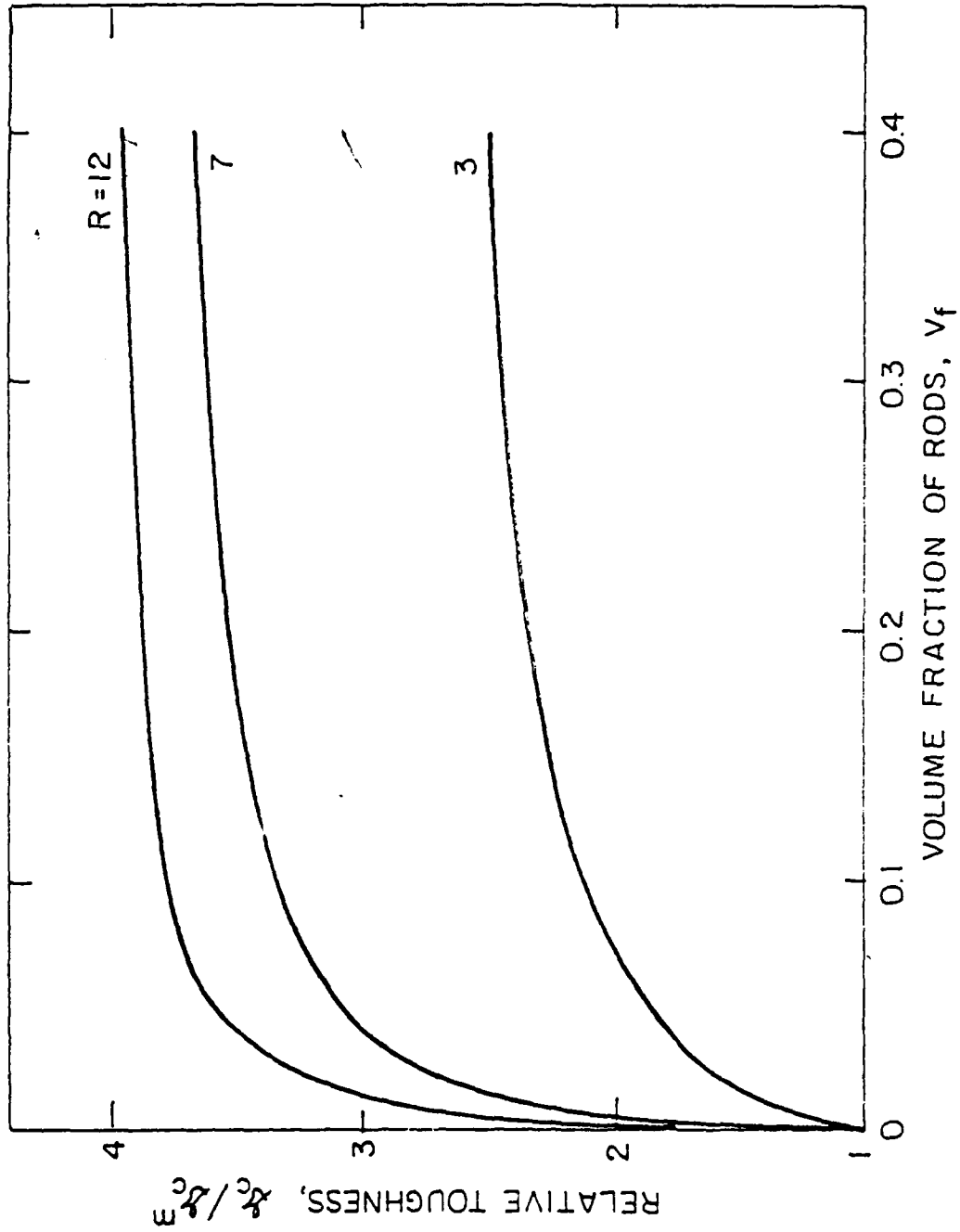
Fig. 7





XBL 8111-12858

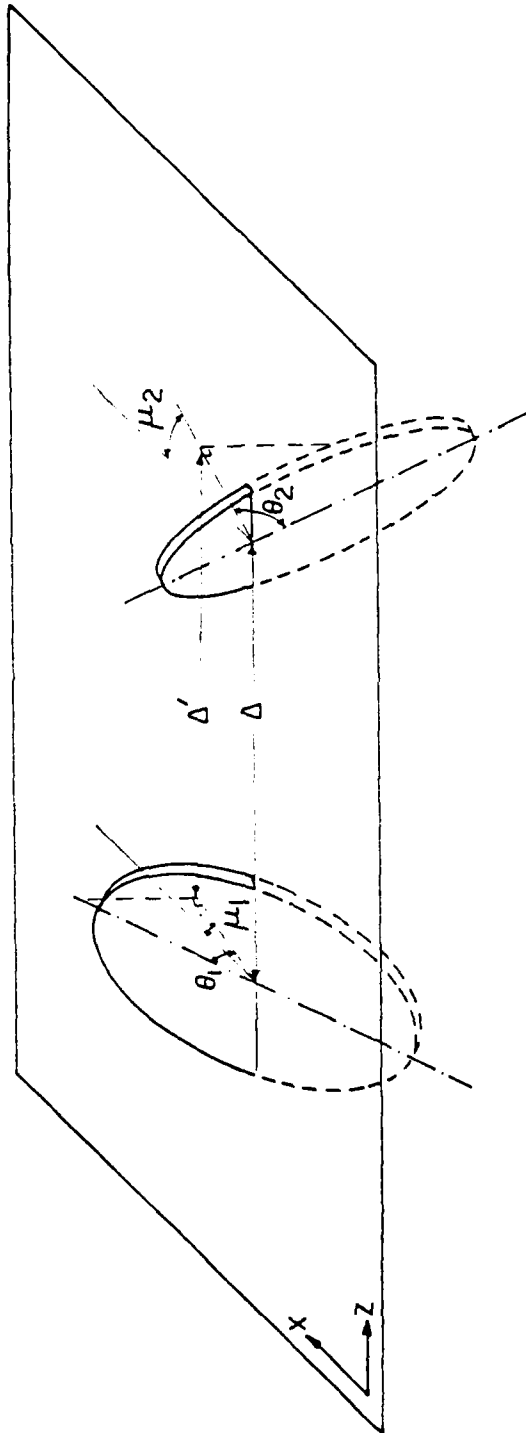
Fig. 8



XBL 823-5481

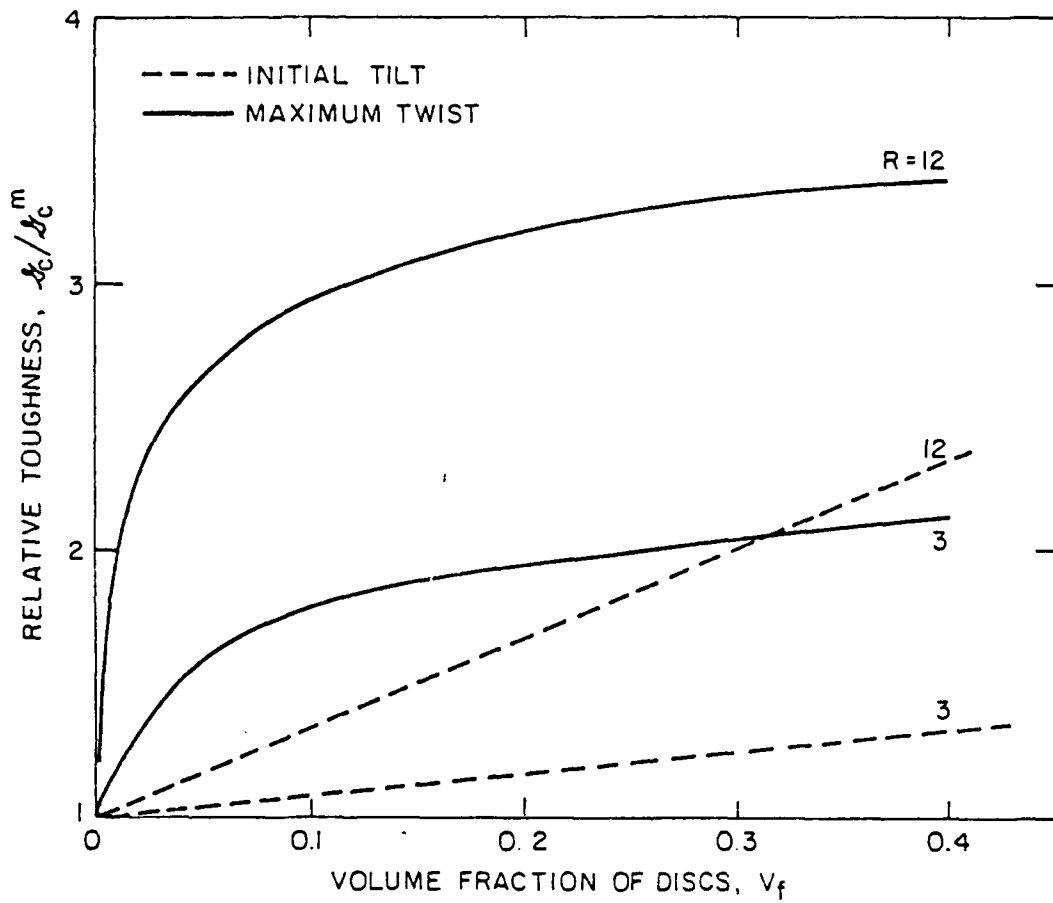
Fig. 9





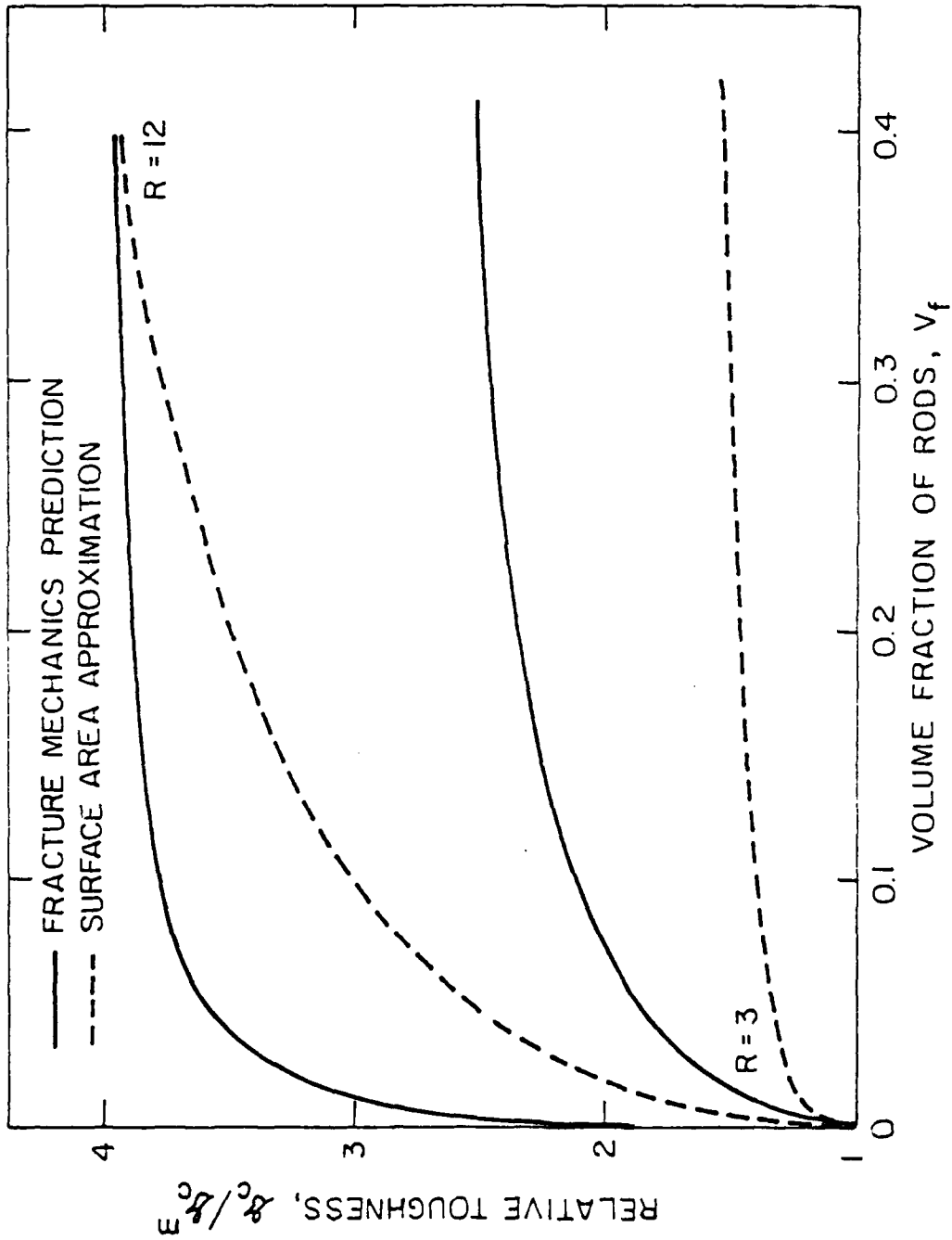
XBL 823 - 5484

Fig. 10



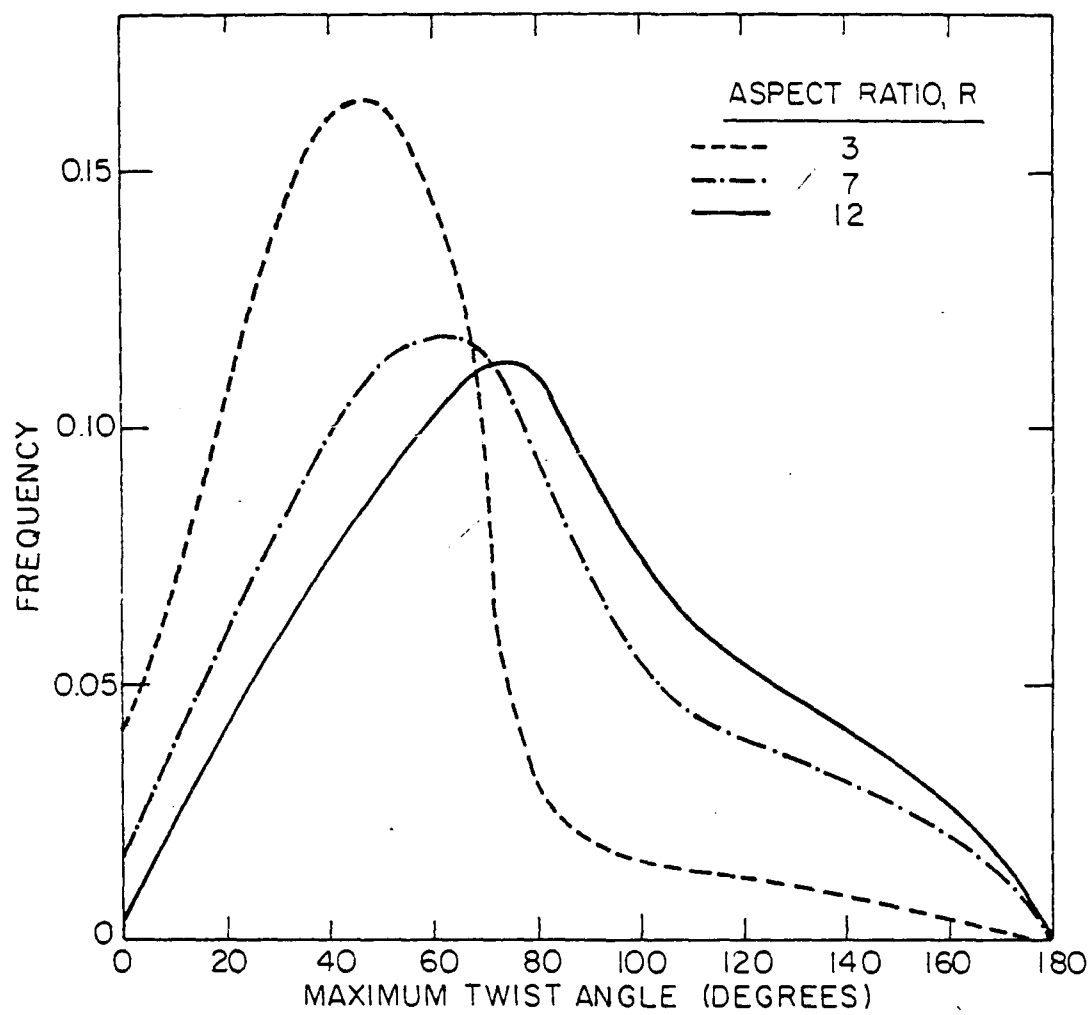
XBL 823-5483

Fig. 11



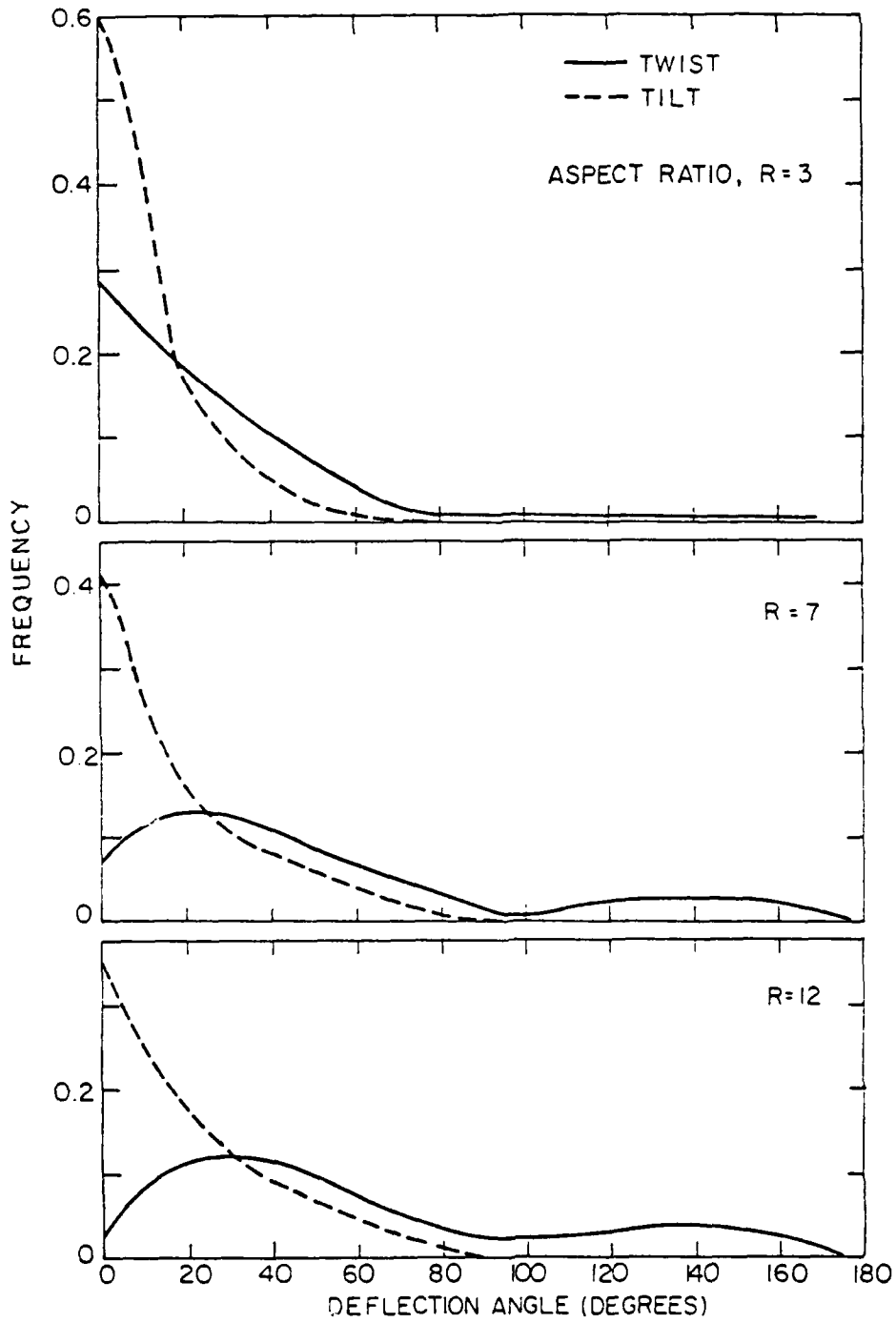
XBL 823-5482

Fig. 12



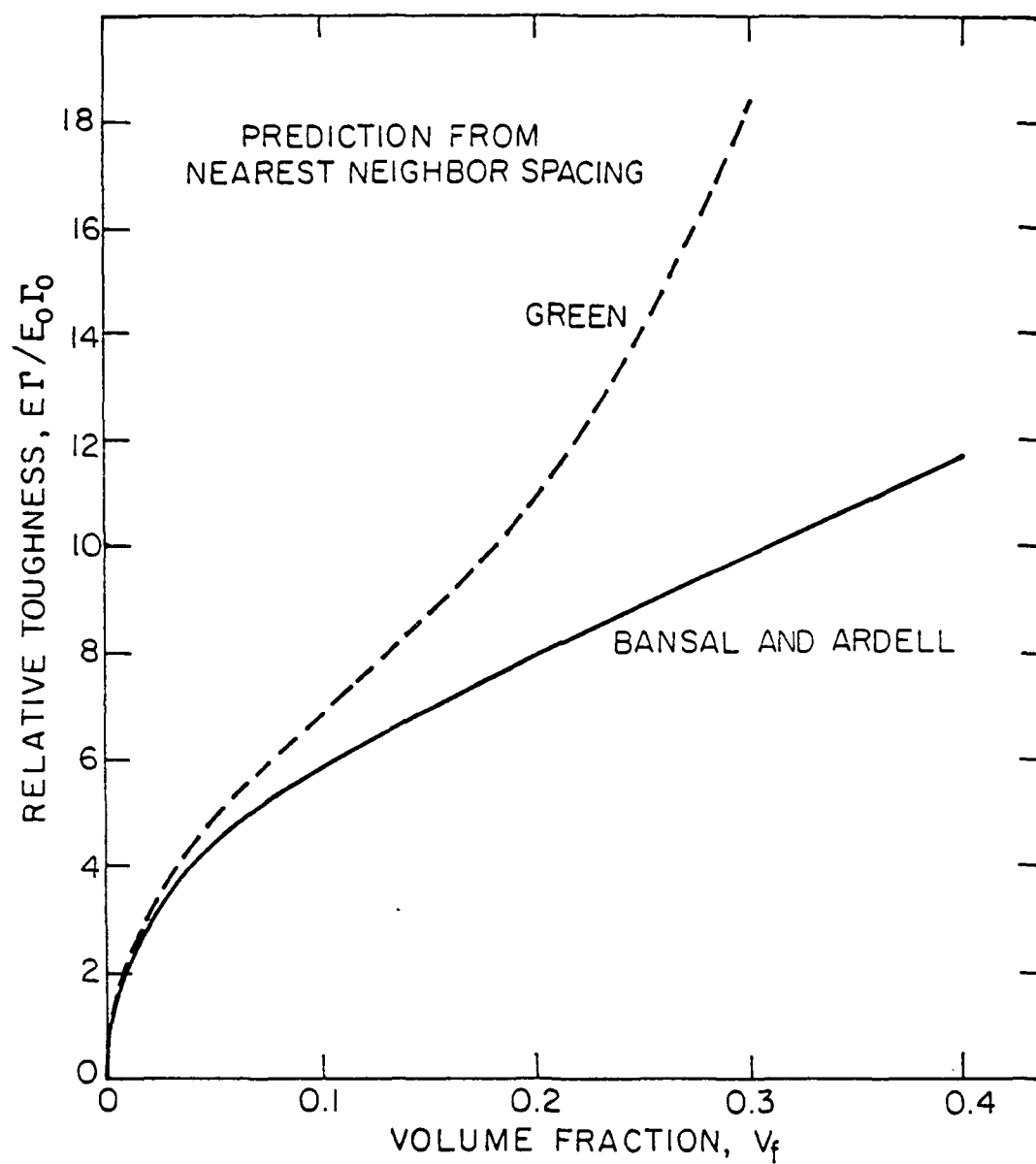
XBL 825-5795

Fig. 13



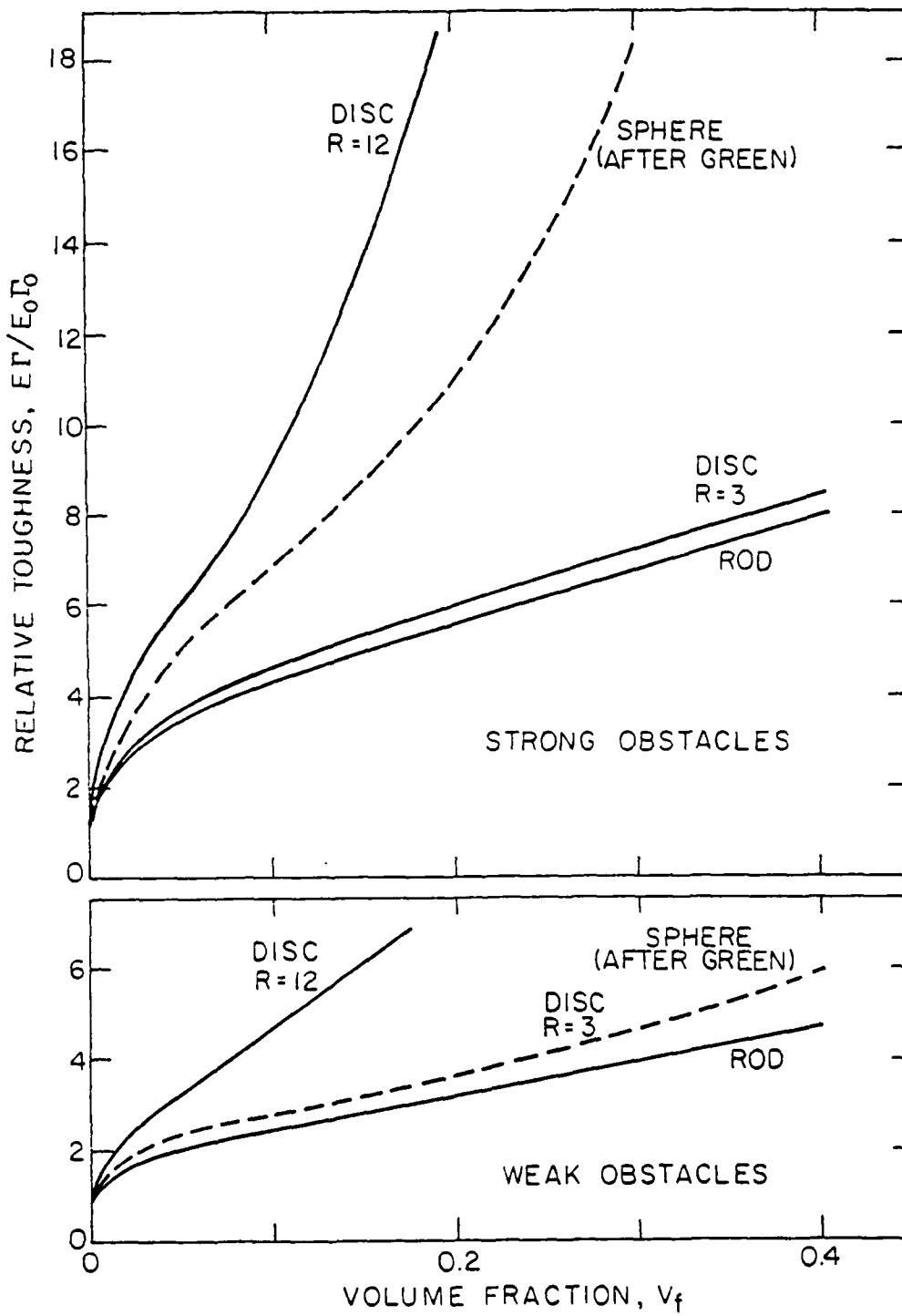
XBL025-5796

Fig. 14



XBL 825-5797

Fig. 15



XBL 825-5798

Fig. 16

CHAPTER II

CRACK DEFLECTION PROCESSES: II. EXPERIMENT

by

K. T. Faber and A. G. Evans

Department of Materials Science and Mineral Engineering  
University of California  
Berkeley, CA 94720



Crack Deflection Processes: II. Experiment

K. T. Faber and A. G. Evans

Department of Materials Science and Mineral Engineering  
University of California  
Berkeley, CA 94720

ABSTRACT

Two microstructural characteristics, particle morphology and size, have been examined with respect to toughening by crack deflection. Particle morphology effects were evaluated in a series of hot-pressed silicon nitrides comprised of rod-shaped grains of various aspect ratios and a barium-silicate glass ceramic containing spherulites. Lithium-alumino-silicate glass ceramics containing  $\text{Li}_2\text{Si}_2\text{O}_5$  lath-shaped crystals were studied for particle size effects. Independent measures of the fracture toughness and the crack deflection process were performed and results were correlated with a crack deflection model.

## 1. Introduction

Crack deflection is a commonly observed fracture characteristic in brittle materials, associated either with crack attraction or repulsion by second phase particles (due to residual strains) or with the presence of low resistance interfaces. Crack deflection has been associated with improved mechanical properties;<sup>1-3</sup> however, the specific quantitative relation between the fracture surface perturbations and the fracture toughness has never been established.

In a companion paper<sup>4</sup>, a quantitative crack deflection model was presented. Two aspects of this model are explored experimentally in the present paper: the effects on toughening of second phase particle morphology and particle size. Morphology effects are studied using two material systems, hot-pressed silicon nitrides comprised of rod-shaped grains with a range of aspect ratios and a barium-silicate glass ceramic containing a spherical crystalline phase. Particle size effects are investigated using a lithium-alumino-silicate glass ceramic containing  $\text{Li}_2\text{Si}_2\text{O}_5$  lath-shaped crystals.

## 2. Materials and Fabrication

### 2.1 Particle Morphology Effects

Silicon nitride provides a useful material for study, not only because of its potential as a high performance material, but also because rod-shaped grain morphologies with various aspect ratios can be easily fabricated. The microstructural characteristics of  $\text{Si}_3\text{N}_4$  are attributed to the  $\alpha \rightarrow \beta$  phase transformation, which occurs in the presence of a liquid phase at elevated temperatures. Specifically, the  $\alpha \rightarrow \beta$  transformation is accompanied by the development of rod-shaped grains,

believed to occur when pre-existing equiaxed  $\beta$ - $\text{Si}_3\text{N}_4$  particles grow along specific crystallographic directions (during fabrication) by consuming  $\alpha$ - $\text{Si}_3\text{N}_4$ <sup>5</sup>. Consequently, starting powders with large concentrations of  $\beta$ - $\text{Si}_3\text{N}_4$  powders result in equiaxed grain morphologies, while large initial concentrations of  $\alpha$ - $\text{Si}_3\text{N}_4$  powder lead to highly elongated microstructures.

A previous study of the fracture toughness of hot-pressed  $\text{Si}_3\text{N}_4$ <sup>6</sup> made with various initial proportions of  $\alpha$ - $\text{Si}_3\text{N}_4$  powders revealed that the fracture toughness increased with higher starting  $\alpha$  contents, corresponding to higher aspect ratio grain morphologies.<sup>+</sup> It is plausible that the toughening induced by the high aspect ratio grains occurs by crack deflection. Consequently, this series<sup>++</sup> of  $\text{Si}_3\text{N}_4$  materials is examined with reference to the crack deflection model proposed in the companion paper.

The effects of a spherical particle morphology are assessed from studies on  $3\text{BaO} \cdot 5\text{SiO}_2$  glass ceramics by Freiman et al..<sup>7</sup> Specific heat treatments resulted in the spherulitic crystallites of present interest. The corresponding mechanical properties are listed in Table 1.

---

<sup>+</sup> It has previously been assumed that the aspect ratio,  $R$ , of the rod-shaped grains can be described in terms of the starting  $\alpha$  and  $\beta$  contents by the relation<sup>6</sup>

$$R = 1 + (\alpha/\beta) .$$

<sup>++</sup> Provided by F. F. Lange of the Rockwell International Science Center. Starting powders were comprised of different proportions of high  $\alpha$ - $\text{Si}_3\text{N}_4$  (85% $\alpha$ , 15% $\beta$ ) and high  $\beta$ - $\text{Si}_3\text{N}_4$  (25% $\alpha$ , 75% $\beta$ ) and combined with 5%  $\text{MgO}$ . Powders were hot pressed in  $\text{N}_2$  at 1750°C for 2 hours and resulted in densified compacts consisting entirely of  $\beta$ - $\text{Si}_3\text{N}_4$ .

## 2.2 Particle Size Effects

A lithium-alumino-silica material was selected for studies of particle size effects. The particular composition, listed in Table 2, has previously been studied over a wide range of nucleation and growth temperatures.<sup>1</sup> The present study is limited to a heat treatment which produces a single crystalline phase,  $\text{Li}_2\text{Si}_2\text{O}_5$ , which, due to its thermal expansion mismatch with the glass matrix, will be subject to residual strain.

The lithium-alumino-silicate glass was prepared in one hundred gram batches using dry mixed  $\text{SiO}_2$ ,  $\text{LiCO}_3$ ,  $\text{Al}_2(\text{SO}_4)_3$ ,  $\text{K}_2\text{CO}_3$ ,  $\text{H}_3\text{BO}_3$  and  $(\text{NH}_4)_2\text{HPO}_4$ . (The specific role of the  $\text{P}_2\text{O}_5$  was to act as a nucleating agent during the heat treatment.) The mixes were melted in Pt crucibles in a  $\text{MoSi}_2$  resistance quench furnace in air at  $1350^\circ\text{C}$ . One inch discs were cast into graphite molds and annealed at  $450^\circ\text{C}$  for 1 hour to remove residual strain.

Heat treatments were completed in an electrical resistance tube furnace. All nucleation treatments were carried out at  $645^\circ\text{C}$  for 1 hour and subsequent growth treatments at  $850^\circ\text{C}$  for the desired period. Heat (growth) treatment times were based upon an arbitrary schedule of 1, 4, 16, 64 or 256 hours. The particle grain size changed by more than an order of magnitude over the range of heat treatments examined, as manifest in the etched fracture surfaces depicted in Figure 1. In addition, one sample was given no nucleation treatment, but underwent only a growth treatment of 250 hours. The latter heat treatment would suppress the number of nuclei formed, and promote the growth of few, large crystalline grains.

### 3. Fracture Toughness Measurements

Fracture toughness measurements were obtained for the hot-pressed silicon nitride and lithium-alumino-silicate glass ceramic using the indentation technique.<sup>8</sup> For the  $\text{Si}_3\text{N}_4$  samples, toughness measurements were made using indentation loads of 20N to 250N. Values of  $\mathcal{G}_c$  are plotted in Figure 2 as a function of the estimated aspect ratio. Fracture toughness values increase up to 2.5 times through the development of elongated grains. From the fracture surfaces in Figure 3, note the development of needle-like grains in the progression of micrographs A through G, corresponding to increasing amounts of starting  $\alpha\text{-Si}_3\text{N}_4$ . Fracture is primarily intergranular; however, some transgranular fracture is evident (from cleavage steps) in each of the specimens. Also apparent are remnants of WC milling media (white angular particles) and the lack of appreciable texturing in the  $\text{Si}_3\text{N}_4$  grains.

The fracture toughness of the lithium-alumino-silicate precursor glass and the resultant glass ceramics were determined in oil, due to the high susceptibility of glasses and glass ceramics to stress corrosion cracking. A fine layer of gold was sputtered onto each polished surface to enhance the visibility of the indentation cracks in reflected light through the oil (as the refractive indices of the glass ceramic and indenting oil were nearly the same.) All measurements were made using a micro-hardness indenter with a load of 20N. A plot of the strain energy release rate versus the growth time is shown in Figure 4. The most striking feature of the plot is the invariance of

toughness with growth time and, consequently, crystalline particle size, including the material which underwent no nucleation treatment (corresponding to the open circle in Figure 4).

#### 4. Crack Deflection Profiles

Fracture toughness measurements are not sufficient to correlate toughening behavior with crack deflection processes. In order to substantiate that crack deflection is responsible for the increase in fracture toughness, an independent measure of the deflection process is necessary. Post-failure examination of fracture surfaces, although capable of providing valuable information about the type of fracture (transgranular or intergranular) and the failure origin, does not allow determination of the precise path and direction of the crack (or a trace of the crack front) at any instant during propagation. Both features are necessary for comparison with the predicted tilt and twist of the crack front.

Stable cracks, produced by indentation, can be used to obtain a reasonable measure of the crack front profile. Shown schematically in Figure 5 is a Vickers indentation produced above a critical load, with two orthogonal semi-circular radial cracks (labelled R) emanating from the indent corners. The radial cracks along the surface,  $c_R$ , provide a reliable deflection profile, if the distribution of angles along the surface trajectory is equivalent to that along the subsurface crack front. It is expected that these distributions will be identical in the absence of grain texturing.

Indentation cracks for four members of the  $\text{Si}_3\text{N}_4$  series (Samples A, C, E, G) have been examined. The lengths and angles with respect to the direction of propagation of three to four hundred crack segments per sample were measured and deflection histograms prepared. Representative deflection traces of both end members (samples A and G) are shown in Figure 6. The frequency distributions from smoothed histograms associated with these measurements are presented in Figure 7. Both materials demonstrate bimodal crack deflection distributions. The lower distribution is centered near  $0^\circ$  and its frequency decreases for the higher toughness material. The second distribution is translated toward a higher angle for the higher toughness material. Trends for the  $\text{Si}_3\text{N}_4$  series are more reliably envisaged from Figure 8, where four cumulative distribution functions are plotted. From the curves, it can be seen that the median deflection angle increases with increasing aspect ratio: from  $22^\circ$  for the low toughness material to  $40^\circ$  for the highest toughness material.

Two glass-ceramic materials were chosen for crack deflection measurements: one heat treated for one hour at  $645^\circ$  (nucleation) and for four hours at  $850^\circ$  (growth), the second heat treated at  $850^\circ$  for 250 hours (expected to have the largest crystallite size). Approximately 250 segments were measured for each material. Plotted in Figure 9 are the cumulative distribution functions for the two glass ceramics, compared with the precursor glass. The glass ceramic distributions are strikingly similar, with median deflection angles of  $12^\circ$  and  $15^\circ$  for the short and long heat treatment times respectively.

### 5. Correlation with the Crack Deflection Model

Direct correlation between theory and experiment, contingent upon independent knowledge of the aspect ratio of the deflecting particles, is possible in the case of the lithium-alumino-silicate glass ceramics. In the glass ceramic, the lath-like  $\text{Li}_2\text{Si}_2\text{O}_5$  crystals can be regarded as rods having an aspect ratio,  $R > 12$  (see Figure 1). For such large aspect ratio rods, the deflection angles (see Figure 11) and the measured toughening are both substantially smaller than predicted by the deflection theory.<sup>4</sup> However, examination of fracture paths in Figure 10 reveals that the  $\text{Li}_2\text{Si}_2\text{O}_5$  grains are not always circumvented by the cracks. Instead, the grains fracture prematurely at deflection distances characteristic of rods with "effective" aspect ratios in the range  $2 < R < 5$ . This observation is consistent with the comparison of the measured and predicted crack deflection profiles (Figure 11) which indicate,  $3 < R_{\text{eff}} < 4$ . Such aspect ratios predict toughness increases ( $\mathcal{G}_c / \mathcal{G}_c^m$ ) in the range 2.5 to 2.7, also in good accord with the measured increase,  $\mathcal{G}_c / \mathcal{G}_c^m \cong 3.0$ . It is thus concluded that the toughening measurements conform with the crack deflection predictions, provided that the fracture characteristics of the grains are adequately incorporated. In addition, it is noted that the fracture toughness measurements and crack deflection profiles provide complimentary evidence that crack deflection processes are independent of particle size, as required by principles of geometric similarity.

Similar consistency with crack deflection expectations is exhibited by the spherulitic microstructure in  $3\text{BaO} \cdot 5\text{SiO}_2$ , wherein the predicted toughening,  $\mathcal{G}_c / \mathcal{G}_c^m = 1.8$ , compares well with the measured toughening,  $\mathcal{G}_c / \mathcal{G}_c^m = 1.6$  (Table 1).



Direct aspect ratio information could not be obtained for the  $\text{Si}_3\text{N}_4$  systems.<sup>†</sup> Toughness correlations are, thus, based upon the measured mean deflection angles. Additionally, since none of the  $\text{Si}_3\text{N}_4$  compositions examined demonstrate planar fracture characteristics, selection of an arbitrary reference is required. Selecting the highest toughness material (Composition G, median deflection angle of  $40^\circ$ ) as the reference, the measured relative toughness and deflection angle can be compared with predictions for toughening by rod-shaped particles (Figure 12). Only the lowest toughness, equiaxed material deviates significantly from the prediction. Electron micrographs comparing the high and low toughness materials indicate greater amounts of glassy phase in the low toughness material (Figure 13). The additional glass may have a direct influence on the toughening characteristics and may, thus, be the source of deviation from the predicted behavior.<sup>††</sup> Extrapolating the predicted toughness trend to the value for the flat crack ( $\mathcal{G}_c/\mathcal{G}_c^m = 1$ ), suggests that  $\text{Si}_3\text{N}_4$  which fractures in a transgranular mode should exhibit a fracture toughness,  $K_{Ic} \approx 2.5 \text{ MPa}\sqrt{\text{m}}$ . This is consistent with the toughness level determined for covalent materials which fail transgranularly (e.g. sintered SiC and sapphire<sup>10,11</sup>). It is

---

<sup>†</sup>Single phase systems containing randomly arrayed elongated particles, such as  $\text{Si}_3\text{N}_4$ , pose unique problems in evaluating the characteristic aspect ratio, and, hence, in comparing experiment with theory. In the particular system studied,  $\text{Si}_3\text{N}_4$  grains cannot be etched from the sintered compact for particle size analysis. In situ analysis of aspect ratios from fracture surfaces provides inadequate estimates because only a portion of the grain is revealed.

<sup>††</sup>The glass causes enhanced surface relief during polishing which may skew the deflection angle measurements; moreover it is likely to modify the basic toughness,  $\mathcal{G}_c^m$ , upon which the deflection toughening is superposed.

thus concluded that the toughening trends in the  $\text{Si}_3\text{N}_4$  materials are, again, in general accord with the expectations of crack deflection dominated toughening behavior.

In all of the above experiments, some deviations from the crack deflection predictions occur, undoubtedly because several toughening mechanisms are likely to operate simultaneously in most materials. In addition to crack deflection, crack bowing, microcracking, crack branching or bridging are possible.<sup>2,9,12-14</sup> For example, the thermal expansion mismatch between  $\text{Li}_2\text{Si}_2\text{O}_5$  and the matrix glass is sufficiently large that stress-induced microcracking operates. The microcracking that occurs in a small zone near the propagating crack in the lithium-alumino-silicate composition heat treated for 250 hours is illustrated in Figure 10.<sup>†</sup> These occurrences are not observed in the glass ceramic heat treated for shorter times, consistent with the notion that the microcracking process is strongly size dependent.<sup>9</sup> However, since the data reveal no significant size effect on the toughening, it is unlikely that the microcracking process contributes significantly to the toughness of this specific material.

Deviations between experiment and predicted deflection distributions may also result from inaccurate predictions of the deflection distribution. All predictions were based upon the intersecting plane, parallel to the crack front. However, nearest neighbor particles would not lie on a

---

<sup>†</sup>The microcracking can be distinguished from crack branching by noting the origin of the secondary crack. Branched cracks always originate from the main crack; microcracks can nucleate away from the main crack, followed by coalescence.

straight line parallel to the intersecting plane in a randomly distributed system. This omission could account for variances in the predicted distributions, since the distribution of twist and tilt angles would change with direction. Accounting for the possible angles between the crack front and the intersecting plane would, at best, provide upper and lower bounds on the deflection distribution.

#### 6. Summary

Two prime features of crack deflection toughening have been confirmed experimentally. In particular, particle morphology effects were examined in two systems: a barium-silicate glass ceramic and a series of hot-pressed  $\text{Si}_3\text{N}_4$  compositions. The former, comprised of spherical crystals in a glassy matrix, demonstrated toughness increases over the precursor glass consistent with predictions. The latter, hot-pressed  $\text{Si}_3\text{N}_4$  with variations in grain morphology, was studied for grain aspect ratio effects. The toughness and deflection angles monotonically increased with aspect ratio. Using one composition in the  $\text{Si}_3\text{N}_4$  series as a reference, the observed toughening trends were in agreement with those predicted from the crack deflection model.

In addition, a series of lithium-alumino-silicate glass ceramics was examined as a function of heat treatment time (and consequently particle size variations). The fracture toughness was found to be invariant with particle size. Complimentary evidence for the size-independent behavior was attained from crack deflection profiles, which were nearly identical for end members of the glass ceramic series. Furthermore, the magnitude of the toughness increases were in accord with expected values.

The experimental evidence correlates well with the guidelines developed for toughening brittle materials by crack deflection processes. Fracture toughness can be maximized with additions of high aspect ratio rod-like particles, and should remain invariant with particle size.

Acknowledgments

The research of K. T. Faber was sponsored by The Carborundum Company, Niagara Falls, N.Y., and of A. G. Evans by ONR (Contract N00014-81-K-0362).

References

1. M. P. Borom, A. M. Turkalo and R. H. Doremus, J. Amer. Ceram. Soc. 58, 385 (1975).
2. J. C. Swearingen, E. K. Beauchamp and R. J. Eagan, in Fracture Mechanics of Ceramics, Vol. 4, 973 (Ed. R. C. Bradt, D. P. H. Hasselman and F. F. Lange) Plenum Pub. Co., New York (1978).
3. T. Mah, M. G. Mendiratta and H. A. Lipsitt, Amer. Ceram. Soc. Bull. 60, 1229 (1981).
4. K. T. Faber and A. G. Evans, Part I.
5. J. L. Iskoe and F. F. Lange, in Ceramic Microstructures '76 (Ed. R. M. Fulrath and J. A. Pask) Westview Press, Boulder, CO (1977).
6. F. F. Lange, J. Amer. Ceram. Soc. 59, 336 (1976).
7. S. W. Freiman, G. Y. Onoda, Jr. and A. G. Pincus, J. Amer. Ceram. Soc. 57, 8 (1974).
8. A. G. Evans and E. A. Charles, J. Amer. Ceram. Soc. 59, 371 (1976).
9. A. G. Evans and K. T. Faber, J. Amer. Ceram. Soc. 64, 394 (1981).
10. S. G. Seshadri and M. Srinivasan, Comm. Amer. Ceram. Soc., C69 (1981).
11. G. R. Anstis, P. Chantikul, B. R. Lawn and D. B. Marshall, J. Amer. Ceram. Soc., 64, 533 (1981).
12. A. G. Evans, Phil. Mag., 26, 1327 (1972).
13. H. P. Kirchner, R. M. Gruver, M. V. Swain and R. C. Garvie, J. Amer. Ceram. Soc., 64, 529 (1981).
14. A. G. Evans, Int. J. Frac. 16, 485 (1980).

Table 1

Fracture Toughness and Related Parameters of  $38\text{a}0.5\text{SiO}_2$  Glass Ceramics

Microstructure	Heat Treatment	Elastic Modulus (GPa)	$\mathcal{G}_c$ ( $\text{Nm}^{-1}$ )	Toughness Ratio	
				Observed	Predicted
Glass	2h/600°C	64	4.2	1	-
Spherulites	48h/700°C 1h/825°C	84	6.6	1.6	1.8

Table 2: Precursor Glass Composition for  
Lithium-Alumino-Silicate Glass Ceramic

<u>Constituent</u>	<u>Weight Percent</u>
SiO <sub>2</sub>	71.8
Li <sub>2</sub> O	12.6
Al <sub>2</sub> O <sub>3</sub>	5.1
K <sub>2</sub> O	4.8
B <sub>2</sub> O <sub>5</sub>	3.2
P <sub>2</sub> O <sub>5</sub>	2.5

Figure Captions

- Figure 1. Scanning electron micrographs of lithium-alumino-silicate glass-ceramic fracture surfaces, heat treated (a) 1 hour, 645°C, 4 hours, 850°C (b) 1 hour 645°C, 256 hours, 850°C. Specimens were etched 5 sec in concentrated HF to reveal crystal morphology.
- Figure 2. Fracture toughness of a series of hot-pressed  $\text{Si}_3\text{N}_4$  materials versus calculated aspect ratio.
- Figure 3. Scanning electron micrographs of fracture surfaces of four hot-pressed  $\text{Si}_3\text{N}_4$  materials of various aspect ratios.
- Figure 4. Fracture toughness of a series of lithium-alumino-silicate glass ceramics plotted versus increasing growth time of the crystalline phase.
- Figure 5. Schematics of the top and cut-away side views of a Vickers indentation indicating the radial cracks,  $C_R$ , and the sub-surface radial crack front.
- Figure 6. Crack deflection profiles for end member of the  $\text{Si}_3\text{N}_4$  series traced from scanning electron micrographs.
- Figure 7. Frequency distributions of measured deflection angles for end members of the  $\text{Si}_3\text{N}_4$  series.
- Figure 8. Cumulative frequency distributions of measured deflection angles of four hot-pressed  $\text{Si}_3\text{N}_4$  materials of various aspect ratios.
- Figure 9. Cumulative frequency distributions of measured deflection angles of two lithium-alumino-silicate glass ceramics and the precursor glass.



- Figure 10. Indentation crack profiles in lithium-alumino-silicate glass ceramic (heat treated 250 hours at 850°C), etched in 2.5% HF for 5 sec., indicating fracture of the  $\text{Li}_2\text{Si}_2\text{O}_5$  grains accompanying crack deflection. Also note microcracks near the main crack.
- Figure 11. Cumulative frequency distributions of measured deflection angles of two lithium-alumino-silicate glass ceramics compared with predicted frequency distributions for various aspect ratios.
- Figure 12. Relative toughness-median deflection angle correlations for the hot-pressed  $\text{Si}_3\text{N}_4$  series.
- Figure 13. Polished surfaces of hot-pressed  $\text{Si}_3\text{N}_4$  A and G, etched in 52% HF for 30 sec. Greater etching is observed in  $\text{Si}_3\text{N}_4$  A, indicative of a greater amount of grain boundary glass. (Bar = 2  $\mu\text{m}$ ).

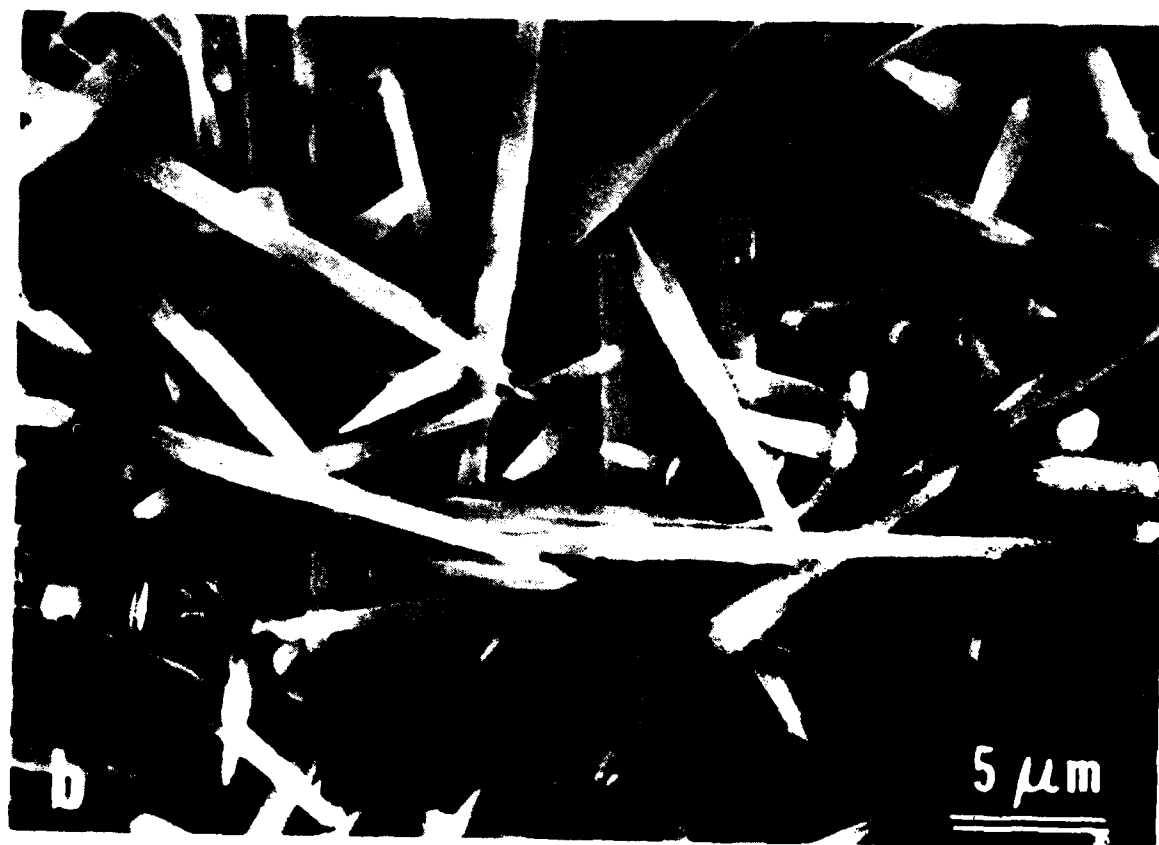
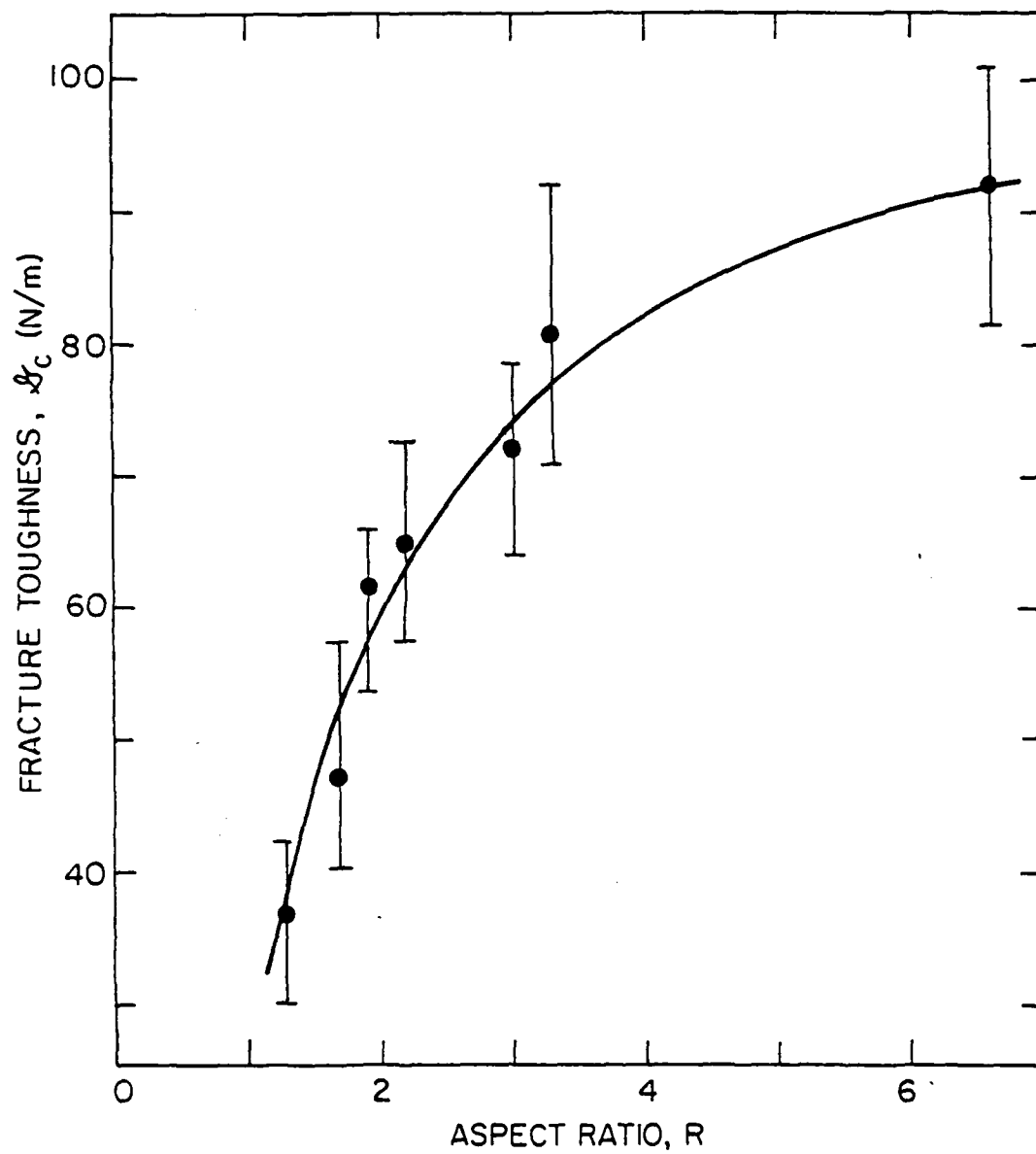


Fig. 1



XBL 824-5590

Fig. 2

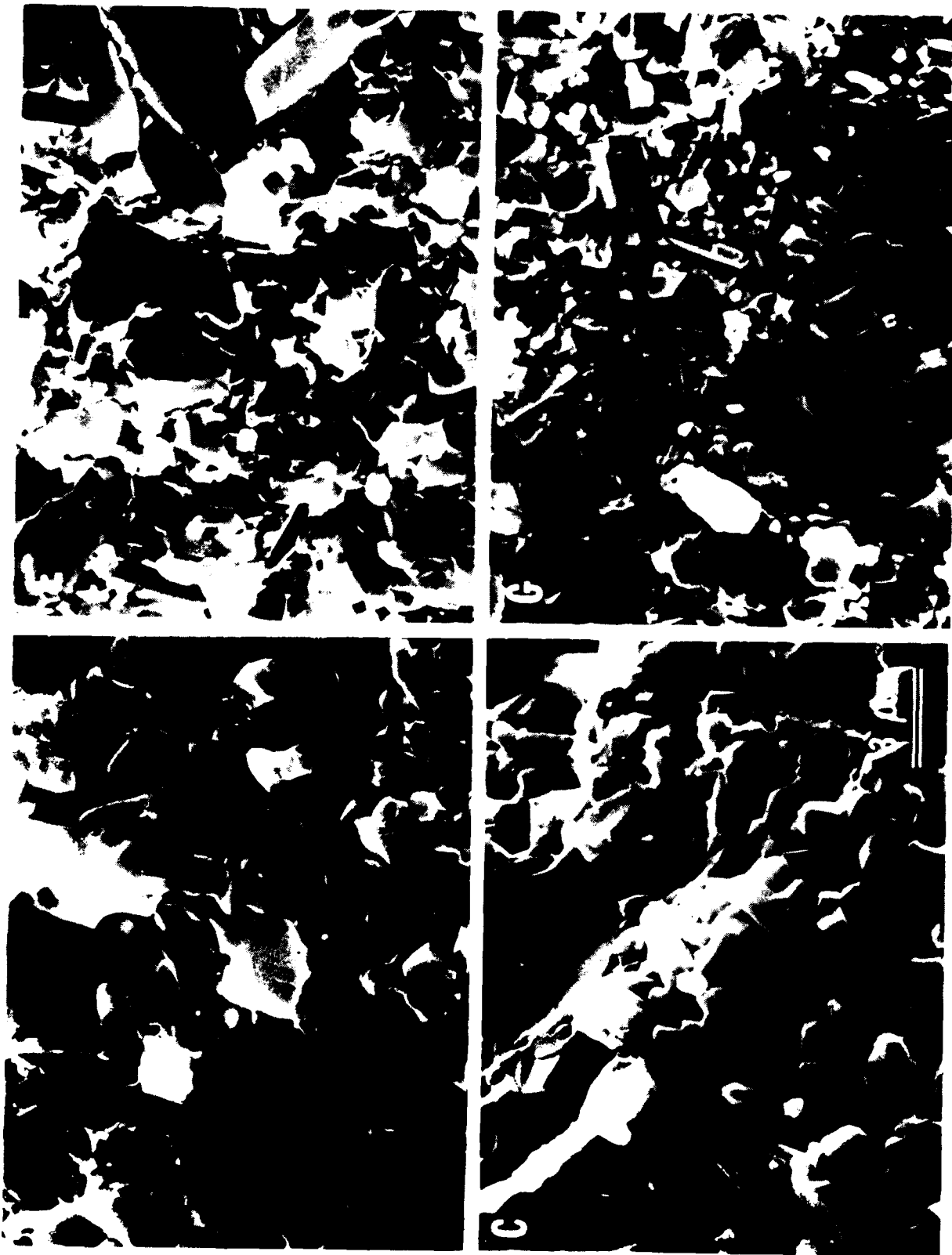
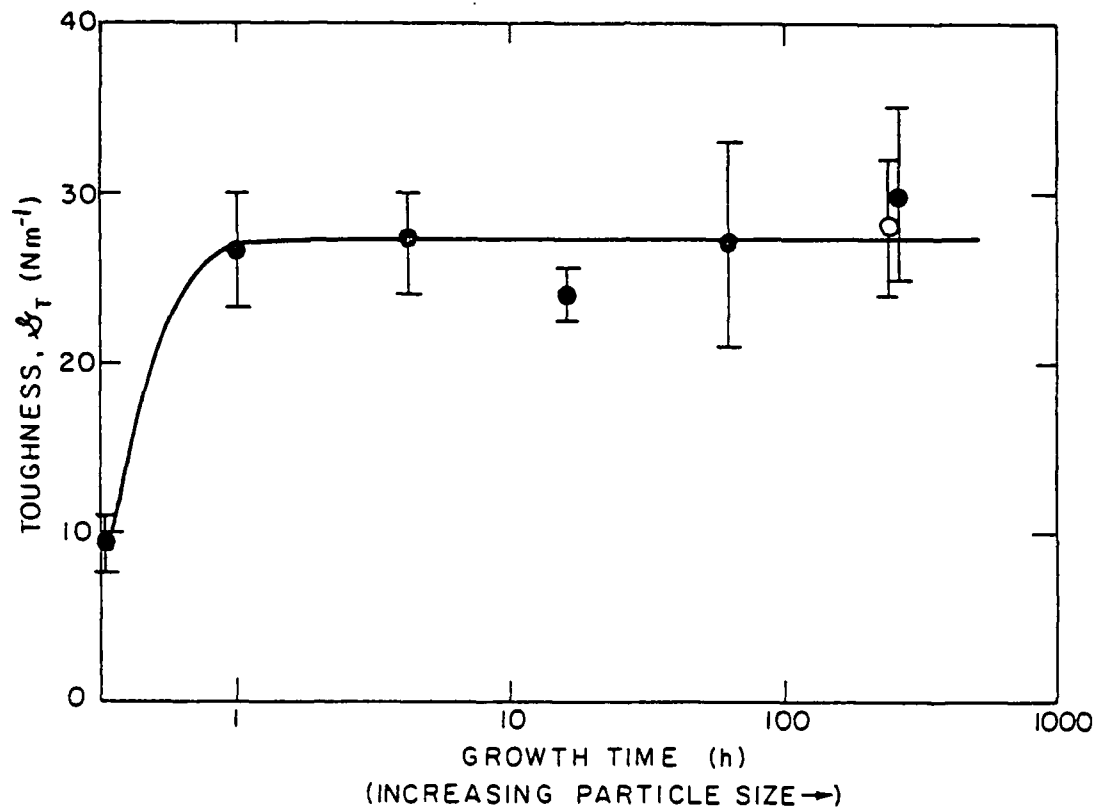


Fig. 3



XBL 825-5788

Fig. 4

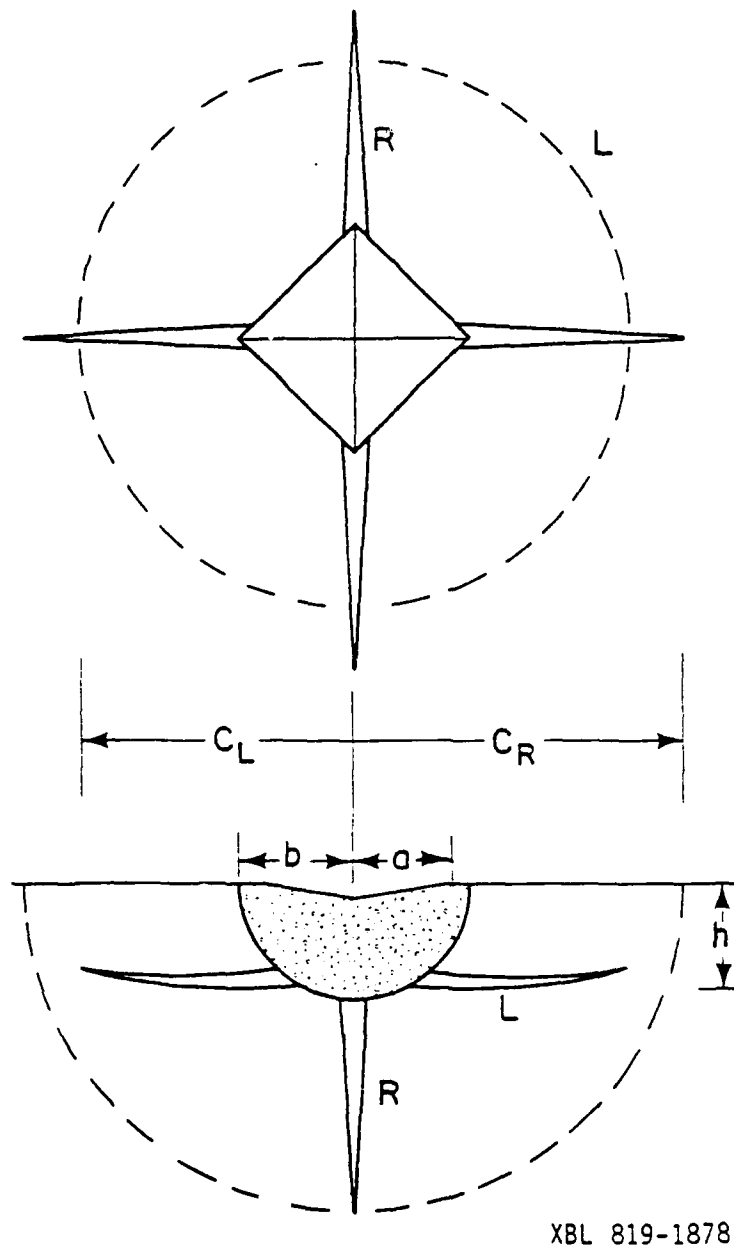
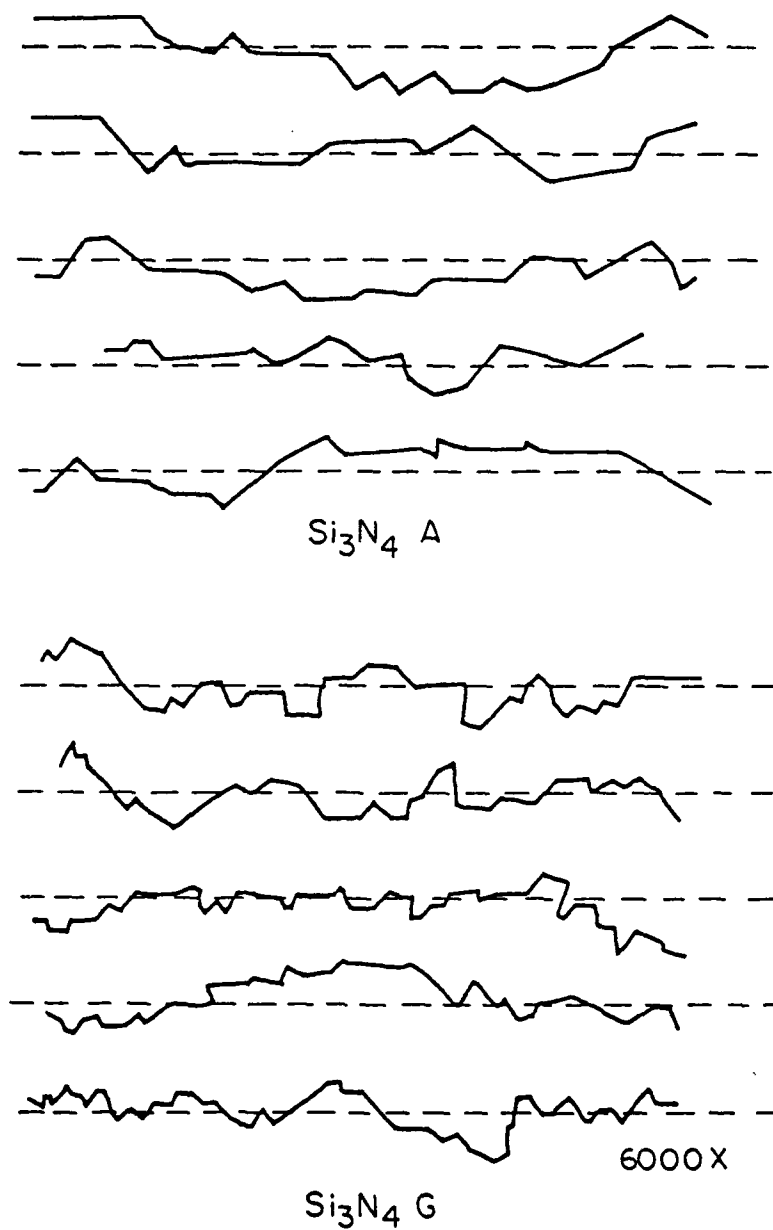
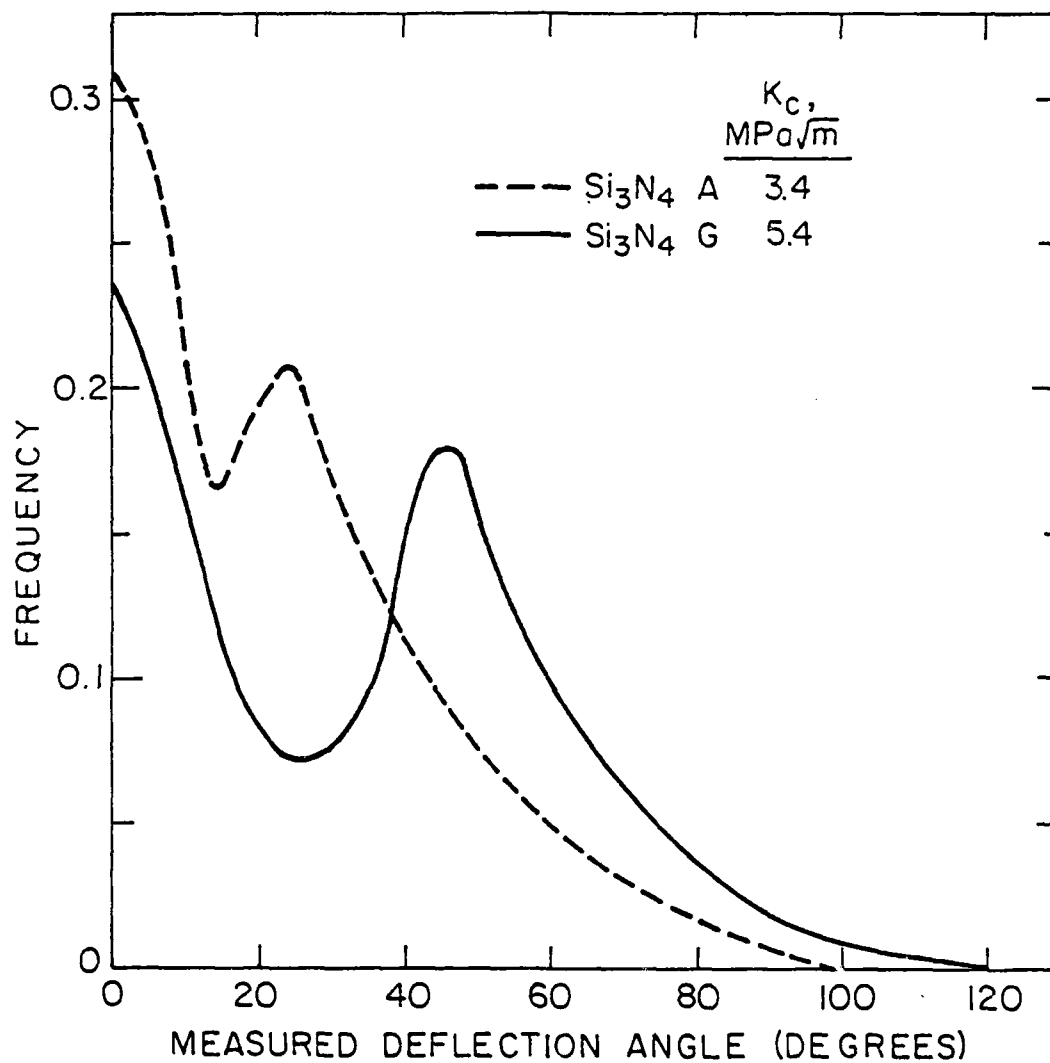


Fig. 5



XBL 825-5794

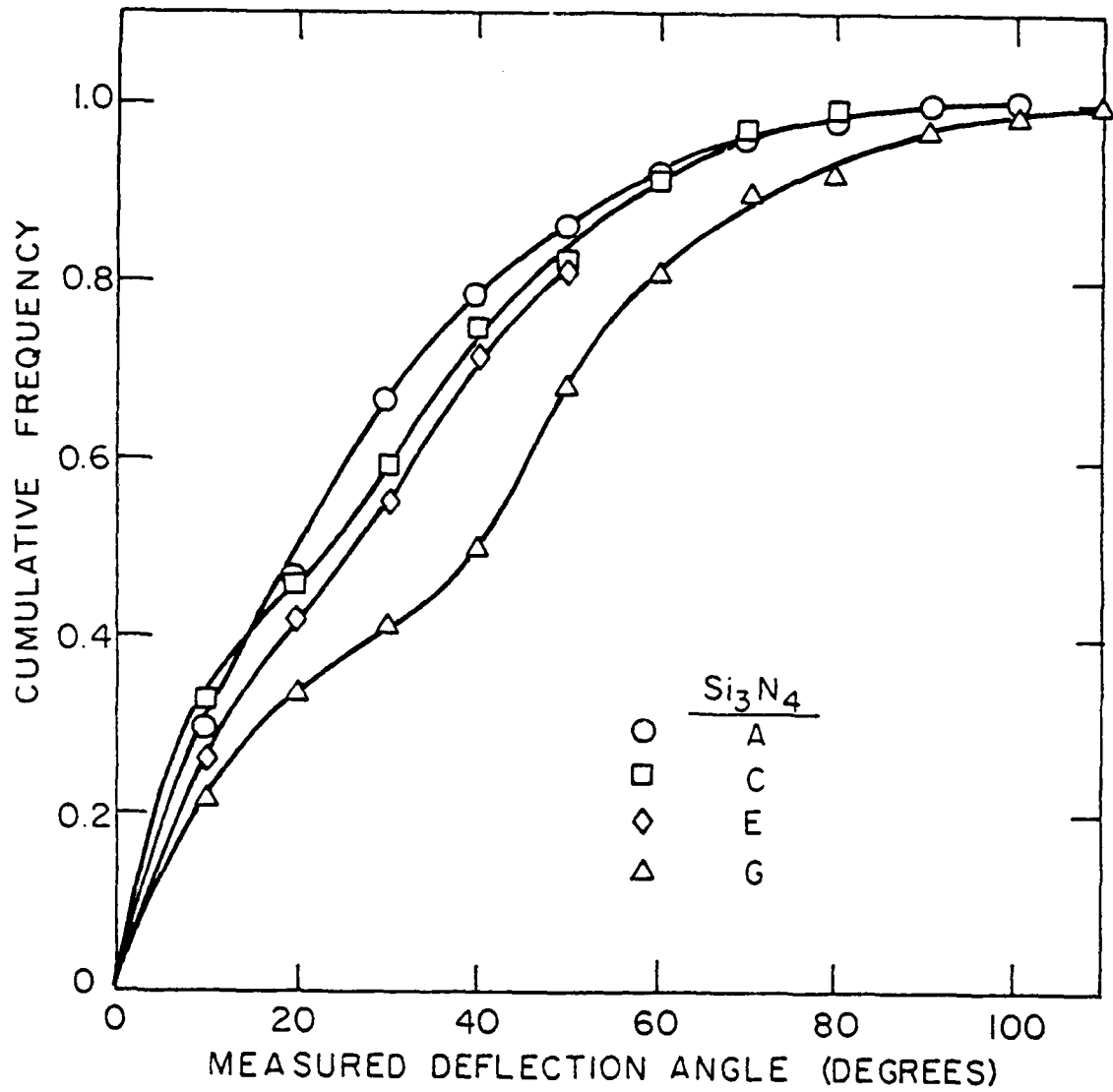
Fig. 6



XBL 824-5589

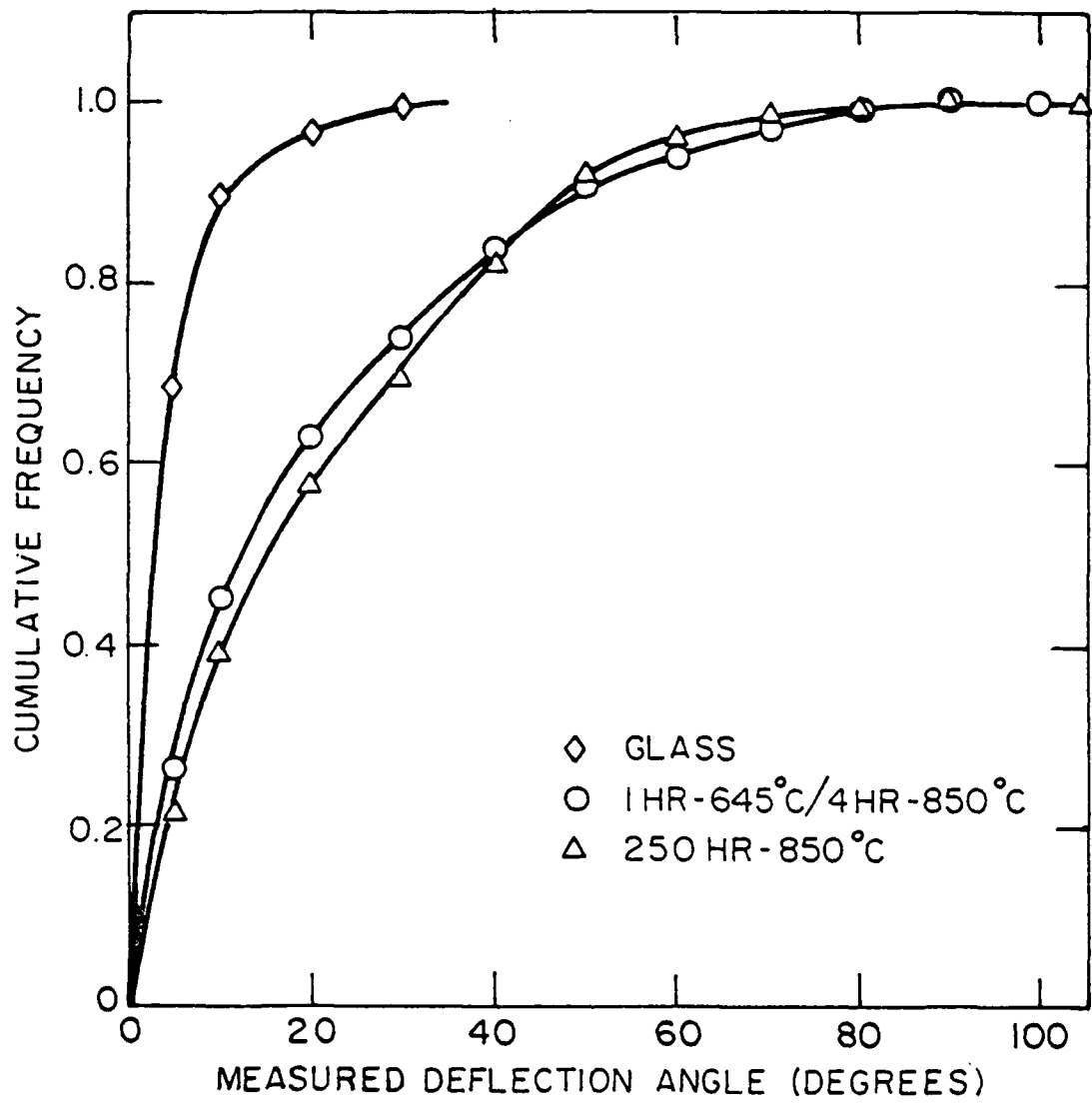
Fig. 7





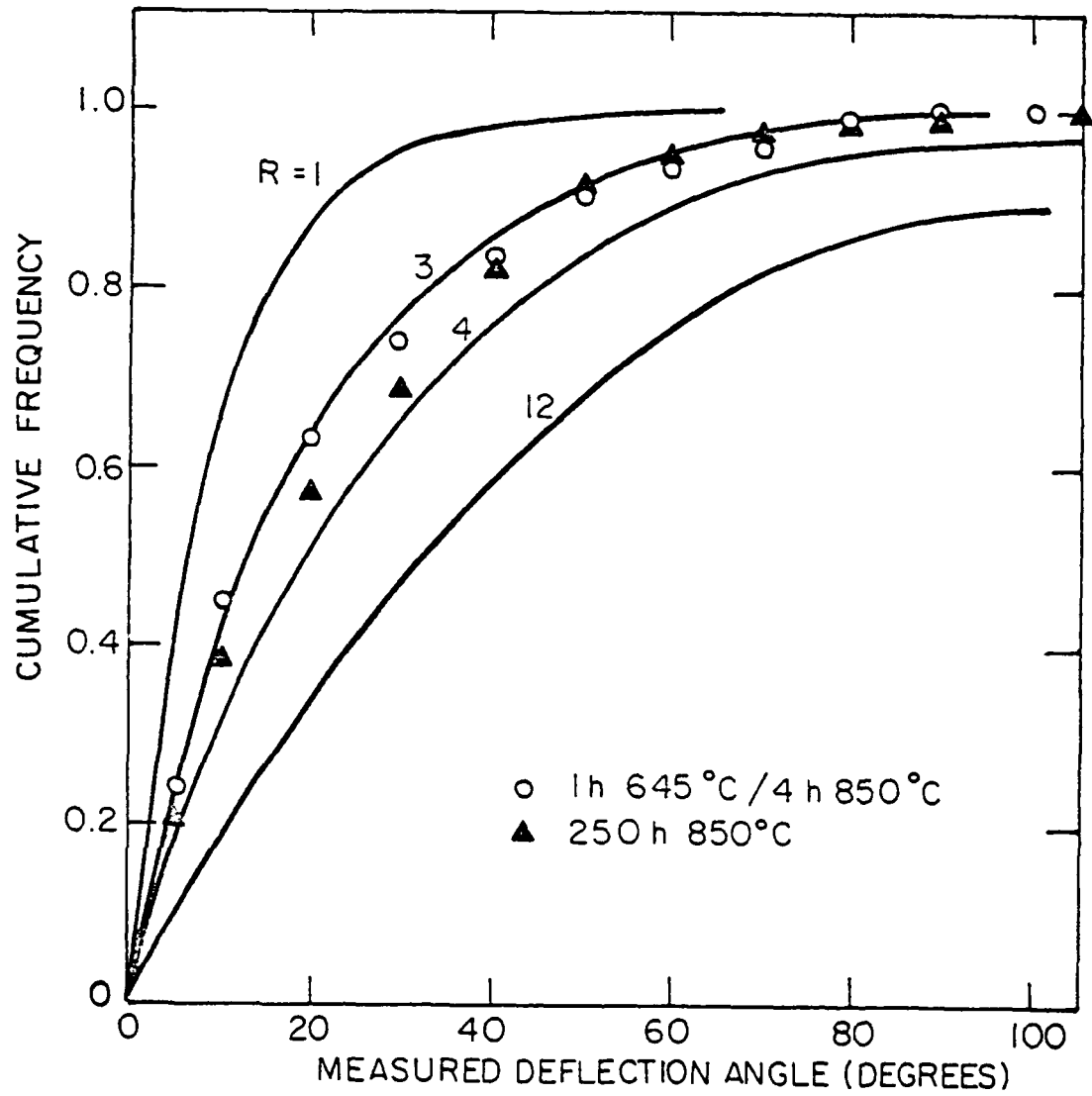
XBL 825-5791

Fig. 8



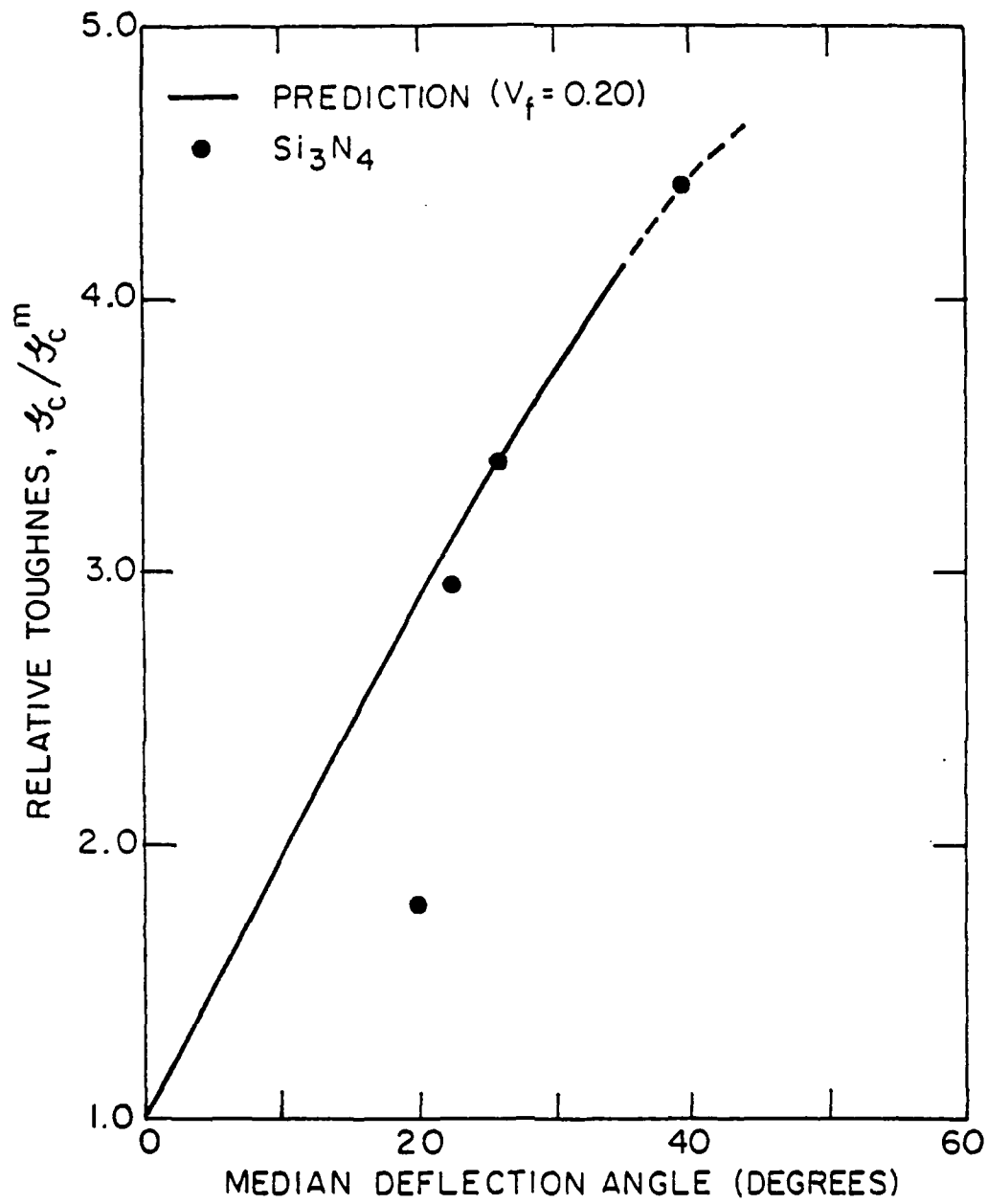
XBL 825-5792

Fig. 9



XBL 827-5962

Fig. 11



XBL 827-5961

Fig. 12



Fig. 13

CHAPTER III

TOUGHENING BY MONOCLINIC ZIRCONIA  
USING A CRACK DEFLECTION MECHANISM

by

H. Ruf and A. G. Evans

Department of Materials Science and Mineral Engineering  
University of California  
Berkeley, CA 94720

## TOUGHENING BY MONOCLINIC ZIRCONIA

by

H. Ruf and A. G. Evans

Department of Materials Science and Mineral Engineering  
University of California  
Berkeley, CA 94720

### ABSTRACT

An investigation of the toughening induced by monoclinic  $\text{ZrO}_2$  in the absence of microcracking has been conducted, using ZnO as the host material. Toughness levels  $\mathcal{G}_c$  in excess of the host toughness  $\mathcal{G}_c^m$  have been achieved: attaining a peak toughness  $\mathcal{G}_c/\mathcal{G}_c^m \approx 3$ , at monoclinic  $\text{ZrO}_2$  volume concentrations  $\geq 0.2$ . This toughening has been attributed to crack/particle interactions, associated with the deflection and bowing of the crack by the residual strain field around the monoclinic  $\text{ZrO}_2$  particles.

## 1. INTRODUCTION

Microstructural enhancement of fracture toughness can be achieved in accord with two basic approaches. A non-linear, crack shielding zone can be induced near the crack tip,<sup>1,2</sup> or the motion of the crack front can be locally impeded<sup>3-5</sup>. The former is exemplified by stress induced martensitic<sup>1</sup> and microcracking mechanisms,<sup>2</sup> while the latter category encompasses crack bowing<sup>3,5</sup> and crack deflection effects<sup>4</sup>. Several of these mechanisms can be realized by incorporating  $ZrO_2$  particles into ceramic matrices<sup>6</sup>, with the operative toughening mechanism depending upon such variables as the matrix stiffness and toughness, the  $ZrO_2$  particle size and chemical composition, and the temperature. However, a thorough understanding of the conditions that favor specific toughening mechanisms (and of optimum toughening levels) does not yet exist.

Preliminary toughening can be achieved in the presence of monoclinic, thermally transformed,  $ZrO_2$ . The toughening by monoclinic  $ZrO_2$  can be attributed to either a non-linear, microcrack zone<sup>6</sup> or to crack impediment by the  $ZrO_2$  particles (involving crack deflection or bowing mechanisms). The monoclinic modes of toughening also exist in the presence of tetragonal  $ZrO_2$  particles that experience a stress induced transformation, because the particles directly ahead of the crack tip transform to the monoclinic phase prior to crack extension<sup>1</sup> (as superposed, of course, on the transformation toughening<sup>1</sup>).

The transformation toughening process has been subject to analysis and preliminary experimental substantiation. The predicted toughening increment is given by;<sup>1,7</sup>



$$\Delta K_C^T = 0.22 V_f e^T E \sqrt{w}/(1-\nu) \quad (1)$$

where  $\Delta K_C^T$  is the transformation toughening increment,  $e^T$  is the unconstrained dilational transformation strain,  $E$  is Young's modulus,  $\nu$  is Poisson's ratio and  $w$  is the width of the transformation zone. The toughening mechanisms in the presence of monoclinic  $ZrO_2$  have not been subject to a similarly definitive level of analysis (in part, because the microcrack and particle interaction effects have not been experimentally distinguished). The intent of the present paper is to attempt to isolate and study that component of toughening associated with particle interaction. This is achieved by selecting a system that suppresses the incidence of microcracks at the transformed particles. (The separate influence of microcracks that obtain in other systems may then be subject to a more systematic, subsequent investigation).

The study of toughening by monoclinic  $ZrO_2$  in the absence of microcracking requires the choice of a host that encourages transformation, while suppressing microcracking. A judicious material selection can be made by invoking critical size concepts. Microcracking and transformation both exhibit characteristic critical particle sizes,  $r_C^m$  and  $r_C^t$  respectively.<sup>8,9</sup> A host that offers the maximum separation between the critical sizes, contingent upon  $r_C^m > r_C^t$ , would be most appropriate for the present study.

The incidence of microcracking depends upon the fracture resistance of the matrix,  $K_{IC}^m$ , (e.g. the grain boundary fracture toughness for boundary located particles) the transformation strain and the elastic modulus, such that the critical particle size,  $r_C^m$ , is given by,

$r_c^m \propto (K_{IC}^m / E e_{ij}^T)^2$ . The critical transformation size is less well comprehended. Nevertheless, each of the potential mechanisms<sup>8,9,10</sup> predict that  $r_c^t$  increases as the elastic energy,  $\propto E(e_{ij}^T)^2$ , increases or as the chemical free energy,  $\Delta F_c$ , decreases. Comparison of the trends in  $r_c^m$  and  $r_c^t$  with material properties indicates inverse dependencies on the product  $E e_{ij}^T$ , such that small values of the product diminish  $r_c^t$  but enhance  $r_c^m$ ; as required to create microcrack-free monoclinic  $ZrO_2$ . The most expedient approach for separating  $r_c^m$  and  $r_c^t$  is thus to select a host with a low elastic modulus,  $E$ , and a smaller thermal contraction coefficient,  $\alpha$ , than the tetragonal  $ZrO_2$  phase (the latter tends to minimize  $e_{ij}^T$ ). The choice of ZnO, being a chemically compatible material that satisfies these requirements ( $E = 120$  GPa,  $\alpha = 7 \times 10^{-6}$ ), is thus considered to be appropriate for the present study. The ZnO is used primarily in conjunction with a pure  $ZrO_2$ , which maximizes the chemical free energy change and hence, depresses  $r_c^t$ . However, several materials containing partially stabilized  $ZrO_2$  (with  $Y_2O_3$ ) are also prepared, in order to retain tetragonal  $ZrO_2$  and thus, to examine the relative role of transformation toughening.

## 2. EXPERIMENTAL PROCEDURES AND RESULTS

The experimental procedures conducted during the present study are designed to establish that the basic microstructural requirements for the study of crack deflection toughening are satisfied; notably, that the thermal, martensitic, transformation of the  $ZrO_2$  particles to the monoclinic structure occurs without the incidence of microcracks. Hence, following fabrication by hot pressing, an examination of the monoclinic  $ZrO_2$  content is conducted by using x-ray diffraction and electron optical methods;

while the martensitic character of the monoclinic phase is verified using dilatometer measurements. The incidence of microfracture is more difficult to determine. Direct observations are ambiguous, because of the small crack opening displacements. However, measurements of the elastic modulus, hardness and acoustic activity, all of which are sensitive to the microcrack size distribution and density, are used to provide a convenient and adequate measure of the microcrack propensity. Finally, fracture toughness measurements are performed and the fracture morphology characterized.

## 2.1 Fabrication Procedures

Three composite series were fabricated: one contained pure  $\text{ZrO}_2^*$  (volume fractions up to 0.6) and the others contained  $\text{ZrO}_2$  with 4 w/o or 8 w/o  $\text{Y}_2\text{O}_3^{**}$  (volume fractions up to 0.4). The  $\text{ZnO}^+$  and  $\text{ZrO}_2$  powders were mechanically milled and mixed using  $\text{Al}_2\text{O}_3^{++}$  balls in isopropyl alcohol. A constant particle size and  $\text{Al}_2\text{O}_3$  abrasion were ensured by standardizing the mixing procedure. The dried powders were densified by hot pressing in vacuum. A temperature of  $1200^\circ\text{C}$  was chosen to allow the  $\text{ZrO}_2$  to assume the tetragonal structure and sufficient time was allowed to permit the attainment of full density ( $\sim 1$  hr).

## 2.2 Microstructural Characteristics

The room temperature structures of the hot pressed materials were firstly evaluated using x-ray diffraction analysis (in the range,  $26^\circ < 2\theta < 38^\circ$ ). The materials containing pure  $\text{ZrO}_2$  indicated the exclusive

---

\*  $\text{ZrO}_2$ : Johnson Matthey Chemicals Ltd., Royston, England

\*\*  $\text{ZrO}_2 + 4/8$  w/o  $\text{Y}_2\text{O}_3$ : Zircar Products, Inc., Florida, N.Y.

+  $\text{ZnO}$ : J. T. Baker Chemicals Co., Phillipsburg, N.J.

++  $\text{Al}_2\text{O}_3$  balls: Coors Hi-Purity  $\text{Al}_2\text{O}_3$  media.

existence of monoclinic  $\text{ZrO}_2$ , while the partially stabilized materials contained a proportion of tetragonal  $\text{ZrO}_2$ <sup>†</sup>. The relative proportions of the monoclinic and tetragonal phase were ascertained from the integral intensities of the  $(11\bar{1})$  monoclinic and  $(111)$  tetragonal diffraction peaks. Specifically, the fraction,  $f_m$ , of monoclinic  $\text{ZrO}_2$  was obtained from the relation;

$$f_m = 1.63 I_m(11\bar{1}) / [1.63 I_m(11\bar{1}) + I_t(111)] \quad (2)$$

The relative proportions of monoclinic  $\text{ZrO}_2$  obtained for the partially stabilized materials are plotted in fig. 1, as a function of the total volume concentration of  $\text{ZrO}_2$ .

Diffraction peaks indicative of the existence of small concentrations of  $\text{ZnAl}_2\text{O}_4$  were evident in all materials. This phase undoubtedly occurred because of incorporation of  $\text{Al}_2\text{O}_3$  during the milling procedure and subsequent reaction with  $\text{ZnO}$  during hot pressing. The quantity of  $\text{ZnAl}_2\text{O}_4$  ( $\sim 7$  wt.%) and the size of the  $\text{ZnAl}_2\text{O}_4$  particles (see fig. 6) were relatively independent of the  $\text{ZrO}_2$  content. This phase thus contributes uniformly to the toughness in all systems studied and should not influence the trends in toughness with  $\text{ZrO}_2$  content.

Dilatometer measurements (fig. 2) invariably indicated the existence of the tetragonal to monoclinic phase transformation upon cooling (in those materials that contained monoclinic  $\text{ZrO}_2$  at room temperature). The trend in the transformation temperature with  $\text{ZrO}_2$  particle concentration (for pure  $\text{ZrO}_2$ ), depicted in fig. 2, indicates two regimes. For volume concentrations  $\leq 0.2$ , the transformation temperature varies slowly with

<sup>†</sup>Cubic  $\text{ZrO}_2$  was not detected from X-ray diffraction measurements, even in materials containing 8 wt.%  $\text{Y}_2\text{O}_3$ .

concentration ( $M_s \sim 600^\circ\text{C}$ ) and the transformation extends over an appreciable temperature range (such that  $M_f \sim 100^\circ\text{C}$ ). However, a transition to a higher transformation temperature ( $M_s \sim 850^\circ\text{C}$ ) occurs at concentrations  $\geq 0.3$ , and the transformation proceeds to completion over a narrow range of temperature ( $M_f \sim 550^\circ\text{C}$ ). The latter behavior undoubtedly derives from particle interaction effects, which encourage cooperative transformations in neighboring (or contacting) particles.

Transmission electron microscopy studies indicate that the  $\text{ZrO}_2$  particles are located primarily at  $\text{ZnO}$  grain boundaries, either at two grain interfaces or at three grain junctions. The  $\text{ZnO}$  grains typically range in size between  $\sim 0.7$  to  $\sim 2.5 \mu\text{m}$ , essentially invariant with  $\text{ZrO}_2$  content, and the  $\text{ZrO}_2$  particles range between  $0.1$  and  $1.2 \mu\text{m}^+$  in diameter. Scanning electron fractographs indicate a porosity level  $\approx 1\%$ .

Transmission electron microscopy also revealed that the pure  $\text{ZrO}_2$  containing material contained only monoclinic  $\text{ZrO}_2$ . The monoclinic particles were invariably twinned (fig. 3). The twin spacing tended to increase with particle size, ranging between  $22$  and  $100 \text{ nm}$  for  $\text{ZrO}_2$  particles between  $0.16$  and  $1.3 \mu\text{m}$  in size. Very small microcracks ( $\sim 30 \text{ nm}$  in length) were occasionally identified at twin terminations.<sup>11</sup> These microcracks are not considered to be of sufficient size to influence the mechanical properties, and are unlikely to be the source of stress induced microcracks (sections 2.4 and 2.5). Larger, grain-sized, microcracks of the type that exert an important influence on fracture were not detected.

---

<sup>+</sup>High  $\text{ZrO}_2$  content materials can exhibit  $\text{ZrO}_2$  agglomerates up to  $2 \mu\text{m}$  in diameter.

### 2.3 Elastic Modulus and Hardness

Young's modulus was measured by using a resonance method in the fundamental flexure mode of vibration. Hardness was determined by Vickers indentation (load: 200N) on polished surfaces.<sup>†</sup> The trends in E and H with  $ZrO_2$  volume concentration are plotted in fig. 4. Both quantities increase linearly between the values for pure ZnO and  $ZrO_2$ , as expected for intact, intimate mixtures of two discrete phases. Deviations from linearity, toward lower values of E or H, typify behavior that obtains in the presence of significant microcracking. The observed trends in E and H are thus indicative of the absence of significant spontaneous microcracking.

### 2.4 Acoustic Emission Studies

Materials prone to stress induced microcracking (such as  $Al_2O_3$ <sup>12</sup> and porcelain<sup>13</sup>) yield substantial low load (pre-fracture) acoustic emission activity during flexure tests. Consequently, the detection of acoustic emission during such tests provides a measure of a material's susceptibility to stress induced microfracture. Four point flexure tests were thus performed on several of the monoclinic  $ZrO_2$  containing materials and acoustic emission monitored, using a transducer attached to the test specimens.<sup>12,13</sup> Significant acoustic emission activity was only detected just prior to failure (at  $\geq 95\%$  of the failure load). The incidence of stress induced microcracking in the monoclinic  $ZrO_2$  containing materials has thus been discounted.

---

<sup>†</sup>200 N loads were used to obtain the load independent hardness.<sup>12</sup> Note that the resultant hardnesses are not affected by cracking, because the cracks form during unloading.<sup>13</sup>

AD-A124 025

MICRO AND MACRO MECHANICS OF FRACTURE IN CERAMICS(U)  
CALIFORNIA UNIV BERKELEY DEPT OF MATERIALS SCIENCE AND  
ENGINEERING A G EVANS ET AL. 30 OCT 82

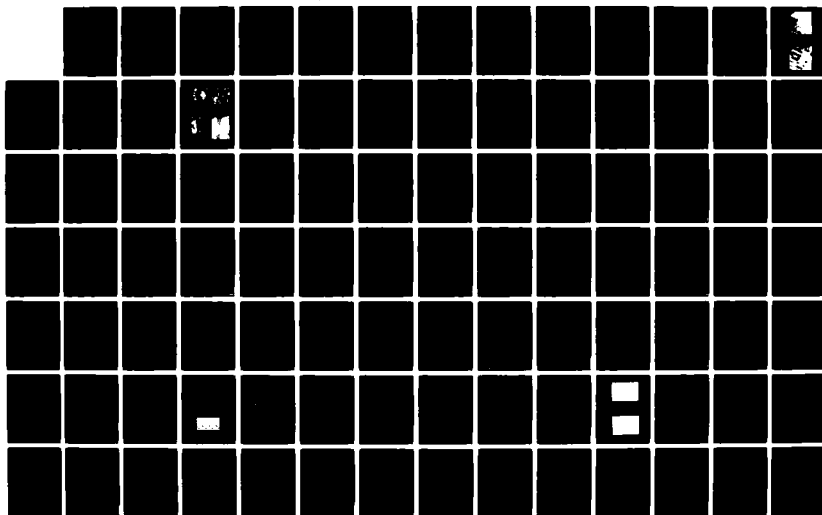
2/4

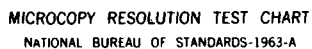
UNCLASSIFIED

NO0014-81-K-0362

F/G 11/2

NL







## 2.5 Fracture Studies

The fracture toughness of each material was determined using both the indentation<sup>14,15</sup> and single edge notched beam methods.<sup>16</sup> Selected values were also obtained using the surface crack method.<sup>17</sup> The toughness trends were essentially the same for each method, although some differences in absolute values were evident. The trends with a total  $ZrO_2$  content are exemplified by the toughness data plotted in fig. 5a. The influence of the monoclinic  $ZrO_2$  content on toughness (obtained by excluding the tetragonal  $ZrO_2$  content from the abscissa) is indicated on fig. 5b. The correlation of the data evident from fig. 5b suggests that the monoclinic particles exert the dominant influence on the toughening imparted by the  $ZrO_2$ , and that transformation toughening is relatively unimportant in this material system.

Fractographic studies, using the scanning electron microscope, indicate that fracture in the ZnO matrix is predominantly transgranular. However, the cracks are deflected around the  $ZrO_2$  particles, usually along the ZnO/ $ZrO_2$  interface. An increase in crack surface area thus obtains as the  $ZrO_2$  content increases (fig. 6). Finally, inspection of the region around the tip of an arrested crack, using the SEM in the backscatter mode, following a silver nitrate penetration treatment, did not reveal the existence of a discrete zone of microcracks. These observations confirm the absence of a stress-induced microcrack zone, in accord with the implications of the acoustic emission measurements.

(as evidenced by the isolation of  $ZrO_2$  particles at three grain junctions in the ZnO matrix) and hence, at volume concentrations of  $ZrO_2$  in excess of  $\sim 0.2$ , some of the monoclinic  $ZrO_2$  grains are expected to be in intimate contact. Thereafter, as an increasingly continuous network of  $ZrO_2$  develops, with increase in  $ZrO_2$  content, the crack will be required to propagate through  $ZrO_2/ZrO_2$  interfaces.<sup>†</sup> The fracture toughness will thus be limited by the toughness of monoclinic  $ZrO_2$ , modified by the presence of isolated or contiguous regions of ZnO. At this limiting condition, the role of the ZnO (being a low modulus material) should be similar to that of retained porosity; namely, eliciting a toughness degradation (vis-a-vis  $ZrO_2$ ) approximately proportional to the ZnO volume concentration. The toughness of intact monoclinic  $ZrO_2$  is not known, but should be similar to that for cubic  $ZrO_2$ <sup>20</sup>, i.e.  $\sim 3 \text{ MPa}\sqrt{\text{m}}$ . The observed toughness level  $\sim 3 \text{ MPa}\sqrt{\text{m}}$ , between  $ZrO_2$  concentrations of  $\sim 0.2$  to 0.5, is thus consistent with a toughness limitation imposed by the intrinsic toughness of the  $ZrO_2$ . Conversely, the toughness in the glass, alumina systems is unlikely to exhibit a similar limitation<sup>4</sup>, because the glass matrices wet the alumina and a continuous glassy phase invariably exists. Cracks are thus required to deflect and bow around the  $Al_2O_3$  spheres, over the entire range of volume concentrations. It is also noted that the intrinsic toughness of  $Al_2O_3$  ( $\sim 4 \text{ MPa}\sqrt{\text{m}}$ ) is appreciably in excess of that for the glass matrix ( $\sim 0.7 \text{ MPa}\sqrt{\text{m}}$ ) and a limitation imposed by the  $Al_2O_3$  toughness would be less apparent in these data.

---

<sup>†</sup>Concomittant changes in fracture surface morphology were not detected.

### 3. THE TOUGHENING MECHANISM

#### 3.1 General Considerations

It is instructive at the outset to compare the present toughness results with those obtained by Swearingen et al.<sup>18</sup> for a series of glass matrix materials containing  $\text{Al}_2\text{O}_3$  spheres (fig. 7). A reasonable correspondence of the results is evident, up to monoclinic  $\text{ZrO}_2$  volume concentrations of  $\sim 0.2$ . The correspondence pertains despite the considerable range of residual strain levels encompassed by these materials. It is thus tempting to conclude that the absolute magnitude of the residual strain has no explicit effect on the toughness, provided that the strain level is in excess of that needed to induce effective crack deflection and crack bowing. However, further study is needed before explicit residual strain effects can be adequately discounted.

A divergence of the glass/alumina and  $\text{ZnO}/\text{ZrO}_2$  toughness trends occur at volume concentrations in excess of  $\sim 0.2$ . The  $\text{ZrO}_2$  volume concentration at the toughness divergence coincides with the concentration that renders an appreciable increase in  $M_s$  (fig. 2). The latter was interpreted to be indicative of significant interaction, or contact, between neighboring  $\text{ZrO}_2$  particles, since volume concentrations at this level presage the onset of appreciable particle contact in randomly dispersed second phase mixtures.<sup>19</sup> An interpretation of the divergence in terms of the relative propensity for particle contact within the two material systems may thus be plausible.<sup>†</sup> In the  $\text{ZnO}/\text{ZrO}_2$  system, the  $\text{ZnO}$  does not wet the  $\text{ZrO}_2$

---

<sup>†</sup>A  $\text{ZrO}_2$  volume concentration of  $\sim 0.2$  also coincides with the onset of a diminishing residual strain level within the particles, caused by particle interaction effects. Hence, residual strain influences, associated with the very large residual strains in the  $\text{ZnO}/\text{ZrO}_2$  system, could also be involved in the toughness divergence.

#### 4.2 The Toughening Mechanism

The absence both of pre-existent microcracks (inferred from the modulus and hardness measurements) and of stress induced microcracks (suggested from observations of the crack tip, following a penetration treatment), imply that microcrack related mechanisms of toughening are unlikely in the present materials. The level of toughening exhibited by the pure  $\text{ZrO}_2$  is thus considered to derive primarily from crack deflection/crack bowing processes, as manifest in an increase in the deflection intensity with increase in  $\text{ZrO}_2$  content (fig. 6).

A comparison of the toughness trends with those anticipated by the available deflection and bowing models<sup>4</sup> (fig. 7) indicates that both the  $\text{ZnO}/\text{ZrO}_2$  and  $\text{Al}_2\text{O}_3$  /glass systems exhibit initial toughness increases (at  $V_f < 0.2$ ) intermediate between the crack deflection prediction (for spherical particles) and the crack bowing prediction. It is probable, therefore, that some combination of deflection and bowing provides the observed toughening in both systems. Further analysis of crack interaction toughening, based on the concurrence of deflection and bowing, should thus prove fruitful.

The absence of a toughening contribution from the tetragonal  $\text{ZrO}_2$  (evident from a comparison of Figs. 5a and 5b) merits some discussion. A preliminary rationale recognizes that the relatively low Young's modulus and thermal expansion coefficient pertinent to the  $\text{ZnO}/\text{ZrO}_2$  system result in a small value of the product,  $Ee^T$ , that contributes to transformation toughening (eqn 1).<sup>†</sup> Hence, to obtain a significant level of

<sup>†</sup> $Ee^T$  is  $\sim 10^{11}$  Pa for PSZ and  $\text{Al}_2\text{O}_3/\text{ZrO}_2$ , but only  $\sim 3 \times 10^{10}$  Pa for  $\text{ZnO}/\text{ZrO}_2$  (note that  $e^T$  comprises the unconstrained volume strain of the transformation minus the thermal mismatch strain).

transformation toughening ( $\Delta K_C^T \geq 0.2 \text{ MPa}\sqrt{\text{m}}$ ), transformation zone widths  $\geq 2 \text{ }\mu\text{m}$  are required (eqn 1); larger than the zones observed in most PSZ<sup>20</sup> materials. However, the absence of deflection toughening<sup>2,4</sup>, which should obtain even with very small stress induced transformation zones (provided that the transformation occurs ahead of the crack), is less explicable. Further studies of crack tip transformation effects are clearly needed to fully comprehend the negligible influence of the tetragonal  $\text{ZrO}_2$ .

#### 4. CONCLUSION

The toughness of ZnO has been increased by  $\sim 3$  (in the strain energy release rate) through the incorporation of monoclinic  $\text{ZrO}_2$ . This toughening has been achieved in the absence of microcracking and has been attributed to crack deflection by the residual strain field of the monoclinic  $\text{ZrO}_2$ .

The principal toughening develops at  $\text{ZrO}_2$  volume concentrations,  $V_f$ , up to  $\sim 0.2$  (further additions of  $\text{ZrO}_2$  exert a minimal influence on the toughness). This behavior has been considered to result from a limitation imposed by the intrinsic toughness of the monoclinic  $\text{ZrO}_2$ , by virtue of the increased mutual contact between  $\text{ZrO}_2$  particles at volume concentrations  $\geq 0.2$ .

A comparison of the toughness in  $\text{ZnO/ZrO}_2$  with data for the glass/alumina system indicated a divergent trend at high particle volume concentrations, even though the toughening in both systems can most plausibly be attributed to crack/particle interaction. The divergence has been associated with the complete matrix wetting that obtains in the glass/alumina system and the high relative toughness of the second phase. to stronger contributions to the toughness from crack bowing effects, superimposed on crack deflection toughening.

REFERENCES

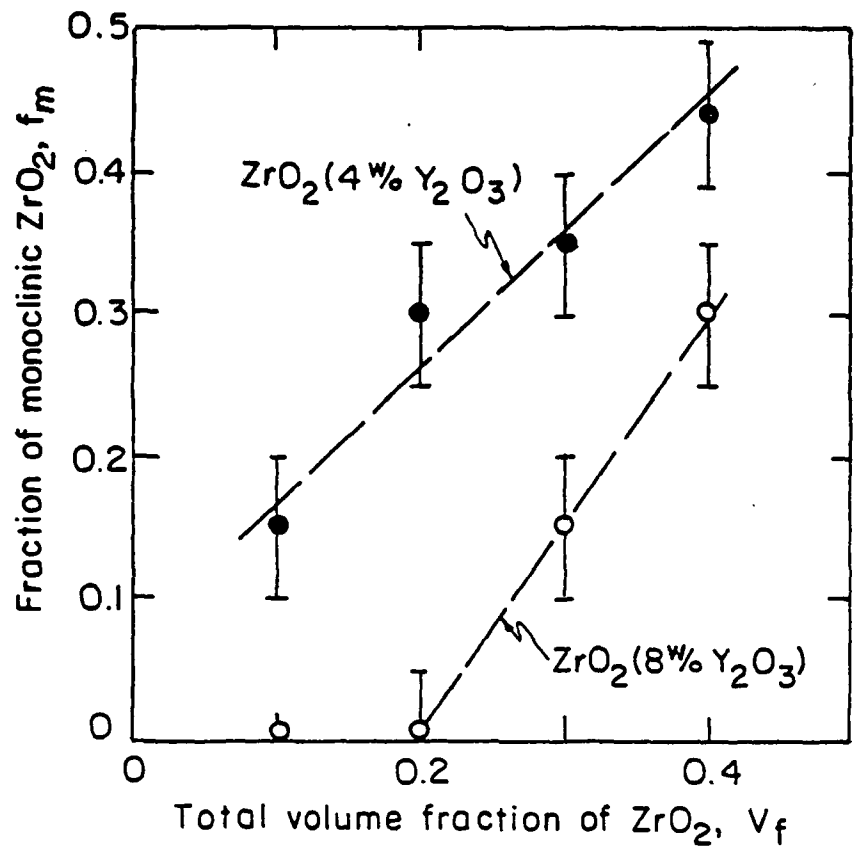
1. R. McMeeking and A. G. Evans, Jnl. Amer. Ceram. Soc., in press.
2. A. G. Evans and K. T. Faber, Jnl. Amer. Ceram. Soc. 64 (1981) 394.
3. F. F. Lange, Phil. Mag. 22, 983 (1970).
4. K. T. Faber, A. G. Evans and M. D. Drory, Fracture Mechanics of Ceramics (Ed. R. C. Bradt, D. P. H. Hasselman, F. F. Lange and A. G. Evans), Plenum, N.Y. (1982), in press.
5. D. J. Green and P. S. Nicholson, Fracture Mechanics of Ceramics (Ed. R. C. Bradt, D. P. H. Hasselman and F. F. Lange) Plenum, N.Y., (1978) vol. 4, p. 945.
6. N. Claussen, and M. Rühle, Advances in Ceramics, Vol. 1 (1981) 137.
7. D. B. Marshall, A. G. Evans and M. D. Drory, Fracture Mechanics of Ceramics (Ed. R. C. Bradt, D. P. H. Hasselman, F. F. Lange and A. G. Evans), Plenum, N.Y. (1982) in press.
8. A. G. Evans, N. H. Burlingame, M. D. Drory and W. Kriven, Acta Met. 29 (1981) 447.
9. F. F. Lange and D. J. Green, Advances in Ceramics, Vol. 1 (1981) 217.
10. N. Claussen, A. G. Evans, A. H. Heuer, M. Rühle, Proceedings of Transformation Toughening Workshop (Schloss Ringberg, Germany, June 1981), to be published.
11. Y. Fu, M. S. Thesis, U. C. Berkeley, Sept. 1981.
12. A. G. Evans, M. Linzer and L. R. Russell, Mat. Sci. Eng. 15 (1974) 253.
13. A. G. Evans and M. Linzer, Jnl. Amer. Ceram. Soc. 56 (1973) 575.
14. A. G. Evans and E. A. Charles, Jnl. Amer. Ceram. Soc. 60 (1977) 22.
15. B. R. Lawn, A. G. Evans and D. B. Marshall, Jnl. Amer. Ceram. Soc. 63 (1980) 574.

16. N. Claussen, Jnl. Amer. Ceram. Soc., 59 (1976) 49.
17. J. J. Petrovic and M. G. Mendiratta, ASTM STP 678 (1978) p. 83.
18. J. C. Swearingen, E. K. Beauchamp and R. J. Eagen, Fracture Mechanics of Ceramics (Ed. R. C. Bradt, D. P. H. Hasselman and F. F. Lange).
19. P. P. Bansal and A. J. Ardell, Metallography 5 (1972) 97.
20. D. L. Porter and A. H. Heuer, Jnl. Amer. Ceram. Soc. 60 (1977) 183.



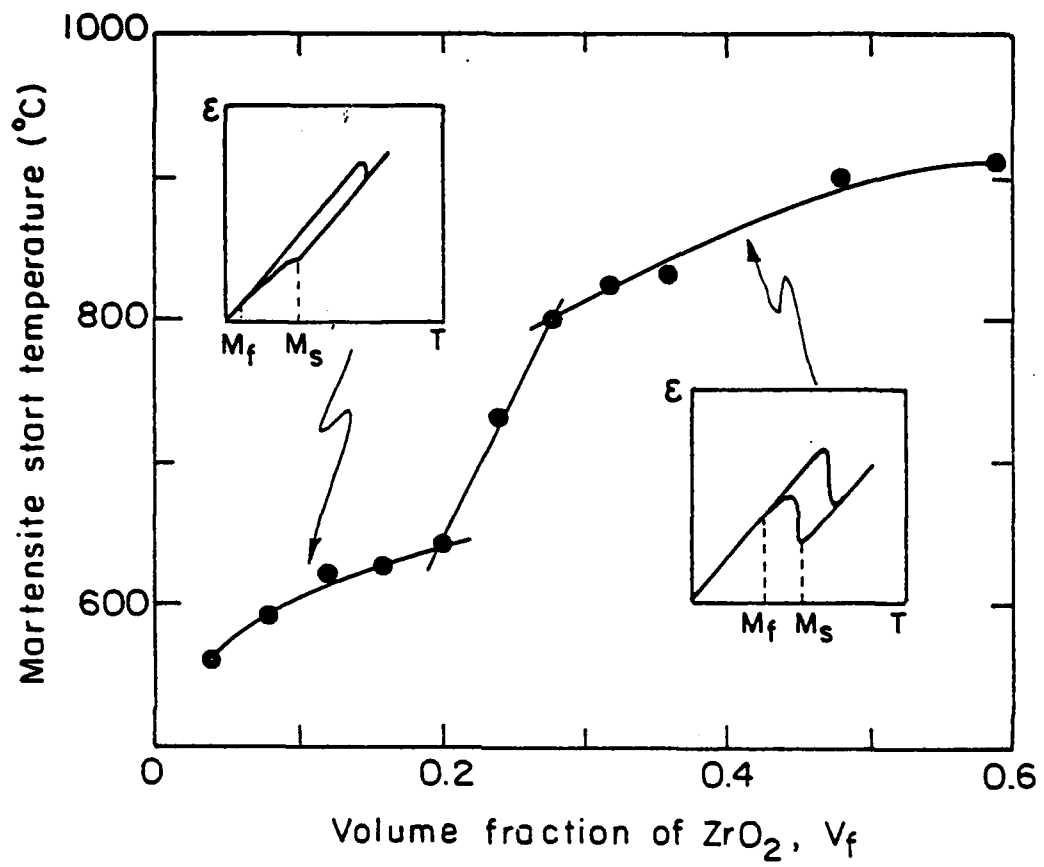
FIGURE CAPTIONS

- Fig. 1 A plot of the monoclinic fraction in the partially stabilized  $\text{ZrO}_2/\text{ZnO}$  composites.
- Fig. 2 A plot of the martensite start,  $M_s$ , temperature as a function of  $\text{ZrO}_2$  volume concentration (for pure  $\text{ZrO}_2$ ), determined from dilatometer studies.
- Fig. 3. Transmission electron micrographs of twinned  $\text{ZrO}_2$  particles in  $\text{ZnO}$ .
- Fig. 4. Plots of the trends in Young's modulus and hardness with  $\text{ZrO}_2$  volume concentration.
- Fig. 5 (a) The critical stress intensity factor as a function of the total  $\text{ZrO}_2$  content.  
(b) The relative critical strain energy release rate as a function of the monoclinic  $\text{ZrO}_2$  content.
- Fig. 6 Secondary electron images of indentation cracks indicating the change in crack deflection intensity with  $\text{ZrO}_2$  content: (a) and (b)  $\text{ZnO}/0.06 \text{ ZnAl}_2\text{O}_4$  (the dark particles are the  $\text{ZnAl}_2\text{O}_4$  phase, which apparently does not deflect the crack), (c)  $\text{ZnO}/0.07 \text{ ZnAl}_2\text{O}_4/0.08 \text{ ZrO}_2$ , (d)  $\text{ZnO}/0.07 \text{ ZnAl}_2\text{O}_4/0.16 \text{ ZrO}_2$ .
- Fig. 7. A comparison of the toughening in  $\text{ZnO}/\text{ZrO}_2$  with that for glass/alumina. Also shown are the toughness levels predicted for the crack deflection and crack bowing mechanisms.



XBL 819-6645

Fig. 1



XBL 819-6644

Fig. 2

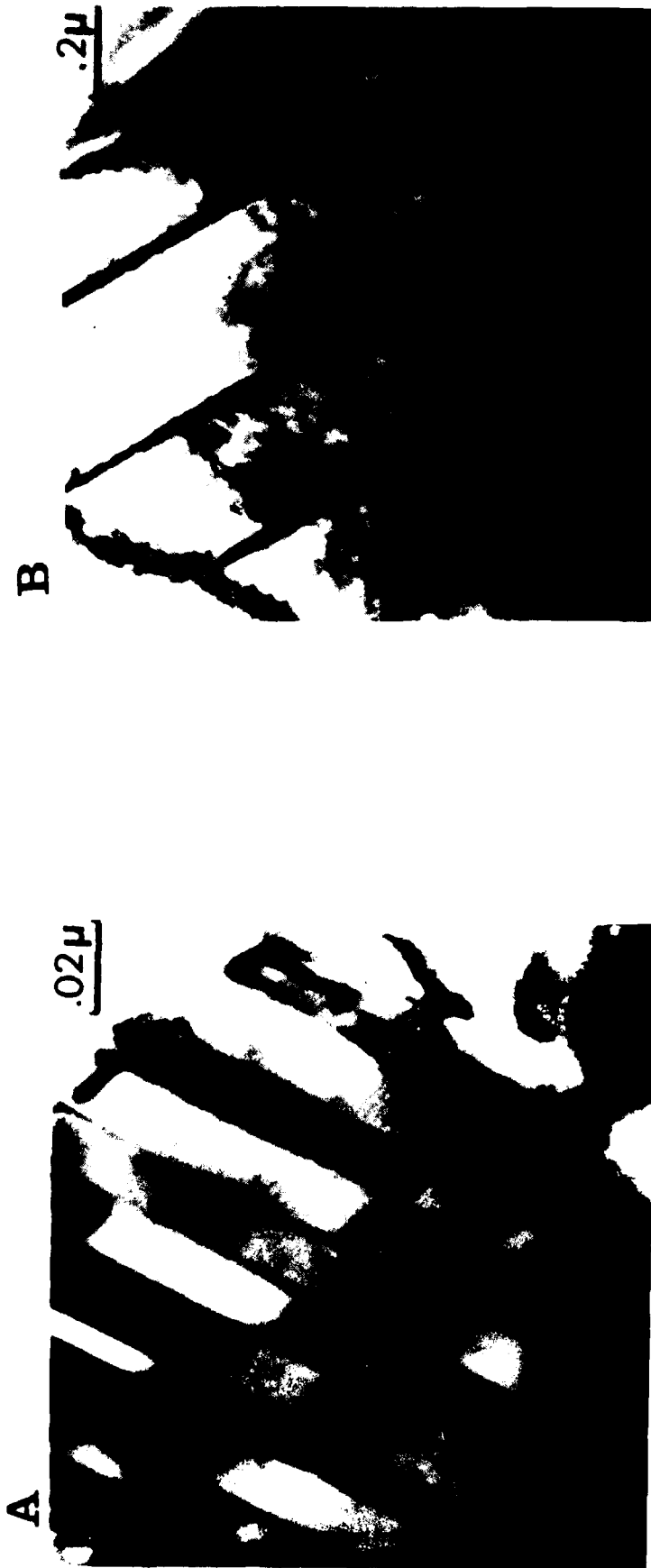
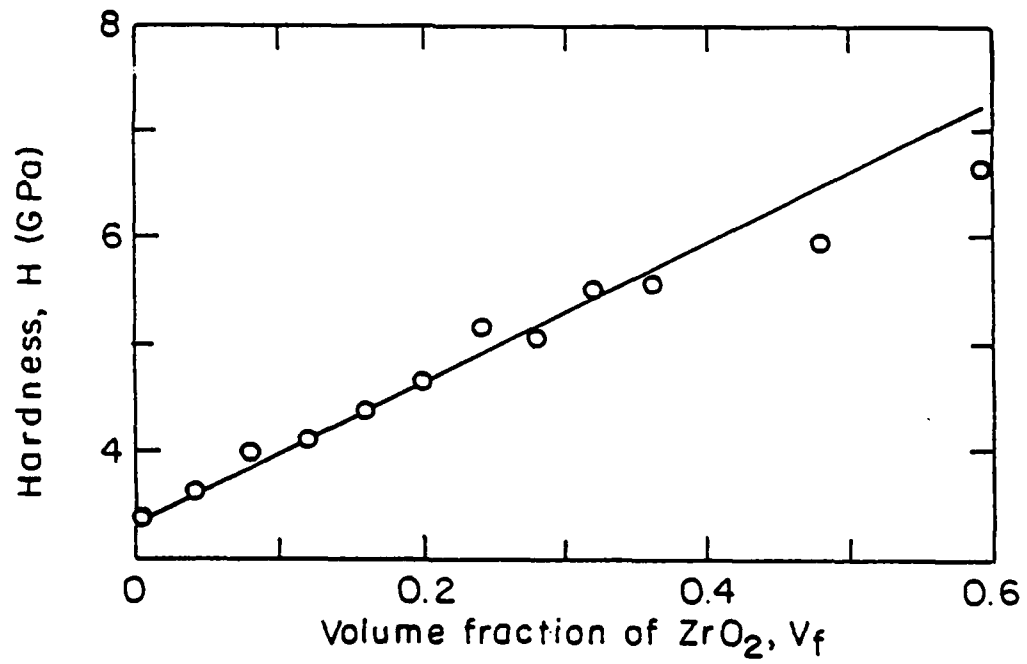
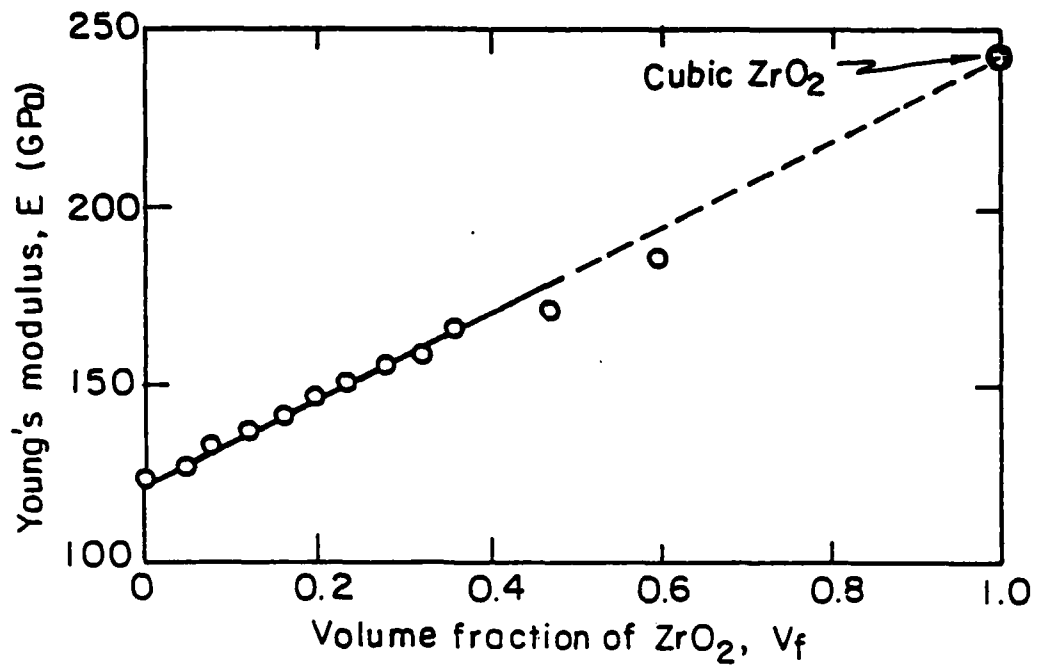
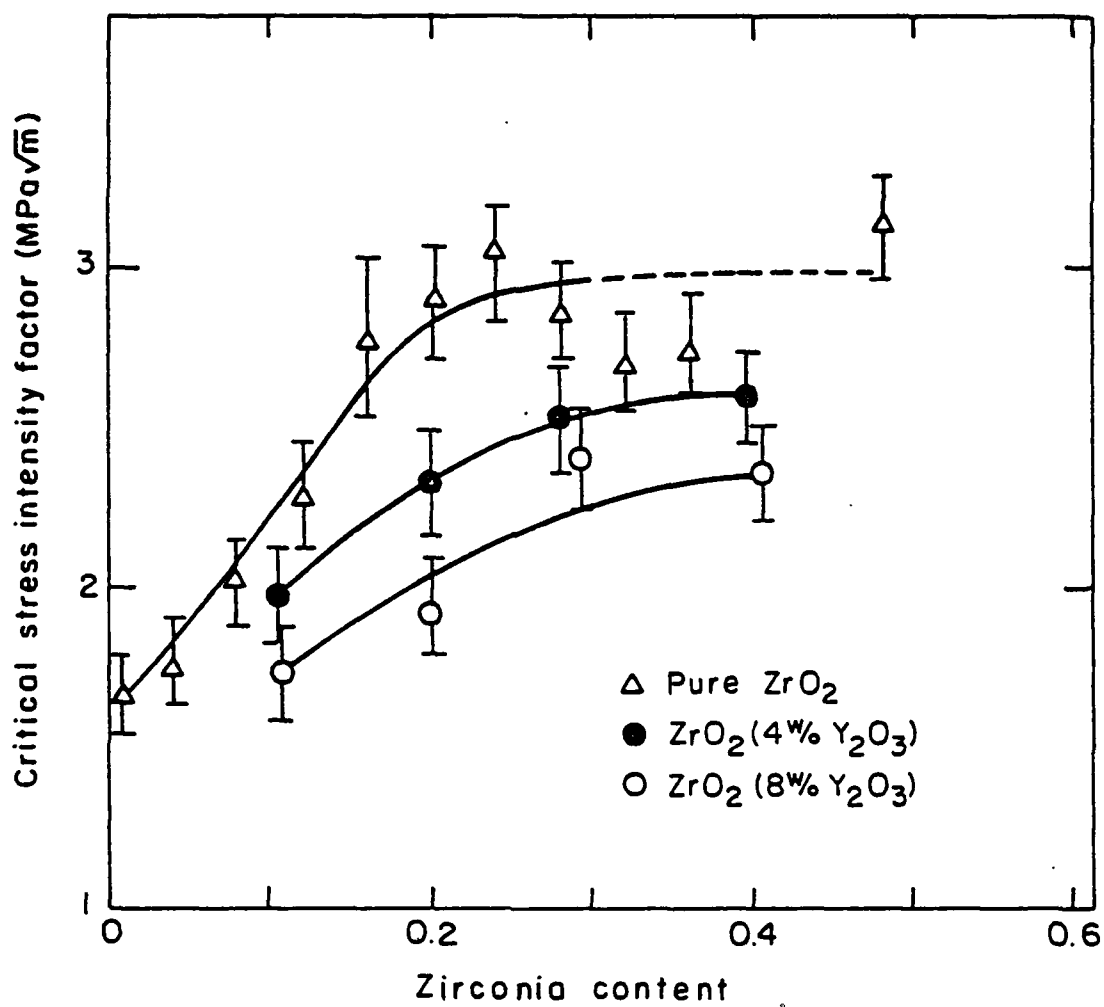


Fig. 3



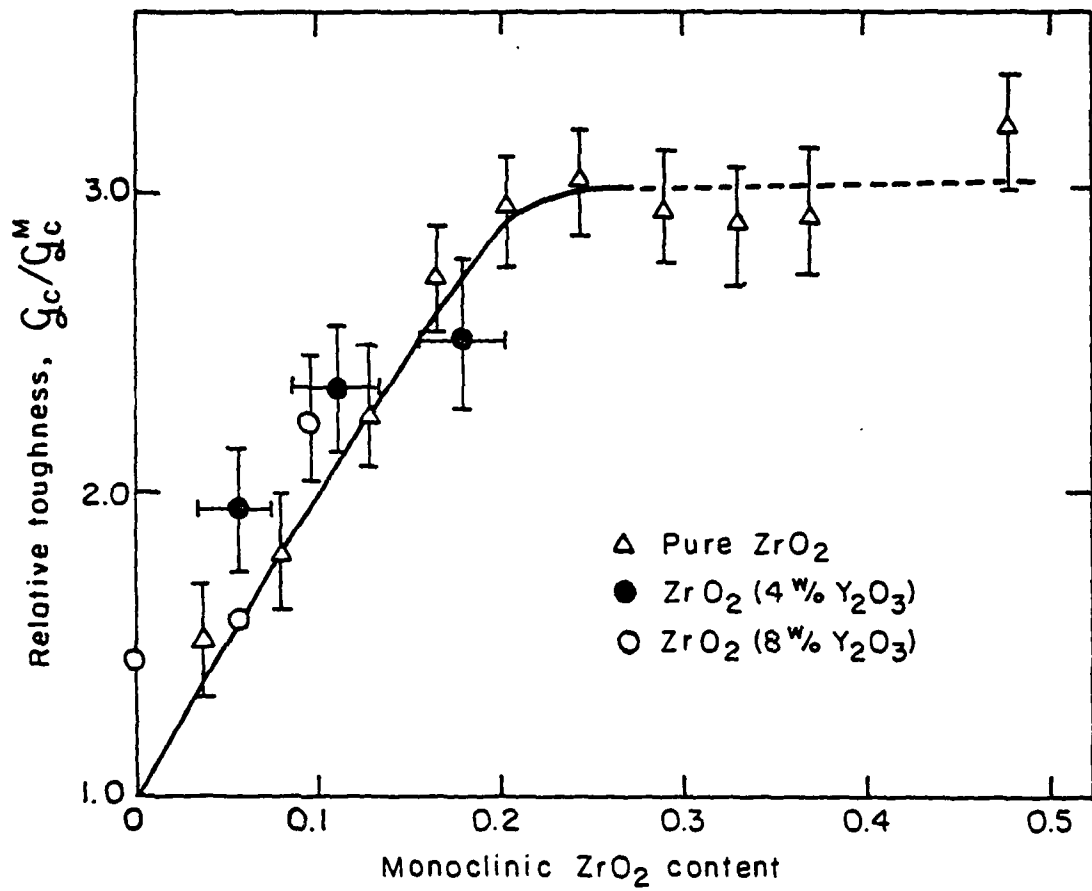
XBL 819-664 6

Fig. 4



XBL 819-6648

Fig. 5a



XBL819-6647

Fig.5b

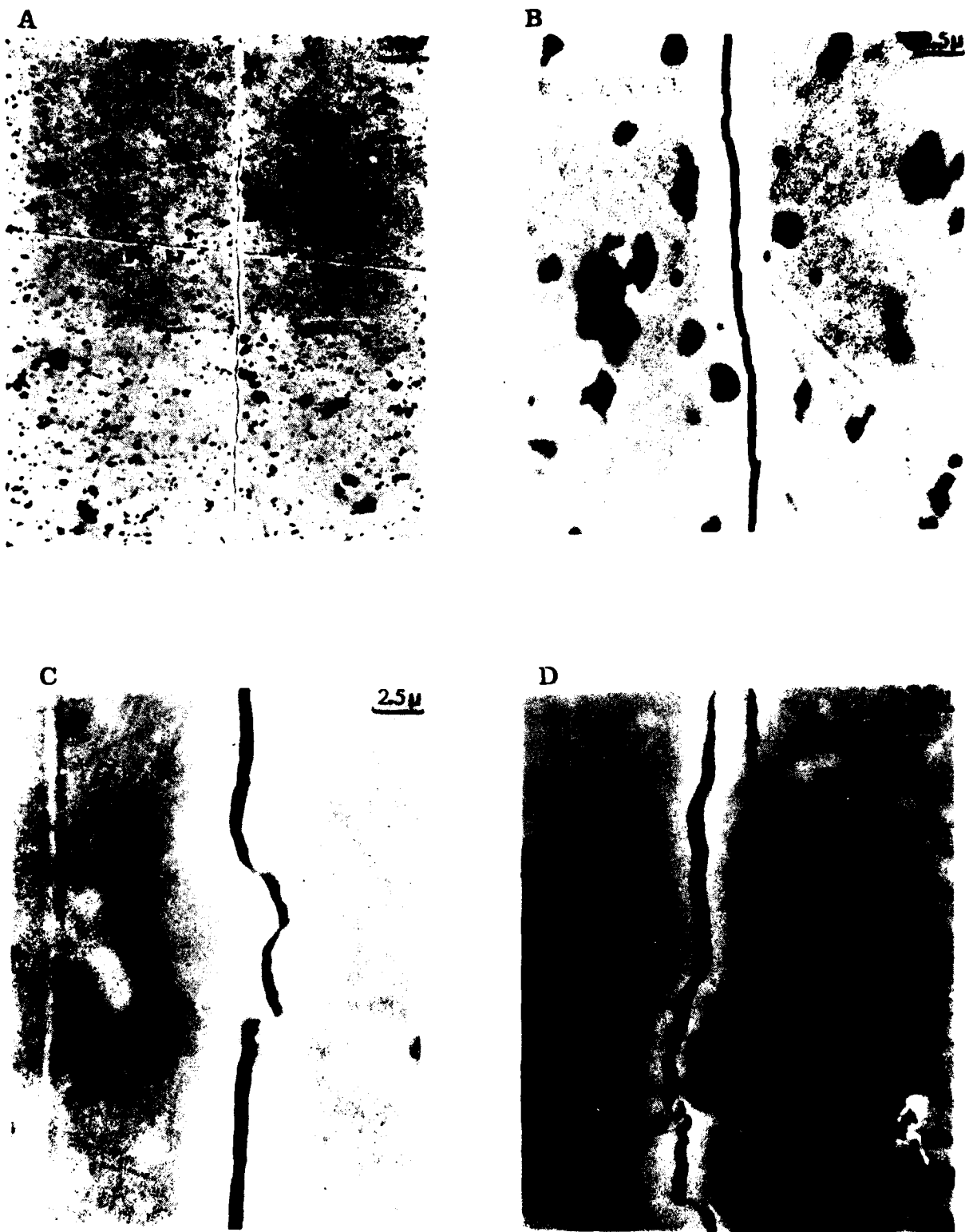
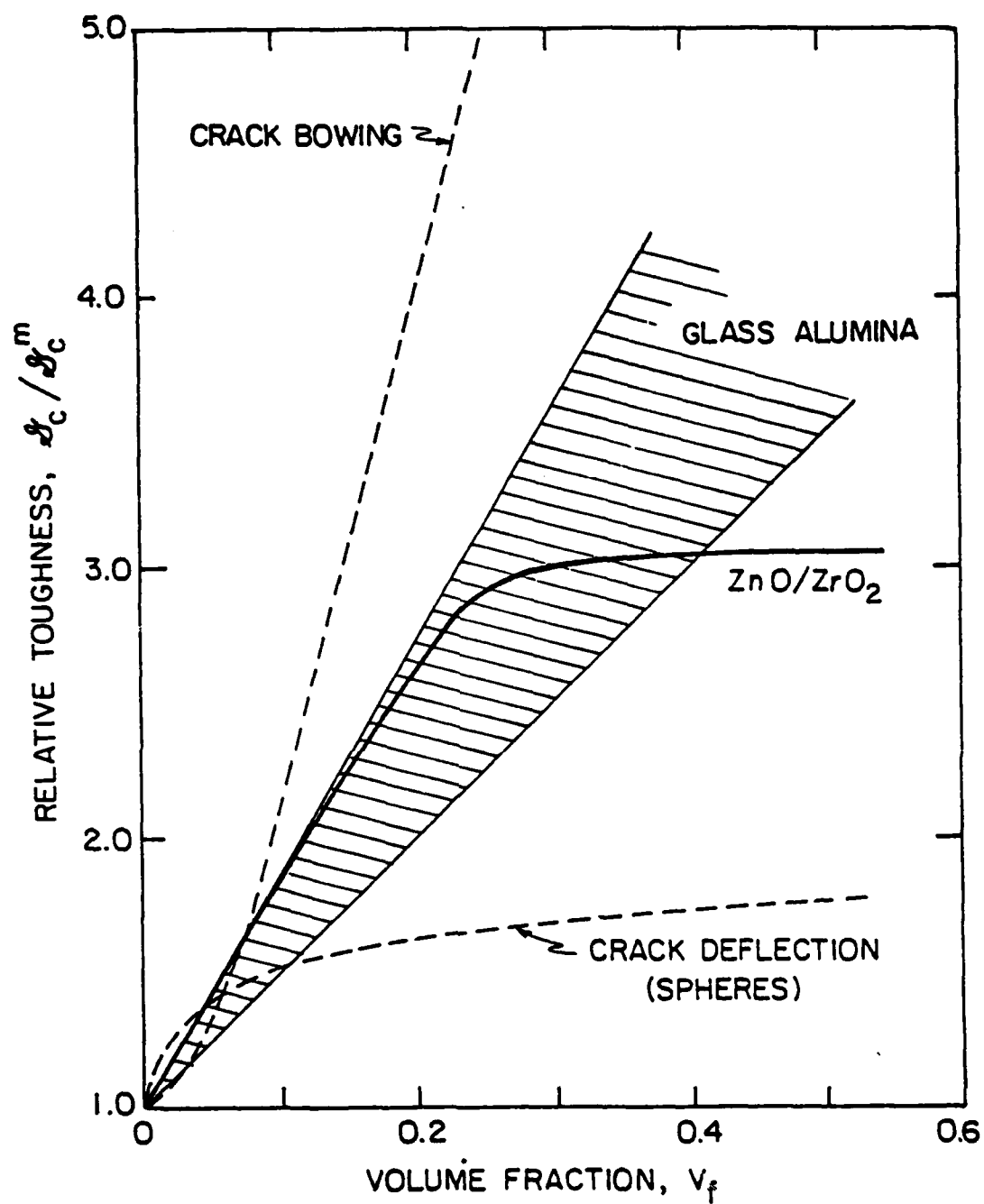


Fig. 6





XBL 823- 5326

Fig. 7

CHAPTER IV

CLEAVAGE FRACTURE IN MILD STEEL

by

A. G. Evans

Department of Materials Science and Mineral Engineering  
University of California  
Berkeley, CA 94720

and

J. W. Hutchinson

Division of Applied Science  
Harvard University  
Cambridge, MA 02138

ON CLEAVAGE FRACTURE IN STEEL

A. G. Evans

Department of Materials Science and Mineral Engineering  
University of California  
Berkeley, CA 94720

and

J. W. Hutchinson

Division of Applied Science  
Harvard University  
Cambridge, MA 02138

ABSTRACT

The fracture of mild steel in the cleavage range has been evaluated using a weakest link statistical model, assuming the pre-existence of a distribution of cracked grain boundary carbides. The model provides a rationale for the critical fracture distance, viz. the distance from the crack tip at which the probability of cleavage cracking exhibits a maximum. The critical distance depends on the size distribution and volume concentration of grain boundary carbides. The model also predicts trends in  $K_{IC}$  with material properties: flow strength, grain boundary carbide size/volume concentration and grain size. The resultant temperature dependence of  $K_{IC}$  is shown to derive exclusively from the temperature dependence of the flow stress (as in prior models); while the effects of grain size are indirect and depend primarily on the concomitant changes in carbide size and in flow strength.

## 1. INTRODUCTION

The cleavage fracture of steel has been rationalized as a phenomenon dictated by the brittle extension of cracked grain boundary carbides into the ferrite matrix, within the elastic/plastic stress field of a major crack.<sup>1,2</sup> This premise is based on extensive work on notched bend bars which indicates that the extension of cracked carbides into the ferrite matrix dictates failure.<sup>2</sup> Circumstances which permit the subsequent stable growth of the cleavage crack can be conjectured (Appendix), but will be neglected for present purposes. The cracked carbides that dictate the failure of notched specimens are considered to be located near the elastic/plastic interface, where the principal tensile stress is a maximum.<sup>1</sup> The stress at this location, at the failure instability, defines an effective cleavage strength,  $S$ . This cleavage strength is usually invariant with temperature<sup>1</sup> and decreases with increase in carbide size,<sup>2</sup>  $r$  (as,  $S \propto r^{-1/2}$ ).

Application of cleavage concepts derived from notched beam tests to the extension of sharp cracks, to determine  $K_{IC}$ , has recognized that the rapid gradient in stress near the crack tip must influence the cleavage condition. Specifically, a realization that the peak tensile stress near the tip,  $\hat{\sigma} > S$  (fig. 1), has lead to the definition of a critical distance,  $x_c$ , at which the crack tip stress reaches the cleavage stress.<sup>1</sup> However, a consistent microstructural significance has not yet been attached to this critical distance.\* It has subsequently been proposed that  $x_c$  is dictated by statistical strength considerations related to the grain boundary carbide

---

\*The original proposal<sup>1</sup> that  $x_c$  is some constant multiple of the grain diameter is not fully consistent with subsequent observations.<sup>2-5</sup>

size and spacing distribution within the variable crack tip field.<sup>6,7</sup> The intent of the present paper is to develop a quantitative cleavage fracture model based on concepts of crack growth from cracked carbide coupled with weakest link statistics. The model provides a rationale for the existence of a critical distance (related primarily to the grain boundary carbide size and spacing distribution) and predicts trends in toughness with material properties that conform with available measurements.

## 2. GENERAL CONSIDERATIONS

In general, cleavage fracture may involve one, or more, sub-critical cracking event in a zone around the major crack. Plastic deformation firstly initiates stable cracks in the grain boundary carbides.<sup>4,8</sup> This process is a consequence of the development of stress concentrations in the carbides. The stress concentrations can be induced either by discrete deformation (such as slip band impingement), whereupon cracking is more prevalent in large grained materials<sup>8</sup>, or by homogeneous plastic straining of the ferrite. Carbide cracking is succeeded by brittle crack extension across the neighboring ferrite grain. The stability of this process is not well comprehended (Appendix). Stable grain-sized cracks have been observed directly ahead of arrested cracks<sup>4</sup> (and can be inferred from the presence of isolated cleavage facets in the ductile-to-brittle transition range). However, (notwithstanding the experimental difficulties associated with their detection) careful studies have not revealed significant stable cleavage cracking,<sup>2</sup> except in a very fine grained steel,<sup>9</sup> and in a low carbon steel<sup>10</sup>. A failure criterion based upon the extension of carbide cracks into the ferrite matrix thus appears to be a plausible initial assumption.

Substantial work by Knott and colleagues<sup>2,5</sup> has revealed that cracked carbides propagate at a characteristic normal stress, or strength, level;

$$S = [\pi E \gamma_p / 2(1-\nu^2)r]^{1/2} \quad (1)$$

where  $r$  is the radius of the cracked carbide,  $E$  is Young's modulus and  $\gamma_p$  the effective cleavage energy of the ferrite. It has also been proposed that emplacing a distribution of cracked carbides within the elastic/plastic stress field of a major crack, and evaluating their extension probabilities, would provide a basis for predicting trends in  $K_{IC}$  with temperature and microstructure.<sup>5</sup> A formal analysis, based on weakest link statistics,<sup>11,12</sup> is presented herein: with emphasis upon parametric prediction of the trends, with temperature and microstructure, in both the characteristic distance,  $x_c$ , and the toughness  $K_{IC}$ . Requirements pertinent to the ductile/brittle transition are also addressed.

### 3. THE STATISTICAL MODEL

Weakest link statistics stipulates that a preexisting distribution of cracks will result in an elemental survival probability,<sup>11</sup>

$$1 - \Delta\phi = \exp [-\Delta V G(S)] \quad (2)$$

where  $\Delta V$  is the element of volume,  $\Delta\phi$  is the failure probability of the element (due to unstable extension of the weakest crack) and  $G(S)$  is the number of cracks in unit volume of material with a strength  $< S$ . A versatile strength distribution, capable of describing the size or strength characteristics of cracked carbides, has the form:

$$G(S) = \frac{1}{V_0} \left( \frac{S - S_u}{S + S_0} \right)^m \quad (3)$$

where  $S_u$  is the minimum strength (of the largest feasible carbide particle in unit volume),  $S_0$  is a scale parameter and  $m$  a shape parameter characteristic of the carbide size distribution and  $V_0$  is the total number of cracks in unit volume,

$$V_0 = 4\pi \langle r \rangle^3 / 3f \quad (4)$$

$\langle r \rangle$  is the average radius of the boundary carbides (related to  $S_0$  and  $m$ ) and  $f$  is the volume concentration of carbides located at grain boundaries.

Emplacing the cracked carbides into the stress field of a crack permits evaluation of  $\Delta\phi$ . Assuming that the normal stress  $\sigma_{yy}$  is the dominant stress component in the cleavage process<sup>†</sup>, the pertinent stress distribution can be expressed as;<sup>13,14</sup>

$$\frac{\sigma_{yy}}{\sigma_0} = f(N) \left( \frac{1-\nu^2}{I} \right)^{1/(1+N)} \left( \frac{K}{\sigma_0 \sqrt{x}} \right)^{2/(1+N)} \quad (5)$$

where  $x$  is the distance from the crack tip,  $\sigma_0$  is the yield stress,  $N$  is the hardening exponent,<sup>††</sup>  $f(N) \approx 2.5$ ,  $I \approx 4.5$ , and  $K$  is the stress intensity factor. An active volume element must now be defined, as the volume element within which extension of a carbide crack permits coalescence with the major crack and hence, an increment in crack advance.

This volume is considered to be encompassed by the curve depicted in fig. 2,

<sup>†</sup> The maximum principal tension does not occur directly ahead of the crack.<sup>13</sup> The choice of  $\sigma_{yy}$  as the predominant cleavage stress can only be approximate, therefore. Furthermore, the trajectory of cleavage cracks activated by the principal tensile stress will not encourage coalescence with the primary crack. This complexity requires further study.

<sup>††</sup>  $N \equiv 1/n$ , where  $n$  is the work hardening exponent.



$$y = y_0 (x/x_0)^k \quad (6)$$

where  $k$  is an exponent  $\leq 1$ . The rationale for this choice recognizes that the activation of cracked carbides by the  $\sigma_{yy}$  stress results in cleavage cracks nearly coplanar with the major crack. Hence, coalescence of the resultant cleavage crack with the major crack is restricted to carbides located within a narrow angular range out of the major crack tip. This concept is consistent with the observation of stable cleavage cracks ahead of an arrested major crack.<sup>4</sup> More complete volume element definition would require consideration of the angular dependence of the maximum principle tensile stress around the crack.

The volume element  $\Delta V$  can now be defined as;

$$\Delta V = y_0 x^k \lambda \Delta x / x_0^k \quad (7)$$

where  $\lambda$  is a characteristic sampling distance along the crack front (fig. 3). The distance  $\lambda$  recognizes that it will generally be insufficient to activate a single cracked carbide along the crack front. Instead, unstable extension of the major crack will require that the cracking process occur at intervals along the crack front (with spacing  $\lambda$ ).<sup>†</sup> Equating  $\sigma_{yy}$  to the carbide strength  $S$  now permits determination of the elemental failure probability: close to the crack tip ( $\sigma_{yy} \gg S_u$ ),

$$-\lambda n[1-\Delta\phi] = \left( \frac{3f\lambda y_0}{4\pi\langle r \rangle^3} \right) \left[ \frac{(x/x_0)^k \Delta x}{\left\{ 1 + \frac{2S_0}{5\sigma_0} \left[ \frac{9}{2} \left( \frac{\sigma_0 \sqrt{x}}{K} \right)^2 \right]^{1/(1+N)} \right\}^m} \right] \quad (8)$$

---

<sup>†</sup> Subsequently,  $\lambda$  will be regarded as some multiple of the grain diameter, as dictated by cleavage crack stability considerations (Appendix).

The elemental failure probability pertinent to crack growth thus exhibits the form depicted in fig. 4, with a maximum occurring at a distance  $x_c$  from the crack tip. The distance  $x_c$  represents the carbide location most likely to induce unstable crack extension and hence, may be regarded as a characteristic distance. Differentiation of eqn (8) to obtain the maximum gives,

$$x_c = \frac{2}{9} \left[ \frac{5(N+1)k}{2(m-k(N+1))} \right]^{N+1} \left( \frac{\sigma_0}{S_0} \right)^{N+1} \left( \frac{K_{IC}}{\sigma_0} \right)^2 \quad (9)$$

This relation exhibits the same material dependence as the characteristic length defined by Ritchie et al.<sup>1</sup>, qualified by the parameter containing  $m$ ,  $N$  and  $k$ . It is important to recognize that the peak in  $\Delta\phi$  develops ahead of the crack tip because the volume element containing cracked carbides tends to zero at the tip.<sup>†</sup>

The total survival probability,  $1 - \phi$ , of all volume elements is the product of the survival probability of individual elements,<sup>11</sup> and can be obtained from eqn (8) as;

$$-\ln[1-\phi] = \left( \frac{3f\ell y_0}{4\pi r > \frac{3}{2} x_0 k} \right) \int_0^\infty \frac{x^k dx}{[1+Ax^{1/(1+N)}]^m} \quad (10)$$

where

$$A = \frac{3}{5} \frac{S_0}{\sigma_0} \left[ \frac{9}{2} \left( \frac{\sigma_0}{K_c} \right)^2 \right]^{1/(1+N)}$$

<sup>†</sup>This result still obtains for volume elements of cylindrical symmetry and is not contingent upon the specific choice of  $k$  in eqn (7): provided that  $k > 0$ .

Integration of eqn (10) gives;

$$-\ln[1-\phi] = \frac{3f_0 y_0 (N+1) \Gamma[(k+1)(N+1)] \Gamma[m-(N+1)(k+1)]}{4\pi \langle r \rangle^3 A^{(k+1)(N+1)} \Gamma(m) x_0^k} \quad (11)$$

where  $\Gamma$  is the gamma function. This relation represents the cumulative distribution of  $K_{IC}$  values; the existence of such a distribution is a necessary consequence of a statistical model. The dependence of  $K_{IC}$  on material properties can now be ascertained at specified probability levels. At the median level ( $\phi = 1/2$ ), eqn (11) becomes;

$$K_{IC} = B \frac{S_0^{(N+1)/2} \langle r \rangle^{3/2(k+1)}}{(f_L)^{1/2(k+1)} \sigma_0^{(N-1)/2}} \quad (12)$$

where

$$B = \left[ \frac{4\pi y_0 (N+1) \Gamma[(k+1)(N+1)] \Gamma[m-(k+1)(N+1)]}{3(2/5)^{(k+1)(N+1)} (9/2)^{k+1} \Gamma(m) [\ln 2] x_0^k} \right]^{-2(k+1)}$$

The parametric dependence of  $K_{IC}$  on material parameters given by eqn (12) can be predicated on either  $\langle S \rangle$  or  $\langle r \rangle$ , by combining eqns (1) and (12);\*

$$K_{IC} \sim \frac{\langle S \rangle^{[(N+1)(k+1)-6]/2(k+1)} (E_{Y_p})^{3/2(k+1)}}{\sigma_0^{(N-1)/2} (f_L)^{1/2(k+1)}} \quad (13a)$$

or

$$K_{IC} \sim \frac{(E_{Y_p})^{(N+1)/4}}{\sigma_0^{(N-1)/2} (f_L)^{1/2(k+1)} \langle r \rangle^{[(N+1)(k+1)-6]/4(k+1)}} \quad (13b)$$

---

\*Note that  $\langle S \rangle \approx S_0$  when  $S_u \ll S_0$

Note that  $K_{IC}$  decreases as  $\sigma_0$  increases such that the temperature dependence of  $K_{IC}$  is identical to preceding models<sup>1</sup>. Otherwise,  $K_{IC}$  depends primarily on the volume concentration and size distribution of grain boundary carbides. The grain size is only involved if the separation distance,  $\lambda$ , is some multiple of the grain size.

#### 4. COMPARISON WITH EXPERIMENT

The predicted trends in  $K_{IC}$  with material properties are compared with available measurements in fig. 5a, b, by assuming:  $k = 1$  (i.e. a wedge shaped active element),  $\lambda$  is a multiple of the grain diameter,  $d$ , and  $m$  remains invariant with carbide size. The toughness trend then reduces to;

$$K_{IC} \sim \frac{\langle S \rangle^{(N-2)/2} (E_{Yp})^{3/4}}{\sigma_0^{(N-1)/2} (fd)^{1/4}} \quad (14a)$$

$$\sim \frac{(E_{Yp})^{(N+1)/4}}{\sigma_0^{(N-1)/2} \langle r \rangle^{(N-2)/4} (fd)^{1/4}} \quad (14b)$$

Using the highest value of  $K_{IC}$  as the reference toughness, the Curry and Knott<sup>5</sup> data (fig. 5a) conform closely with the trends predicted by eqn (14a). The dominant influences of yield strength and carbide 'strength' distribution, and the moderate role of grain size, are thus reinforced.

Strong effects of carbide size and volume concentration, at essentially constant grain size, are clearly evident in the Rawal and Gurland<sup>4</sup> data (fig. 5). However, quantitative comparison with predicted trends (eqn 14b) is impeded by a lack of information concerning the size,  $r$ , and volume concentration,  $f$ , of the grain boundary carbides that purportedly dictate

the distribution of strength,  $S$ . Nevertheless, it is interesting to note that the trends in toughness with the size and concentration of the intragranular carbides (fig. 5b) are correctly ordered by eqn (14b).

##### 5. THE DUCTILE-TO-BRITTLE TRANSITION

The temperature range for the transition from brittle to ductile fracture can be approximately estimated by recognizing that  $\sigma_{yy}$  exhibits a maximum (fig. 1),  $\lambda\sigma_0(N)$ : with  $\lambda$  in the range 2-4.<sup>1</sup> This maximum occurs at a location  $x_0$  from the crack tip

$$x_0 \approx (2/9)(5/2\lambda)^{1/(1+N)}(K/\sigma_0)^2 \quad (15)$$

When the location,  $x_c$ , of maximum failure probability reduces to  $x_0$ , the failure probability (at given  $K$ ) will decrease rapidly with further reductions in  $x_c$ . Hence, invoking the following approximate transition criterion;

$$x_c < x_0 \quad (16a)$$

gives a critical transition yield stress

$$\sigma_0 < S_0 [M-k(N+1)]/\lambda k(N+1) \quad (16b)$$

The temperature at which  $\sigma_0$  first satisfies eqn (16b) causes  $K_{IC}$  to deviate above the prediction given by eqn (14b). It is directly evident from eqn (16b) that either an increase in the work hardening rate (decrease  $N$ ) or decrease in grain boundary carbide size (increase in  $S_0$ ) will permit the transition to occur at larger  $\sigma_0$  and hence, translate the transition to lower temperatures. However, prediction of the magnitude of  $K_{IC}$  in the transition range requires more detailed statistical analysis.

Furthermore, the rapid increase in  $K_{IC}$  with temperature, at the transition in some steels,<sup>15</sup> suggests that blunting of the carbide cracks may intervene and cause an abrupt change in the failure mode, to a plastic hole growth mechanism.

## 6. DISCUSSION

The statistical description of cleavage fracture based on the pre-existence of cracked grain boundary carbides is subject to a number of restrictions. Firstly, the model requires that the cleavage cracks which initiate from the carbides and coalesce with the primary crack must result directly in fracture instability. The existence of stable crack advance (Appendix) would modify the stress field (i.e. eqn (5) would not apply) and alter the propensity for subsequent activation of the cracked carbides by the crack tip field. The instability condition would then be more complex than addressed by the present analysis. Careful experimental observations of the fracture instability are needed to examine conditions that encourage stable crack advance.

Secondly, the pre-existence of the cracked carbides is contingent upon a dislocation structure that permits the formation of narrow slip bands and substantial stress concentrations ahead of slip bands terminating at grain boundary carbides. Reduction of the stress concentration at the slip band termination (achieved by reducing the grain size or increasing the slip band width) could inhibit stable cracking of the grain boundary carbides. Then, fracture would be dictated by the initiation of the carbide cracks, rather than their propagation, and considerations of the distribution of stress concentrations at slip band terminations would be needed to predict the onset of fracture.

Finally, it is noted that the deformation of the ferrite matrix within the crack tip plastic zone may modify the sensitivity of the ferrite to cleavage fracture (in the presence of the cracked carbides). Specifically, the plastic strain may introduce dislocation sources that tend to blunt the carbide crack, thereby converting the crack into a hole and inducing limited plastic hole growth. The effective strength  $S$  of the cracked carbides may then increase with plastic strain and hence, depend on the distance of the carbide from the crack tip. Such behavior would be consistent with the observation of a limited zone of ductile fracture adjacent to the initial crack tip.<sup>4</sup> Modification of the present model to account for such effects would require incorporation of a position sensitive cleavage strength.

## 7. CONCLUSIONS

A statistical model of cleavage fracture in mild steel, in the presence of cracked grain boundary carbides, has been presented. The model uses weakest link statistics and the crack tip singularity field to predict the onset of the fracture instability. The model predicts that the maximum elemental failure probability occurs ahead of the crack tip, and provides a natural definition of the 'critical distance.' The magnitude of the critical distance depends on the size distribution and volume concentration of cracked grain boundary carbides and on the flow stress.

The dependence of fracture toughness on material properties and temperature is also predicted by the model. It is found that the temperature dependence (consistent with prior studies<sup>1</sup>) resides exclusively in the

temperature dependence of the flow stress. The most important additional, microstructural property is the size distribution of the cracked boundary carbides. Only small effects of the carbide volume concentration and of the grain size (aside from possible effects on yield) are predicted. Comparison with limited experimental data reveals trends consistent with the model.

The stability of cleavage cracks in the ferrite grains is also discussed, with emphasis on restrictions inherent in weakest link statistical models. Such stability effects may be particularly important at the brittle-to-ductile transition condition.



# APPENDIX

## Some Considerations of Cleavage Crack Stability

### 1. Homogeneous Stress Fields

Studies of cleavage fracture in notched bend bars<sup>2,5</sup> have suggested that the cleavage energy of the ferrite is  $\sim 14 \text{ Jm}^{-2}$ : viz. a cleavage resistance,  $K_{I0} \approx 3 \text{ MPa}\sqrt{\text{m}}$ . This compares with a macroscopic fracture resistance,  $K_{IC} \approx 30 \text{ MPa}\sqrt{\text{m}}$ . Consequently, as the cleavage crack expands to encompass an increasing number of grains, the crack growth resistance,  $K_R$ , must increase by about an order of magnitude (fig. 6). In slowly varying imposed stress fields, the crack driving force  $K$  also increases, as  $\sim \sqrt{a}$ , commencing at the initial value,  $K_{I0}$ , needed to obtain growth of the carbide-sized crack (fig. 6). Stability of the cleavage crack is clearly dictated by the relative rates of increase of  $K$  and  $K_R$ : instability occurring when  $dK/da > dK_R/da$ . The crack growth resistance curve is unknown, but the large total increase in  $K_R$  with crack growth suggests that stability may be encountered in certain situations. Hence, some simple considerations pertinent to cleavage crack stability are presented to illustrate the essential trends.

Assuming a resistance curve (fig. 6),

$$\begin{aligned} K_R &= K_{I0} & (\Delta a < d) \\ K_R &= (2K_{IC}/\pi) \tan^{-1} \zeta [(\Delta a/d) - 1] & (\Delta a > d) \end{aligned} \tag{A1}$$

where  $\zeta$  is a dimensionless coefficient that dictates the rate of increase of  $K_R$ , and noting that

$$K = (2/\pi) \sigma \sqrt{a_0 + \Delta a} \tag{A2}$$

where  $a_0$  is the initial crack size (equivalent to the dimensions of the grain boundary carbide), differentiation allows the instability condition to be expressed as ( $\Delta a > d$ );

$$\frac{1 + \zeta^2(\Delta a/d - 1)^2}{\sqrt{1 + \Delta a/a_0}} > 4\zeta \left( \frac{K_{IC}}{K_{IO}} \right) \left( \frac{a_0}{d} \right) \quad (A3)$$

If the inequality is satisfied at  $\Delta a/d = 1$ , stable grain-sized cracks will not be observed. For example, if the ratio of grain size to carbide size is  $\sim 100$  and  $K_{IC}/K_{IO} \sim 10^{2.5}$ , then the absence of stable grain-sized cracks requires that  $\zeta < 1/4$ , i.e. a relatively slowly increasing  $K_R$  curve.

For the case  $\Delta a \gg d$ , eqn (A3) permits a critical crack advance length,  $\Delta a_c$ , to be derived as;

$$\Delta a_c^{3/2} \approx 4\zeta(K_{IC}/K_{IO})d \sqrt{a_0} \quad (A4)$$

For the same example used above ( $d/a_0 = 10^2$  and  $K_{IC}/K_{IO} = 10$ ),  $\Delta a_0/d = (4\zeta)^{2/3}$ . Hence, for a rapidly increasing  $K_R$  curve ( $\zeta \approx 1$ ),  $\Delta a_c \approx 3d$ , i.e., stable cracks encompassing about three grains are anticipated.

The magnitude of  $\zeta$  depends on the rate of development of the plastic zone around the advancing grain-sized cleavage crack. Specifically, slip homogeneity should affect  $\zeta$ , perhaps causing it to increase with increase in temperature. The development of stable cleavage cracks within the ductile-to-brittle transition range may be a consequence of such changes.

## 2. Crack Tip Fields

The initiation of cleavage cracks at carbide particles, located ahead of a large crack (fig. 2), results in cleavage crack growth, toward the crack tip, into regions of increasing tension (fig. 1). The driving force

for cleavage crack extension thus increases rapidly with  $\Delta a$ ; thereby, discouraging the formation of isolated, grain-sized cracks. Coalescence of the cleavage cracks with the primary crack is likely to occur, as required by the present model. However, it is improbable that a single cleavage crack will extend unstably along the entire crack front. Hence, cleavage crack formation at several sites along the crack front constitutes a probable fracture prerequisite (fig. 3).

It is important to recognize that coalescence of the cleavage crack with the primary crack may not coincide with fracture instability, because the distribution of plastic strains associated with the crack in its new position may sufficiently modify the COD that unstable growth is prohibited:<sup>†</sup> Macroscopic R-curve effects extending over several grain dimensions may obtain in some situations. Such behavior has been observed in a large grained, high nitrogen containing steel.<sup>16</sup> The failure condition must then be congruent of the modified stress field that obtains in advance of the crack (associated with the modified plastic zone, coupled with unloading effects in the wake).

---

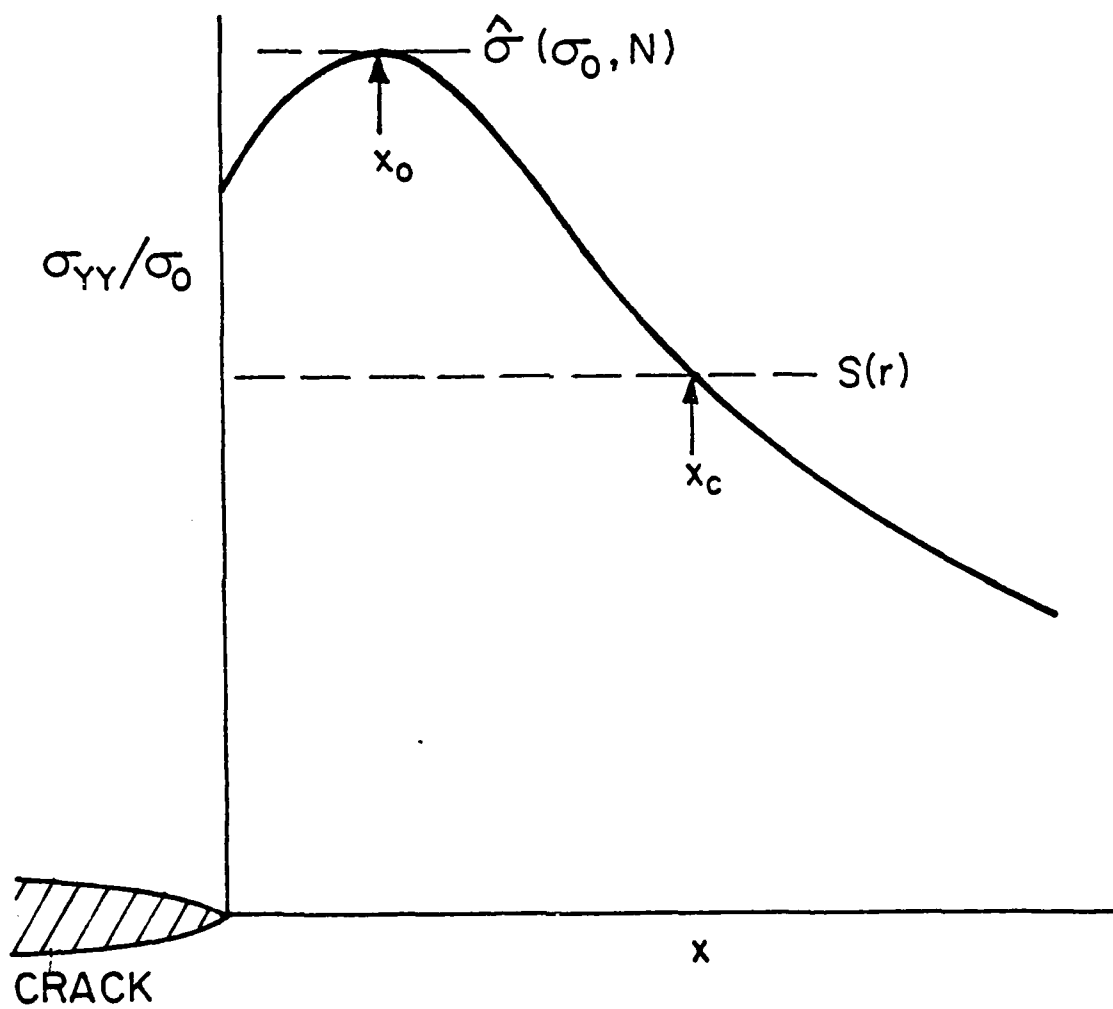
<sup>†</sup>The difference in the shape of the moving and stationary crack that obtains in the presence of crack tip plasticity persists in the small scale yielding range. R-curve effects are thus quite plausible.

References

1. R. O. Ritchie, J. F. Knott and J. R. Rice, J. Mech. Phys. Sol. 21 (1973) 395.
2. D. A. Curry and J. F. Knott, Metal Science 12 (1978) 511.
3. D. M. Parks, Jnl. Eng. Mtls. Technology (1976) 30
4. S. P. Rawal and J. Gurland, Met. Trans. 8A (1977), 691.
5. D. A. Curry and J. F. Knott, Metal Science 10 (1978) 1.
6. D. A. Curry and J. F. Knott, Metal Science 13 (1979) 341.
7. D. A. Curry, Metal Science 14 (1980) 319.
8. E. Smith, Physical Basis of Yield and Fracture, Inst. Phys/Phys. Sci., Oxford (1966) p. 36.
9. J. D. G. Groom and J. F. Knott, Metal Science 9 (1975) 390.
10. M. Holtzmann and J. Man, Jnl. Iron and Steel Institute, Oct (1971) p. 836.
11. J. R. Matthews, W. Shack, F. A. McClintock, Jnl. Amer. Ceram. Soc., 59 (1976) 304.
12. S. B. Batdorf and J. G. Cross, Jnl. Amer. Ceram. Soc.
13. J. W. Hutchinson, J. Mech. Phys. Solids 16 (1968) 13.
14. J. R. Rice and G. F. Rosengren, J. Mech. Phys. Solids 16 (1968) 1.
15. R. O. Ritchie, W. L. Server and R. A. Wullaest, Met. Trans. 10A (1979) 1557.
16. R. O. Ritchie, private communication.

Figure Captions

- Figure 1. The stress field ahead of a crack with the carbide 'strength'  $S$  superposed, indicating the critical distance<sup>1</sup>,  $x_c$ .
- Figure 2. A schematic illustrating the active zone and the cleavage crack coalescence process.
- Figure 3. A schematic of the spacing  $\lambda$  between cleavage cracks needed to induce fracture instability.
- Figure 4. A schematic of the elemental failure probability as a function of distance from the crack tip, illustrating the existence of a maximum at a distance,  $x_c$ , from the tip.
- Figure 5. a) A comparison of the model with the Curry and Knott<sup>5</sup> data ( $N=5$ ).  
b) Trends in  $K_{IC}^4$  with the parameters suggested by eqn (14b), assuming that the grain boundary carbide parameters,  $f$  and  $r$ , are proportional to the equivalent parameters for the intra-granular carbides.
- Figure 6. A schematic of the  $K_R$  curves for small, grain-sized, cleavage cracks, with the  $K$  variation typical of uniform stress fields superposed.



XBL 829-6473

Fig. 1

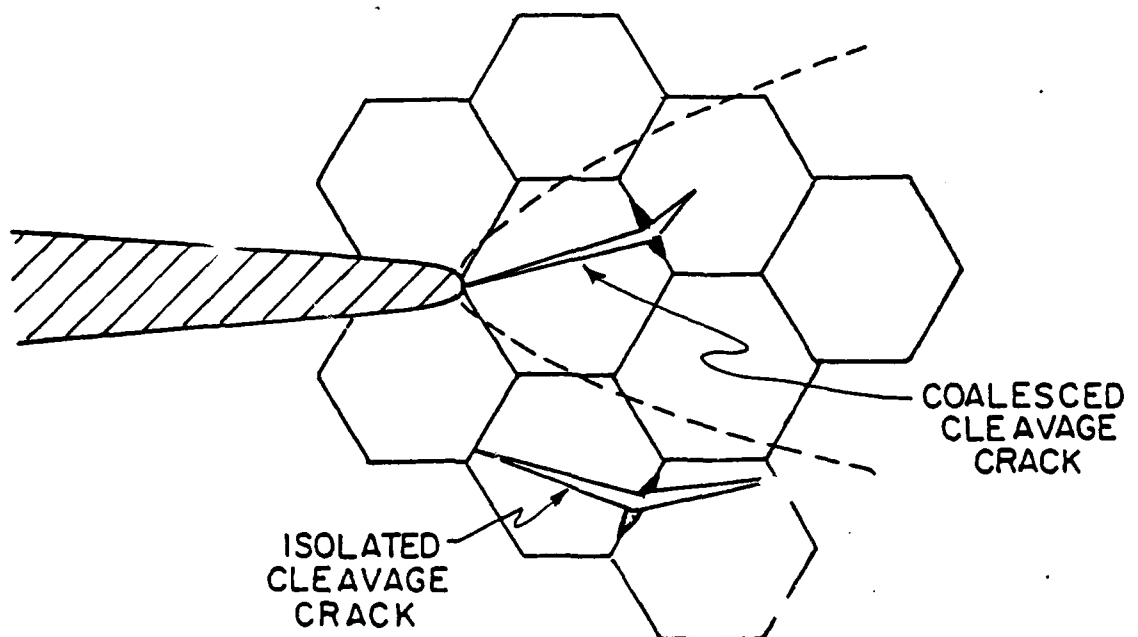
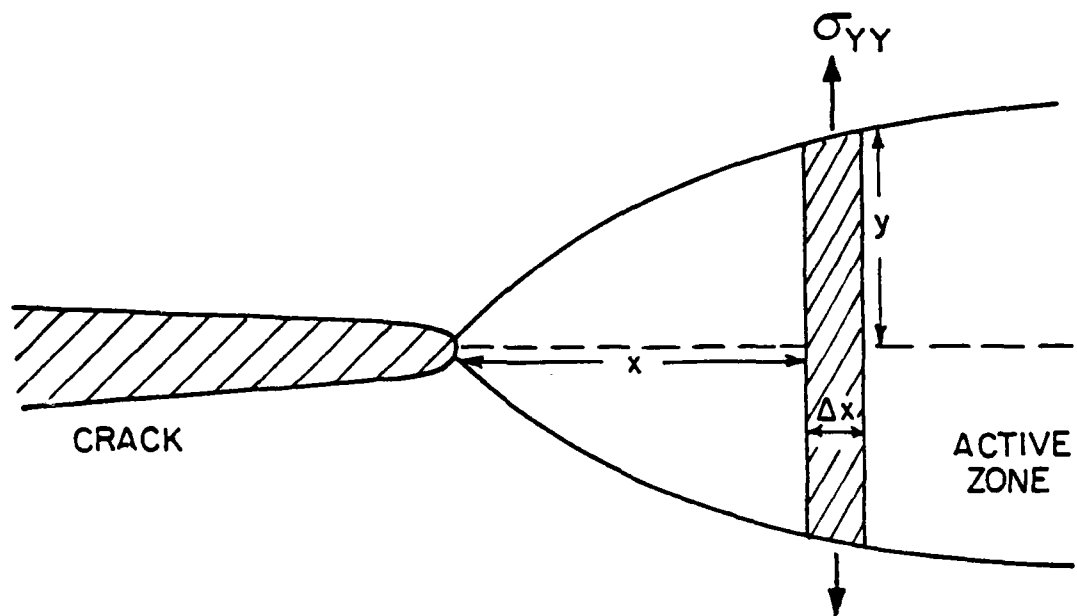
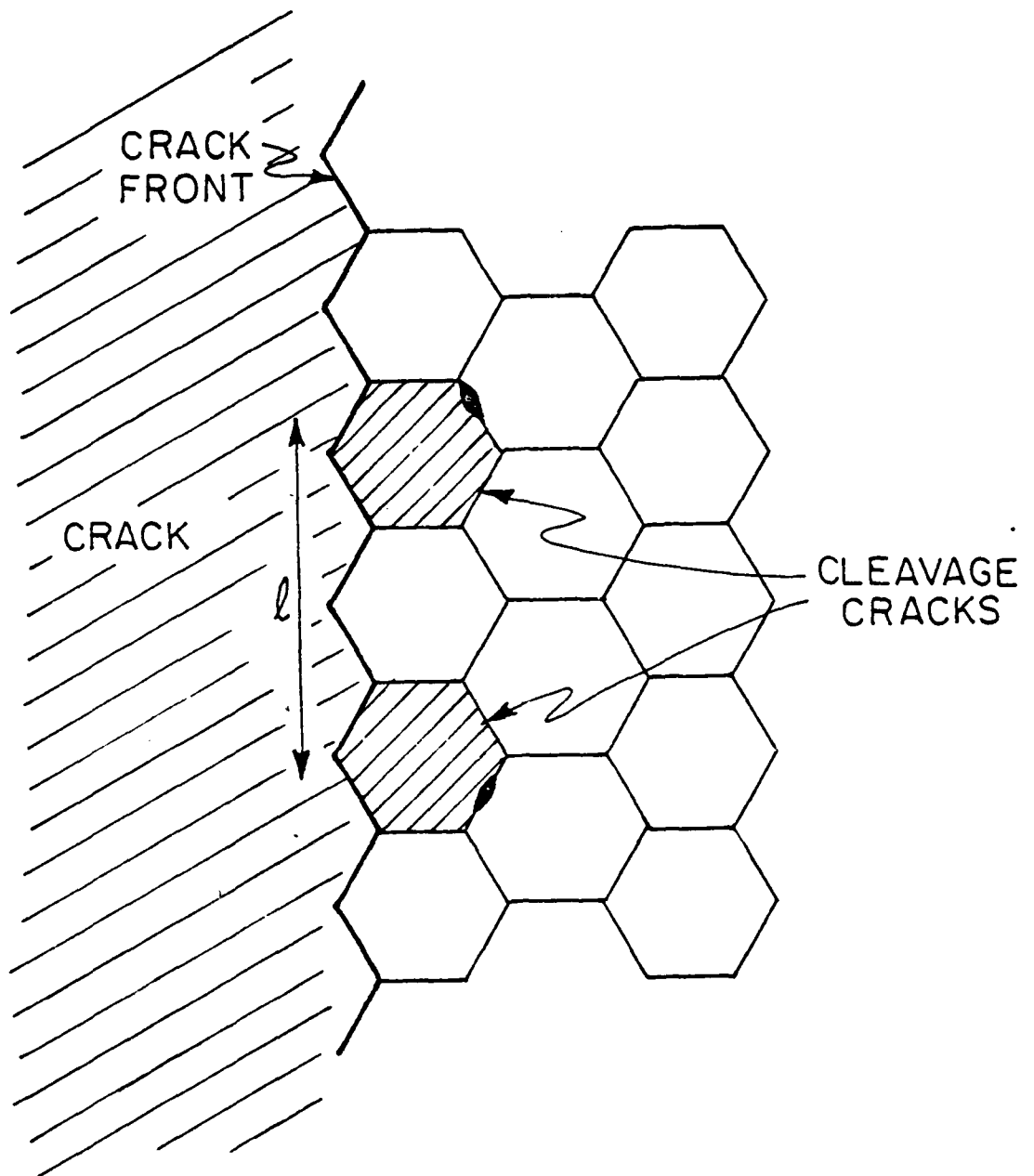


Fig. 2

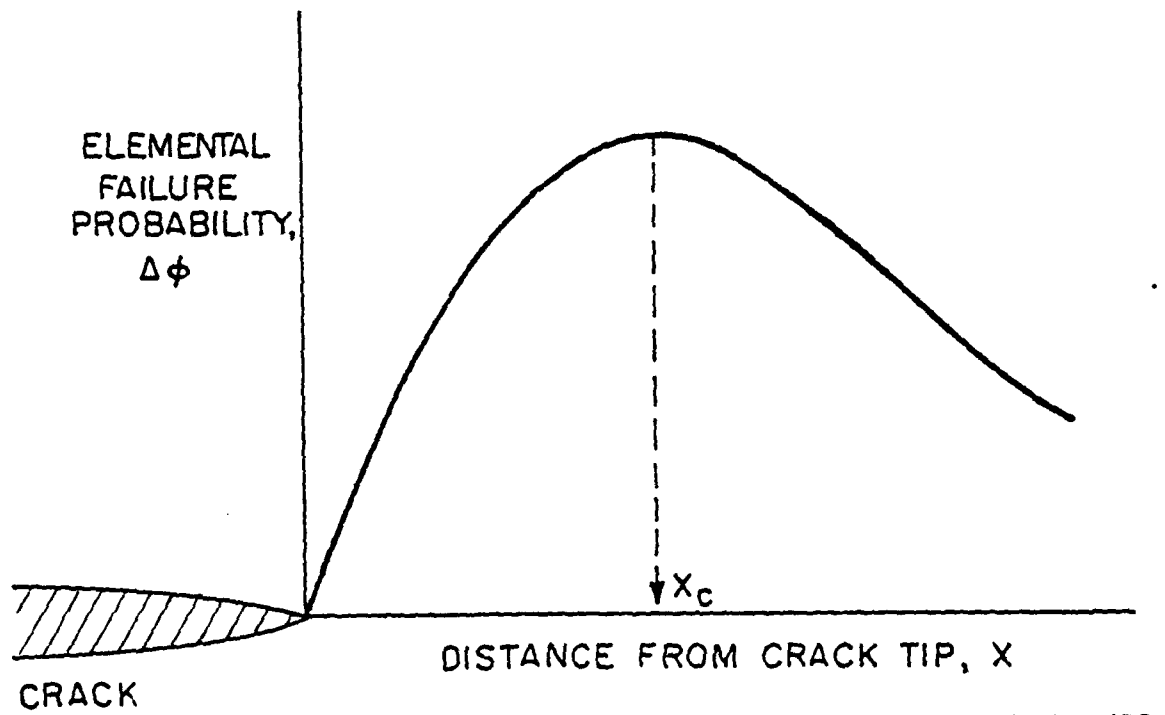
XBL829-6472



XBL829-6471

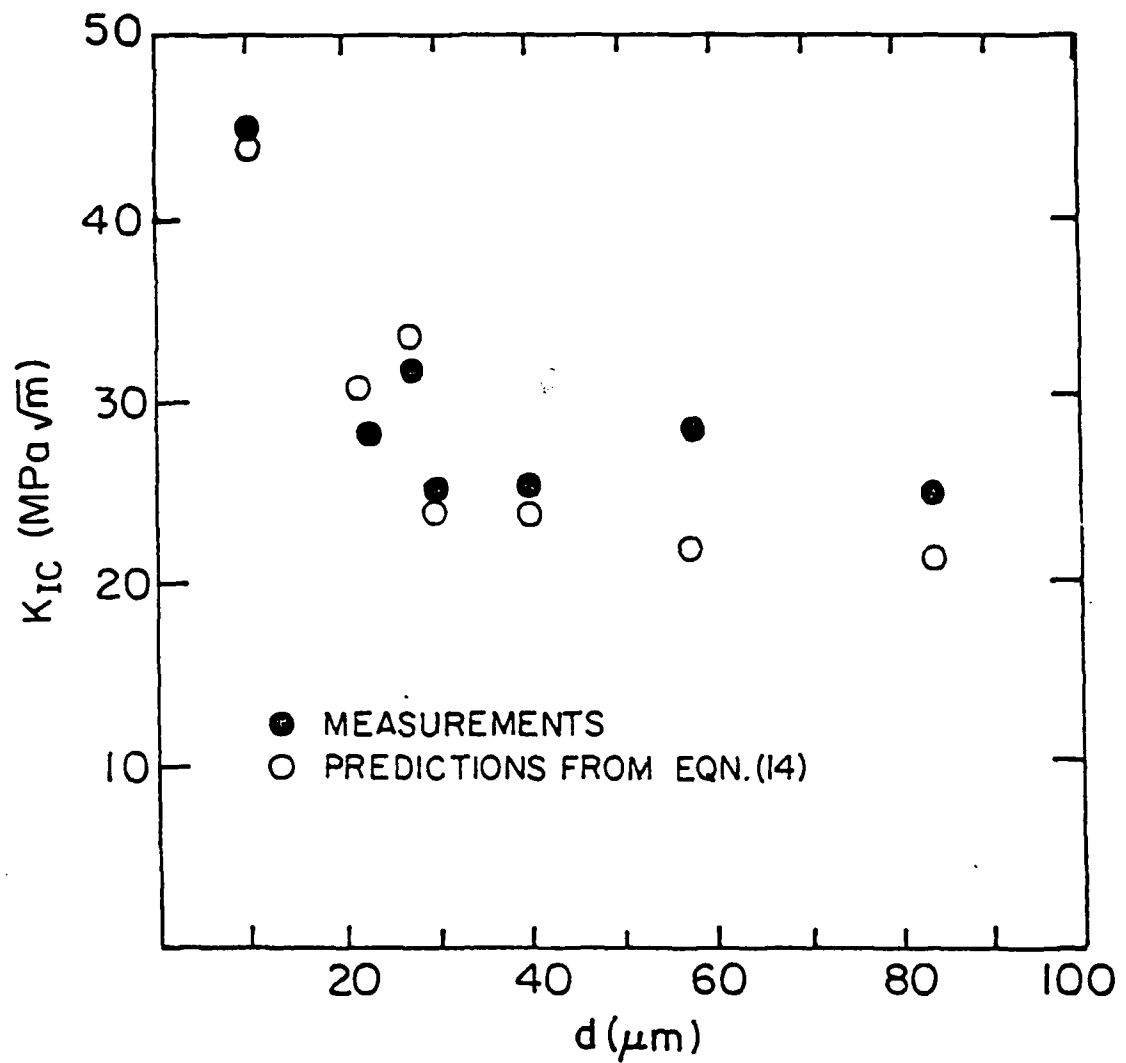
Fig. 3





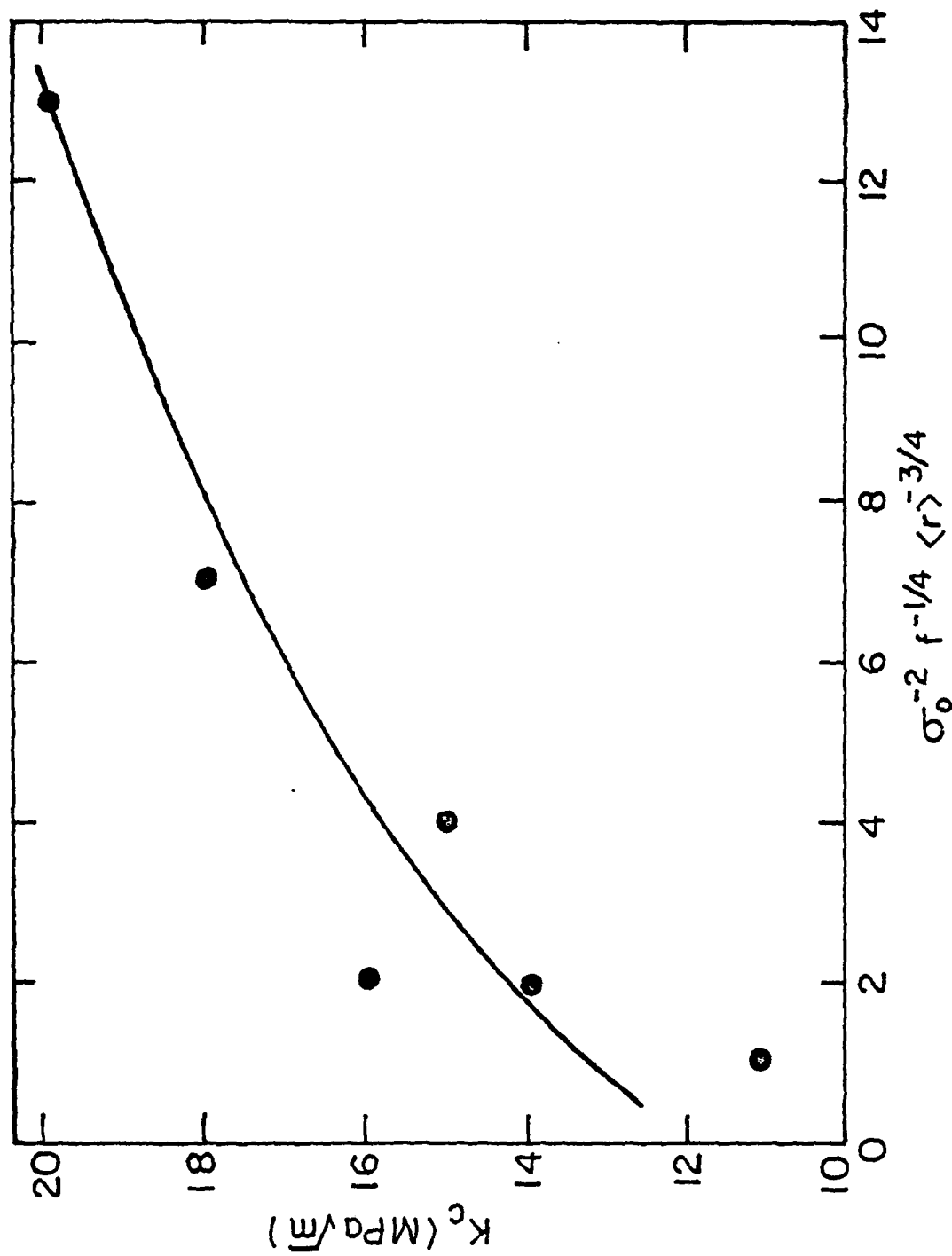
XBL 829-6470

Fig. 4



XBL 829-6469

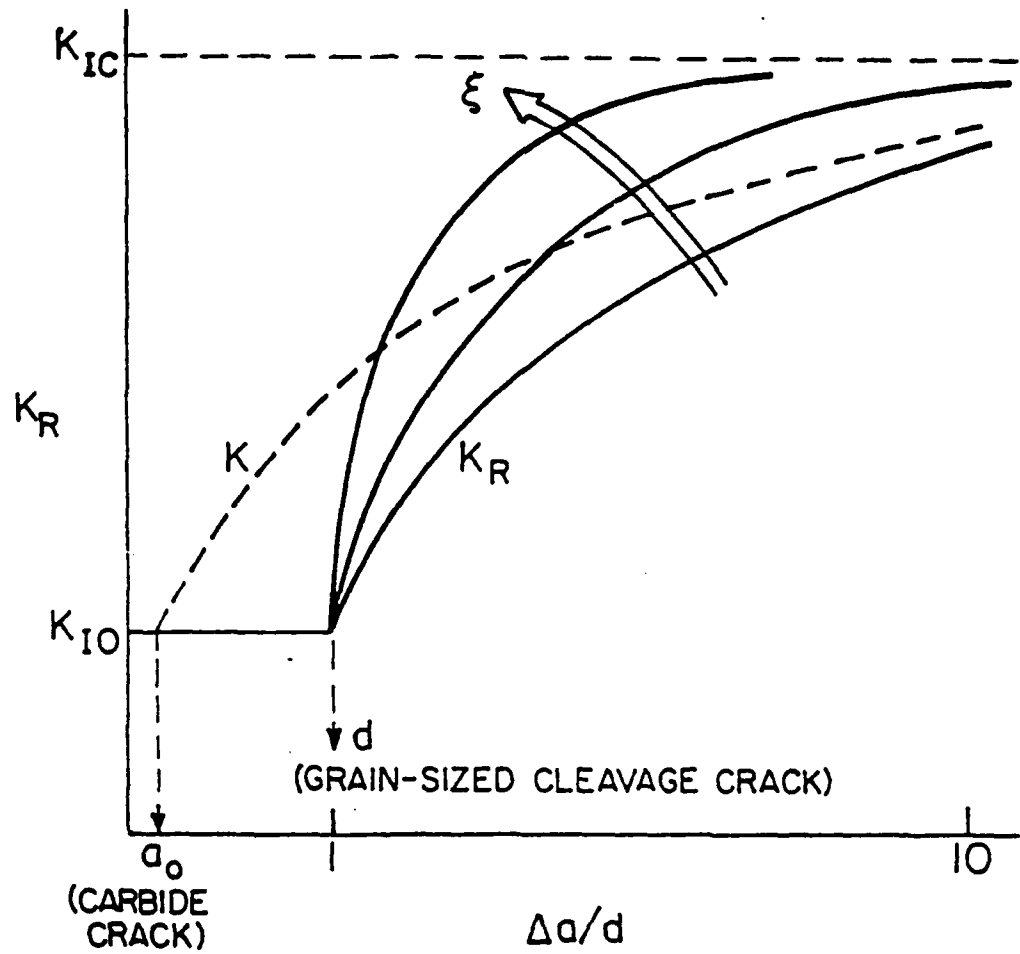
Fig. 5a



XBL829-6468

Fig. 5b

(7)



XBL 829-6467

Fig. 6

SURFACE DAMAGE

CHAPTER V

SURFACE DAMAGE IN BRITTLE SOLIDS:  
STUDIES OF THE DEVELOPMENT AND INFLUENCE OF GRINDING FORCES

by

T. Uchiyama, D. B. Marshall and A. G. Evans

Department of Materials Science and Mineral Engineering  
University of California  
Berkeley, CA 94720

SURFACE DAMAGE IN BRITTLE SOLIDS:  
STUDIES OF THE DEVELOPMENT AND INFLUENCE  
OF GRINDING FORCES

T. Uchiyama, D. B. Marshall  
and A. G. Evans

Department of Materials Science and Mineral Engineering  
University of California  
Berkeley, CA 94720

ABSTRACT

Grinding forces have been measured on a range of brittle solids. The forces vary with the depth of cut and are strongly dependent on material properties. Dimensional analysis of the results reveals that most data are correlated by a parameter,  $H(K_c/E)^{5/2}d^{3/4}$ , where  $K_c$  is the toughness,  $E$  is Young's modulus,  $H$  is the hardness, and  $d$  is the depth of cut. This parameter is not predicted by available material removal models. Preliminary strength  $\sigma_f$  measurements have also been obtained, and suggest the trend,  $\sigma_f \sim K_c/\sqrt{d}$ .

## 1. INTRODUCTION

The mechanical preparation of surfaces on brittle solids (by grinding, sawing, machining, etc.) involves material removal processes induced by the plastic penetration of hard particles (such as diamonds) into the surface.<sup>1,2</sup> The penetration of particles results in plastic cutting and chipping, dictated by the extent of penetration and the pertinent material properties. The requisite particle penetration is achieved by the application of forces to the mechanical system.<sup>2</sup> These forces are the principal source of surface crack damage (fig. 1). The surface cracks are subject to a residual driving force, associated with the plastic deformation zone, and grow stably to a critical size upon application of external loads.<sup>3,4</sup> Consequently, the strength,  $\sigma_f$ , in the presence of machining damage, is dictated uniquely by the magnitude of the machining force,  $P$ , and the pertinent material properties;<sup>3</sup>

$$\sigma_f \sim 2(K_C^4/P)^{1/3}(H/E)^{1/6} \quad (1)$$

where  $K_C$  is the fracture toughness,  $H$  the hardness, and  $E$  is Young's modulus. Control of the forces that develop during a mechanical surfacing operation thus appears to be a prime factor in quality control (whenever mechanical strength influences material performance). The intents of the present paper are to describe measurements of the forces that develop during the grinding of brittle materials and to present a preliminary assessment of the influence of these forces on mechanical reliability.

Prior analysis of the grinding force dependence on material properties<sup>5</sup> has been restricted to two extreme modes of material removal: plastic cutting and chipping (by lateral cracks). The plastic cutting mechanism



anticipates a grinding force dictated exclusively by the hardness,  $P \sim H$ ; while the lateral crack chipping mechanism predicts a grinding force that varies as,  $P^{9/8} \sim K_C^{1/2} H^{5/8} (H/E)^{4/5}$ . Grinding force data generated in this study, on a wide range of brittle materials, will be compared with the expectations of these simple models, and deficiencies will be used as a basis for indentifying more complete descriptions of effects of microstructure on the magnitude of the grinding forces. This identification will be attempted using dimensional analysis techniques, and facilitated by conducting ancillary measurements of surface profiles and residual stresses, coupled with indentation and single point scribing studies.

The strengths of selected materials will also be measured and the results, in conjunction with strength data generated by Freiman et al.,<sup>6</sup> compared with the available models (eqn 1). Deficiencies will again be addressed using dimensional analysis techniques.

## 2. EXPERIMENTAL

### 2.1 Materials and Properties

The materials tested have been selected to encompass as wide a range as possible of the potentially important material variables,  $K_C$ ,  $H$  and  $E$ , as summarized in Table I. The magnitudes of  $H$  and  $K_C$  have been deduced from overload Vickers hardness tests,<sup>3,7</sup> as pertinent to surface damage problems. The elastic modulus  $E$  has been evaluated from measurements of the relative dimensions of Knoop indentations.<sup>8</sup>

## 2.2 Force Determinations

The force determinations were conducted using an automatic grinding system, arranged to provide a specific depth of cut and feed rate for each pass of the material beneath the grinding wheel. The depth of cut could be varied in  $1\text{ }\mu\text{m}$  steps between 1 and  $20\text{ }\mu\text{m}$ . The test specimen was mounted on a pedestal attached to load transducers that permit in situ determination of the normal and lateral forces induced by the passage of the grinding wheel (fig. 2). An oscilloscope and a chart recorder connected to the load cell output determine the load amplitude and duration. The table and wheel speed were also monitored in conjunction with the force measurements. For the range of materials and test conditions used in the present study the table and wheel speeds remained invariant at  $0.02\text{ ms}^{-1}$  and 3400 r.p.m. respectively.

Typical force records (as displayed on the chart recorder and oscilloscope) are depicted in figs. 3a, b. Systematic differences between the up and down grinding forces were not discerned within the range of cut depths used in the present study ( $1\text{--}7\text{ }\mu\text{m}$ ). Subsequent results thus refer with equal facility to either process. The grinding forces characteristically increase during the initial sequence of passes, and then attain a steady-state that depends on the material, the depth of cut and the feed rate. This same steady-state is attained irrespective of the initial condition of the surface. The behavior is exemplified by noting the force variations that accompany abrupt changes in the depth of cut (fig. 4). Specifically, the force levels that develop in response to the change in grinding conditions tend to the same steady-state value whether approached

from either larger or smaller initial force levels (associated with deeper or shallower depths of cut, respectively). The steady-state force is thus used as the pertinent grinding force measurement in subsequent studies.

The force records exhibited on the oscilloscope (fig. 3b) reveal that, during each pass, the force is intermittent and that the force is exerted at intervals determined by the rotational frequency of the grinding wheel.<sup>†</sup> Similar observations have been made during the grinding of ferrites.<sup>1</sup> Evidently, therefore, the machining action is confined to a single, small region of the wheel surface. The chart recorder thus yields a measure of the forces exerted at each contact, averaged over the pass duration. This average force is related to the peak force at contact (fig. 5) by a material independent proportionality constant. However, this constant varies with wheel use: a variation that coincides with changes in the force profile displayed on the oscilloscope. The profile variation causes the average force to deviate with wheel use by up to a factor of  $\sim 2$ , for the same material and machining conditions. These deviations must clearly be recognized when attempting to correlate force measurements with material properties.

Studies of force variations between materials indicate that the steady-state normal and lateral forces exhibit the same trends, over the range of conditions used in the study. Preliminary subsequent significance is attached to the normal force, which exhibits superior reproducibility. The steady-state normal force was determined to increase monotonically with the depth of cut,  $d$  (table II) such that the essential

---

<sup>†</sup>It is emphasized that the contact intermittence is not associated with poor wheel alignment. The misalignment is  $\leq 1 \mu\text{m}$  and chatter modes have been eliminated. Perturbations on the wheel surface are the probable cause.

essential trend, exemplified for Si and soda lime glass in fig. 6, is described by  $P \sim d^{3/4}$ .

The measured influence of material properties on the machining forces is visualized, for preliminary presentation purposes, by employing a plotting scheme predicated on the combination of material parameters suggested by the simple plastic cutting and chipping models. The results for a 2  $\mu\text{m}$  depth of cut are summarized in figs. 7a and 7b. It is evident that neither plotting scheme provides an effective correlation of the data. In fact, the plots could be interpreted to suggest the existence of two dominant material groups; one group exhibiting substantially higher grinding force levels at equivalent values of the material property combination anticipated by the lateral fracture model. It is important to recognize at this juncture that these grinding force characteristics differ appreciably from the material trends in solid particle erosion, wherein removal rates can be uniquely correlated by a material property combination predicated from lateral crack models<sup>9</sup> (fig. 8).

### 2.3 Surface Profiles

The characteristics of the ground surfaces have been assessed using a combination of scanning electron microscopy and surface profilometry. The surface morphology ranges between two extremes. One extreme morphology, characterized by  $\text{Si}_3\text{N}_4$ , consists of continuous linear plastic grooves (fig. 9a) which afford identical surface profiles at all locations along the machined surface (fig. 10). Additionally, the profile exhibits identical features on succeeding passes, even after the removal of appreciable quantities of material (fig. 10). The corresponding peak amplitudes of the surface undulations are relatively small, typically < 1  $\mu\text{m}$ , and independent of the depth of cut.

The other morphological extreme, typified by sapphire, consists of random features characteristic of brittle chipping processes (fig. 9b). In such instances, the surface profile varies along the machined surface and the peak amplitudes of the surface roughness are relatively larger (1 to 3  $\mu\text{m}$ ) but, again, independent of the depth of cut.

Most materials displayed a hybrid of plastic grooving and brittle chipping characteristics, as indicated by the trend depicted in fig. 11. This trend suggests the possibility that materials with a preponderance of plastic grooving might provide reasonable grinding force correlations based upon plastic grooving mechanisms ( $P \propto H$ ); while the force data for the group of materials that exhibit primarily brittle chipping characteristics might be correlated using lateral fracture models. However, inspection of fig. 7b reveals that the high and low force material groups cannot be distinguished on this basis, because both surface morphologies exist within each group.

#### 2.4 Single Point Scribing

Scribes have been emplaced onto polished surfaces of each test material using diamonds subject to a constant normal force. In all cases, plastic grooves formed at low force levels and cracking/chipping developed at the perimeter of the plastic grooves at forces in excess of a material dependent threshold, as noted in prior studies.<sup>10</sup> Threshold forces for several materials are presented in Table III. The trends in the threshold force are similar to those encountered for lateral cracking at indentations.<sup>11</sup>

## 2.5 Residual Stresses

The detection of residual stresses in machined surfaces provides unequivocal evidence of a remnant plastic zone beneath the surface. The presence of residual stresses in materials that exhibit the extreme surface morphologies,  $\text{Si}_3\text{N}_4$  and sapphire, was thus assessed, as a basis for interpreting the role of plasticity on both the machining forces and the resultant strength. Residual stresses can be conveniently detected by continuously reducing the section thickness of a beam specimen containing one polished and one machined surface and monitoring the deflection (fig. 12). The deflection measurements provide a measure of the residual force,  $\sigma_R h$  (Appendix I) where  $h$  is the depth of the plastic zone. Such studies indicate appreciable deflections, at small section thickness, for both  $\text{Si}_3\text{N}_4$  and sapphire, thereby establishing the presence of residual stress in both materials. The magnitudes of  $\sigma_R h$  for 2  $\mu\text{m}$  depths of cut are similar for both materials.

## 2.6 Strength Measurements

Post machining strength behavior has been evaluated on two materials: the hot pressed  $\text{SiC}$  and  $\text{Si}_3\text{N}_4$  materials. The machining was conducted transversely, on four point flexure specimens, in order to provide the most sensitive measure of the influence of machining damage. The results are presented in Table IV. A comparison of the measured stress ratio,  $\sigma_{\text{Si}_3\text{N}_4} / \sigma_{\text{SiC}} = 1.09$ , with the ratio, 0.83, predicted from eqn (1), with the local force  $P$  replaced by the average force  $\langle P \rangle$ , indicates an appreciable discrepancy.

### 3. DIMENSIONAL ANALYSIS

#### 3.1 Grinding Forces

The poor correlation of the grinding force data with the simple plastic cutting and chipping models indicates that the dominant mechanism of material removal has not been adequately indentified. The elucidation of the important mechanism is thus attempted using dimensional analysis of the machining force data. Dimensionless groups of the important material and cutting variables are thus assembled and used to correlate the data. The most prominent variables  $P$ ,  $K_c$ ,  $H$ ,  $E$  and  $d$  can be assembled into the following dimensionless expression

$$P/Ed^2 = A (K_c/E\sqrt{d})^\alpha (E/H)^\beta \quad (2)$$

where  $\alpha$ ,  $\beta$  and  $A$  are the coefficients to be ascertained from the experimental data.

It is immediately evident from the depth of cut exponent,  $P \sim d^{3/4}$ , that  $\alpha = 5/2$  and hence, that this group of dimensionless parameters must exhibit the form,

$$(P^4 E^6 / K_c^{10} d^3)^{1/4} = A(E/H)^\beta \quad (3)$$

A plot of the dimensionless force,  $P^4 E^6 / K_c^{10} d^3$ , as a function of  $E/H$  (fig. 13) reveals a moderate correlation of the data, based on the given parameters, expressed by the best fit relation,

$$P \sim K_c (K_c/E)^{3/2} (H/E) d^{3/4} \quad (4)$$

as plotted in fig. 14. The correlation expressed by eqn (4) is appreciably better than the correlations provided by either the plastic grooving (fig. 7a) or lateral cracking (fig. 7b) models and indicates, with the obvious exception of hot pressed SiC, a singular dependence on the specified material properties. However, the correlation is certainly not of sufficient quality to conclude that all of the important material properties have been identified. For example, it is noteworthy that the materials with the lowest dimensionless forces, at a specified  $(E/H)$ , have distinctive thermal properties: viz, properties that render good thermal shock resistance such as a low thermal expansion coefficient and/or large thermal conductivity. Local heating effects may thus be involved in the material removal process.

### 3.2 Strength

The relationship between strength and material properties has been amply defined for indentation conditions<sup>3</sup> (eqn 1), but has yet to be adequately modelled for the more complex crack/residual stress field characteristics that prevail at a machined surface.<sup>4</sup> It is again expedient, therefore, to use dimensional analysis techniques to provide the necessary insights. Prior studies of indentation dominated strengths have established that the dimensions of the indentation induced cracks do not explicitly enter strength expressions<sup>3</sup> (c.f. eqn 1), because the residual field results in stable crack advance and a consequent critical crack dimension that can be uniquely described in terms of material parameters ( $K_c$ ,  $H$ ,  $E$ ) and the indentation load. With the premise that similar residual stress dominated behavior prevails for machining induced



cracks, as elicited from recent experimental measurements of stable crack extension prior to the failure of machined  $\text{Si}_3\text{N}_4$  samples,<sup>4</sup> the strength should be described by the following dimensionless parameters,

$$\sigma_f/E = B(K_C^4/PE^3)^\gamma (H/E)^\Delta \quad (5)$$

where  $B$ ,  $\gamma$  and  $\Delta$  are the coefficients that require experimental evaluation. Alternatively, by incorporating dimensionless expressions for the machining force, the strength can be expressed as,

$$\sigma_f/E = B'(K_C/E\sqrt{d})^{\gamma'} (H/E)^{\Delta'} \quad (6)$$

where  $B'$ ,  $\gamma'$  and  $\Delta'$  constitute a new set of coefficients.

Evaluation of the coefficients in eqns (5) or (6) can be most effectively achieved by appealing both to the present strength data and to the data obtained on glass ceramic materials by Freiman et al.<sup>6</sup> (Table IV). Comparison of the glass ceramic data with eqn (16) reveals that, since  $H/E$  is essentially invariant,  $\gamma' \approx 1$ , and hence,

$$\sigma_f \sim (K_C/\sqrt{d})(H/E)^{\Delta'} \quad (7)$$

Additionally, since  $H/E$  is similar for both  $\text{Si}_3\text{N}_4$  and  $\text{SiC}$ , and comparable in magnitude to the value for the glass ceramics, eqn (7) can be used to predict the strength ratio for the  $\text{SiC}$  and  $\text{Si}_3\text{N}_4$ . This prediction, 1.11, is close to the measured ratio, 1.09.

The data are, of course, too sparse to permit general conclusions. But, the important influences of the toughness and depth of cut implied by the present data, through eqn (7), are amenable to direct experimental evaluation. Such evaluations will form the basis of subsequent strength

studies. Additionally, it is noted that eqns (4) and (7) imply a strength relation;

$$\sigma_f \sim (K_c^4/P)^{2/3} E^{-2} (H/E)^{2/3+\Delta'} \quad (8)$$

It is of interest to compare this result with the indentation fracture solution (eqn 1). Most notable are the stronger dependence of  $\sigma_f$  on,  $K_c^4/P$ , characteristic of the change from axisymmetric to linear plastic zones<sup>4,12</sup>, and the appearance of an additional dependence on the elastic modulus.

#### 4. DISCUSSION

The moderate correlation of the grinding force data obtained using a unique expression (eqn 4) involving material properties and the depth of cut, suggests that a single material removal mechanism dictates the force magnitude. Credence in this suggestion is provided both by the wide range of material properties and depths of cut encompassed by the present data and by the general similarity in single point scribing and indentation response of each material. However, it is also recognized that the characteristics of the machined surfaces vary appreciably (from domination by plastic grooving to brittle chipping) amongst the materials studied: a result ostensibly inconsistent with the single mechanism notion.

The strong influence of both the toughness and elastic modulus on the grinding forces and the relatively minor role of the hardness indicate a brittle fracture mechanism of material removal, motivated primarily by the elastic stresses. The significance of the elastic stress influence

requires qualification. All brittle fracture processes are governed by the magnitude of the tensile elastic stress. However, the amplitudes of the elastic stresses that motivate surface cracking (e.g. at indentations) are usually dictated by the hardness<sup>11</sup>, because the predominant tensile stresses are residual in nature (a behavior characteristic of most elastic/plastic situations). The hardness is thus a prominent parameter both in indentation fracture<sup>7</sup> and in solid particle erosion<sup>9</sup> (the modulus only enters through the influence on the size of the plastic zone, by virtue of the ratio,  $(H/E)$ ). The observations of plastic grooves on many machined surfaces and the presence of substantial plasticity induced residual stresses undoubtedly account for the proportional dependence on hardness. However, the strong dependence on,  $K_c/E$ , cannot yet be explained.<sup>†</sup> Additionally, it is recalled that certain thermal properties may also be involved in the removal process. It is thus evident that much additional study is needed to elucidate the precise material removal mechanism. In this context, it is important to recognize that the presence of the residually stressed layer demands that the material removal mechanism operate within spatial regime located toward the upper portion of the plastic zone (a requirement inconsistent, for example, with the lateral cracking mechanism).

Preliminary measurements of the strength of two materials after machining are consistent with prior measurements on glass ceramics, which indicated a failure strength directly proportional to the fracture

---

<sup>†</sup>The strong inverse dependence of  $P$  on  $E$  is not associated with compliance effects (which are dominated by the modulus of the wheel), but may perhaps be attributed to stress wave interactions with the damage in the plastic layer.

toughness. Dimensional analysis reveals that this proportionality requires an increase dependence of strength on the depth of cut,  $\sigma_f \propto d^{-1/2}$ , and a separate influence of  $E/H$ . Subsequent studies should evaluate the self-consistency of these predictions. Finally, it is noted that the proportionality,  $\sigma_f \propto K_c$ , does not imply that the dimensions of the surface cracks introduced by machining are independent of material properties. Specifically, machining induced cracks can not be treated as simple Griffith flaws, by virtue of the influence of the residual stress upon the sub-critical extension (stable growth) of the surface cracks, and the strength does not relate explicitly to the initial crack size. In fact, the dependence of  $\sigma_f$  on the magnitude of the machining force (eqn 8) suggests, by analogy with fracture from indentation flaws, that the initial crack size does exhibit significant dependence on material properties.

## 5. CONCLUSIONS

Grinding force measurements performed on a wide range of brittle materials have examined the role of hardness, modulus, fracture toughness and depth of cut. Correlations between these variables are not in good accord with simple plastic grooving and lateral cracking models of material removal. The best correlation involving these variables, ascertained using dimensional analysis techniques, yields a dependence,  $P \sim H(K_c/E)^{5/2}d^{3/4}$ . However, the correlation also suggests a significant influence of additional material parameters (probably thermal parameters such as the thermal conductivity and thermal expansion coefficient). The strong inverse dependence of the machining forces on the

elastic modulus contrasts with its minimal influence on solid particle erosion and indentation fracture. Material removal mechanisms involving brittle chipping (crack growth dictated by  $K_{IC}$ ) and plastic penetration (residual stresses determined by  $H$ ) are undoubtedly involved, but modified perhaps by concurrent thermal and stress waves effects.

Preliminary strengths tests performed on machined specimens confirm the strong influence of the fracture toughness on strength (when limited by machining damage) and suggest an important influence of the depth of cut.

Appendix I

Residual Force Determinations

Force equilibrium requires that the stresses in the residually stressed beam (fig. 12) subject to pure bending, are given by;

$$\begin{aligned}\sigma_y &= -\sigma_R + (Et/2R)(1-2z/t) & z \leq h \\ &= \sigma_t + (Et/2R)(1-2z/t) & h \leq z \leq t\end{aligned}\tag{A1}$$

where  $t$  is the beam thickness,  $h$  is the thickness of the residually stressed layer,  $z$  is the distance from the top (machined) surface, and  $R$  is the radius of curvature of the beam; while  $\sigma_R$  and  $\sigma_t$  are the residual compression in the plastic zone and the residual tension in the elastic zone if bending is prohibited, such that

$$\sigma_R h = \sigma_t (t-h)\tag{A2}$$

Taking moments about the plane,  $z=0$ , gives

$$\begin{aligned}&\int_0^h \sigma_R z dz - (Et/2R) \int_0^h (z-2z^2/t) dz \\ &= \int_h^t \sigma_t z dz + (Et/2R) \int_t^h (z-2z^2/t) dz.\end{aligned}\tag{A3}$$

Solving eqn (A3) and substituting for  $\sigma_t$  from eqn (A2), the residual stress becomes;

$$\sigma_R h = Et^2/6R\tag{A4}$$

REFERENCES

1. A. Broese van Groenou and R. Brehm, The Science of Ceramic Machining and Surface Finishing II (Ed. B. J. Hockey and R. W. Rice) N.B.S. Special Technical Publication (1979) p. 43.
2. B. G. Koepke and R. J. Stokes, The Science of Ceramic Machining and Surface Finishing II, *ibid.*, p. 75.
3. B. R. Lawn, A. G. Evans and D. B. Marshall, *Jnl. Amer. Ceram. Soc.* 63 (1980) 574.
4. D. B. Marshall, A. G. Evans, B. T. Khuri-Yakub and G. S. Kino, to be published.
5. A. G. Evans and D. B. Marshall, Fundamentals of Friction and Wear of Materials (Ed. D. A. Rigney) ASM (Metals Park, Ohio) 1981, p. 439.
6. S. W. Freiman, G. Y. Onoda and A. G. Pincus, *Jnl. Amer. Ceram. Soc.*, 57 (1974) 8.
7. A. G. Evans and E. A. Charles, *Jnl. Amer. Ceram. Soc.* 59 (1976) 371.
8. D. B. Marshall, T. Noma and A. G. Evans, *Jnl. Amer. Ceram. Soc.*, in press.
9. S. M. Wiederhorn and B. J. Hockey, to be published.
10. A. Broese van Groenou, N. Maan and J. B. D. Veldkamp, The Science of Ceramic Machining and Surface Finishing, *ibid.*, p. 43.
11. J. Lankford and D. L. Davidson, *Jnl. Mater. Sic.* 14 (1979) 1662.

TABLE I  
MATERIALS AND PROPERTIES

MATERIAL	GRAIN SIZE ( $\mu\text{m}$ )	$K_c$ (MPa $\sqrt{\text{m}}$ )	H(GPa)	E(GPa)
As <sub>2</sub> S <sub>3</sub> Glass		0.23	1.43	16
Soda-lime glass		0.7	5.5	70
Silicon		0.7	9.0	170
ZnSe (CVD)	200	0.8(Polycrystal) 0.5(Single Grain)	0.9	54
ZnS (CVD)	50	1.0	1.9	103
ZnS (H.P.)	10	0.6	1.9	103
Sapphire		1.5	22.0	420
MgO	300	1.5 (Single Grain)	5.0	240
Porcelain		1.2	3.4	90
Al <sub>2</sub> O <sub>3</sub> (H.P.)	3	2.9	20.0	410
$\alpha$ -SiC (Sintered)	4	2.4	27.0	420
SiC (H.P.)	8	3.6	20.0	420
B <sub>4</sub> C (Sintered)	15	2.4	34.0	500
Si <sub>3</sub> N <sub>4</sub> (H.P.)	2	4.0	19.0	300



TABLE II  
AVERAGE GRINDING FORCE DATA

MATERIAL	FORCE (N)						
	7 $\mu\text{m}$	6 $\mu\text{m}$	5 $\mu\text{m}$	4 $\mu\text{m}$	3 $\mu\text{m}$	2 $\mu\text{m}$	1 $\mu\text{m}$
ZnS (H.P.)	60	57	51	41	30	21	12
ZnS (CVD)			60	51	49	39	27
As <sub>2</sub> S <sub>3</sub>	180	170	150	130	110	90	60
S.L. Glass	230	200	190	170	140	120	80
Porcelain	260	230	200	170	140	120	80
Si <sub>3</sub> N <sub>4</sub>				800	600	400	240
Al <sub>2</sub> O <sub>3</sub> (H.P.)				700	550	400	250
SiC (S)	160	140	120	100	80	60	30
B <sub>4</sub> C	400	320	270	220	170	110	60
Sapphire	180	160	130	110	90	60	30
SiC (H.P.)	300	280	230	170	120	100	60
MgO	160	140	120	100	90	70	50
Si	60	60	50	40	40	30	20
	50 $\mu\text{m}$	40 $\mu\text{m}$	30 $\mu\text{m}$	20 $\mu\text{m}$	10 $\mu\text{m}$		
ZnS	110	90	70	50	30		

TABLE III

Cracking Threshold Forces For Sliding Contacts

MATERIAL	THRESHOLD (N)
Soda Lime Glass	3
Si	0.04
Sapphire	0.5
ZnS (CVD)	5.0
Si <sub>3</sub> N <sub>4</sub> (H.P.)	30.0
$\alpha$ -SiC (Sintered)	5

TABLE IV

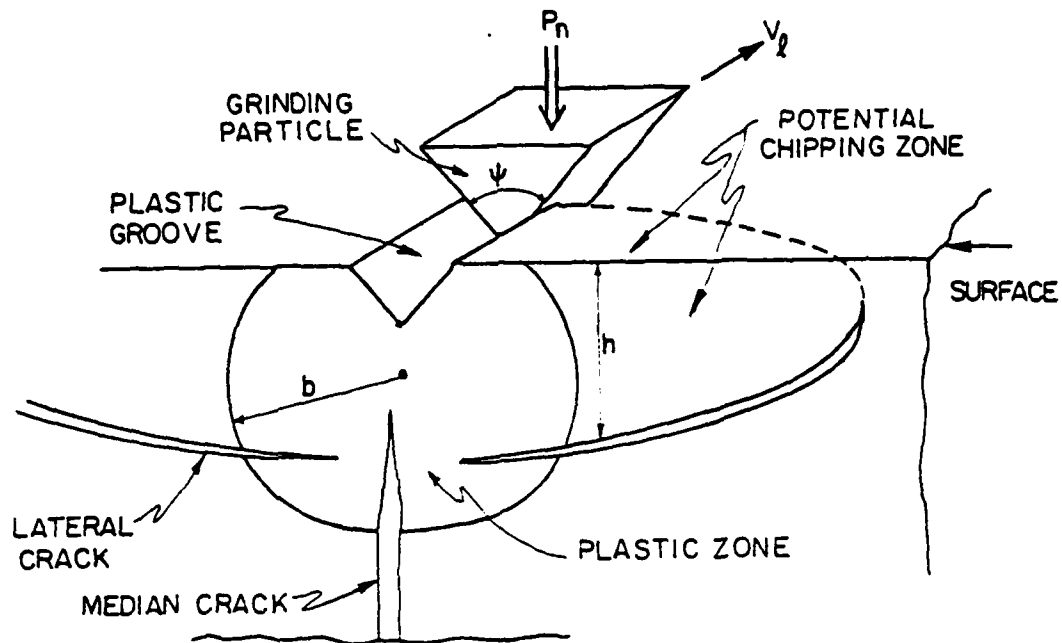
RELATIVE STRENGTHS OF MACHINED SPECIMENS

MATERIAL	$K_C$ (MPa $\sqrt{m}$ )	STRENGTH (MPa)
$Si_3N_4$ (d = 2 $\mu m$ )	4.0	590 $\pm$ 30
SiC (d = 2 $\mu m$ )	3.6	560 $\pm$ 30
GLASS CERAMICS <sup>6</sup>		
1	0.51	170 $\pm$ 20
2	0.74	120 $\pm$ 20
3	1.1	90 $\pm$ 17
4	1.5	50 $\pm$ 10

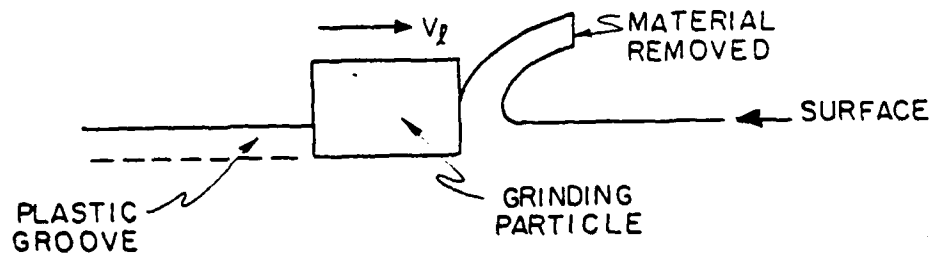
FIGURE CAPTIONS

- Fig. 1 A schematic indicating the penetration of a diamond into the surface of a brittle solid and the resultant formation of both a plastic zone and lateral/median cracks.
- Fig. 2 A schematic of the mechanical system used to determine the machining forces.
- Fig. 3 a) A typical force, time record on the chart recorder; each indication is a single pass.  
b) A typical force, time record on the oscilloscope; each indication refers to a single wheel contact: several contacts constitute a pass.
- Fig. 4 Force variations accompanying abrupt changes in the depth of cut.
- Fig. 5 Relation between the peak contact force and the average force per pass for three different materials.
- Fig. 6 The variation of the normal force with depth of cut for Si and soda lime glass.
- Fig. 7 a) The variation of the normal force with hardness ( $d = 2 \mu\text{m}$ ).  
b) The variation of the normal force with the lateral cracking parameters ( $d = 2 \mu\text{m}$ ).
- Fig. 8 The correlation of erosion data with the predictions of material removal by lateral cracking.<sup>9</sup>
- Fig. 9 a) A scanning electron micrograph of a  $\text{Si}_3\text{N}_4$  surface ( $d = 2 \mu\text{m}$ ) indicating the presence of plastic grooves.
- Fig. 9b A scanning electron micrograph of a sapphire surface ( $d = 2 \mu\text{m}$ ) indicating brittle chipping characteristics.

- Fig. 10 Profilometer traces on  $\text{Si}_3\text{N}_4$  surfaces ( $d = 2 \mu\text{m}$ ) for i) two different positions on the same surface and ii) a newly machined surface.
- Fig. 11 The trend in surface characteristics amongst materials.
- Fig. 12 The deflection of a thin  $\text{Si}_3\text{N}_4$  beam subject to grinding on one surface.
- Fig. 13 A plot of the dimensionless grinding force with the modulus to hardness ratio.
- Fig. 14 A plot of the grinding force data with the parameter suggested by the dimensionless analysis.



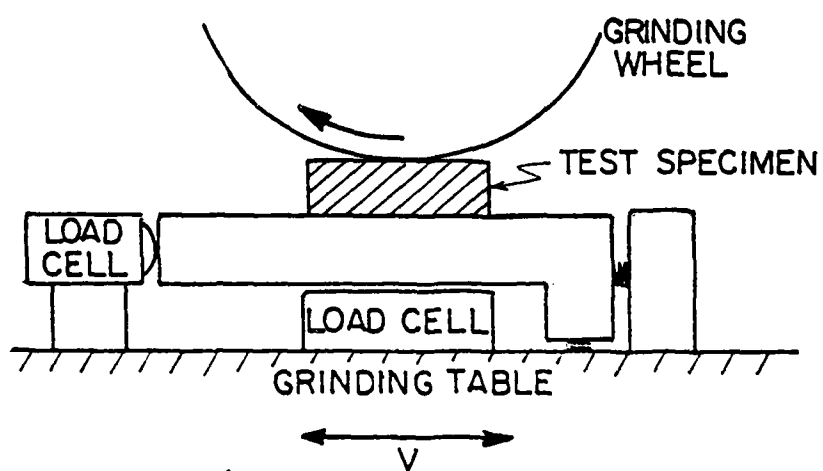
(a) LATERAL FRACTURE MECHANISM



(b) PLASTIC GROOVING MECHANISM

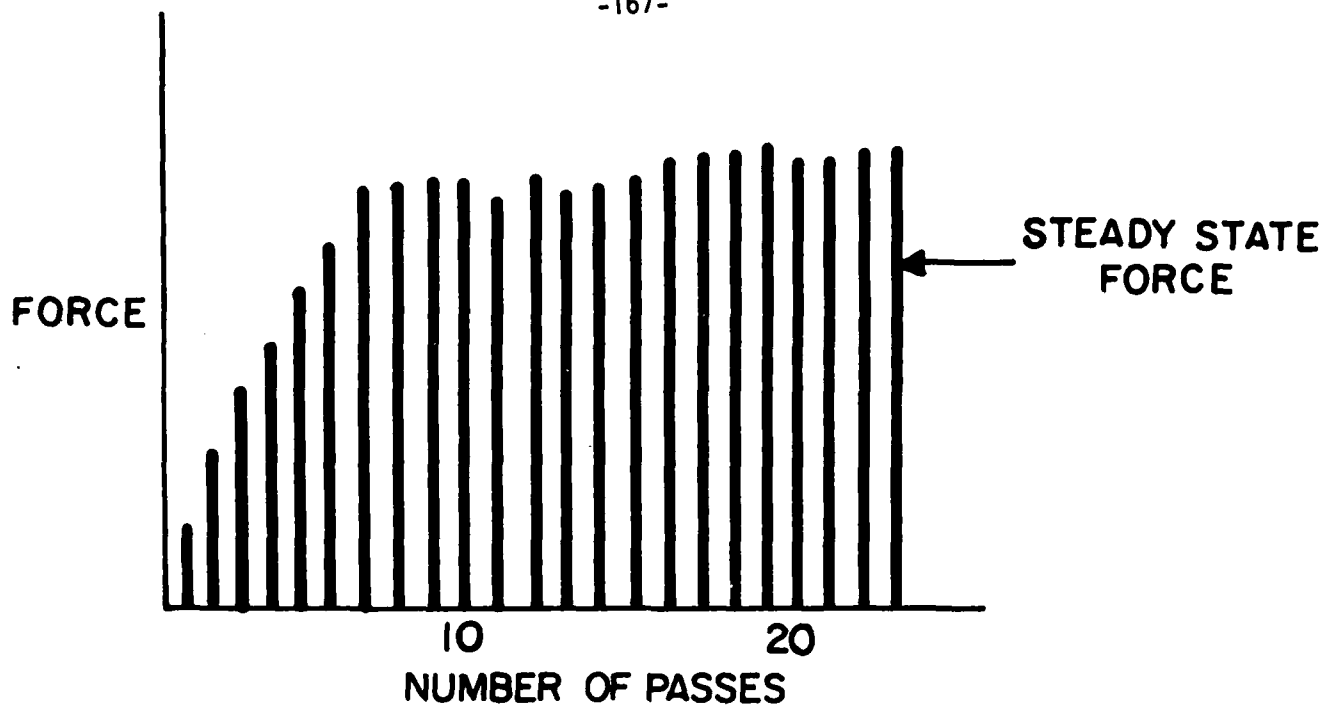
XBL 8011-6355

Fig. 1

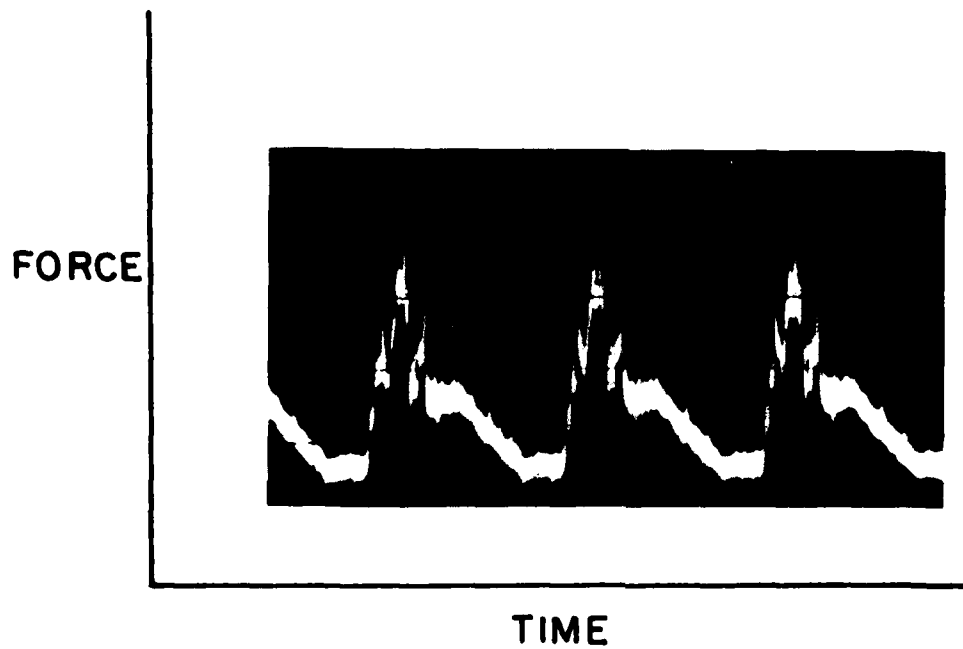


XBL 828-6330

Fig. 2



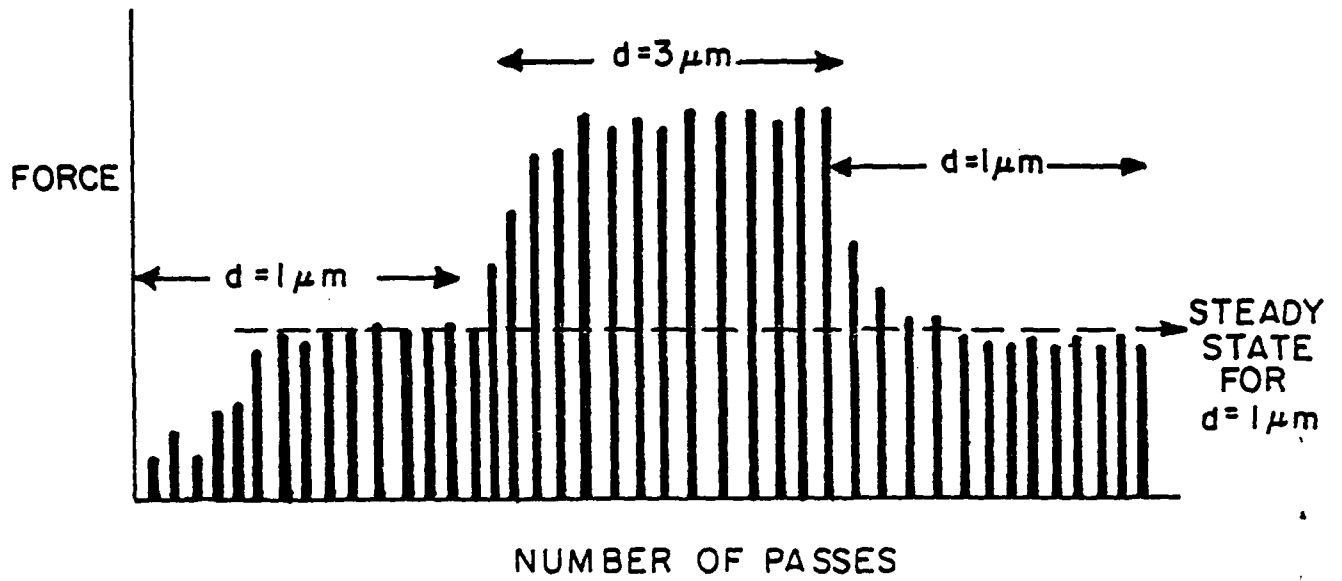
a) CHART RECORDING



b) OSCILLOSCOPE TRACE

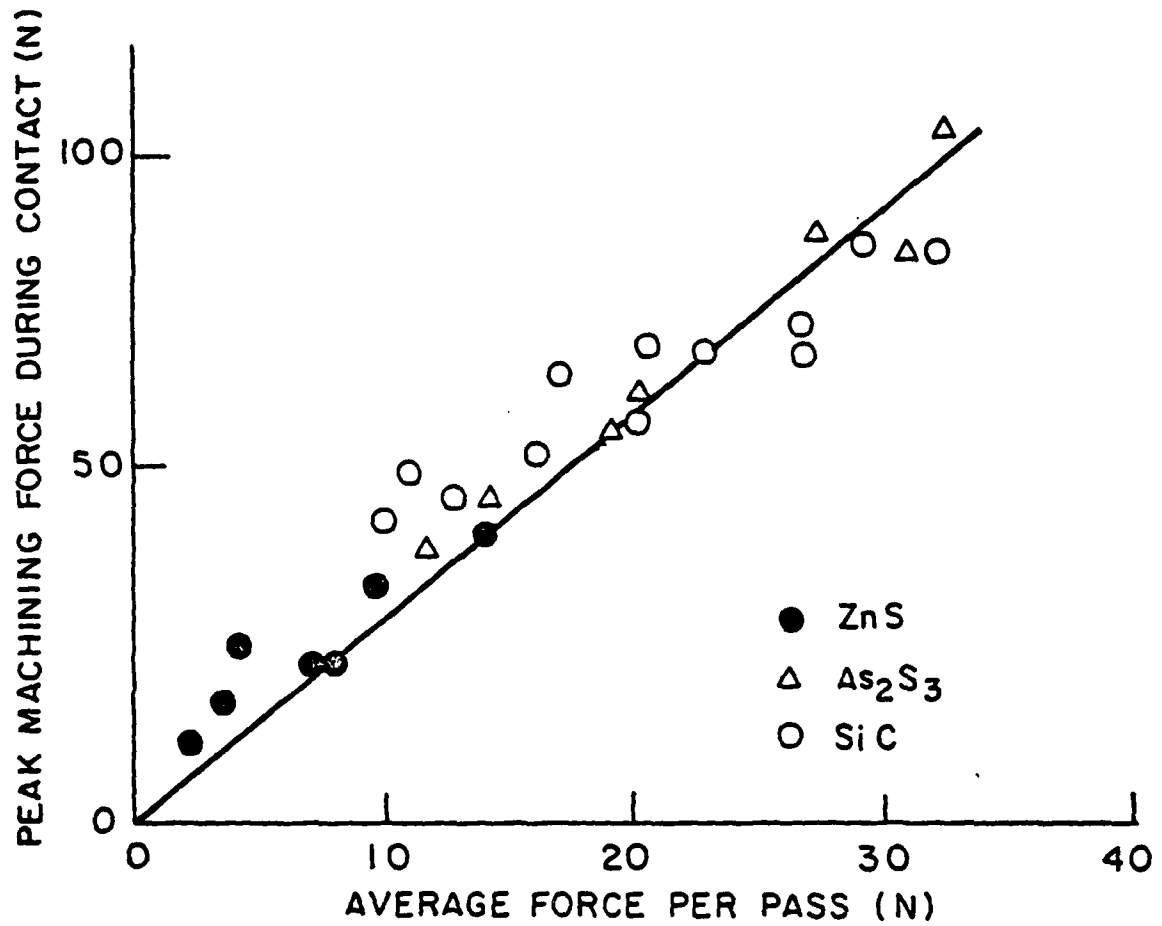
Fig. 3





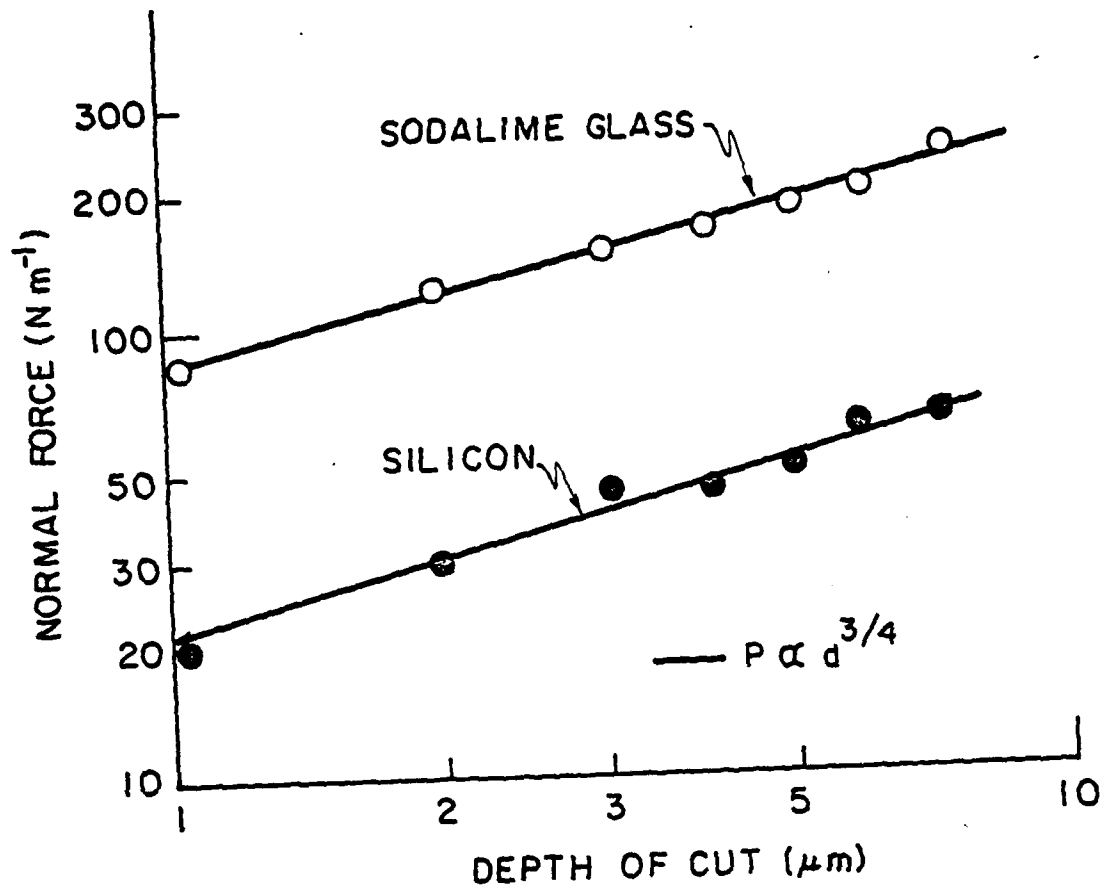
XBL 828 - 6332

Fig. 4



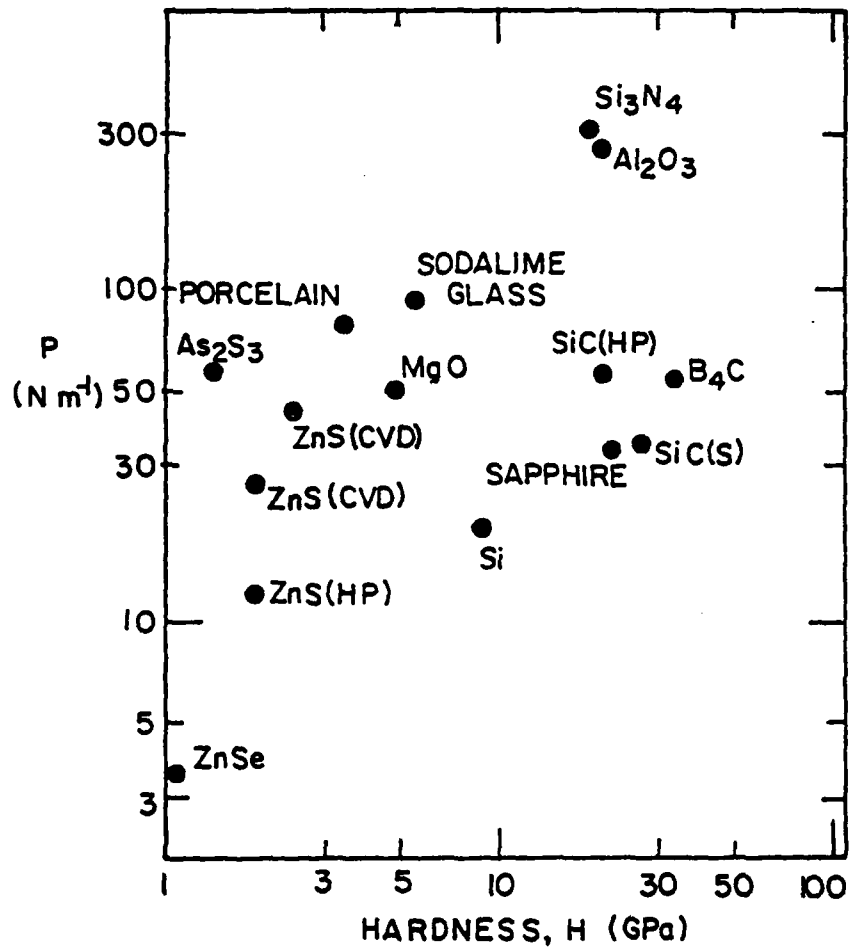
XBL 828-6333

Fig. 5



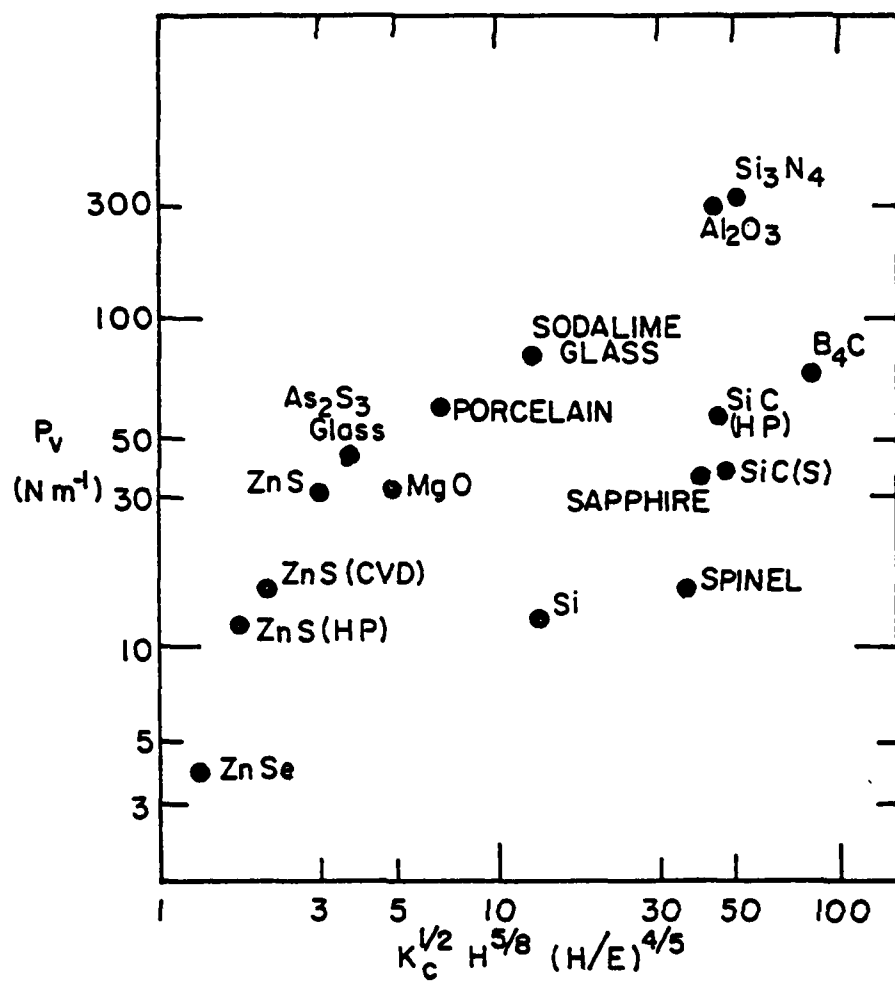
XBL 828-6334

Fig. 6



XBL 828-6335

Fig. 7a



XBL 82B - 6336

Fig. 7b

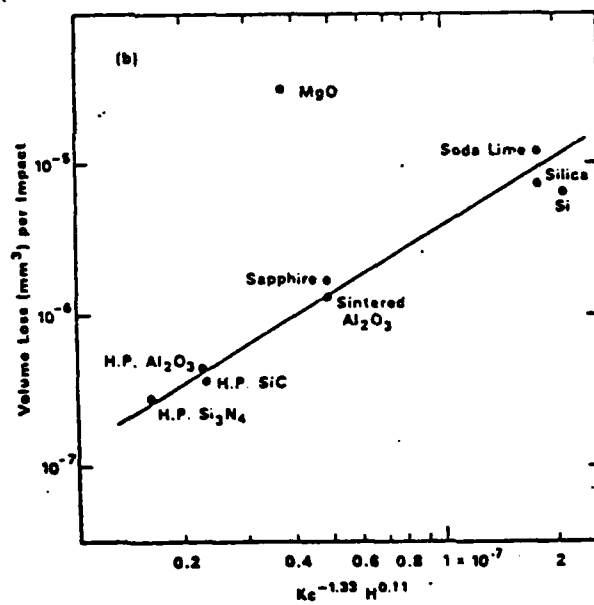
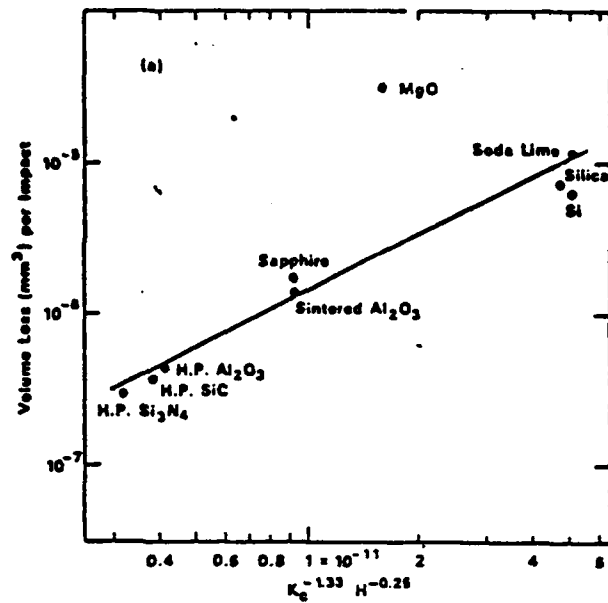


Fig. 8

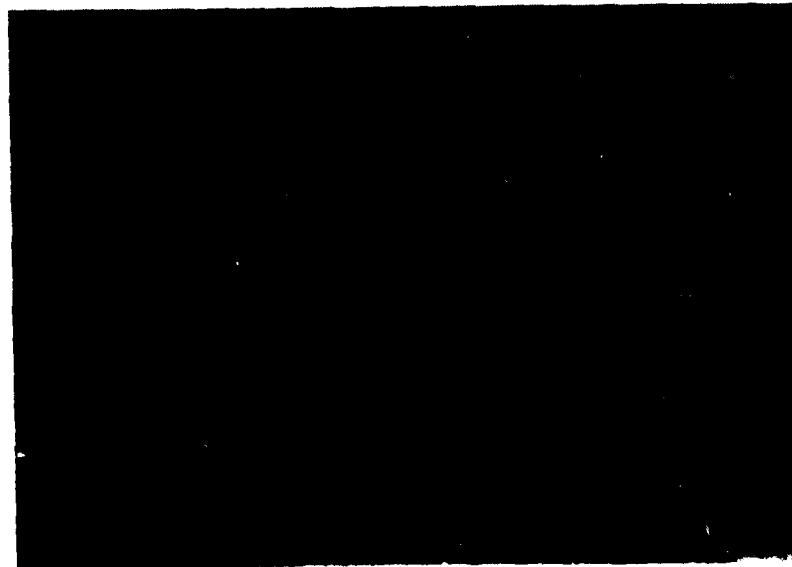
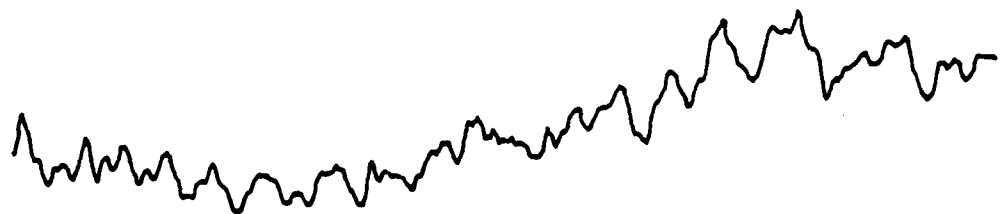


Fig. 9a



i) TWO DIFFERENT LOCATIONS ON SAME SURFACE

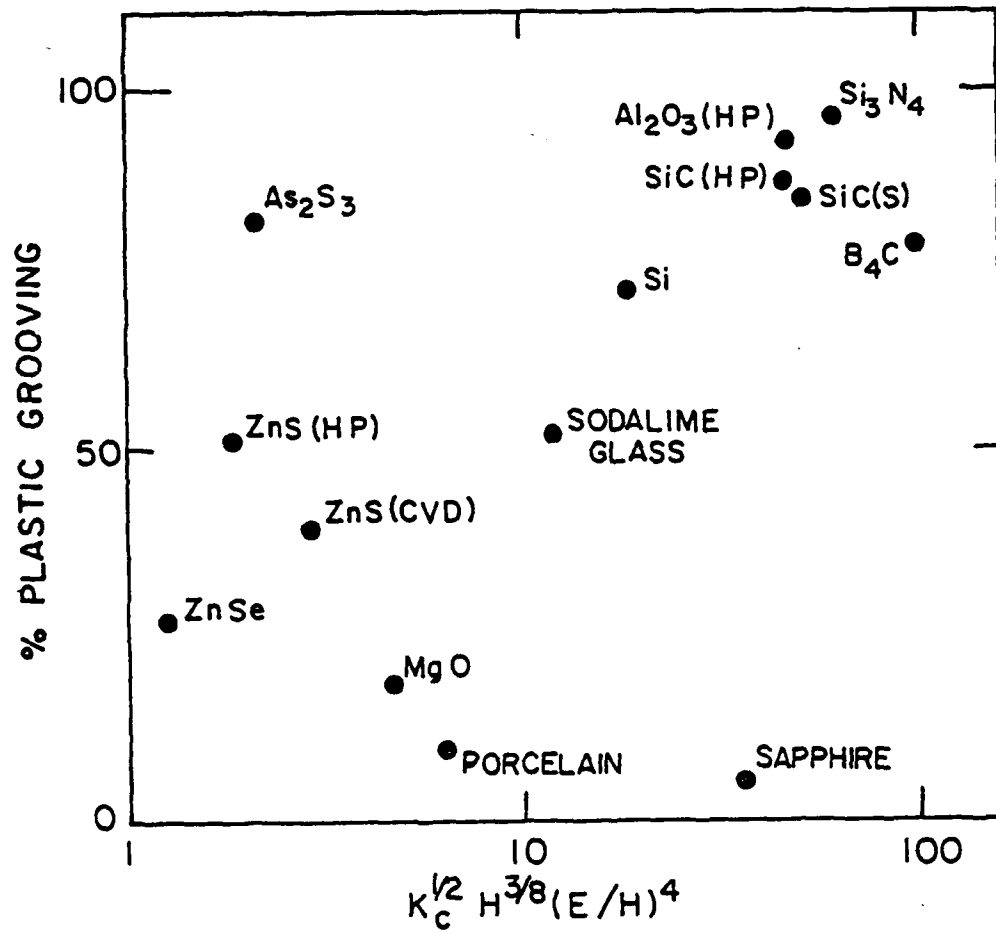


ii) NEWLY MACHINED SURFACE

XBL 828-6337

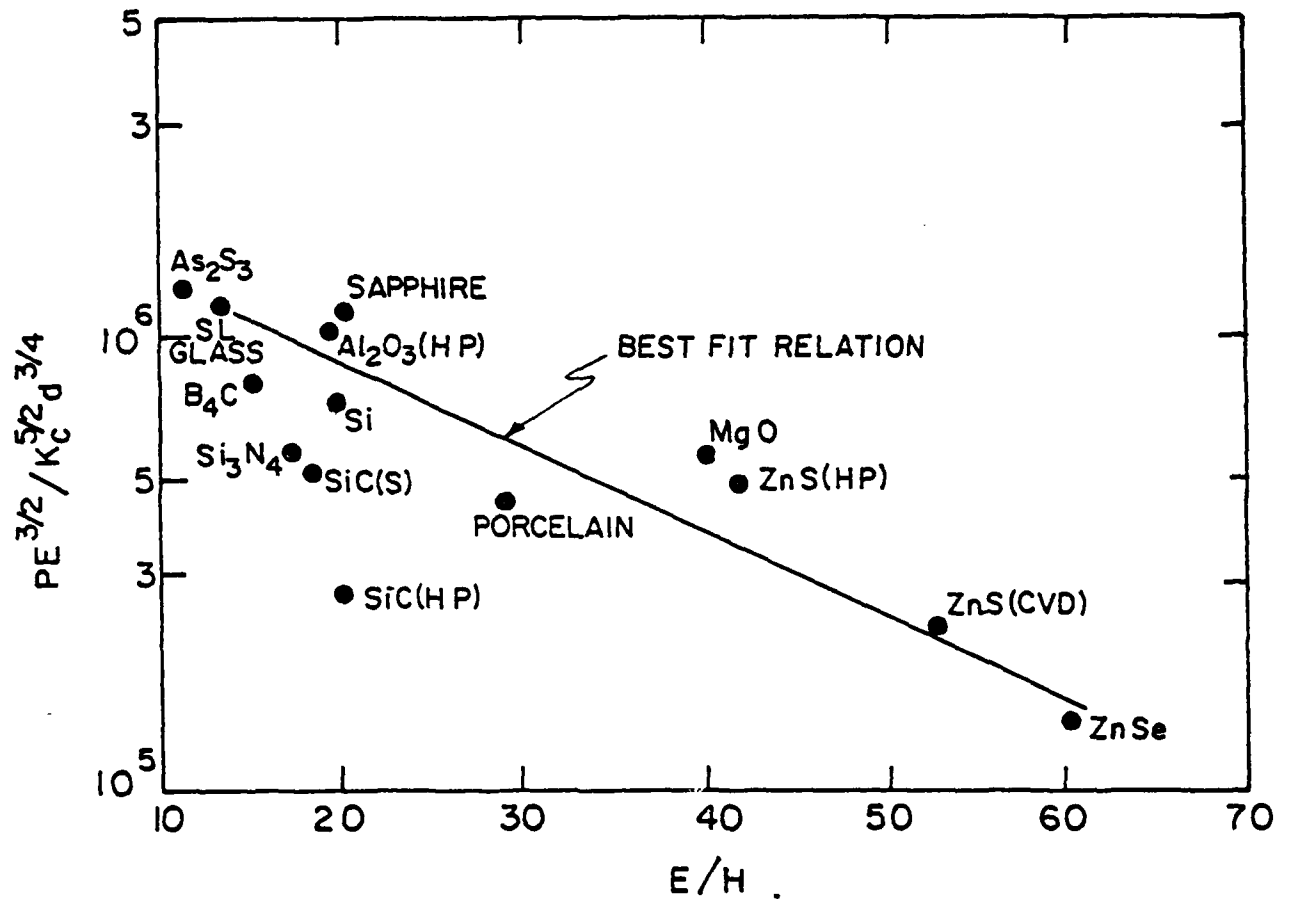
Fig. 9b





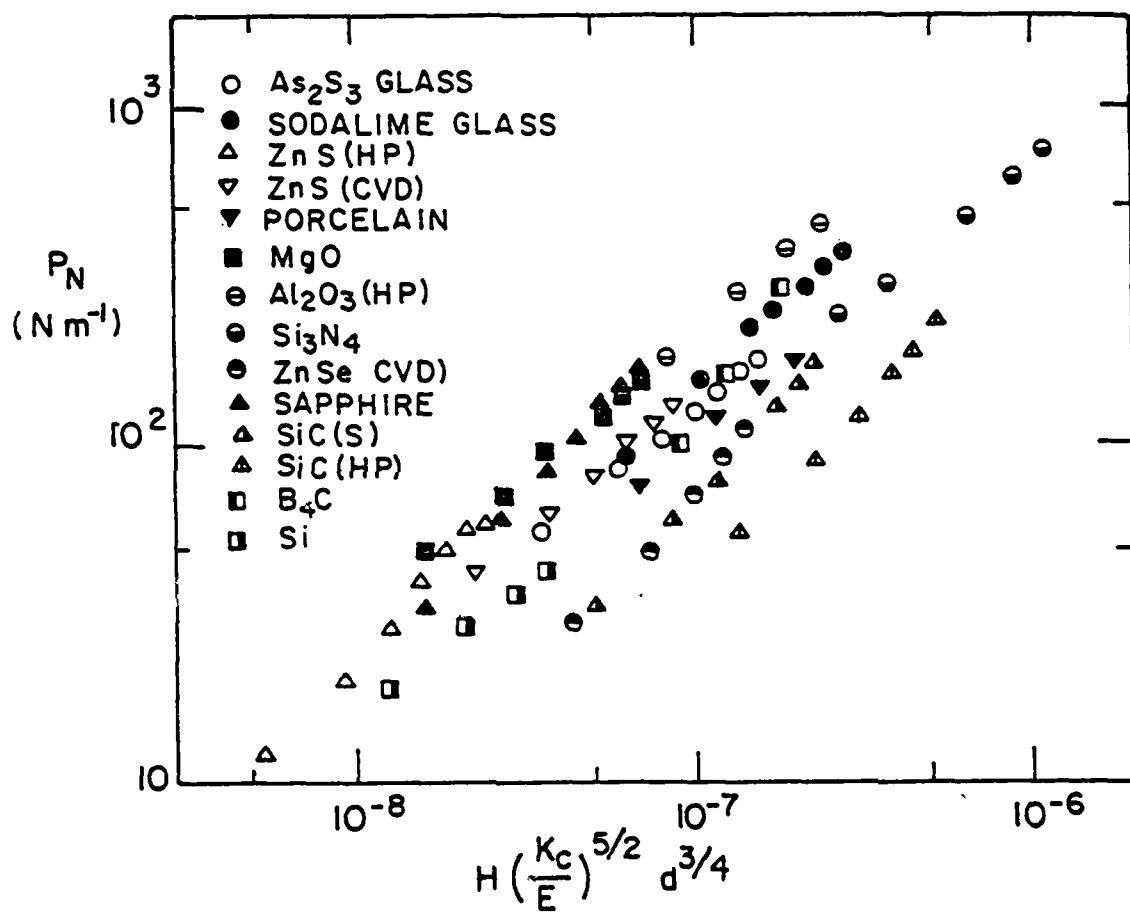
XBL 828-6338

Fig: 11



XBL 828 - 6339

Fig. 13



XBL 828 - 6340

Fig. 14

CHAPTER VI

THE NATURE OF MACHINING DAMAGE IN BRITTLE MATERIALS

by

D. B. Marshall and A. G. Evans

Department of Materials Science and Mineral Engineering  
University of California  
Berkeley, CA 94720

and

B. T. Khuri-Yakub, J. W. Tien and G. S. Kino

Edward L. Ginzton Laboratory  
Stanford University  
Stanford, CA 94305

THE NATURE OF MACHINING DAMAGE IN BRITTLE MATERIALS

D. B. Marshall and A. G. Evans

Department of Materials Science and Mineral Engineering  
University of California, Berkeley, CA 94720

and

B. T. Khuri Yakub, J. W. Tien, and G. S. Kino

Edward L. Ginzton Laboratory  
Stanford University  
Stanford, CA 94305

ABSTRACT

The micromechanics of failure emanating from machining-induced cracks in brittle materials is investigated. In-situ monitoring of crack response during breaking tests (using acoustic wave scattering), strength measurements, and post failure fractography all indicate that the crack response is dominated by residual stresses. Two components of residual stress have been identified; a crack wedging force due to the plastic zone beneath the strength-controlling machining groove, and a compressive surface layer due to adjacent grooves. The wedging force dominates and causes stable equilibrium crack extension during a breaking test. The implications of the results for non-destructive evaluation of surface damage using acoustic wave scattering is discussed.

## 1. INTRODUCTION

Surface finishing of ceramic components is typically achieved by multipoint surface grinding. In this process the workpiece traverses beneath, and contacts, the outer surface of a rotating grinding wheel. Localized penetrations of the workpiece by hard, sharp particles (usually diamonds), embedded in the wheel surface create a complex combination of plastic flow (even in the most brittle materials) and fracture (Hockey 1971; Evans et al. 1978; Hockey and Lawn 1975). Material removal is effected mainly by chipping and intersection of cracks from adjacent penetration sites, while cracks generated in an orientation normal to the surface assume a strength-controlling role if they are more severe than preexisting defects. An understanding of the nature of machining damage is therefore an essential prerequisite for evaluating the reliability of brittle materials as structural components.

The existence of machining-induced cracks oriented normal to the surface has been established in several studies. The most definitive evidence comes from fractographic observations by Rice and Mecholsky (1979) and Mecholsky et al. (1977), of failure origins associated with machining damage. Other observational techniques include methods which induce crack surface separations while suppressing crack extension [e.g., high temperature creep (Rice and Mecholsky 1979), etching or ion-exchange treatments (Bowels 1979)] and thereby enhance crack visibility on the specimen surface (or in cross section). Two populations of strength-controlling cracks have been identified; one set oriented

normal to the direction of motion of the grinding particles, and the other, more severe, set parallel to the grinding direction.

Attempts have been made to correlate the observed flaw dimensions with failure strengths, in accord with conventional Griffith concepts (Rice and Mecholsky 1979). However, on the basis of recent indentation fracture studies (Marshall et al. 1979, Marshall and Lawn 1980), substantial differences might be expected in the mechanics of failure from ideal Griffith flaws and from cracks generated by sharp particle contact during a machining process. The indentation studies have shown that the difference in behavior of the two crack types results from the influence of a residual stress field associated with elastic/plastic contact damage. The residual field assumes a dominant role in the evolution of indentation cracks, and in the subsequent response of the cracks to an applied loading. Instead of failure occurring at a critical applied stress, without precursor crack extension (as in the case for Griffith cracks) the instability of indentation flaws is achieved after a region of stable, equilibrium growth. The failure stress, which can be expressed in terms of residual stress parameters, independent of initial crack length, is appreciably lower than the strength associated with stress-free cracks of equivalent initial dimensions.

The deformation and fracture generated by individual particle contacts during machining are expected to resemble the damage associated with sharp diamond indentations. The micromechanics of crack formation and propagation in machining damage might therefore be expected to exhibit analogous residual stress dominated effects.

In support of this assertion, Kirchner and Isaacson (1982a,b) have demonstrated that residual stresses reduce the strengths of ceramic surfaces containing single-point machining damage. However, machining damage differs morphologically from isolated indentation damage, with regard to the configurations of the plastic deformation zone and associated cracks, as well as the multiplicity of neighboring damage sites. Consequently, the specific influences of the residual field on fracture evolution from machining damage and from indentation damage can be expected to show quantitative differences.

The intent of this study is to identify the factors that determine the role of the residual stress in the micromechanics of failure from machining damage, and thereby to establish a basis for the analysis and prediction of strength. This is achieved by monitoring the response of machining-induced cracks during breaking tests, using the scattering of acoustic waves. (The use of optical methods is precluded by the extensive surface damage on a machined surface and the lack of a priori knowledge of the precise failure origin). The results of the acoustic measurements are used, in combination with fractographic observations, to indicate that the indentation model provides a qualitative description of the response of machining induced cracks. However, the detailed quantitative description requires the incorporation of specific geometrical and interaction effects.



## 2. FRACTURE FROM INDENTATION CRACKS: AN ASSESSMENT

One of the main issues to be addressed in the present study is the role played by residual contact stresses in failure from machining cracks. The basic insight for elucidating that role has been provided by the understanding of failure from relatively well-defined, isolated cracks produced by indentation of brittle surfaces with standard diamond indenters such as Vickers and Knoop (Marshall et al. 1979; Marshall and Lawn 1980; Chantikul et al. 1981; Marshall 1982a,b). In this section the mechanics of failure from indentation cracks is reviewed.

Direct observations of crack evolution during indentation of optically transparent materials have demonstrated that the final crack configurations (Fig. 1) are achieved as the indenter is removed from the surface (Marshall and Lawn 1979). Such observations unequivocally establish that the driving force for crack growth is provided by a residual field. The residual field, which arises because of the elastic/plastic nature of the deformation beneath the indenter, (Chiang et al. 1982), supplements the applied loading during a subsequent breaking test. The existence of a post-indentation crack opening force is readily demonstrated by observing the subcritical extension of indentation cracks after indenter removal, in materials that are susceptible to environmentally-assisted slow crack growth (Anstis et al. 1981; Gupta and Jubb 1981).

Determination of the stress intensity factor  $K_I$  due to the residual field is central to any fracture mechanics analysis involving indentation cracks. The residual field may be evaluated in terms of an outward-acting pressure at the boundary of the plastic zone (Lawn et al. 1980). For approximately axisymmetric indenters, such as the Vickers pyramid, the plastic zone occupies an almost hemispherical volume centered beneath the indentation (Fig. 1). If the crack dimension,  $c$ , is sufficiently large compared with the plastic zone radius,  $b$ , the pressure may be treated as a point force located at the crack center. Under this condition a straightforward solution for the stress intensity factor for the radial crack has been derived (Marshall and Lawn 1979b; Lawn et al. 1980);

$$K_I = \chi_I P / c^{3/2}, \quad (2.1)$$

where  $P$  is the indenter load and  $\chi_I = \$(E/H)^{1/2}$ , with  $E$  and  $H$  the elastic modulus and hardness of the material and  $\$$  a dimensionless constant dependent only on indenter geometry. The crack dimension,  $c_0$ , after indentation is obtained by equating  $K_I$  to the material toughness,  $K_{IC}$ , in Eq. (2.1);

$$c_0 = (\chi_I P / K_{IC})^{2/3}. \quad (2.2)$$

The validity of Eq. (2.2) has been tested with Vickers indentation in a wide range of ceramic materials (Anstis et al. 1981).

The mechanics of failure from radial cracks under the combined influences of the residual stress and a normal applied tension,  $\sigma_a$ , has been analyzed in detail by Marshall and Lawn (1979a; 1980). The crack response is described by an applied-stress/equilibrium-crack-size function

$$\sigma_a = [K_c / \pi \Omega c]^{1/2} [1 - \chi_r P / K_c c^{3/2}] , \quad (2.3)$$

(where  $\Omega$  is a crack geometry parameter) which results from superimposing the stress intensity factors due to the residual and applied fields ( $K_r$  from Eq. (2.1) and  $K_a = \sigma_a (\pi \Omega c)^{1/2}$ ) and setting  $K_r + K_a = K_c$  for equilibrium crack extension. The failure condition is defined by the maximum in the  $\sigma_a(c)$  function,

$$c_m = (4 \chi_r P / K_c)^{2/3} = 4^{2/3} c_0 , \quad (2.4)$$

$$\sigma_m = [27/256 K_c^4 / \chi_r (\pi \Omega)^{3/2}]^{1/3} P^{-1/3} \quad (2.5a)$$

$$= 3 K_c / 4 (\pi \Omega c_m)^{1/2} , \quad (2.5b)$$

and failure is preceded by stable equilibrium crack growth from  $c_0$  to  $c_m$ . This behavior contrasts with the response of ideal, stress free cracks, where crack instability is achieved at a critical applied stress level without precursor extension ( $\chi_r = 0$ ,  $c = c_0$  in Eq. (2.3)).

In situ measurements of the surface traces of Vickers cracks during failure testing have demonstrated the existence of stable crack extension according to Eq. (2.3) in a wide variety of ceramic materials

[glass (Marshall et al. 1979), silicon (Lawn et al. 1981), glass ceramics (Cook et al. 1982) and silicon nitride (Marshall 1982a)]. Extensive strength degradation measurements by Chantikul et al. (1981) have confirmed the predicted dependence of strength on material properties and contact load (Eq. (2.5.a)).

The indentation fracture analysis has also been extended to the linear deformation/fracture configuration (Kirchner and Isaacson, 1982a,b). The modified analysis predicts a similar crack response under applied load, although, the region of stable precursor crack growth is more extensive ( $c_m/c_o = 4$ ) than for axisymmetric penetration ( $c_m/c_o = 2.5$ ). The linear-damage analysis applies strictly to cracks generated by the penetration of a wedge indenter. However the observations, by Rice and Mecholsky (1979), of semi-elliptical (rather than linear) cracks beneath scratches and machining grooves (see also Section 4) suggest that the loading during machining may resemble more closely the axisymmetric indentation. Such geometrical deviations from linear geometry would be expected to reduce the ratio  $c_m/c_o$ .

Another factor which may cause the response of machining cracks to differ from that of the idealized indentation crack (linear or axisymmetric) is the interaction of residual stresses from grinding grooves in the neighborhood of the strength-controlling damage. For example, Cook et al. (1981) have recently demonstrated the existence of interaction effects by measuring the strengths of glass ceramic flexure bars with indentation cracks introduced into polished and machined surfaces. At identical indentation loads, the machined surfaces exhibited higher strengths than the polished surfaces. Cook et al.

concluded that the machined surfaces contain a layer of residual compressive stress. The competing influences of the compressive layer and the localized tensile residual stresses associated with the sites of maximum particle penetration will be addressed in the following sections.

### 3. CRACK OBSERVATIONS USING ACOUSTIC WAVE SCATTERING

The occurrence of stable crack extension prior to failure from contact-induced flaws provides a convenient indication of the existence of residual crack-opening stresses. For indentation cracks, optical observation of radial surface traces, during load application, has confirmed the expected crack response. However optical monitoring of machining-induced flaws would appear to be precluded by the requirement for measurement of crack depth rather than surface trace dimensions, and by the lack of a priori knowledge of the precise failure origin. Techniques of crack detection based on the scattering of acoustic waves (Khuri-Yakub et al. 1980) are not restricted by these factors, and thus provide a means of monitoring crack response and thereby determining the influence of residual stresses.

#### 3.1 Experimental Method

An acoustic scattering technique designed specifically for the detection of surface cracks (Tien et al. 1982) is illustrated in Fig. 2; transducer 1 excites surface (Rayleigh) waves incident nearly normal to the crack surface, and transducer 2 detects the backscattered waves. The relative amplitude of the backscattered signal is related, via scattering analysis, to the crack dimensions, and the time delay between

generating and receiving the signal defines the crack position. In the present experiments the incident wave comprised a pulse of four cycles at 8 MHz (700  $\mu\text{m}$  wavelength) with a lateral width  $\sim 2$  mm. The reflected signal was displayed on an oscilloscope, which was triggered by the pulse generator. Using this technique, separate reflected signals were obtained from the major grinding grooves (resolvable crack separation  $\sim 1$  mm) and could be recorded photographically as a function of applied loading.

Hot pressed silicon nitride<sup>†</sup> was used as a test material, both because of its importance as a structural ceramic and because of the absence of stress corrosion cracking at room temperature. Specimens were in the form of bars ( $80 \times 25 \times 6.25$  mm<sup>3</sup>) with the test surface initially polished. Contact damage was introduced into the center of the test surface, and the acoustic scattering was monitored during the application of load in a three-point bending mode (Fig. 2). Several types of contact damage (all oriented normal to the bending stress) were investigated. First, the responses of 50N Knoop indentation cracks in polished surfaces were monitored both acoustically and optically. These tests provided basic information about the scattering process, essential to the interpretation of the results of the subsequent experiments. Then, configurations that successively approached the machining damage condition were investigated: a row of Knoop indentations (50N load), a scratch generated by sliding a normally loaded (5N) Knoop indenter across the test surface, and machined surfaces (240 grit, 8" diameter wheel, 3300 RPM, 2  $\mu\text{m}$  depth of cut, 2 cm s<sup>-1</sup> horizontal velocity, transverse machining direction). Finally the response of a

---

<sup>†</sup> Norton, NC132.

50N Knoop indentation crack in a longitudinally machined test surface provided additional insight into the effect of the compressive surface layer.

### 3.2 Acoustic Scattering Results

#### Indentation Cracks

The acoustic scattering from surface cracks is sensitive to the existence of residual crack opening. This sensitivity is demonstrated by comparing the acoustic scattering from an indentation crack and an initially stress-free crack<sup>†</sup> of similar dimensions (Fig. 3). Optical observations confirmed that the stress-free crack did not extend prior to failure. However the reflected acoustic signal [expressed, in Fig. 3a, in terms of a calculated crack radius, assuming an open, surface half-penny crack (Kino 1978)] shows a reversible increase with applied load. This increase can be interpreted in terms of a reversible opening and closing of the crack surfaces under the applied loading (Tien et al. 1982). At zero applied stress, complete crack closure is prevented by contacts at asperities over the crack surface. The areas between the contacts scatter as small cracks but, since the scattered amplitude is approximately proportional to  $c^3$ , the total scattered amplitude is considerably smaller than that of a fully open crack. Applied tension relieves the contacts continuously until, at the failure point, the crack faces are fully separated and the true crack radius is measured (c.f. optical crack length measurement, Fig. 3a).

---

<sup>†</sup>The stress-free crack was obtained by removing the plastic zone (and therefore the residual stress) of an indentation crack by mechanical polishing. Similar acoustic scattering results have also been obtained from cracks which had the residual stress eliminated by annealing (Tien et al. 1982).

Acoustic scattering from indentation cracks (which are subject to residual crack opening) does not show the reversible opening and closing effects (Fig. 3b). However, an irreversible increase in acoustic signal with applied tension, corresponding to genuine stable crack extension, is detected. Despite some complication in modelling the crack geometry for acoustic scattering analysis,<sup>†</sup> a true measure of the crack dimension is obtained at all stages during the failure test; comparison of acoustic measurements, optical measurements and fracture mechanics predictions (Eq. (2.3)) are shown in Fig. 3c. The irreversibility of the acoustic scattering response with applied loading provides a definitive indication of the presence of residual crack opening stresses.

The acoustic scattering from a 50N Knoop indentation introduced into a machined surface is shown in Fig. 4. The irreversible increase in scattering with applied load indicates that a residual opening stress exists. However, both the initial crack length and the extent of stable crack growth during the failure test are smaller than the corresponding values for a crack in a polished surface (Fig. 3b). Moreover the crack in the machined surface exhibited a higher strength (290 MPa compared with 240 MPa, see Figs. 3b and 4). These observations are consistent with the postulate of Cook et al. (1981) that a compressive surface layer exists in machined surfaces, albeit the local opening force exerted on the crack by the immediate indentation deformation zone still exceeds the closure force due to the compressive layer.

---

<sup>†</sup> The crack does not penetrate the plastic zone. Therefore the crack exhibits the geometry of a semi-annulus with inner radius dictated by the plastic zone radius. Calculations based on a subsurface elliptical crack have provided a good approximation (Tien et al. (1982)).



UNCLASSIFIED

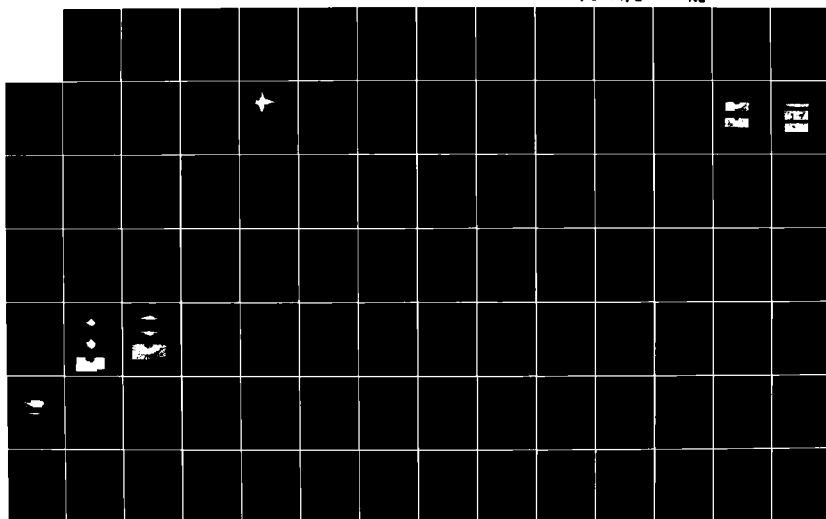
ENGINEERING A G EVANS ET AL. 30 OCT 82

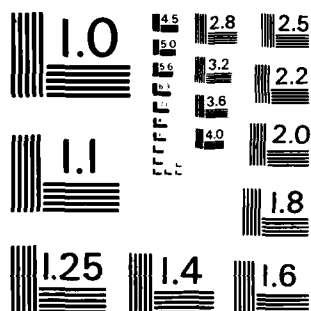
NO0014-81-K-0362

F/G 11/2

NL

3/4





MICROCOPY RESOLUTION TEST CHART  
NATIONAL BUREAU OF STANDARDS-1963-A

### Linear Damage Processes

The variation of acoustic scattering from a scratch in a polished surface and from a machined surface are shown in Fig. 5. The irreversible increases in scattering amplitudes in both cases provide measures of stable crack extension prior to failure, and thus afford direct evidence for the existence of residual crack-opening stresses at scratches and at machining induced cracks.

## 4. FRACTOGRAPHIC OBSERVATIONS

### 4.1 Indentation Cracks

Optical observation of the fracture surface in hot pressed  $\text{Si}_3\text{N}_4$ , under carefully controlled conditions,<sup>†</sup> enables identification of the crack front at various stages of propagation. The fracture surface of a 50N Knoop indentation crack on a polished surface is shown in Fig. 6a. The reflectivity is high in the regions of crack formation and post-failure extension, but low in the intermediate region of stable crack growth during loading.<sup>‡</sup> Direct correspondence between these regions and the various stages of crack extension has been established empirically, by comparison with in-situ surface trace measurements.

---

<sup>†</sup>The fracture surface markings are most clearly observable using a stereo microscope with the fracture surface oriented at about 70° to the optical axis and the illumination set for specular reflection.

<sup>‡</sup>The different reflectivities are due to different proportions of transgranular/intergranular fracture (possibly associated with different crack velocities).

The fracture surface from the specimen with the 50N Knoop indentation on a machined surface is shown in Fig. 6b. The dimensions of the crack measured along the specimen surface ( $c_o$  and  $c_m$ ) are considerably smaller than the corresponding dimensions for the crack in a polished surface (Fig. 6a), whereas the crack depths are almost identical. These observations are consistent with the acoustic scattering and strength results in Section 3.2.1, and indicate that the compressive stress due to the surrounding machined surface is confined to a shallow surface layer.

#### 4.2 Linear Damage

The fracture surfaces for three linear damage processes are shown in Fig. 7; in (a) a row of 50N Knoop indentations, in (b) the scratch generated by a sliding Knoop indenter (specimen from Fig. 5a), and in (c) a machined surface (specimen from Fig. 5b). The crack configurations on all fracture surfaces are similar, as illustrated schematically in Fig. 8. The initial cracks appear as a series of semicircular (or semi elliptical) surface cracks beneath the scratch or grinding groove. Under the influence of an applied tension some of the cracks coalesce and extend stably to an elongated semi-elliptical surface crack configuration at failure. The identification of a region of stable crack growth is consistent with the acoustic scattering results of Section 3.2.2.

## 5. EVALUATION OF COMPRESSIVE LAYER

A series of strength measurements were performed in order to clarify the influence of the residual compressive layer on the strength properties of machined surfaces. The specific objectives were to provide a comparison of the influence of the compressive layer on axisymmetric and linear damage configurations, and to investigate variations of the compressive stress with orientation relative to the machining direction.

The strength tests were performed by four-point bending of  $\text{Si}_3\text{N}_4$  bars ( $40 \times 5 \times 3 \text{ mm}^3$ ) which had been prepared with various combinations of surface finish and strength controlling flaws. Each prospective test surface was prepared by one of the following procedures: polishing, longitudinal machining or transverse machining.<sup>†</sup> Then the strength controlling flaws were introduced either by a row of Knoop indentations or by scratching with a Knoop indenter, both in the transverse direction.

The results are summarized in Table 1. Also included are the strengths of the single Knoop indentations in polished and machined surfaces from Section 3. For each of the strength-controlling flaw configurations, the specimens with machined test surfaces were stronger than specimens with polished test surfaces. Thus it may be concluded that all flaw configurations are influenced by the compressive layer. Moreover, the compression is evident for flaws oriented both normal

---

<sup>†</sup>In order to avoid failure from the machining damage the grinding wheel used here had a smaller abrasive particle size (400 grit) than the wheel used to produce the machining damage which was investigated in the previous sections (240 grit).

and parallel to the machining direction (although, for a given flaw configuration, the transversely machined specimens were slightly stronger than the longitudinally machined specimens). Comparison of the strengths of single indentations and scratches suggests that, at a given strength level, the magnitude of the strength increase due to the compressive layer is the same for axisymmetric and linear flaw configurations. However, the magnitude of the strength increase is sensitive to the size of the strength controlling flaw (compare the strength increases for rows of indentations and scratches). This last observation is consistent with the suggestion that the compression is confined to a shallow surface layer.

## 6. DISCUSSION

### 6.1 Mechanics of Crack Formation and Growth

The observations of Sections 3-5 have demonstrated that the damage due to machining of  $\text{Si}_3\text{N}_4$  involves a combination of deformation and fracture. The strength-controlling flaws are evident as a series of semi-elliptical cracks beneath the most severe grinding groove. This observation is in accord with the observations of Mecholsky et al. (1977) and is consistent with the notion that the strength controlling damage results from a series of localized contacts from a single particle on the grinding wheel. Under the combined influences of an applied load and residual stresses (associated with the deformation) the cracks extend stably prior to failure. Crack extension begins at preferred locations (presumably regions of high local residual stress),

and is followed by coalescence and propagation of a single semi-elliptical entity. Preferential extension from such locations is emphasized, because most of the stable crack advance occurs close to the failure load (Fig. 5).

The competing influences of the localized tensile residual field associated with the strength-controlling machining damage, and the overall compressive influence of neighboring damage sites, can be rationalized with reference to Fig. 9. An isolated grinding groove (or indentation) is surrounded by a plastic zone which accommodates the volume of the groove (Fig. 9a). The residual stress, which can be evaluated in terms of an outward-acting pressure at the boundary of the plastic zone (Lawn et al. 1980), creates compression adjacent to the zone and tension on median planes beneath the zone. The cumulative effect of many neighboring damage sites of similar depths, and with a high degree of overlap in their residual fields, is the development of a uniform thin layer of residual compression and an underlying residual tension of relatively low magnitude. However, the strength-controlling damage is expected to extend to a greater depth than the damage in neighboring regions (Fig. 9b). In this circumstance, the upper portion of the outward acting pressure (depth  $d_c$ , Fig. 9) can be regarded as being negated by the surrounding layer of residual compression, while the opening force associated with the lower portion (depth  $d_t - d_c$ ) persists. Therefore the multiple damage sites in a machined surface reduce the residual crack opening force associated with the strength controlling groove (by a factor  $d_c/d_t$ ).

The response of machining-induced cracks (with the deformation/fracture geometry of Figs. 8 and 9) to applied loading is not amenable to straightforward fracture mechanics analysis. However, some useful empirical relations can be gained from measured strength/crack-size variations and from the observed extent of stable crack growth prior to failure. Crack length measurements from the fracture surfaces of the specimens tested in Sections 3 to 5 are summarized in Table 2. The dimensions of the semi-elliptical cracks associated with the linear damage configurations at the failure point were measured as indicated in Fig. 8, with  $c_m = \sqrt{c_s c_d}$ .<sup>†</sup> The extent of stable crack growth is approximately constant for all combinations of linear damage and prior surface preparations, with

$$c_m/c_o \approx 5 \quad (6.1)$$

This compares with  $c_m/c_o = 2.5$  for the isolated indentation damage and  $c_m/c_o = 4$  predicted for the linear crack (wedge indenter) configuration (Section 2). The relatively large value of  $c_m/c_o$  for the machining damage derives from the substantial stable extension of the crack parallel to the surface. However, a specific rationale for the magnitude of  $c_m/c_o$  has not yet emerged.

---

<sup>†</sup>The rationale for choosing  $c_m = \sqrt{c_s c_d}$  originates from the analysis of Bansal (1976) which demonstrated that the stress intensity factor for uniform tension applied to a semi-elliptical surface crack (with semi-major and semi-minor axes  $c_s$  and  $c_d$  respectively) and a semi-circular surface crack of radius  $c = \sqrt{c_s c_d}$  are approximately the same. Attempts to correlate the extent of stable crack growth and the strength based on  $c_d$  or  $c_s$  individually were unsuccessful.



The measured strengths are plotted as a function of  $c_m$  in Fig. 10.

Most of the data conform to the relation<sup>†</sup>

$$\sigma c_m^{1/2} = 3.9 \pm 0.2 \text{ MPa.m}^{1/2} \quad (6.2)$$

Equation (6.2) is of the same form as the Griffith strength equation, but it involves the crack length at the point of failure, rather than the initial crack length  $c_0$ .

## 6.2 Implications for Non-Destructive Evaluation

The acoustic wave scattering technique used in Section 3 was developed primarily as a method for performing non-destructive evaluation (Tien et al. 1982; Khuri-Yakub et al. 1980). Strength prediction from ultrasonic measurements of surface cracks requires two steps. First, the size of the largest crack,  $c_0$ , is evaluated from the analysis of acoustic scattering measurements (made in the absence of applied loading), and then  $c_0$  is related to the strength using fracture mechanics. The experiments in Sections 3 to 5 provide essential information for both steps.

The strength of a polished surface containing an isolated indentation crack (of length  $c_0$ ) is related to the crack length at the point of failure,  $c_m$ , by Eq. (2.5b), while  $c_m$  is related to  $c_0$  by Eq. (2.4). Since the acoustic wave measurements provide a reliable measure of  $c_0$ , Eqs. (2.4) and (2.5b) constitute a sound basis for non-destructive strength prediction.

---

<sup>†</sup> It is noted that the similarity between Eqs. (6.1) and (6.2) and the corresponding relations for indentation cracks (Eqs. 2.4 and 2.5b) might be expected on the basis that the replacement of  $K_I$  in Eq. (2.1) with any function of the form  $K_I = \chi_I p/c^n$  ( $n > 0$ ) yields a set of equations of the same form as (2.2) to (2.5) but with numerical factors dependent upon  $n$ .

However strength prediction for a surface containing a stress-free crack is tenuous. The apparent crack length measured acoustically, in the absence of applied loading, is not related in a simple way to the true crack length. Analysis of the crack separation process has been performed by Budiansky (1982), but the relation between the true and apparent crack lengths is sensitive to many material parameters (fracture surface topography, grain size, thermal expansion anisotropy, elastic modulus) and the crack size. Therefore, ultrasonic measurements of stress-free cracks do not appear to provide a sound basis for strength prediction. However, it is noted that, in the case of  $\text{Si}_3\text{N}_4$ , the strength calculated by treating a stress-free crack as an indentation crack, in both the scattering and fracture mechanics analyses, is conservative (Tien et al. 1982).

Cracks associated with linear damage processes are subject to residual opening stresses. The residual crack opening allows a true measure of crack size to be obtained from acoustic measurements (provided the initial crack geometry can be adequately modelled in the scattering analysis). Therefore acoustic measurements in conjunction with Eqs. (6.1) and (6.2) provide a basis for non-destructive prediction of the strengths of machined and scratched surfaces of  $\text{Si}_3\text{N}_4$ .

### 6.3 Damage Resistance

The competing influences of the strength-degrading dominant flaw and the compressive surface damage layer in a machined surface present a possibility to optimize the machining procedure for a given application. Generally, the strength of a machined surface would be expected to decrease with increasing severity of machining (large abrasive

particles, high machining forces), but the depth of the compressive layer would be expected to increase. The compressive layer provides resistance to in-service strength degradation from mechanical contact events, as exemplified by the data in Table 1. Therefore, for structural applications in mechanically hostile environments, optimum performance could be provided by the most severe machining procedure (i.e., maximum resistance to in-service mechanical damage) that maintains the strength of the machining damage above some minimum requirement.

Finally it is noted that the experiments in this study were restricted to one test material and only to the more severe of the two sets of cracks that have been identified in machining damage (Rice and Mecholsky 1979). On the basis of indentation studies, which have identified the existence of residual contact stresses in a wide range of brittle materials, the concepts developed in this paper would be expected to be widely applicable. However a tendency toward chipping in certain materials could cause a reduction in the residual fields. Kirchner and Isaacson (1982a) have identified the influence of residual crack opening stresses in strength measurements from single point machining damage in  $\text{Si}_3\text{N}_4$  and  $\text{Al}_2\text{O}_3$ , but not in glass and  $\text{SiC}$ . Further studies, utilizing sensitive methods for detection of residual stresses in other materials are needed. The influence of residual stresses on the second set of cracks, oriented normal to the machining direction, is not clear. The compressive layer must influence such cracks, but the existence of a residual crack opening force will depend on the degree of isolation of individual particle contacts along the grinding groove.

REFERENCES

- Anstis, G.R., Chantikul, P., Lawn, B.R. and Marshall, D.B. 1981.  
J. Amer. Ceram. Soc. 64, 533.
- Bansal, G.K. 1976. J. Am. Ceram. Soc. 59, 87.
- Bowles, R. 1979. in The Science of Ceramic Machining and Surface  
Finishing II (Eds. Hockey, B.J. and Rice, R.W.), National Bureau of  
Standards (U.S.) Special Technical Publication 562. p. 351.
- Budiansky, B. 1982. unpublished work.
- Chantikul, P., Anstis, G.R., Lawn, B.R. and Marshall, D.B. 1981.  
J. Amer. Ceram. Soc. 64, 539.
- Chiang, S.S., Marshall, D.B., and Evans, A.G. 1982. J. Appl. Phys. 53,  
298.
- Cook, R.F., Lawn, B.R. and Anstis, G.R. 1982. J. Mat. Sci. 17, 1108.
- Cook, R.F., Lawn, B.R., Dabbs, T.P. and Chantikul, P. 1981. J. Amer.  
Ceram. Soc. 64, c121.
- Evans, A.G., Gulden, M.E. and Rosenblatt, M. 1978. Proc. Roy. Soc.  
A361, 343.
- Gupta, P.K., and Jubb, N.J. 1981. J. Amer. Ceram. Soc. 64, c112.
- Hockey, B.J. 1971. J. Amer. Ceram. Soc. 54, 223.
- Hockey, B.J. and Lawn, B.R. 1975. J. Mat. Sci. 10, 1275.
- Khuri-Yakub, B.T., Kino, G.S. and Evans, A.G. 1980. J. Amer. Ceram.  
Soc. 63, 65.
- Kino, G.S. 1978. J. Appl. Phys. 49, 3190.
- Kirchner, H.P. and Isaacson, E.D. 1982a in Fracture Mechanics of  
Ceramics (eds. Bradt, R.C., Hasselman, D.P.H. and Lange, F.F.).  
New York: Plenum.

- Kirchner, H.P., and Isaacson, E.D. 1982b. J. Amer. Ceram. Soc. 65, 55.
- Lawn, B.R., Evans, A.G. and Marshall, D.B. 1980. J. Amer. Ceram. Soc. 63, 574.
- Lawn, B.R., Marshall, D.B. and Chantikul, P. 1981. J. Mat. Sci. 16, 1769.
- Marshall, D.B. 1982a. Progress in Nitrogen Ceramics. Proceedings of NATO Advanced Study Institute on Nitrogen Ceramics, Sussex, 198 (Ed. Riley, F.L.)
- Marshall, D.B. 1982b. J. Amer. Ceram. Soc., in press.
- Marshall, D.B. and Lawn, B.R. 1979. J. Mat. Sci. 14, 2001.
- Marshall, D.B. and Lawn, B.R. 1980. J. Amer. Ceram. Soc. 63, 532.
- Marshall, D.B., Lawn, B.R. and Chantikul, P. 1979. J. Mat. Sci. 14, 2225.
- Mecholsky, J.J., Freiman, S.W. and Rice, R.W. 1977. J. Amer. Ceram. Soc. 60 114.
- Rice, R.W. and Mecholsky, J.J. 1979. in the Science of Ceramic Machining and Surface Finishing II. (Eds. Hockey, B.J. and Rice, R.W.) National Bureau of Standards (U.S.) Special Technical Publication 562, p. 351.
- Tien, J.J.W., Khuri-Yakub, B.T., Kino, G.S., Evans, A.G. and Marshall, D.B. 1982. J. Non. Destructive Testing, in press.

TABLE 1. STRENGTHS OF SURFACE-DAMAGED  $\text{Si}_3\text{N}_4$ .

Strength- Controlling Damage \ Surface Preparation	Polishing	Longitudinal Machining	Transverse Machining
Single Indentation (50N Knoop)	$240 \pm 5$ MPa	290	
Row of Indentations (10N Knoop)	$310 \pm 14$	$464 \pm 40$	$523 \pm 10$
Scratch (5N Knoop)	$247 \pm 19$	$312 \pm 11$	$330 \pm 10$

TABLE 2. EXTENT OF STABLE CRACK GROWTH DURING FAILURE,  $c_m/c_o$ .

Strength-Controlling Damage \ Surface Preparation	Polishing	Longitudinal Machining	Transverse Machining
Single Indentation (50N Knoop)	$2.4 \pm 0.1$	2.1	
Row of Indentations (10N Knoop)	$5.2 \pm 0.8$		
Scratch (5N Knoop)	$5.5 \pm 0.6$	$4.4 \pm 0.2$	$4.3 \pm 0.5$
Machining Damage	$5.0 \pm 0.2$		

FIGURE CAPTIONS

1. (a) Vickers indentation in ZnS.  
(b) Schematic cross section of indentation, showing deformation zone and fractures.
2. The acoustic scattering and mechanical loading configurations used for monitoring crack growth during failure testing:  $A_0$  = amplitude of wave excited by transducer 1,  $A_1$  = amplitude of scattered wave received by transducer 2,  $F$  = applied bending force.
3. Variation of acoustic scattering, from indentation cracks in polished surfaces of  $\text{Si}_3\text{N}_4$ , during tensile loading.
  - (a) Stress-free crack. Note reversible increase in acoustic scattering (expressed as crack length calculated for an open half-penny surface crack) with applied tension.
  - (b) Knoop indentation crack (50N load). Note irreversible increase in acoustic scattering.
  - (c) Knoop indentation crack (50N load): comparison of acoustic measurements, in-situ optical measurements, and fracture mechanics prediction of the variation of crack length with applied tension.
4. Variation of acoustic scattering with applied tension for Knoop indentation (50N load) in a machined surface of  $\text{Si}_3\text{N}_4$ .
5. Variation of acoustic scattering with applied tension:
  - (a) for a scratch in a polished surface of  $\text{Si}_3\text{N}_4$  (5N normal load on Knoop indenter)
  - (b) for the strength-controlling flaw in a machined surface of  $\text{Si}_3\text{N}_4$ .



6. Fracture surfaces in  $\text{Si}_3\text{N}_4$  (width of field 830  $\mu\text{m}$ ):
  - (a) Knoop indentation (50N load) in a polished surface (specimen tested in Fig. 3b).
  - (b) Knoop indentation (50N load) in a machined surface (specimen tested in Fig. 4).
7. Fracture surfaces resulting from linear damage configurations in  $\text{Si}_3\text{N}_4$ :
  - (a) Row of Knoop indentations (50N load) on polished surface.  
Width of field 2.8 mm.
  - (b) Scratch (5N normal load on Knoop indenter) on polished surface (specimen tested in Fig. 5a). Width of field 1.1 mm.
  - (c) Machining damage (specimen tested in Fig. 5b). Width of field 0.97 mm.
8. Schematic representation of the crack configurations generated by linear damage processes (row of indentations, scratching, or machining) and the crack front at failure.
9. Residual stresses in contact damage:
  - (a) Isolated grinding groove (or indentation): residual pressure  $p$  at the boundary of the plastic zone creates compression adjacent to the zone and tension on median planes beneath the zone.
  - (b) Machined surface: compressive layer due to overlap of neighboring residual fields negates the upper portion of the outward acting pressure from the strength controlling (i.e., deepest) groove, thus reducing the residual crack opening force  $P_r$ .

10. Plot of measured strengths of  $\text{Si}_3\text{N}_4$  as a function of the crack dimensions at failure (measured by post-failure fractography), for a variety of damage configurations and prior surface preparations (P = polished, L = longitudinally machined, T = transversely machined).

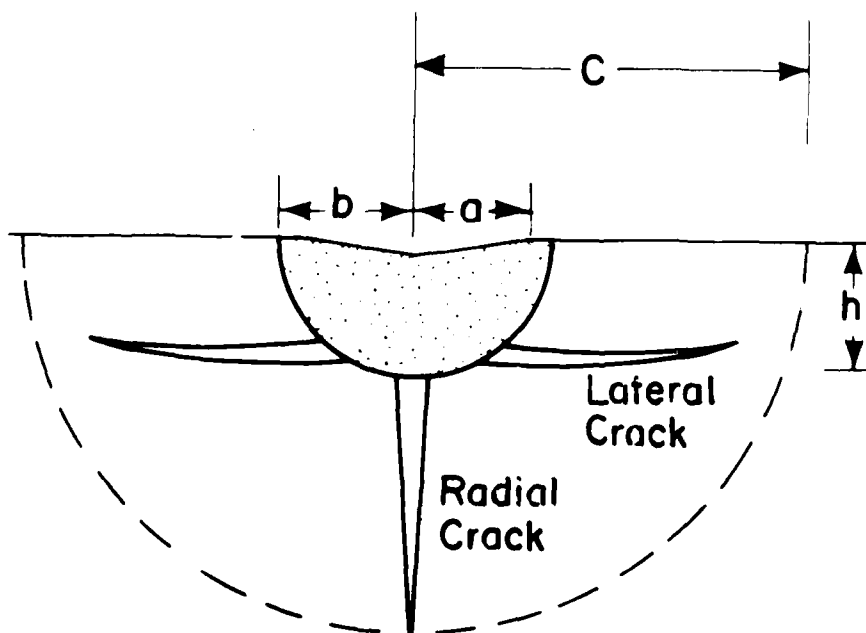
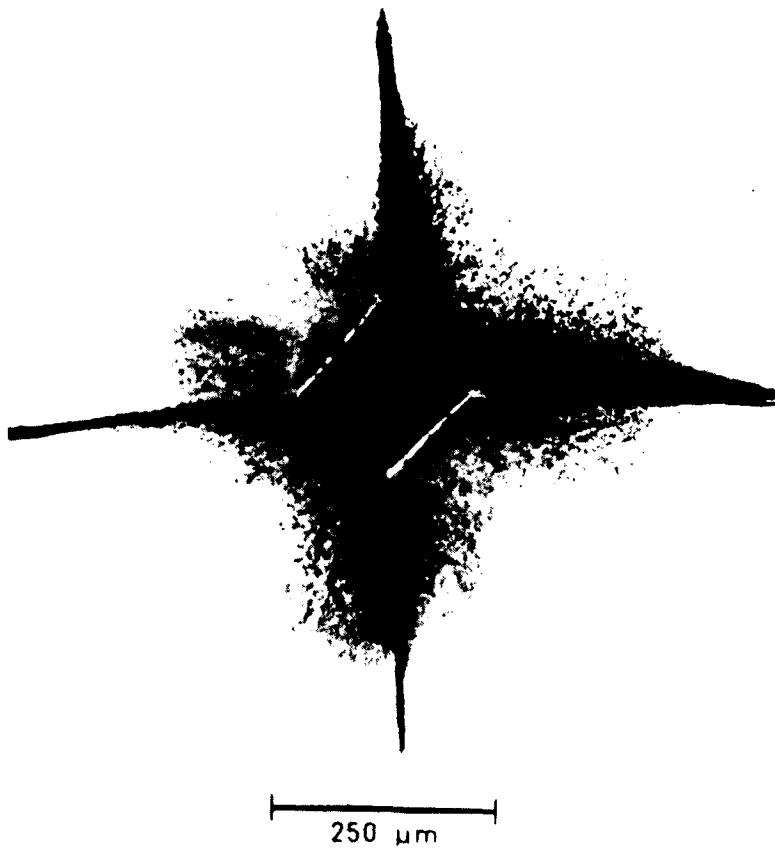
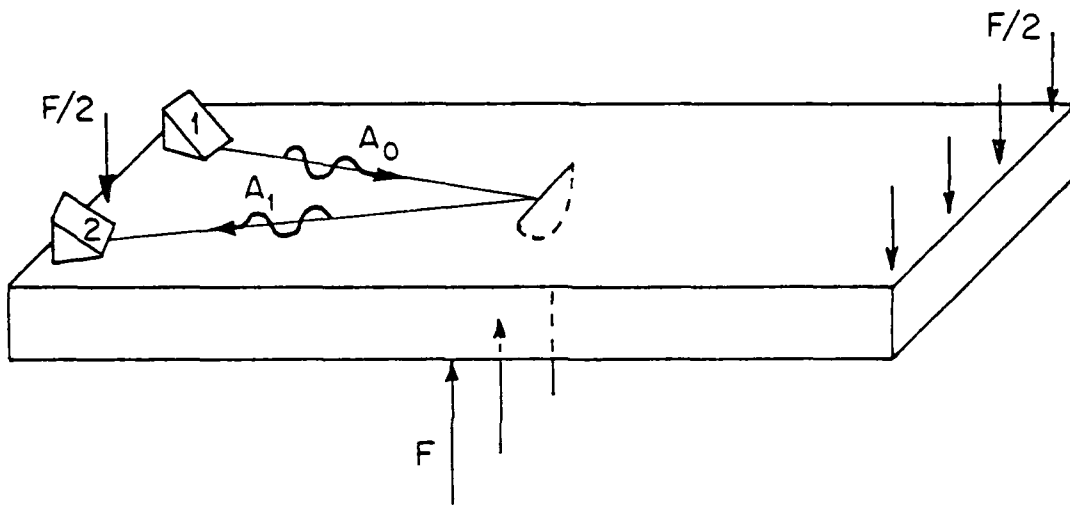
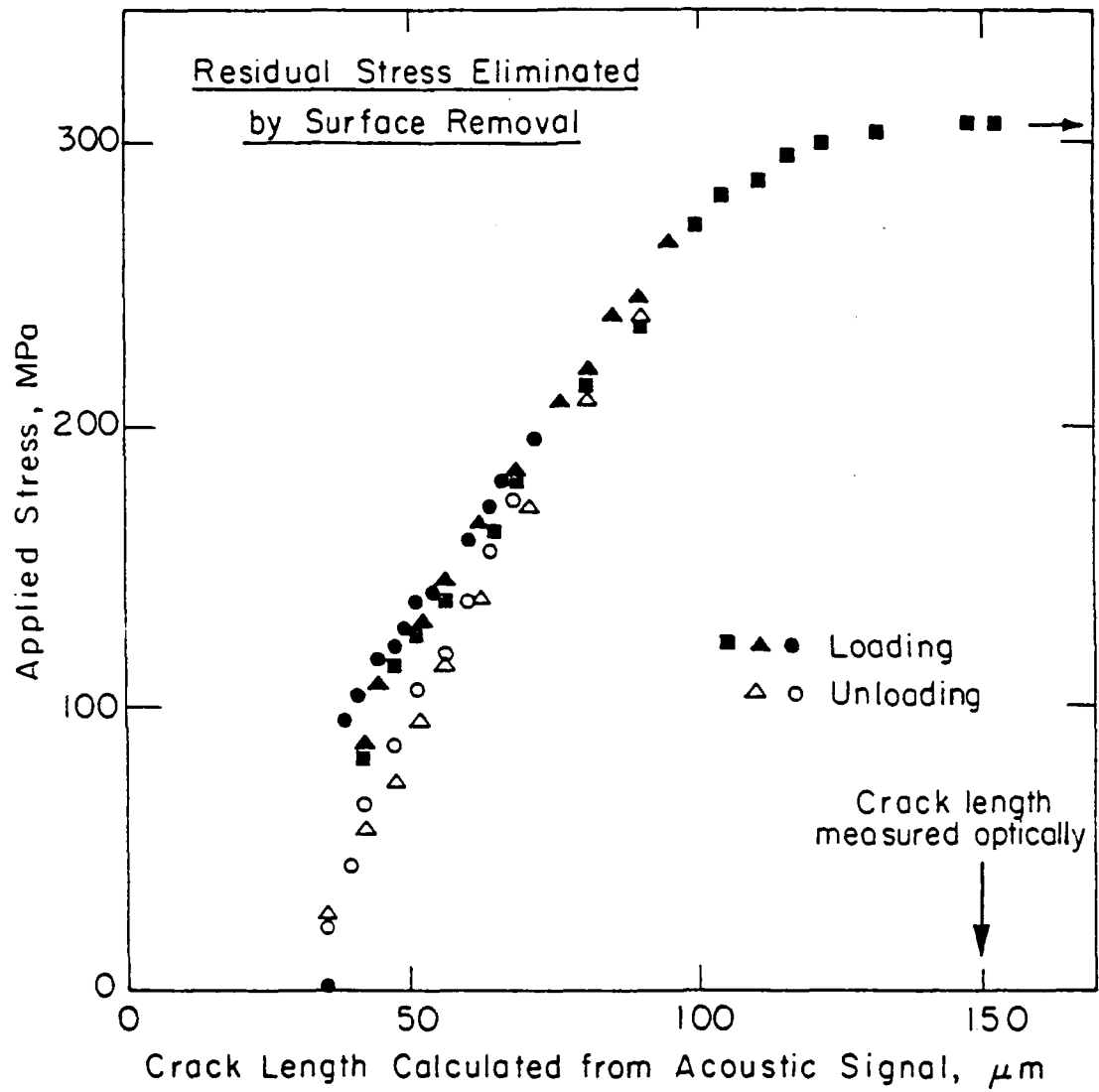


Fig. 1



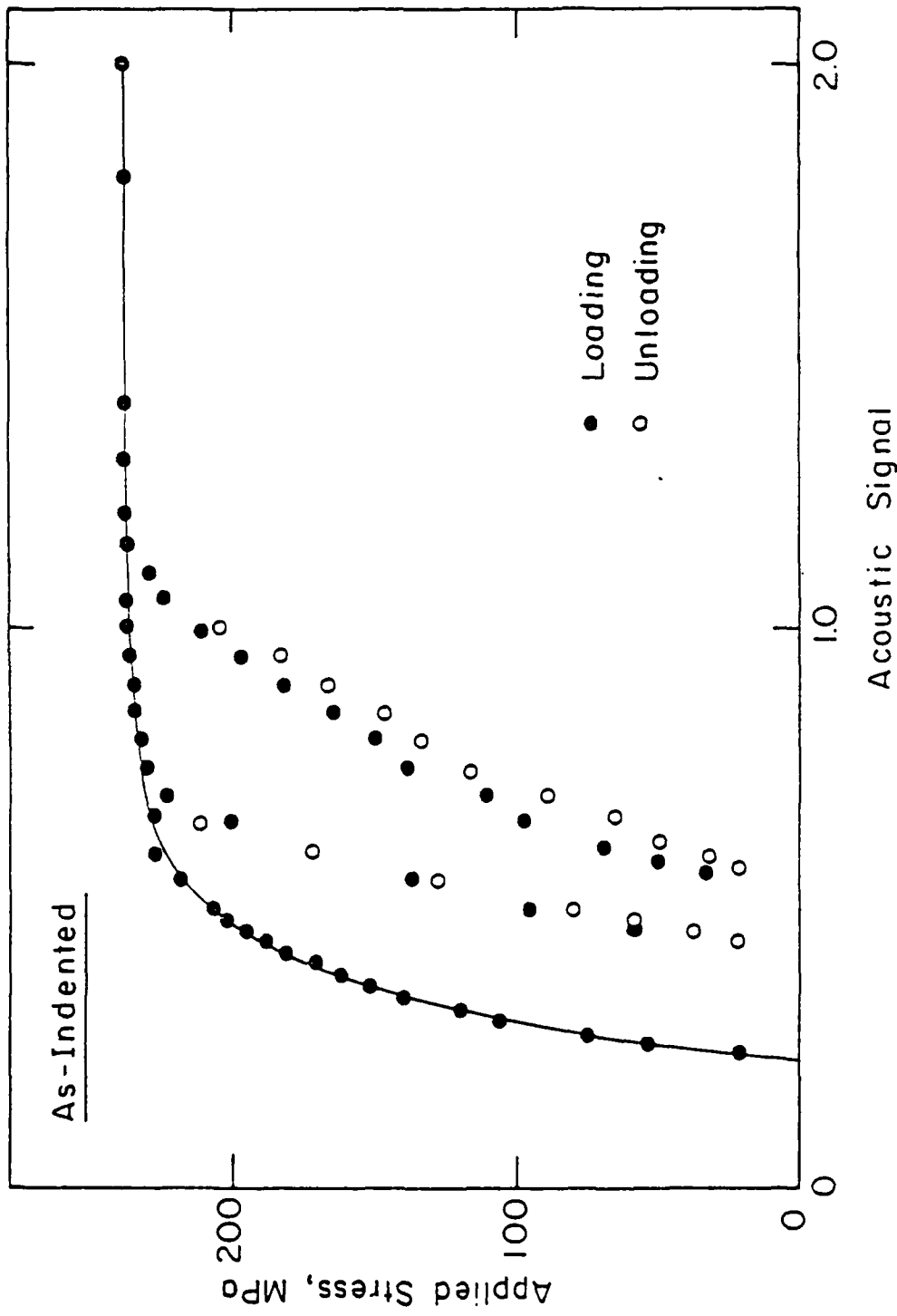
XBL 826-5934

Fig. 2



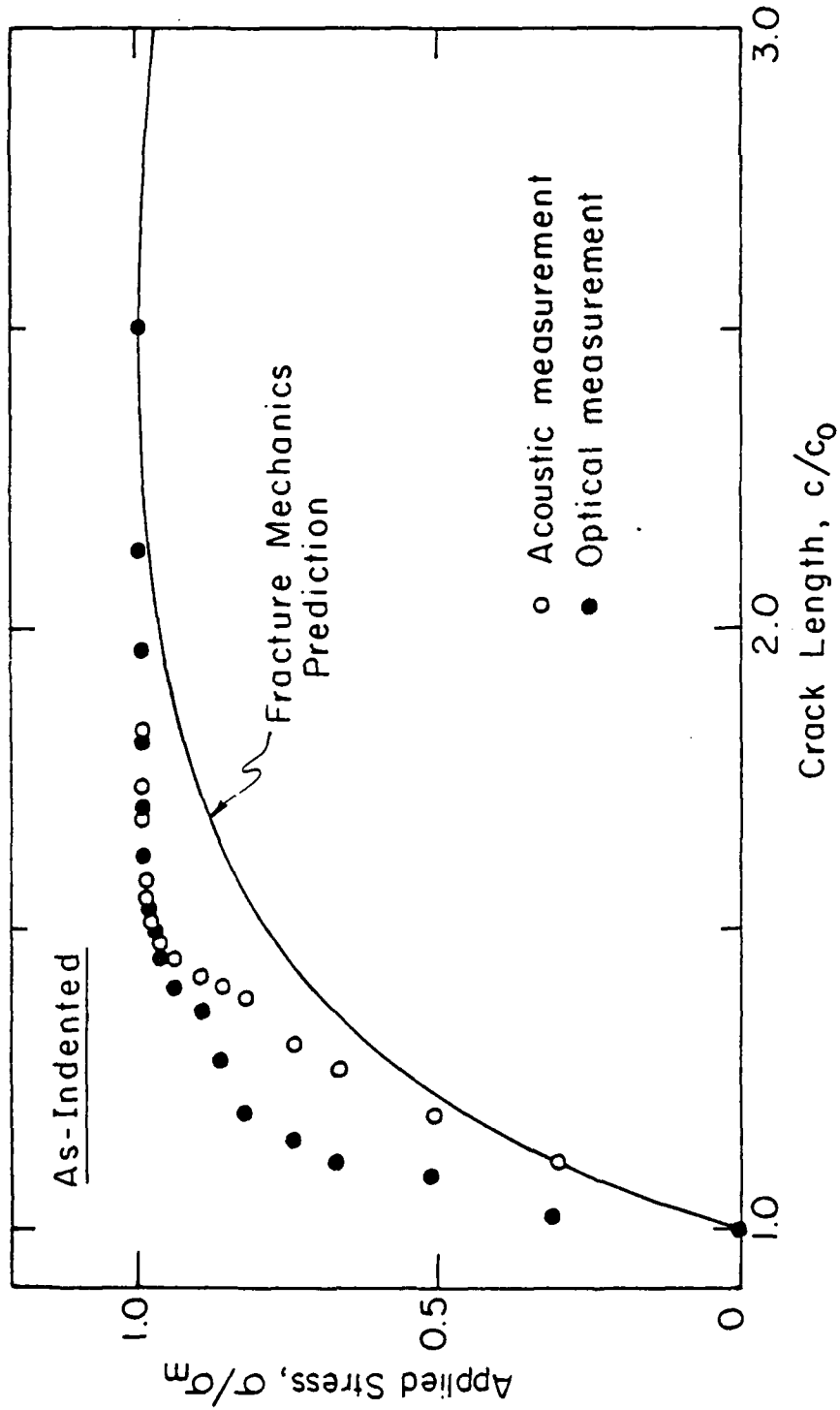
XBL 814-5614

Fig. 3a



XBL 814-5615

Fig. 3b



XBL 814-5616

Fig. 3c

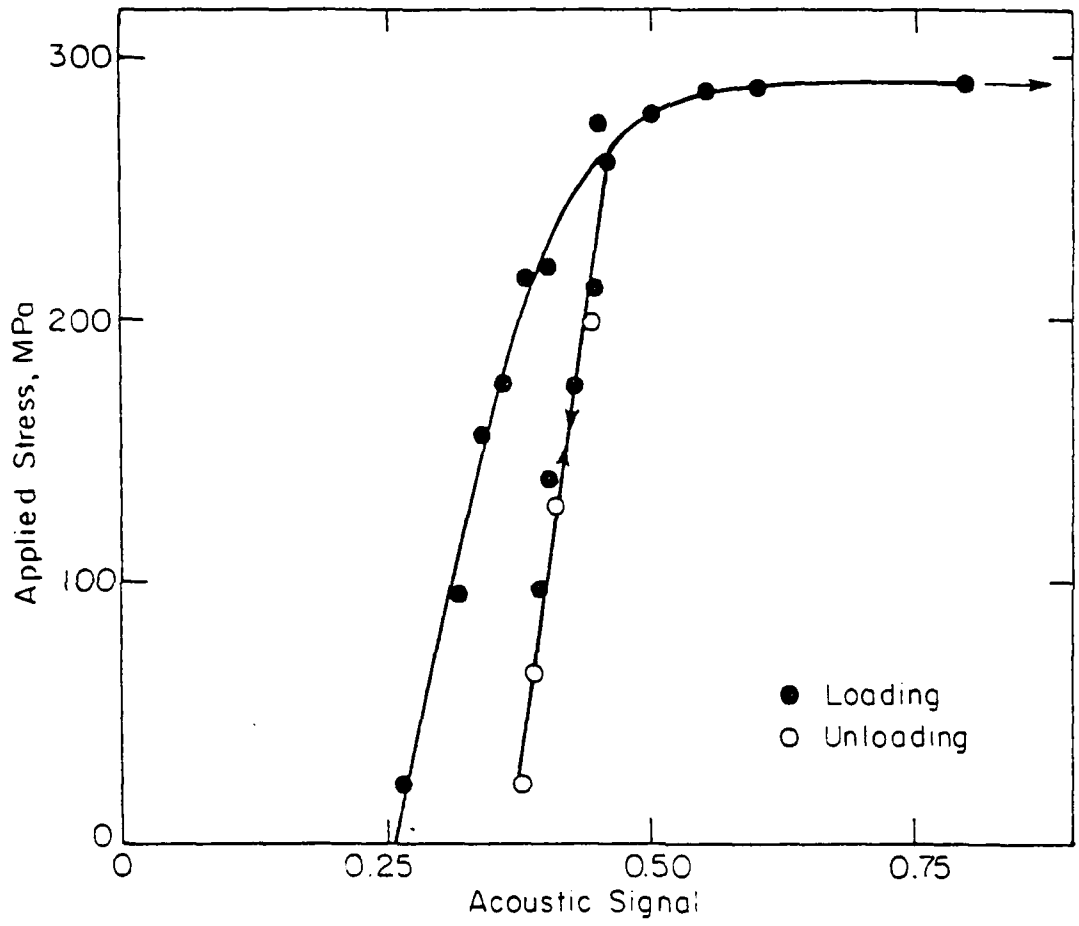
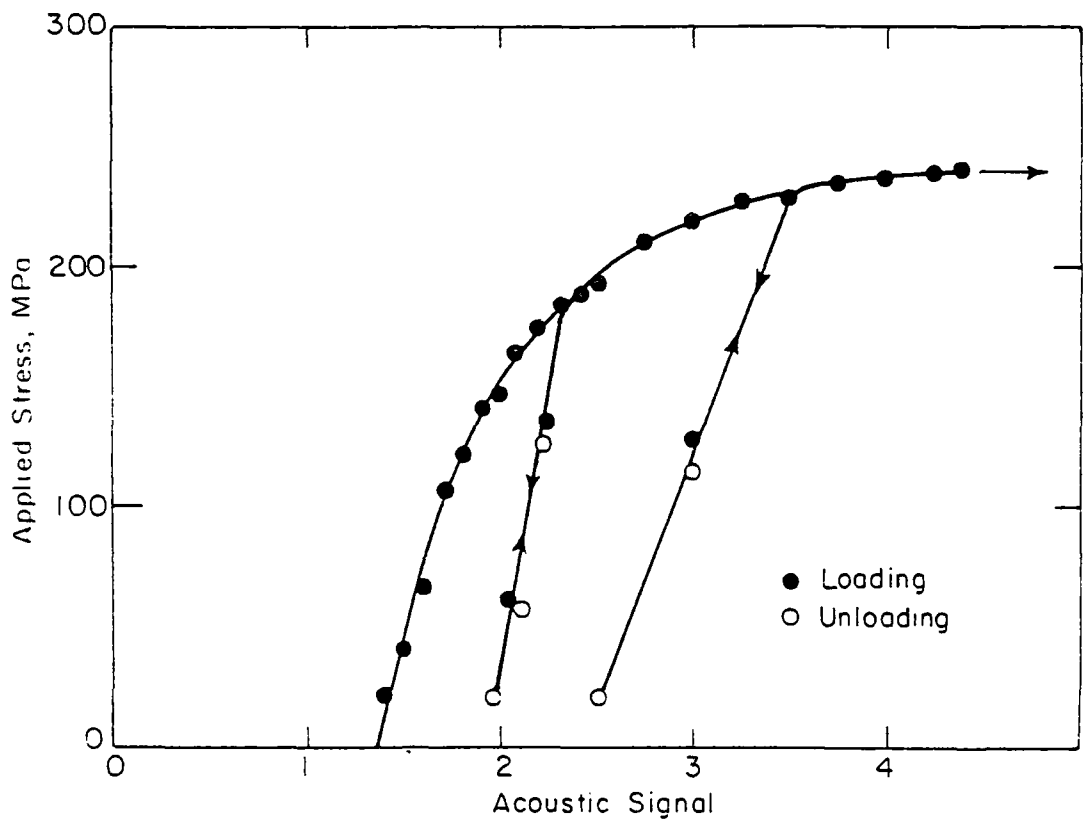


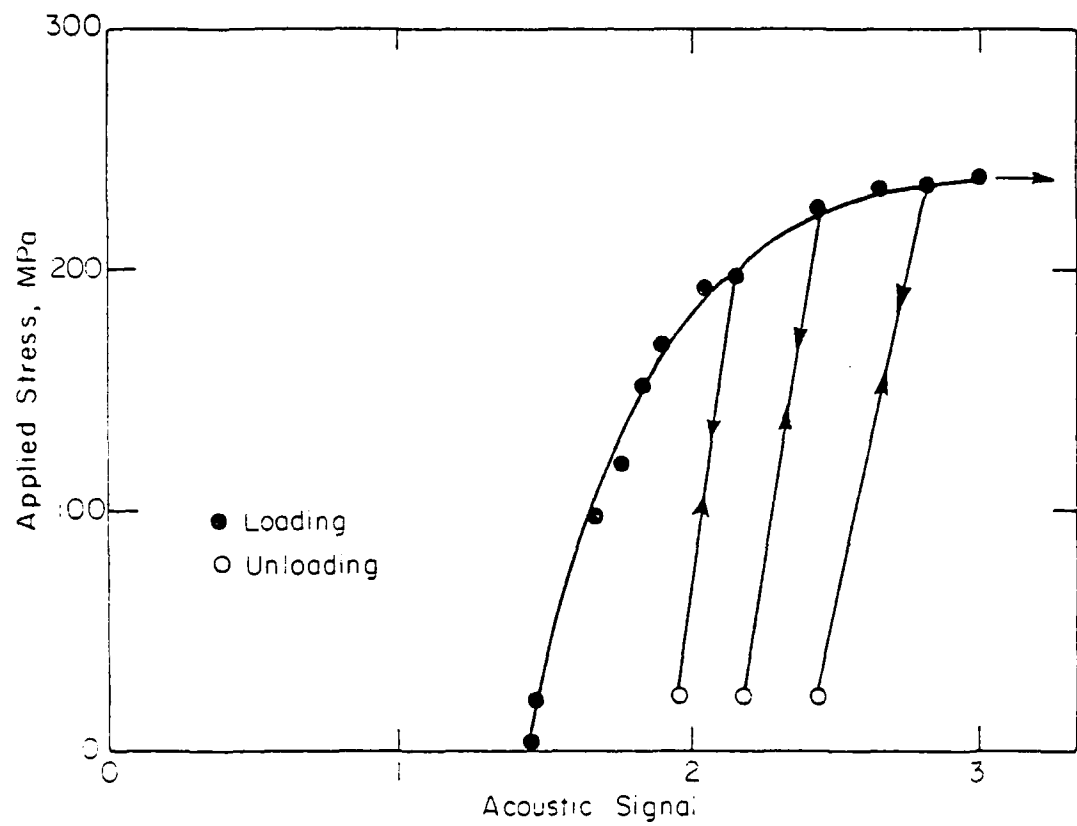
Fig. 4





XBL826-5936

Fig. 5a



XBL 826-5937

Fig. 5b

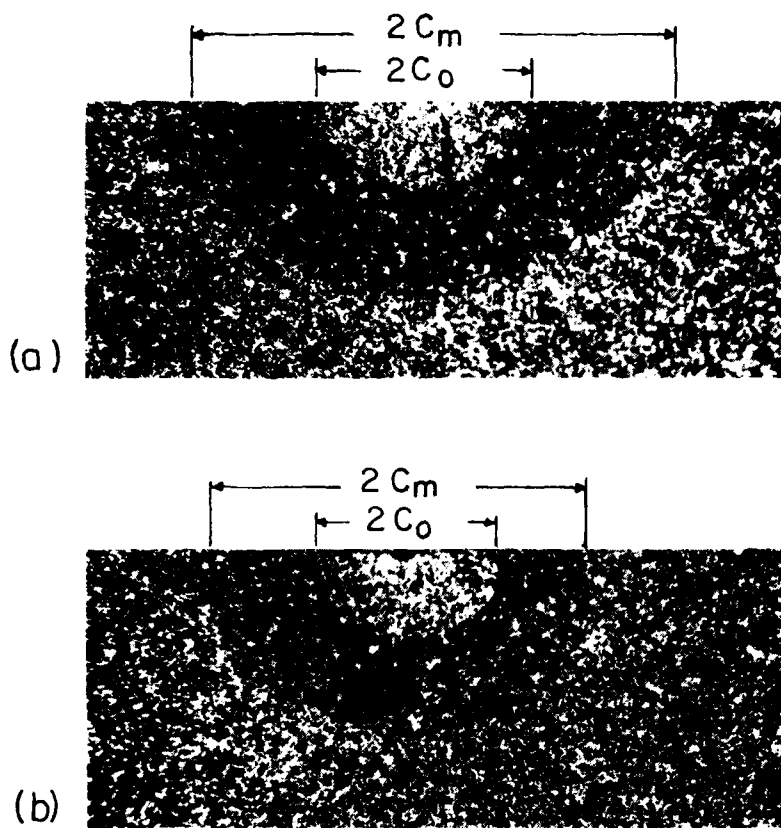


Fig. 6

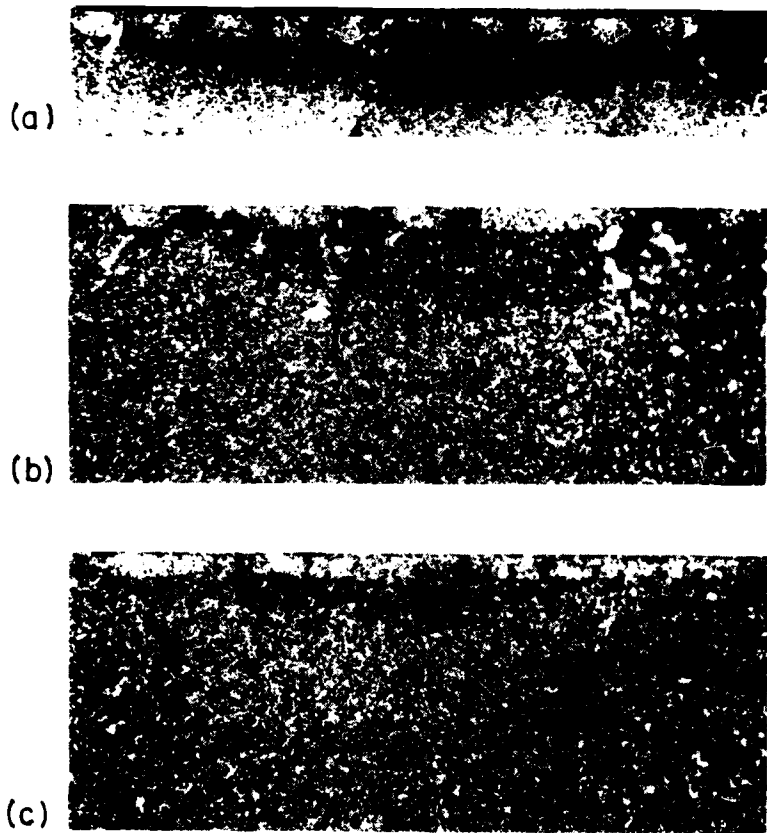
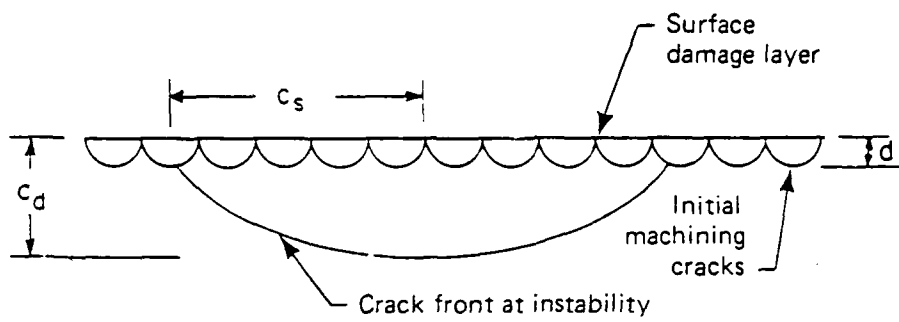
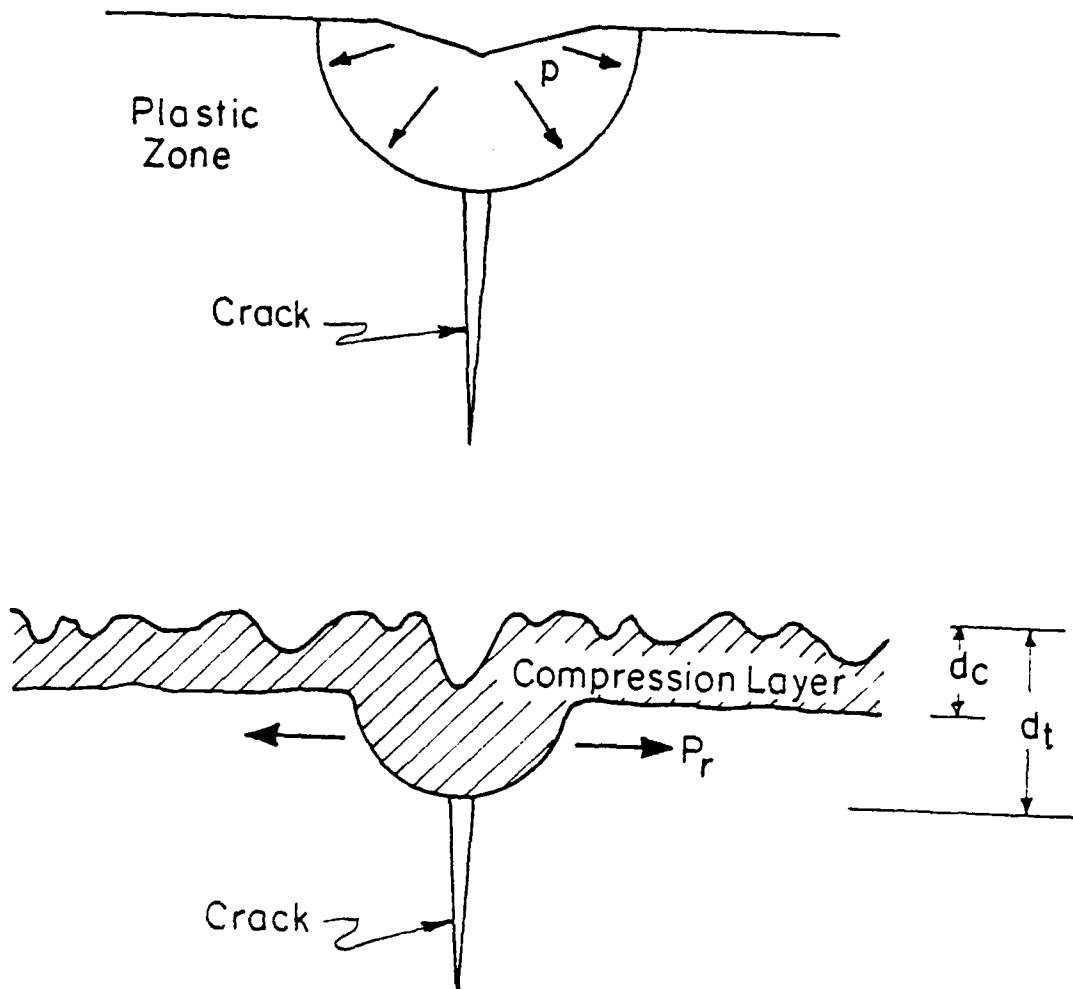


Fig. 7



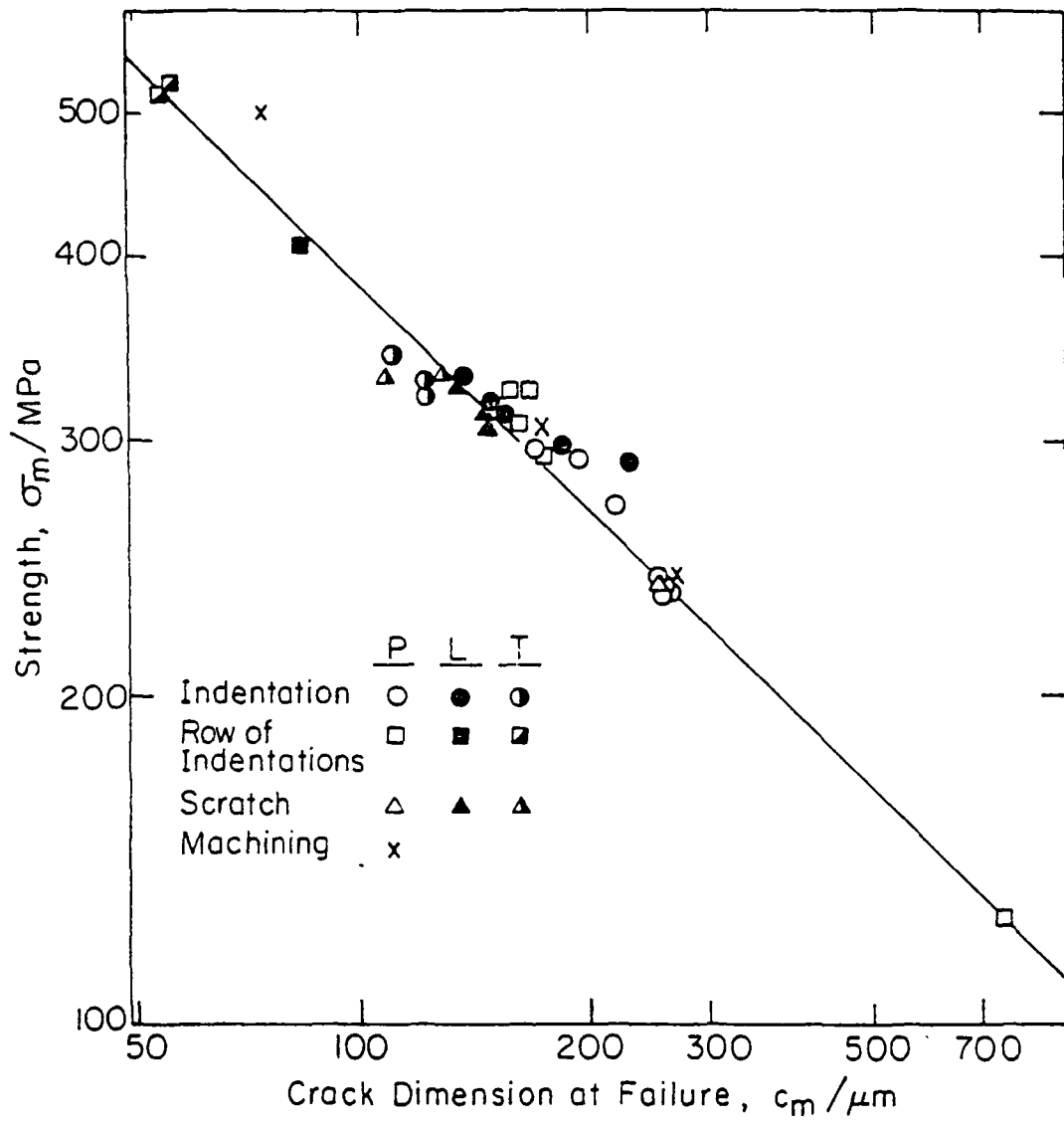
XBL 819-1882

Fig. 8



XBL 826-5938

Fig. 9



XBL 824-5591A

Fig. 10

-221-

CHAPTER VII

CONTROLLED FLAWS IN CERAMICS

by

D. B. Marshall

Department of Materials Science and Mineral Engineering  
University of California  
Berkeley, CA 94720



CONTROLLED FLAWS IN CERAMICS:  
A COMPARISON OF KNOOP AND VICKERS INDENTATION

D. B. Marshall

Department of Materials Science and Mineral Engineering  
University of California, Berkeley, CA 94720

ABSTRACT

Application of indentation fracture analysis to Knoop and Vickers indentation is examined, with particular emphasis on determining the limitations of the point force representation for the residual stress field. Deviation from the point force approximation is insignificant for crack-size/plastic-zone-size ratios  $\geq 1.3$ . The Vickers deformation/fracture configuration in brittle materials invariably conforms to this requirement, whereas the Knoop configuration does not (except at very high indentation loads). However, stable crack growth during a failure test extends the crack sufficiently that the strength degradation for both types of indentation is well described by the point force approximation.

## I. INTRODUCTION

Indentation fracture is now established as an important technique for studying the mechanical properties of ceramics. In its most basic application, controlled indentation provides a means of introducing cracks of predetermined size and shape into ceramic surfaces, thereby allowing some of the uncertainty associated with flaw statistics to be eliminated in fracture testing.<sup>1-4</sup> More important applications stem from recent analysis of elastic/plastic indentation fracture,<sup>5-8</sup> which has enabled the development of models for mechanical surface damage<sup>9,10</sup> (strength degradation, erosion, and wear) and provided a basis for the use of controlled indentation for measurement of material properties (toughness,<sup>11-13</sup> hardness, fatigue parameters<sup>14-18</sup>) and surface stress states.<sup>19</sup>

The indentation analysis is based on the observation that a residual stress, which results from mismatch between the plastic zone beneath the indentation and the surrounding elastic matrix, dominates both the evolution of the cracks during contact and the response of the cracks to an applied tension during a subsequent breaking test.<sup>5</sup> Incorporation of the residual stress into the fracture mechanics analysis has led to prediction of some previously unexpected effects in several areas of study: in inert strength testing stable crack extension precedes failure;<sup>5</sup> in fatigue testing the apparent crack velocity parameters are modified;<sup>14-17</sup> and in fractographic mirror analysis, the mirror-to-flaw size ratio is influenced by the residual stress.<sup>20</sup>

Experimental verification of the analysis has been obtained by Vickers indentation on ceramic materials representing a wide variation of material properties. The Vickers geometry is convenient for crack size measurements because well-defined radial cracks<sup>†</sup> intersect the surface well beyond the central deformation zone (Fig. 1a). Moreover, the deformation/fracture geometry appears to conform to the main simplifying assumption of the analysis, namely that the plastic deformation beneath the indentation be sufficiently localized that the residual stress can be treated as a point force located at the center of the crack. However, for certain applications of controlled flaws, the existence of two intersecting radial cracks in the Vickers configuration presents a complication,<sup>††</sup> and the elongated Knoop indenter (which generates a single semicircular radial crack) would appear to be more suitable. Application of Knoop indentation is currently limited by the unknown influence of the elongated indenter geometry on the fracture analysis; the plastic zone extends over most, or all, of the surface trace of the radial crack, and may present a departure from point loading of the residual field. The purpose of the present paper is to investigate the influence of such departures from point loading on the fracture analysis.

---

<sup>†</sup>In this paper the term radial crack is used to refer to the half-penny cracks which develop on planes parallel to the indentation axis. These cracks are sometimes referred to as "median/radial" or "median" cracks.

<sup>††</sup>The Vickers cracks are better described as quarter pennies rather than half pennies, and this introduces some uncertainty into the geometrical factor in the stress intensity factor solutions. Also, in certain applications such as investigation of mixed-mode fracture,<sup>3</sup> and analysis of scattering of acoustic waves from cracks for non-destructive evaluation,<sup>21</sup> the second crack in the Vickers configuration interferes directly with the desired measurement.

## II. FRACTURE MECHANICS

In situ observations of radial crack evolution during Vickers indentation in transparent materials have shown that the final crack configuration is achieved as the indenter is removed from the surface,<sup>5,7</sup> thus establishing that the driving force for crack growth is provided by a residual stress field. Moreover, the residual stress remains after the indenter is removed, and supplements the applied loading during a subsequent breaking test. The existence of a post-indentation crack opening force is readily demonstrated. For example, continued subcritical extension of indentation cracks occurs after indenter removal in materials that are susceptible to environmentally assisted slow crack growth.<sup>11,18</sup>

### (1) Residual Stress Intensity Factor and Indentation Crack Length

Determination of the stress intensity factor  $K_I$  due to the residual field is central to any fracture mechanics analysis involving indentation cracks. The residual field may be evaluated in terms of an outward-acting pressure at the boundary of the plastic zone.<sup>7</sup> For approximately axisymmetric indenters, such as the Vickers pyramid, the plastic zone occupies an almost hemispherical volume centered beneath the indentation (Fig. 1a). If the crack dimension,  $c$ , is sufficiently large compared with the plastic zone radius,  $b$ , the pressure may be treated as a point force located at the crack center. Under this condition a straightforward solution for the stress intensity factor for the radial crack has been derived;<sup>5,7</sup>

$$K_r = \chi_r P / c^{3/2} \quad , \quad (1)$$

where  $P$  is the indenter load and  $\chi_r = \$(E/H)^{1/2}$ , with  $E$  and  $H$  the elastic modulus and hardness of the material and  $\$$  a dimensionless constant dependent only on indenter geometry.

The crack dimension,  $c_o$ , after indentation is obtained by equating  $K_r$  to the material toughness,  $K_c$ , in Eq. (1);

$$c_o = (\chi_r P / K_c)^{2/3} \quad . \quad (2)$$

The validity of Eq. (2) has been tested with Vickers indentation in a wide range of ceramic materials.<sup>11</sup> Minor systematic deviations from the predicted dependence on material properties exist, but the predicted load/crack-length relation ( $c_o \sim P^{2/3}$ ) is always closely followed for a given material, even to such apparently small ratios of crack size to indentation size as  $c_o/a \sim 2$ . Therefore, the point load approximation appears to be an appropriate choice for the axisymmetric case. However, for the Knoop configuration, (Fig. 1b) the elongated plastic zone extends over most of the surface trace of the crack, and it is not immediately apparent that the same approximation should apply.

## (2) Response of Cracks to Applied Tension

The mechanics of failure from radial cracks under the combined influences of the residual stress and a normal applied tension,  $\sigma_a$ , has been analyzed in detail.<sup>6,9,10,12</sup> The crack response is described by an applied-stress/equilibrium-crack-size function

$$\sigma_a = [K_c / \pi \Omega c]^{1/2} [1 - \chi_r P / K_c c^{3/2}] \quad , \quad (3)$$

(where  $\Omega$  is a crack geometry parameter) which results from superimposing the stress intensity factors  $K_r$  (from Eq. (1)) and  $K_a = \sigma_a(\pi\Omega c)^{1/2}$ , and setting  $K_r + K_a = K_c$  for equilibrium crack extension. The failure condition is defined by the maximum in the  $\sigma_a(c)$  function

$$c_m = (4\chi_r P/K_c)^{2/3} = 4^{2/3} c_o, \quad (4a)$$

$$\sigma_m = [27/256 K_c^4/\chi_r(\pi\Omega)^{3/2}]^{1/3} P^{-1/3} = 3K_c/4(\pi\Omega c_m)^{1/2}, \quad (4b)$$

and failure is preceded by stable equilibrium crack growth from  $c_o$  to  $c_m$ . This behavior contrasts with the response of ideal, stress free cracks, where crack instability is achieved at a critical applied stress level without precursor extension ( $\chi_r = 0$  in Eq. (3)). In situ observations of Vickers cracks during failure testing have demonstrated the existence of stable crack extension according to Eq. (3) in a wide variety of ceramic materials (glass,<sup>6</sup> silicon,<sup>22</sup> glass ceramics<sup>17</sup> and silicon nitride<sup>21</sup>), and extensive strength degradation measurements have confirmed the predicted dependence of strength on material properties and contact load<sup>12</sup> (Eq. (4b)), also for Vickers indentation.

For the purpose of comparing crack growth data from indenters of differing geometries it is convenient to normalize the crack length and stress parameters in Eq. (3). With  $C = c/c_m$  and  $S_a = \sigma_a/\sigma_m$ , Eq. (3) becomes

$$S_a = (4/3) C^{-1/2} [1 - 1/4 C^{3/2}] \quad (5)$$

Then all of the contact details (geometry and load) are incorporated into the normalizing factors, and the responses of cracks generated by differing indenters and loads are described by a single  $S(C)$  curve.

### III. EXPERIMENTAL OBSERVATIONS

Hot-pressed  $\text{Si}_3\text{N}_4^+$  was used as a test material for most experiments, both because of its potential importance as a structural ceramic and because of the absence of stress corrosion cracking at room temperature. However soda-lime glass was chosen for some preliminary observations of crack evolution, because of its transparency. The effects of subcritical crack extension in the glass were minimized by use of a relatively moisture-free oil environment.

#### (1) Preliminary Observations

Radial crack evolution in glass was observed by using an indentation device which allowed in situ microscopic viewing of the crack system through a polished face normal to the indented surface. The cracks invariably propagated to their final configuration upon unloading, thus confirming that crack evolution for both indenter configurations is dictated by the residual field. At loads above a threshold,  $P^*$ , cracks initiated during loading, as subsurface penny-shaped entities, and extended to the surface upon unloading. At peak loads below  $P^*$ , but higher than a second threshold  $P^+$ , crack initiation occurred during unloading, with further propagation to the final configuration as unloading continued. Both thresholds for Knoop indentation ( $P^* = 100\text{--}400\text{ N}$ ,  $P^+ \sim 20\text{--}40\text{ N}$ ) were significantly higher than for Vickers indentation ( $P^* = 50\text{--}150\text{ N}$ ,  $P^+ \sim 5\text{--}15\text{ N}$ ). Therefore, it may be concluded that crack initiation is generally more suppressed in Knoop than in Vickers indentation.

---

<sup>+</sup>Norton, NC132. See ref. 11 for mechanical properties.

(2) Crack Dimensions

The surface trace dimensions of radial cracks, generated by Knoop and Vickers indentation in  $\text{Si}_3\text{N}_4$ , are plotted as  $P/c^{3/2}$  versus indenter load in Fig. 2. The data for Vickers indentation fall along a horizontal line as predicted by Eq. (2). The Knoop indentation data also conform to Eq. (2) at high loads (or,  $c/a \geq 1.3$ ), but at low loads (or low  $c/a$ ) the crack length is larger than predicted by Eq. (2).

(3) Strength Degradation

The strength degradation data, plotted in Fig. 3, were obtained by indenting polished<sup>†</sup> bars (40 x 4 x 3 mm) of  $\text{Si}_3\text{N}_4$  (in the center of the largest face, with one crack oriented normal to the longest edge) and measuring the strength in four-point bending. Within the scatter of measurements, the data for both indenters conform to the prediction of Eq. (4b) over the load range tested. It is noted that, although only a small number of measurements are shown here for Vickers indentation, the strength/load relation of Eq. (4b) has been verified over a wider range of Vickers indentation loads in  $\text{Si}_3\text{N}_4$  during an earlier study.<sup>12</sup>

(4) Response of Radial Cracks to Applied Tension

Two techniques were used to observe the responses of Vickers and Knoop indentation cracks in  $\text{Si}_3\text{N}_4$  to an applied tension. The first involved direct, in situ observation of the radial crack surface trace during

---

<sup>†</sup>Recently, Cook et al.<sup>23</sup> have demonstrated that the strengths of indented ceramic surfaces can be sensitive to surface finish; a compressive residual stress is associated with the surface damage layer of a machined surface. All surfaces tested in this study were polished with 1  $\mu\text{m}$  diamond until most visible signs of machining damage were removed. Typical surfaces are shown in Fig. 4.



strength testing. The second involved placing regularly-spaced indentations along the longitudinal center-line of the tensile surface of a flexure specimen, such that failure occurred from an indentation within the central span. The remaining indentations then experienced an applied tension proportional to their distance from the outer loading points and extended stably, without failure. The second method was experimentally more straightforward, but less effective at generating data very close to the failure point (even though several indentations which were included within the central span should have been stressed close to failure).

The responses of Vickers and Knoop indentation cracks are compared in Fig. 4. After increasing the applied loading to  $0.9 \sigma_m$ , a 30% increase in the crack length is evident for both indentations (Fig. 4a-b and d-e). The full extent of crack extension up to failure can be seen on the fracture surfaces<sup>+</sup> in Fig. 4c and f. In both cases the observed ratio  $c_m/c_0$  approaches the predicted value  $c_m/c_0 = 2.5$ . Crack length measurements as a function of applied tension are plotted in terms of normalized coordinates in Fig. 5. The data for Vickers and Knoop indentations, at two indentation loads, are indistinguishable, and agree reasonably well with the predicted crack extension (solid curve). Therefore, the assumed point loading of the residual field appears to provide a good description of crack propagation under an applied loading for both indenter geometries.

---

<sup>+</sup> Carefully controlled optical illumination conditions are required to make the fracture surface markings in Fig. 4c and f visible. The markings are most clearly observable using a stereomicroscope, with the fracture surface oriented at about  $70^\circ$  to the optical axis and the illumination set for specular reflection. The reason for the different reflectivities of the various regions of crack growth is not known, but the regions have been positively identified by direct comparison with surface trace measurements.

#### IV. DISCUSSION

The crack length measurements in Fig. 2 indicate that deviation from the point force representation of the residual field in the fracture mechanics analysis is significant only for  $c/a$  ratios less than about 1.3. The results in Fig. 2 can be compared with an upper-bound estimate of the deviation, obtained from the stress intensity factor for a half-penny crack subjected to a uniform residual pressure,  $\sigma_r$ , acting normal to the crack plane over a semicircular area of radius  $b$ . For Knoop indentation we take  $b=a$ , a configuration that would give exaggerated departure from point loading (Fig. 1b), and for Vickers indentation  $b = 1.2a$ .<sup>†</sup> The stress intensity factor is given by<sup>24</sup>

$$K_r^u = 2\sigma_r(c/\pi)^{1/2} \{1 - [1 - (b/c)^2]^{1/2}\} , \quad (6)$$

whereas the corresponding point force solution is obtained by allowing the same total force,  $P_r = \sigma_r \pi b^2/2$ , to be concentrated at the center of the crack,

$$K_r^p = 2P_r/(\pi c)^{3/2} = \sigma_r b^2/\pi^{1/2} c^{3/2} . \quad (7)$$

The relative deviation from point loading, defined by the ratio

$$K_r^u/K_r^p = 2(c/b)^2 \{1 - [1 - (b/c)^2]^{1/2}\} , \quad (8)$$

---

<sup>†</sup> Direct measurement of the plastic zone size in  $\text{Si}_3\text{N}_4$  is not available. The value  $b/a = 1.2$  was calculated for  $\text{Si}_3\text{N}_4$  in Ref. 25.

is plotted as the full curve in Fig. 6, with the horizontal broken line representing the point force solution. The experimental data in Fig. 6 were obtained by converting the crack length measurements from Fig. 2 to stress intensity factors. As expected, Eq. (8) represents an over-estimate of the deviation from point loading.

The data and calculation plotted in Fig. 6 are consistent with the observation that Vickers indentation cracks in ceramic materials are usually well described by Eq. (2);<sup>11</sup> the lowest values of  $c/b$  for these materials, even at loads approaching the initiation threshold, are about 1.5 - 2.0, well above the range where deviation from the point force approximation is significant. However, an apparent, minor deviation from the load/crack-length relation of Eq. (2) has been noted in several studies,<sup>13,26</sup> where indentation data for many materials were plotted together on a universal curve. The plot of Fig. 6 reaffirms a previous claim<sup>27</sup> that these deviations are due to an undetermined material dependence in the parameter  $\chi_r$ , rather than to any systematic variation with the  $c/a$  ratio.

The relative levels of residual crack driving force for Knoop and Vickers indentation (as characterized by the parameter  $\chi_r$ ) can be inferred from Figs. 2 and 3. From Eq. (2), in conjunction with values of  $P/c^{3/2}$  calibrated from the crack length data in Fig. 2 (horizontal curves) we obtain  $(\chi_r)_v/(\chi_r)_k = 0.71 \pm 0.04$ , where the subscripts  $v$  and  $k$  refer to Vickers and Knoop. Similarly, the strength data of Fig. 3 in conjunction with Eq. (4b) give  $(\chi_r)_v/(\chi_r)_k = 0.7 \pm 0.2$ . The relative levels of residual stress evaluated from the strength and

crack length measurements are thus in mutual agreement. Moreover, they both agree well with the result of an approximate calculation,  $(\chi_r)_v/(\chi_r)_k = 0.72$ , which takes into account both the relative volumes of Knoop and Vickers indentations (at given load) and the different shapes of the plastic zones (Appendix A).

V. CONCLUSIONS

The indentation fracture analysis based on a point force representation for the residual stress field, provides an adequate description of cracking by Knoop indentation provided the ratio  $c/a$  is larger than about 1.3. Cracks satisfying that condition result from indentation loads above about 100 N in  $\text{Si}_3\text{N}_4$ , but in general the range of validity will vary with the material properties  $E$ ,  $H$  and  $K_{\text{IC}}$ . Therefore, the Vickers indentation, which satisfies the condition more generally, is better suited than the Knoop for toughness determinations using crack length measurements in conjunction with Eq. (2).<sup>11</sup> Similar restriction of the range of useable indentation loads does not appear in the failure analysis; stable crack extension from  $c_0$  to  $c_m$  during a breaking test increases the  $c/a$  ratio sufficiently that, at failure, the point loading analysis appears to hold for all Knoop indentation loads above the cracking threshold. In this regard it is worth noting that even in fatigue studies (e.g., lifetime evaluation), the time to failure is determined by crack propagation at  $c \approx c_m$  (in contrast to the case for ideal stress-free flaws where the region  $c \sim c_0$  dominates). Therefore in strength testing of ceramics, under both inert and fatigue conditions, the Knoop indentation should serve as well as the Vickers as a source of controlled flaws, with the advantage for certain applications that only one crack is generated.

ACKNOWLEDGMENTS

Funding was supplied by the Director, Office of Energy Research, Office of Basic Energy Sciences, Materials Science Division of the U.S. Department of Energy under Contract No. W-7405-ENG-48 and by the U.S. Office of Naval Research, Contract No. N00014-81-K-0362. The author thanks A.G. Evans and B. R. Lawn for comments on the manuscript.

Appendix: Relative Values of  $\chi_r$  for Knoop and Vickers Indenters

The following analysis is based on the procedure used by Lawn, Evans and Marshall<sup>7</sup> to evaluate the residual stress intensity factor. The Knoop and Vickers indenters are related in two steps; in the first the Knoop is related to an "equivalent" square-based pyramidal indenter which displaces the same volume as the Knoop at given load, and in the second step the "equivalent" indenter is related to the Vickers indenter.

The residual stress parameter  $\chi_r$  is given by<sup>7</sup>

$$\chi_r \sim E(\delta V/V) A/P, \quad (A1)$$

where A is the cross-sectional area of the plastic zone, P is the indenter load,  $\delta V$  is the indentation volume, and V is the plastic zone volume. Chiang et al.<sup>25</sup> have shown that V is related uniquely to  $\delta V$ , independent of indenter geometry. Therefore the plastic zone volumes of the Knoop indenter and the equivalent indenter are equal. However, the cross-sectional areas of their plastic zones differ. Using subscripts v, k and e to refer to Vickers, Knoop and equivalent indenters, the relative values of  $\chi_r$  become

$$(\chi_r)_e / (\chi_r)_k = A_e / A_k. \quad (A2)$$

Assuming that the plastic zone of the Knoop indentation is one half of a prolate spheroid, with major and minor axes  $b_y$  and  $b_x$  related to the indentation dimensions  $a_y$  and  $a_x$  (Fig. A1) by  $b_x/b_y = a_x/a_y$ , geometrical evaluation of the cross-sectional areas gives the result

$$(\chi_r)_e / (\chi_r)_k = (\tan \theta_x / \tan \theta_y)^{1/3} = 0.52 , \quad (A3)$$

where  $2\theta_x = 130^\circ$  and  $2\theta_y = 172.5^\circ$  are the angles between opposite edges of the Knoop indenter. The analysis of Lawn, Evans and Marshall<sup>7</sup> provides the relation between the residual stress parameters of the Vickers and equivalent indenters,

$$(\chi_r)_v / (\chi_r)_e = [\cot \psi_v / \cot \psi_e]^{2/3} , \quad (A4)$$

where  $2\psi_v = 148^\circ$  and  $2\psi_e = 160^\circ$  are the angles between opposite edges of the indenters, the angle  $\psi_e$  being related to  $\theta_x$  and  $\theta_y$  by straightforward geometrical considerations

$$\tan^2 \psi_e = \tan \theta_x \tan \theta_y . \quad (A5)$$

Combining Eqs. A3, A4, and A5 yields the relative values of  $\chi_r$  for Vickers and Knoop indentation;

$$(\chi_r)_v / (\chi_r)_k = (\cot \psi_v / \cot \theta_x)^{2/3} = 0.72 . \quad (A6)$$



REFERENCES

1. B. R. Lawn and T. R. Wilshaw, "Indentation Fracture: Principles and Applications," J. Mater. Sci., 10, [6] 1049-1081 (1975).
2. J. J. Petrovic, L. A. Jacobson, P. K. Talty, and A. K. Vasudevan, "Controlled Surface Flaws in Hot Pressed  $\text{Si}_3\text{N}_4$ ," J. Am. Ceram. Soc., 58 [3-4] 113-116 (1975).
3. J. J. Petrovic, and M. G. Mendiratta, "Mixed Mode Fracture from Controlled Surface Flaws in Hot Pressed  $\text{Si}_3\text{N}_4$ ," J. Am. Ceram. Soc., 59 [3-4] 163-167 (1976).
4. T. P. Dabbs, D. B. Marshall and B. R. Lawn, "Flaw Generation by Indentation in Glass Fibers," J. Am. Ceram. Soc., 63 [3-4] 224-225 (1980).
5. D. B. Marshall and B. R. Lawn, "Residual Stress Effects in Sharp Contact Cracking: I," J. Mater. Sci., 14 [8] 2001-2012 (1979).
6. D. B. Marshall, B. R. Lawn, and P. Chantikul, "Residual Stress Effects in Sharp-Contact Cracking: II," J. Mater. Sci., [9] 2225-2235 (1979).
7. B. R. Lawn, A. G. Evans, and D. B. Marshall, "Elastic/Plastic Indentation Damage in Ceramics: The Median/Radial Crack System," J. Am. Ceram. Soc., 63 [9-10] 574-581 (1980).
8. B. R. Lawn, A. G. Evans, and D. B. Marshall, "Elastic/Plastic Indentation Damage in Ceramics; The Lateral Crack System," submitted to J. Amer. Ceram. Soc.
9. D. B. Marshall, in Progress in Nitrogen Ceramics, edited by F. L. Riley, Sijthoff and Noordhoff, in press.

10. B. R. Lawn, in Fracture Mechanics of Ceramics, Vol. 5. Edited by R. C. Bradt, D. P. H. Hasselman and F. F. Lange, Plenum, New York, in press.
11. G. R. Anstis, P. Chantikul, B. R. Lawn, and D. B. Marshall, "A Critical Evaluation of Indentation Techniques for Measuring Fracture Toughness: I, Direct Crack Measurements," J. Amer. Ceram. Soc., 64 [9] 533-538 (1981).
12. P. Chantikul, G. R. Anstis, B. R. Lawn, and D. B. Marshall, "A Critical Evaluation of Indentation Techniques for Measuring Fracture Toughness: II, Strength Method," J. Amer. Ceram. Soc., 64 [9] 539-43 (1981).
13. A. G. Evans and E. A. Charles, "Fracture Toughness Determinations by Indentation," J. Amer. Ceram. Soc., 59 [7-8] 371-72 (1976).
14. D. B. Marshall and B. R. Lawn, "Flaw Characteristics in Dynamic Fatigue: The Influence of Residual Contact Stresses," J. Amer. Ceram. Soc., 63 [9-10] 532-36 (1980).
15. P. Chantikul, B. R. Lawn, and D. B. Marshall, "Micromechanics of Flaw Growth in Static Fatigue: Influence of Residual Contact Stresses," J. Am. Ceram. Soc., 64 [6] 322-25 (1981).
16. B. R. Lawn, D. B. Marshall, G. R. Anstis, and T. P. Dabbs, "Fatigue Analysis of Brittle Materials Using Indentation Flaws: I. General Theory," submitted to J. Mat. Sci.
17. R. F. Cook, B. R. Lawn, and G. R. Anstis, "Fatigue Analysis of Brittle Materials Using Indentation Flaws: II. Case Study on a Glass Ceramic. Submitted to J. Mat. Sci.

18. P. K. Gupta and N. J. Jubb, "Post-Indentation Slow Growth of Radial Cracks in Glasses," J. Am. Ceram. Soc., 64 [8] C112-114 (1981).
19. D. B. Marshall and B. R. Lawn, "An Indentation Technique for Measuring Stresses in Tempered Glass Surfaces," J. Am. Ceram. Soc., 60 [1-2] 86-87 (1977).
20. D. B. Marshall, B. R. Lawn, and J. J. Mecholsky, "Effect of Residual Contact Stresses on Mirror/Flaw-Size Relations," J. Am. Ceram. Soc., 63 [5-6] 358-60 (1980).
21. J. J. W. Tien, B. T. Khuri-Yakub, G. S. Kino, D. B. Marshall, and A. G. Evans, "Surface Acoustic Wave Measurements of Surface Cracks in Ceramics," J. Non-Destructive Testing, in press.
22. B. R. Lawn, D. B. Marshall, and P. Chantikul, "Mechanics of Strength-Degrading Contact Flaws in Silicon," J. Mat. Sci., 16 [7] 1769-75 (1981).
23. R. F. Cook, B. R. Lawn, T. P. Dabbs and P. Chantikul, "Effect of machining damage on the strength of a glass ceramic," J. Amer. Ceram. Soc., 64 [9] C121-122 (1981).
24. G. C. Sih, "Handbook of Stress Intensity Factors," Lehigh University Press, Lehigh, 1973.
25. S. S. Chiang, D. B. Marshall and A. G. Evans, "The Response of Solids to Elastic/Plastic Indentation: I. Stresses and Residual Stresses," J. Appl. Phys., in press.

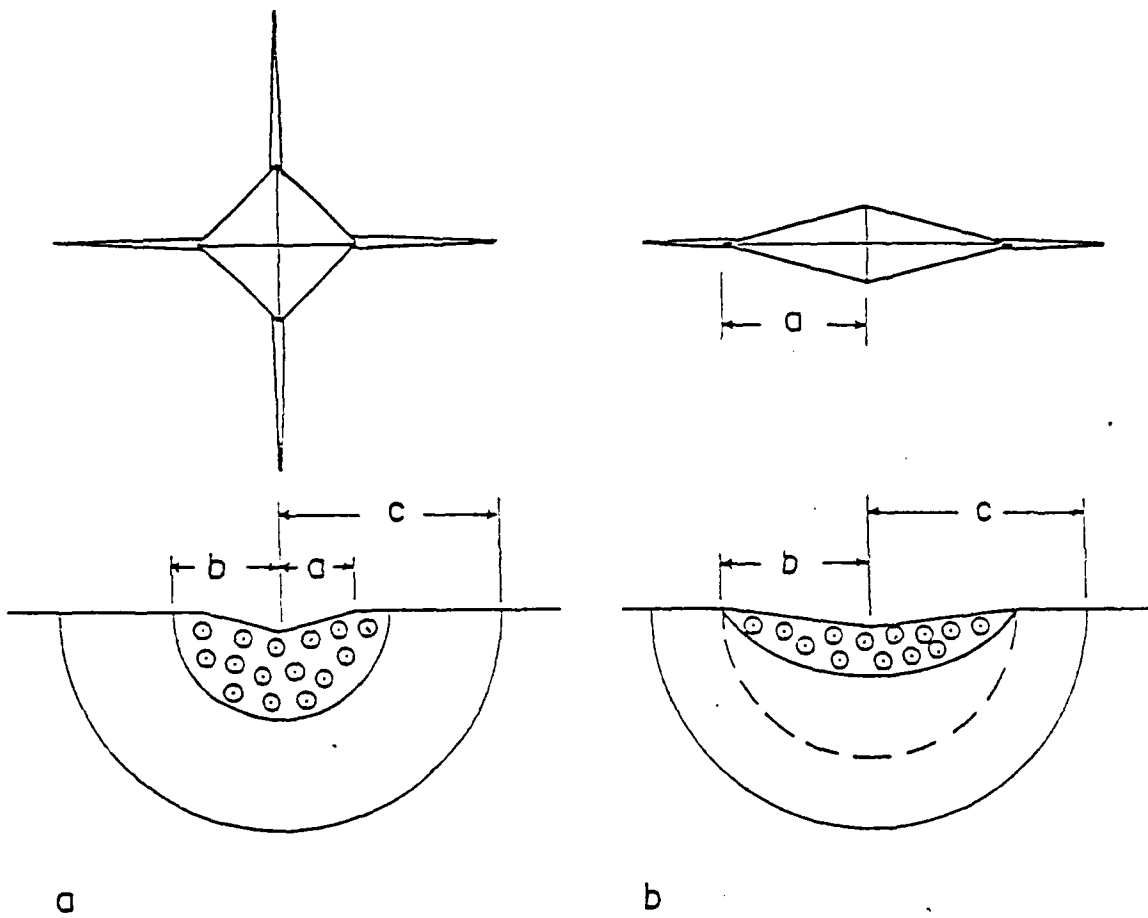
26. D. G. Bhat, Comment on "Elastic/Plastic Indentation Damage in Ceramics: The Median/Radial Crack System," J. Amer. Ceram. Soc. 64 [11] C165-166 (1981).
27. D. B. Marshall and A. G. Evans, "Reply to 'Comment on Elastic/Plastic Indentation Damage in Ceramics: The Median Radial Crack System'," J. Am. Ceram. Soc., in press.

FIGURE CAPTIONS

- Fig. 1. Surface (top) and cross-section (bottom) schematics of (a) Vickers and (b) Knoop indentations. Circled points within the plastic zone represent residual stresses acting normal to the crack plane which lies in the plane of the page. The lateral crack system is not shown.
- Fig. 2. Load/crack-length data for Vickers and Knoop indentation in  $\text{Si}_3\text{N}_4$ . Data points and error bars are mean and standard deviations of at least 8 measurements. Horizontal lines are representations of Eq. (2).
- Fig. 3. Strength degradation data for Vickers and Knoop indentation in  $\text{Si}_3\text{N}_4$ . Horizontal lines are representations of Eq. (4b).
- Fig. 4. Optical micrographs illustrating stable radial crack extension during breaking test; HP  $\text{Si}_3\text{N}_4$  bars indented with Vickers (a-c) or Knoop (d-f) indenters and stressed in bending. (a) and (d) surface views at the beginning of the breaking test, (b) and (e) at  $\sigma_a/\sigma_m = 0.9$ , (c) and (f) fracture surfaces after failure. Indenter load: 50 N for (a), (b), (d-f); 200 N for (c).
- Fig. 5. Surface trace measurements of radial crack extension during breaking test; HP  $\text{Si}_3\text{N}_4$  bars indented with Vickers or Knoop indenters and broken in bending.

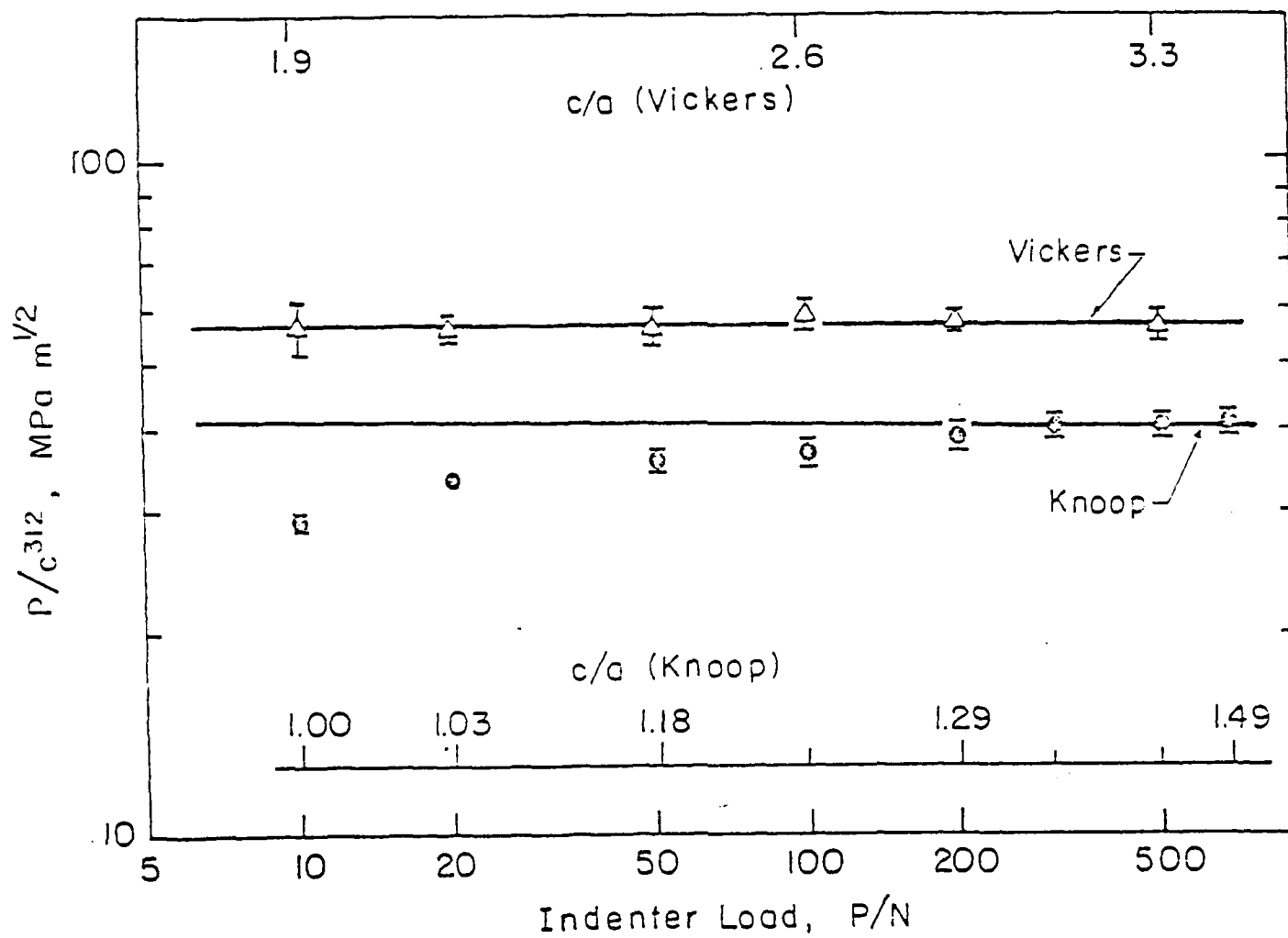
Fig. 6. Plot of an upper bound estimate of the relative deviation of the residual stress intensity factor from the point force representation.  $K_I^U$  is the stress intensity factor corresponding to a uniform distribution of the residual stress normal to the crack plane over the plastic zone;  $K_I^P$  is the corresponding stress intensity factor for the same total force concentrated at a point at the center of the crack. Data from crack length measurements of Fig. 2.

Fig. A1. Indentation and plastic zone dimensions for Knoop indentation, (a) surface view, (b) cross-section view.



XBL 8111-6982

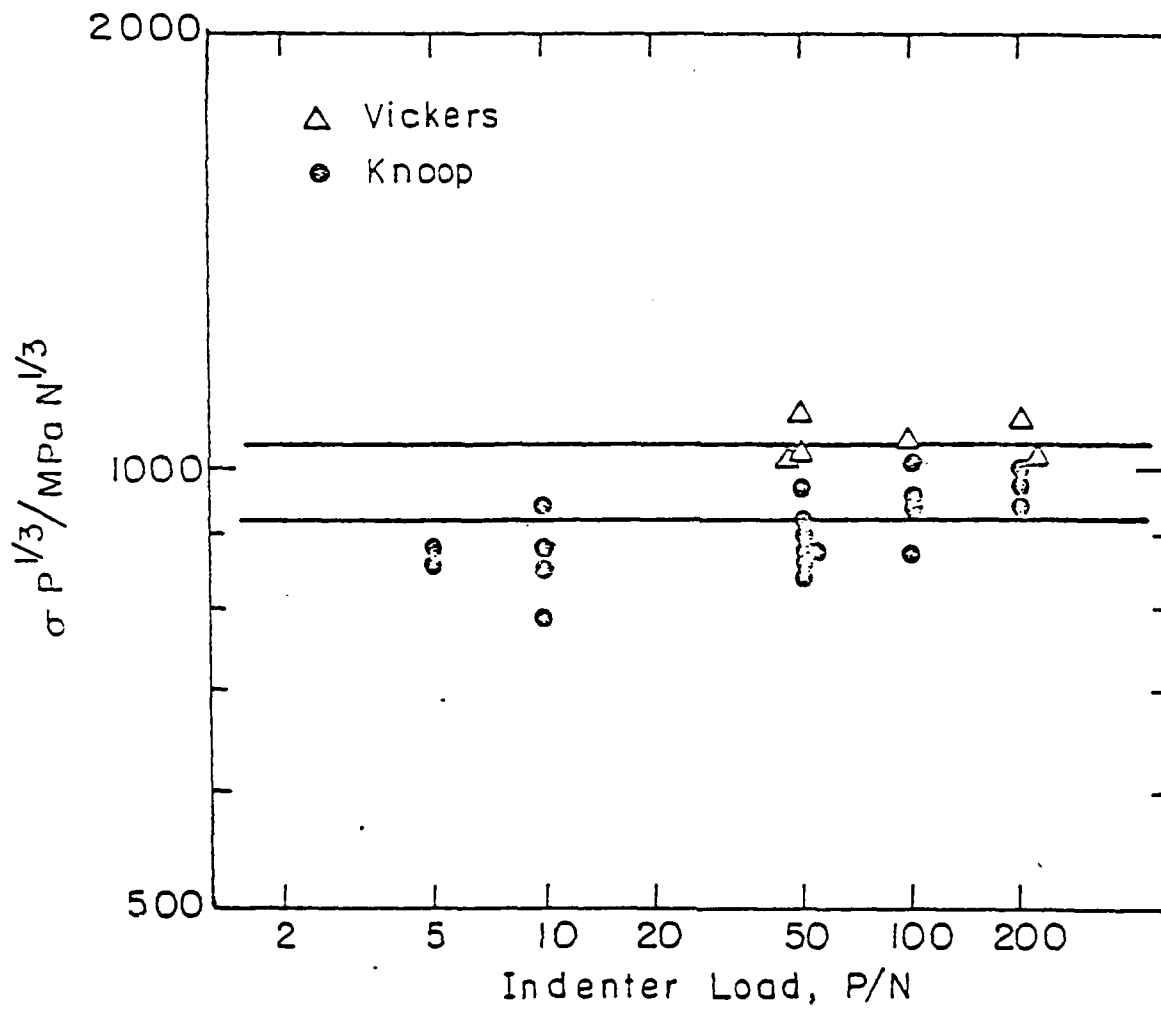
Fig. 1



XBL 8111-6984

Fig. 2





XBL 8111-6985

Fig. 3

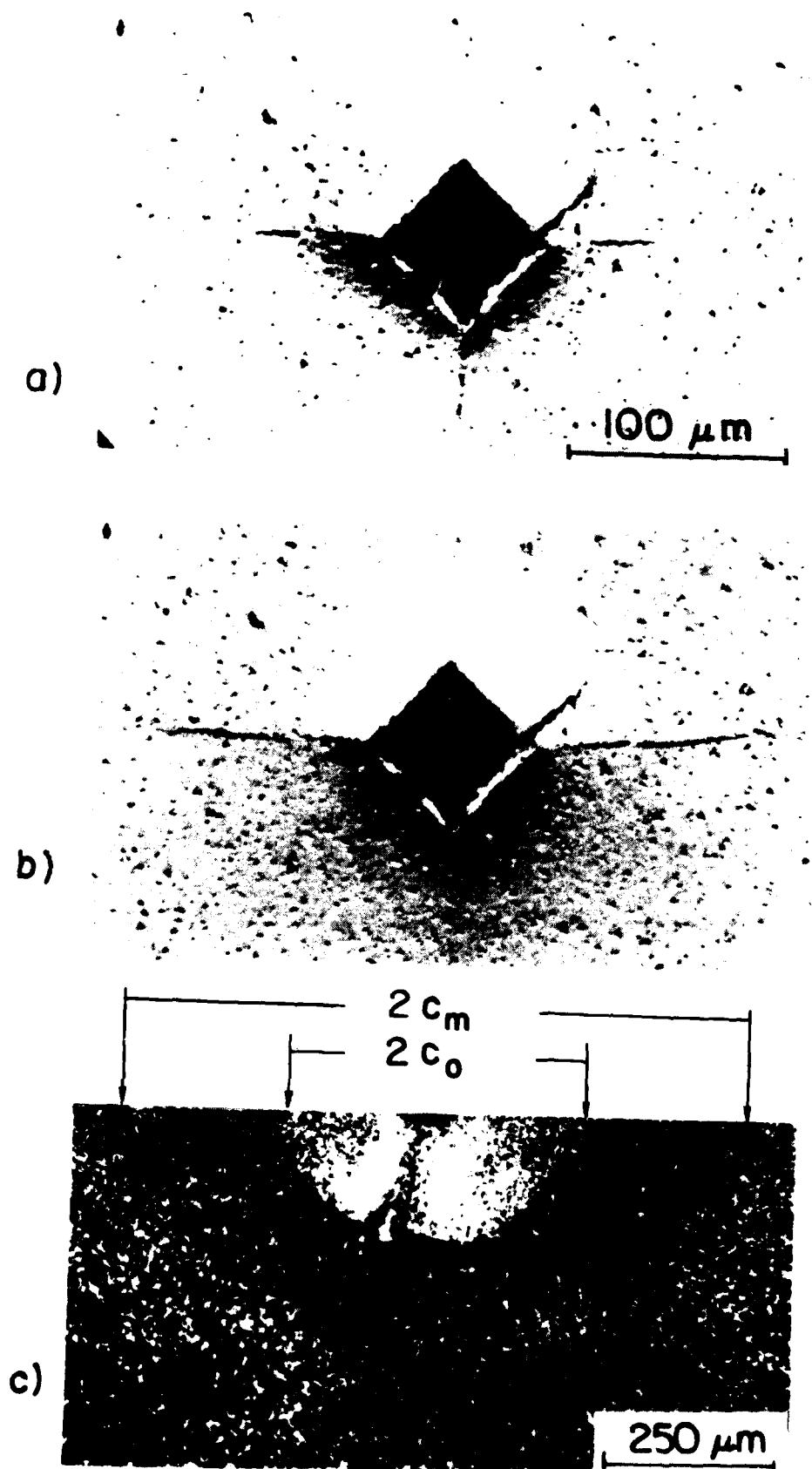



Fig. 4

d) 

100  $\mu\text{m}$

e) 

$2c_m$   
 $2c_o$

f) 

250  $\mu\text{m}$

Fig. 4

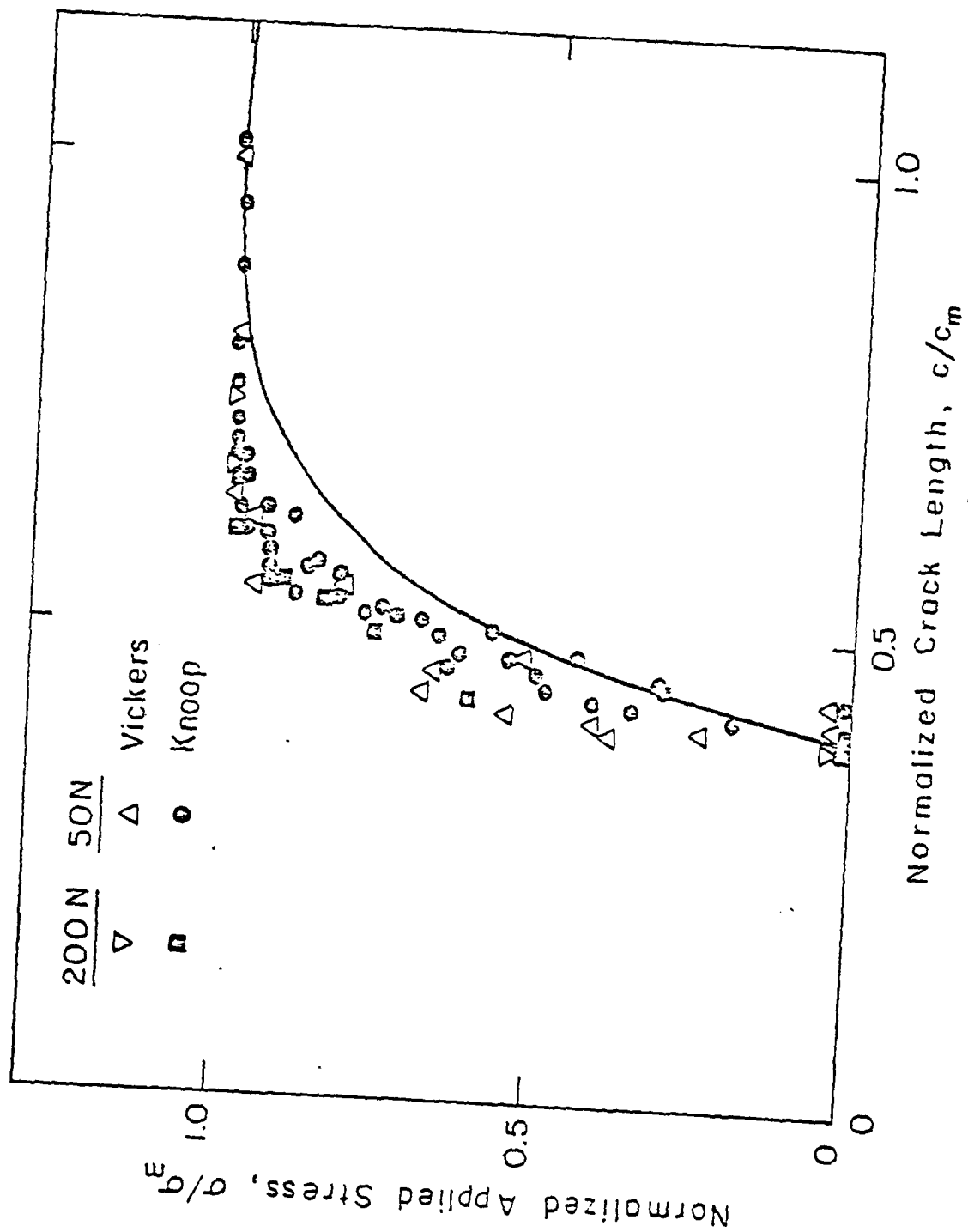
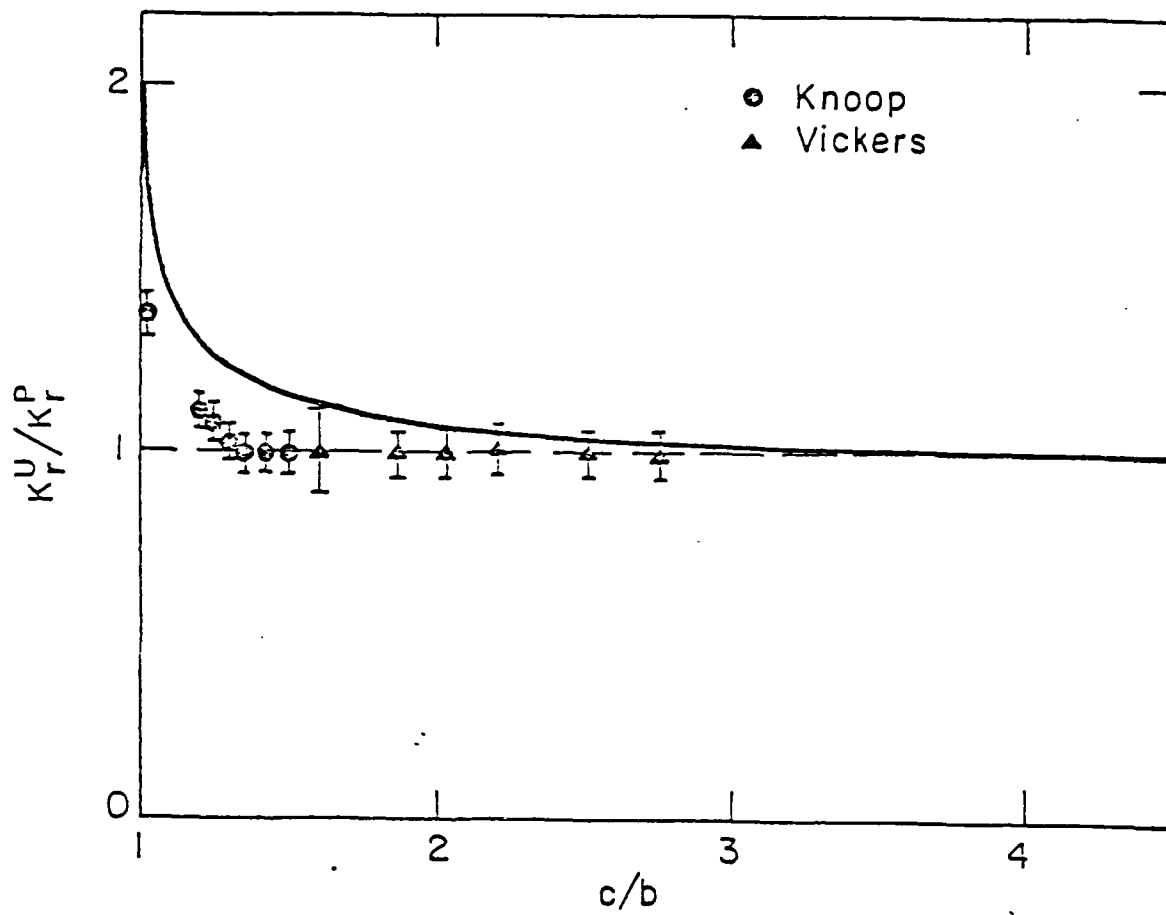


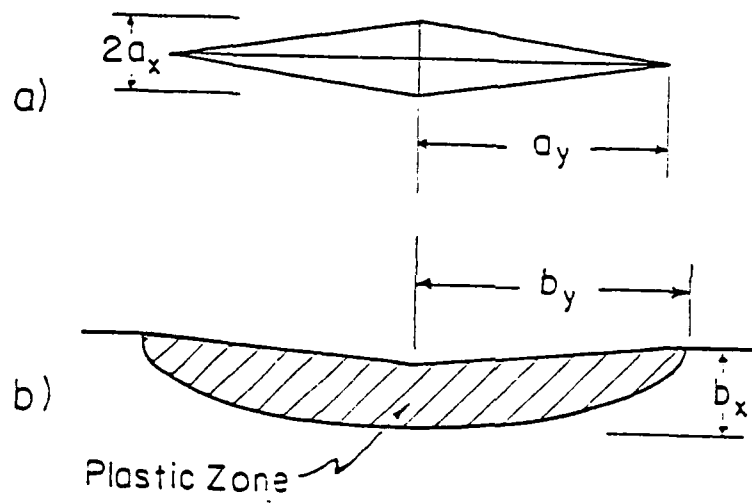
Fig. 5

XBL 8111-6986



XBL8111-6983

Fig. 6



XBL 8111-6987

Fig. A1

CHAPTER VIII

A SIMPLE METHOD FOR THE  
DETERMINATION OF ELASTIC MODULUS TO HARDNESS RATIOS  
USING KNOOP INDENTATION MEASUREMENTS

by

D. B. Marshall, Tatsuo Noma and A. G. Evans

Department of Materials Science and Mineral Engineering  
University of California  
Berkeley, CA 94720

A Simple Method For The  
Determination of Elastic Modulus to Hardness Ratios  
Using Knoop Indentation Measurements

D. B. Marshall, Tatsuo Noma<sup>†</sup> and A. G. Evans

Department of Materials Science and Mineral Engineering  
University of California  
Berkeley, CA 94720

ABSTRACT

A simple indentation technique for measuring the hardness-to-modulus ratio of elastic/plastic materials has been developed. The method is based on measurement of the elastic recovery of the in-surface dimensions of a Knoop indentation, and allows ready evaluation of the hardness-to-modulus ratio to an accuracy better than 10%.

<sup>†</sup>On leave from Materials Dept., Tokyo Institute of Technology, Tokyo, Japan.



The development of a simple method for measuring the hardness-to-modulus ratio,  $H/E$ , on small specimens, has been motivated by the need to determine  $H/E$  as a prerequisite for toughness evaluation using indentation methods.<sup>1,2</sup> Recently Lawn and Howes<sup>3</sup> developed a novel technique for measuring  $E$  and  $H$ , based on their demonstration that the extent of elastic recovery in the depth of Vickers indentations is related directly to  $E/H$ . One restriction of the technique, however, is that measurements must be made in the absence of cracking, a condition which enforces the careful measurement of low-load indentations using scanning electron microscope techniques. In this note, a related, but more convenient, method is described. The method is insensitive to the incidence of cracking and can, therefore, utilize higher load indentations and optical microscopy.

The method is based on the measurement of elastic recovery of the in-surface dimensions of Knoop indentations (Fig. 1). In the fully loaded state, the ratio of the diagonal dimensions,  $a$  and  $b$ , of the Knoop contact area is defined by the indenter geometry,  $a/b = 7.11$ . However, upon unloading, elastic recovery reduces the length of the shorter indentation diagonal (as well as the indentation depth), whereas the longer diagonal remains relatively unaffected. The extent of recovery is dependent on the hardness-to-modulus ratio; recovery is largest in highly elastic materials (high  $H/E$ ) and zero in rigid/plastic materials (low  $H/E$ ). Therefore the distortion of the residual impression, characterized by the ratio of its dimensions,  $b'/a'$ , provides a measure of  $H/E$ .

Measurements of residual Knoop impression dimensions, in a series of materials covering a wide range of  $H/E$  (Table 1), are summarized in Fig. 2.

The data were obtained from optical microscopy of indentations generated by loads in the range 10-100N. Additional measurements were made using a wider range of loads (2-700N) in one material,  $\text{Si}_3\text{N}_4$ . In all cases the ratio  $b'/a'$  was independent of the indenter load. Moreover,  $b'/a'$  was insensitive to the incidence of cracking (the cracking threshold fell within the indentation load range for the tests performed on  $\text{Si}_3\text{N}_4$  and soda-lime glass). The error bars in Fig. 2 represent the measurement error, dictated by the resolution of the optical microscope.<sup>†</sup>

Justification for the assertion that  $b'/a'$  relates to the hardness-to-modulus ratio can be obtained from calculation of the elastic recovery of a related, but simplified, indentation geometry.<sup>††</sup> Consider a two-dimensional elliptical indentation, produced by a pressure  $p$ , with major and minor axes  $a$  and  $b$  in the same ratio as the Knoop indentation diagonals. The volume of the indentation is accommodated by plastic deformation in a localized zone around the indentation and by elastic displacements of the surrounding material. The elastic strains partly relax upon unloading. The unloading may be simulated by applying a pressure, equal in magnitude and opposite in sign to the indentation pressure, at the surface of the loaded indentation. The resulting displacements determine the unloaded indentation shape. The displacements can be obtained from superposition of solutions for an elliptical hole subject to uniaxial stress;<sup>4</sup>

---

<sup>†</sup> Scanning electron microscopy was also utilized for measurement of lower load indentations in  $\text{Si}_3\text{N}_4$ . However, because of limited definition of the edge of the contact, the relative measurement error was similar to that experienced with the higher load optical measurements.

<sup>††</sup> A more detailed model was suggested by Lawn and Howes<sup>1</sup> for relating the depth recovery of Vickers indentations to  $E/H$ . However their approach cannot be applied to in-surface dimensions.

$$b - b' = \alpha a p/E \quad (1a)$$

$$a - a' = \alpha b p/E \quad (1b)$$

where  $\alpha = 3/2$  for the two-dimensional hole. Setting  $p \approx H$ , and noting both that  $H/E < 0.1$  (see Table 1) and that  $b/a \approx 1/7$  for the Knoop geometry, Eq. 1b gives  $a' \approx a$  (i.e. the recovery of the longer diagonal is negligible). Equation 1a then reduces to

$$b'/a' \approx b'/a = b/a - \alpha H/E \quad (2)$$

The solid curve in Fig. 2 is a representation of Eq. 2, obtained by imposing the necessary intercept,  $b/a = 1/7.11$ , and using a gradient ( $\alpha = 0.45$ ) adjusted to fit the data. The value of  $\alpha$  determined from Fig. 2 is lower than that predicted by the elliptical hole model (0.45 c.f.  $3/2$ ), presumably because of the smaller extent of recovery in the more constrained three-dimensional indentation.

The use of Fig. 2 to evaluate  $H/E$  from measurements of Knoop indentation dimensions, coupled with toughness and hardness measurements from Vickers indentation,<sup>1,2</sup> allows the important mechanical properties,  $E$ ,  $H$ , and  $K_C$ , to be determined from only two indentations (one Knoop and one Vickers), with attendant minimal material size requirements. The uncertainty in the calculated  $H/E$  can be estimated from the measurement errors indicated in Fig. 2 and the scatter of data from the fitted line. The relative error is smallest for materials with high values of  $H/E$ . For  $H/E \geq 0.03$ , a range which covers most brittle materials, the error is less than 10%.

References

1. A. G. Evans and A. E. Charles, "Fracture Toughness Determinations by Indentation," J. Am. Ceram. Soc. 59 [7-8] 371-372 (1976).
2. G. R. Anstis, P. Chantikul, B. R. Lawn, and D. B. Marshall, "A Critical Evaluation of Indentation Techniques for Measuring Fracture Toughness: I. Direct Crack Measurements," J. Am. Ceram. Soc. 64 [9] 533-538 (1981).
3. B. R. Lawn and V. R. Howes, "Elastic Recovery at Hardness Indentations," J. Mat. Sci. 16, 2745-2752 (1981).
4. S. P. Timoshenko and J. N. Goodier, Theory of Elasticity, McGraw Hill, New York, 1951.

Table I

Hardness and Modulus of Materials Tested

Material	H(GPa)	E(GPa)
Soda-lime glass	5.5	70
Glass Ceramic <sup>1</sup>	8.4	108
Si <sub>3</sub> N <sub>4</sub> (hot pressed) <sup>2</sup>	18.5	300
Al <sub>2</sub> O <sub>3</sub> (hot pressed) <sup>3</sup>	20.1	406
ZrO <sub>2</sub> (partially stabilized) <sup>4</sup>	10.0	210
MgF <sub>2</sub> (hot pressed) <sup>5</sup>	7.3	170
Steel (hardened) <sup>6</sup>	8.2	200
ZnS (hot pressed) <sup>7</sup>	1.9	98
ZnO (hot pressed) <sup>8</sup>	2.0	120

<sup>1</sup>Pyroceram, Corning

<sup>2</sup>NC132, Norton

<sup>3</sup>AD999, Coors

<sup>4</sup>CSIRO, Australia

<sup>5</sup>Irtran, Kodak

<sup>6</sup>Leitz, test block

<sup>7</sup>Irtran, Kodak

<sup>8</sup>From H. Ruf

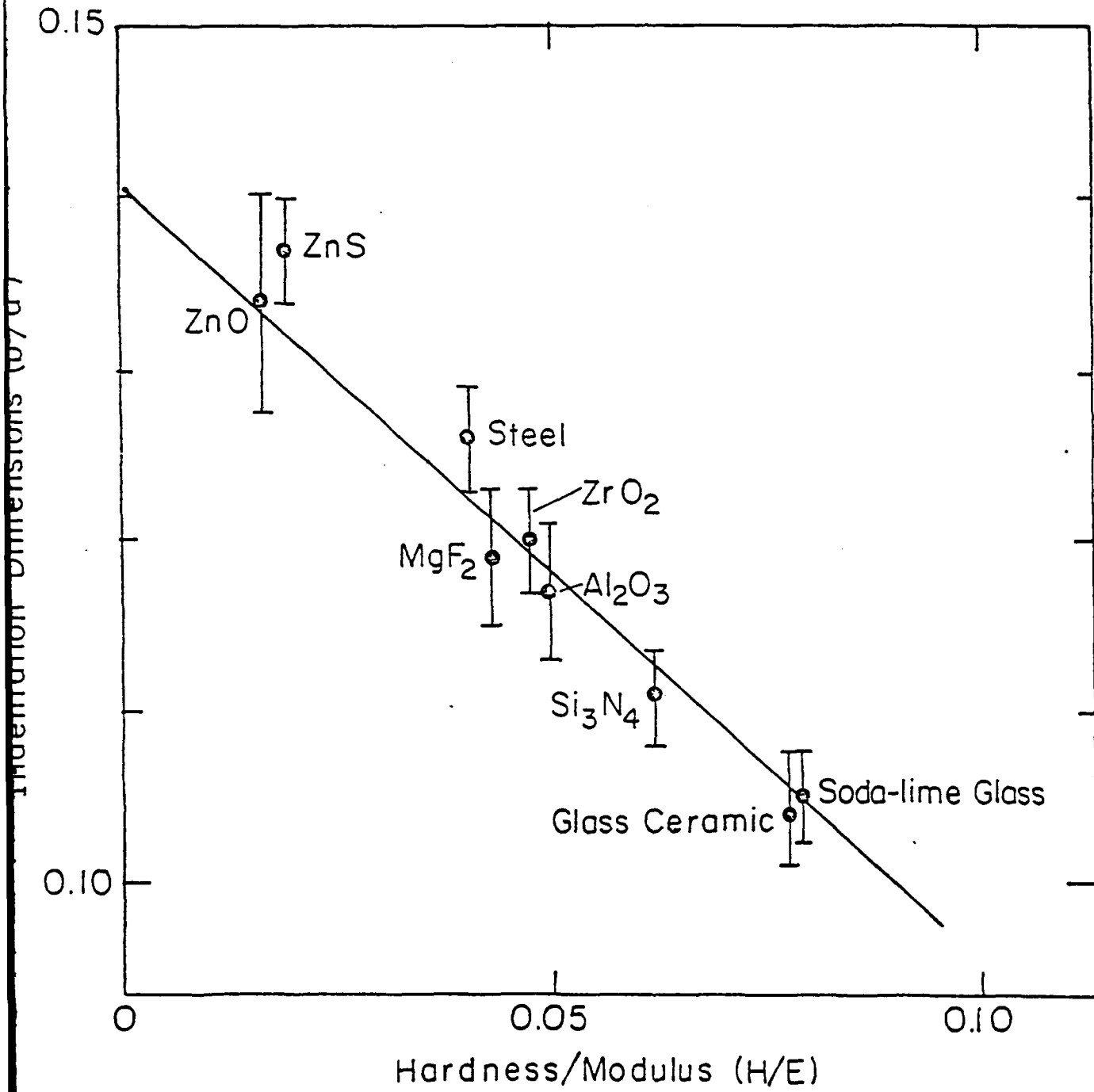
Figure Captions

- Fig. 1. Residual Knoop indentation impressions; (a) in ZnS (low H/E), 20N load, width of field = 526  $\mu\text{m}$ . (b) in Soda-lime glass (high H/E), 25 N load, width of field = 357  $\mu\text{m}$ .
- Fig. 2. Variation of residual Knoop impression dimensions with hardness-to-modulus ratio. Indenter load 10-100N.

-261-



Fig. 1



XBL824-5593

Fig. 2



CHAPTER IX

DELAYED FAILURE IN CERAMICS

D. B. Marshall

Department of Materials Science and Mineral Engineering  
University of California  
Berkeley, CA 94720

Delayed Failure in Ceramics

D. B. Marshall

Department of Materials Science and Mineral Engineering  
University of California  
Berkeley, CA 94720

ABSTRACT

Recent studies of delayed failure of glasses and ceramics containing indentation flaws as failure origins are reviewed. Indentation provides cracks with well defined geometry and driving forces, and predetermined size within the size range of naturally occurring flaws. Direct observation of indentation flaws during failure testing has confirmed that delayed failure is caused by environmentally assisted subcritical crack extension. A distinctive feature of indentation flaws is the presence of the residual stresses that created the crack and which continue to influence the mechanics of failure. With the stress intensity factor modified to incorporate the residual component, the fracture mechanics analysis based on growth laws observed for large-scale cracks completely accounts for the observed fatigue responses of surfaces containing indentation cracks, abrasion damage and machining damage. The analysis resolves some apparent discrepancies between previous crack growth predictions and observed delayed failure, and suggests methods for calibrating the fatigue parameters required for reliability prediction.

## 1. INTRODUCTION

Many ceramics are susceptible to time-dependent failure under applied loading at room temperature. This so-called "fatigue" behavior has been attributed to chemically assisted flaw growth, and has been observed in a number of materials and environments, most notably the oxide material/water system. Silicate glasses are particularly susceptible to fatigue and have received extensive study.

The conventional fracture mechanics approach for fatigue analysis is based on the underlying assumption that fatigue failure occurs by sub-critical extension of a single dominant microscopic flaw to an instability configuration. Provided the rate of crack extension is defined by a unique function of the crack driving force, the analysis of strength characteristics under fatigue conditions follows from two basic starting equations; one equation represents the crack velocity function  $v = dc/dt = v(K)$ , where  $c$  is a characteristic crack dimension,  $t$  is time, and  $K$  is the stress intensity factor, and the other equation represents the crack driving force  $K = K(\sigma, c)$  where  $\sigma$  characterizes the applied loading (which may be time-dependent). Combination of these two equations yields a differential equation in crack length and time which can be solved for arbitrary service conditions once the parameters of the two equations are known. Then, incorporation of a fracture criterion ( $K=K_c$ , where  $K_c$  is the toughness) allows failure times to be predicted.

The crack velocity function  $v(K)$  has been the subject of extensive study, using large-scale cracks in well controlled specimen configurations such as the double cantilever or double torsion beams.<sup>1-4</sup> The use of

these measurements as a basis for lifetime prediction has been successful in predicting the general form of fatigue curves (e.g. lifetime versus applied stress).<sup>5-7</sup> However some apparent discrepancies between predicted and observed slopes of fatigue curves,<sup>8-10</sup> absolute magnitudes of lifetimes,<sup>11</sup> and certain aging effects have arisen. These have led to the suggestion that the fatigue responses of microscopic strength-controlling flaws and macroscopic cracks differ. Indeed, some workers have constructed detailed fatigue theories based on the premise that the fatigue mechanism involves the sharpening of initially rounded crack tips rather than crack lengthening.<sup>11</sup>

In the fracture mechanics analysis that suggested these discrepancies it was assumed that the response of flaws to mechanical loading is described by the stress intensity factor  $K \propto \sigma c^{1/2}$ , appropriate to ideal Griffith flaws. However more recent studies<sup>12-15</sup> have shown that this represents a special case of a more general flaw configuration where the forces initially responsible for creating the flaw persist and augment any ensuing crack driving force. A convenient controlled flaw system for quantifying residual stress effects of this kind is provided by indentation-induced cracks; as well as providing a crack system with well defined geometry and driving forces, the indentation cracks can be observed throughout a test sequence, thus providing a means of directly confirming predicted crack responses.

The purpose of this paper is to review some recent studies of fatigue using indentation cracks with sizes extending into the size range of natural flaws. When proper account is taken of all of the driving forces that influence the growth of cracks the observed fatigue behavior of

abraded and machined surfaces of glasses and ceramics is fully described in terms of macroscopic crack growth laws. Moreover, a convenient scheme for calibrating the kinetic parameters required lifetime prediction emerges from the modified fatigue analysis.

## 2. PREDICTION OF FATIGUE LIFETIMES

In this section the fracture mechanics approach for fatigue analysis is summarized. Particular attention is paid to the comparison of fatigue of ideal Griffith flaws (free of residual stresses) and flaws which continue to be influenced by the residual forces responsible for their creation. The applied loading system is taken as uniform stress,  $\sigma$ , over the flaw surface, either held constant (so-called "static fatigue") or increasing at a constant rate ( $\sigma = \dot{\sigma}t$ , so-called "dynamic fatigue").

### 2.1 Stress free flaws

The first step in setting up a differential equation to describe the crack response is to define the crack velocity function and the crack driving force. The crack velocity function (as measured by direct observation of macroscopic cracks) generally shows several distinct regions of behavior, corresponding to changes in rate controlling mechanisms in a given material/environment system (Fig. 1). The region of lowest velocity (region I in Fig. 1), which is governed by reaction kinetics at the crack tip, is expected to be dominant in determining the time to failure.<sup>7</sup> Several models for the crack extension mechanism have provided analytical predictions of the crack velocity function in this region, but, because  $v$  is a rapidly increasing function of  $K$ , the existing experimental data (which extend over a limited range of  $v$ ) are unable to distinguish

between the various predictions.<sup>17</sup> However, knowledge of the correct analytical form of the velocity function becomes vitally important when extrapolating short term data to long lifetimes.<sup>17</sup> The equation most widely used in fatigue analysis is empirically based, being chosen for its ease of integration:

$$v = v_0 (K/K_c)^n \quad (1)$$

where the parameters  $v_0$  and  $n$  are kinetic constants for the given material/environment system. Then with the standard solution for the stress intensity factor for a crack subject to uniform stress<sup>18</sup>

$$K = \sigma(\pi\Omega c)^{1/2} \quad (2)$$

(where  $\Omega$  is a dimensionless constant dependent on crack geometry and free surface effects), Eqn. 1 becomes

$$v = dc/dt = v_0 [\sigma(\pi\Omega c)^{1/2}/K_c]^n \quad (3)$$

Straightforward integration of Eqn. 3 from the initial condition  $c = c_0$  at  $t = 0$  to the failure condition  $K = K_c$  at  $t = t_f$ ,  $c = c_f$ ,  $\sigma = \sigma_f$  yields the result (for  $\sigma = \text{constant}$  and  $(c_0/c_f)^{(n-2)/2} \ll 1$ )

$$t_f = \lambda_s \sigma_f^{-n} \quad (4)$$

where

$$\lambda_s = [2/(n-2)] \sigma_i^n c_0 / v_0 \quad (5)$$

and  $\sigma_i = K_c/(\pi\Omega c_0)^{1/2}$  is the strength in the absence of fatigue. The corresponding solutions for dynamic fatigue can be expressed either in

an analagous form

$$t_f = \lambda_d \sigma_f^{-n} \quad (6a)$$

or in the more commonly used form with failure stress,  $\sigma_f$ , expressed in terms of stress rate,  $\dot{\sigma}$ ,

$$\sigma_f = (\lambda_d \dot{\sigma})^{1/(n+1)} \quad (6b)$$

where

$$\lambda_d = (n+1)\lambda_s \quad (7)$$

The power law forms of Eqns. 4 and 6 have been experimentally confirmed in many studies.<sup>5-10</sup> However, the values of  $n$  calculated from the slopes of logarithmic plots of Eqns. 4 and 6 are usually lower than the values obtained from direct velocity measurements of macroscopic cracks.<sup>8-10</sup> In the next section it is postulated that the apparent inconsistency is due to the omission from Eqn. 2 of a term due to residual stress.

## 2.2 Flaws with Residual Stress

Indentation of a brittle surface with a sharp indenter, such as a Vickers pyramid, creates a highly localized region of irreversible deformation from which well defined cracks generate.<sup>12-16</sup> Direct observations of crack evolution during indentation of optically transparent materials have demonstrated that the final crack configurations (Fig. 2) are achieved as the indenter is removed from the surface.<sup>12,14</sup> These observations establish that the driving force responsible for forming the cracks is provided by a residual stress field. The residual field, which arises because of the



elastic/plastic nature of the deformation beneath the indenter,<sup>14,19</sup> continues to act after completion of the contact and supplements any subsequently applied load in providing a driving force for crack propagation. The residual stress has been incorporated into fracture mechanics analyses by defining a residual stress intensity factor<sup>12-14</sup> for the half-penny shaped radial cracks,

$$K_r = \chi_r P/c^{3/2} \quad (8)$$

where  $P$  is the load applied to the indenter and  $\chi_r = \xi(E/H)^{1/2}$ , with  $E$  and  $H$  the elastic modulus and hardness of the material and  $\xi$  a dimensionless constant dependent only on indenter geometry. The inverse dependence of  $K$  on crack length reflects the localized nature of the residual field.

It should be noted that the idealized indentation fracture system bears a very close resemblance to the general contact damage that glass and ceramic components experience during surface finishing and during service. The existence of residual stresses characterized by Eqn. 8 (or similar equation) have been identified in machining damage<sup>16</sup> and in sharp particle impact<sup>20</sup> (abrasion). Moreover, strongly analagous residual fields influence cracks that are associated with inclusions<sup>21,22</sup> and other microstructural defects.

Consider now the response of the indentation crack to a subsequently applied uniform tension. The net stress intensity factor is given by the superposition of two components, one due to the residual stress (Eqn. 8) and the other due to the applied load (Eqn. 2)

$$K = X_r P / c^{3/2} + \sigma (\pi \Omega c)^{1/2} \quad (9)$$

In analysing fatigue it is convenient to take the "inert" strength (i.e. strength in the absence of any non-equilibrium crack growth during stressing to failure) as a reference. Inert strengths may be achieved by testing at fast load rates, in an inert environment or at low temperatures. The crack response is then described by an applied-stress/equilibrium-crack-size function<sup>13,15</sup> obtained by putting  $K = K_c$  into Eqn. 9;

$$\sigma_a = [K_c / (\pi \Omega c)^{1/2}] [1 - X_r P / K_c c^{3/2}] \quad (10)$$

The inert strength is defined by the instability condition, which occurs at the maximum in the  $\sigma_a(c)$  function,<sup>13,15</sup>

$$c_m = (4 X_r P / K_c)^{2/3} \quad (11a)$$

$$\sigma_m = 3 K_c / 4 (\pi \Omega c_m)^{1/2} \quad (11b)$$

and failure is preceded by stable equilibrium crack growth from the initial length  $c_0$  ( $= (X_r P / K_c)^{2/3}$ , given by putting  $\sigma_a = 0$  in Eqn. 10) to  $c_m$ . This behavior contrasts with the response of stress-free flaws, where instability occurs at a critical applied stress level without precursor extension ( $X_r = 0$ ,  $c = c_0$  in Eqn. 10). The equilibrium response described by Eqn. 10 has been confirmed by direct crack growth measurements in ceramics<sup>15,23-25</sup> and glasses.<sup>13</sup>

Inert strengths measured in glass are influenced by exposure of the crack system to a non-inert environment in the period between indentation and strength testing. The inert strength increases with aging time, at a rate which is dependent on the environment, ultimately achieving a

constant level  $\sim 20\%$  higher than the non-aged inert strength.<sup>26</sup> This effect has been attributed to the growth of lateral cracks, and will be important in interpreting the relation between macroscopic crack velocity measurements and fatigue strengths in Section 3. Direct observation of the indentation crack system during aging indicates that both the radial and lateral cracks extend subcritically, driven by the residual stress.<sup>23,27,28</sup> However, the development of the lateral crack system tends to lag that of the radial system considerably; for example at 5N indentation load the lateral cracks are contained within the contact zone initially, but after  $\sim 1$  hr in oil (which contains a small amount of water) they grow out to the limits of the radial cracks. Because of the stable precursor crack growth which occurs in a strength test, the increase in radial crack length during aging does not influence the inert strength (provided the crack length does not exceed  $c_m$ ). However the growth of the lateral system can influence the strength in two ways<sup>26</sup>; one is by relieving part of the residual stress (enhanced by the proximity of the lateral crack to the free surface) and the other is due to geometrical interaction of the lateral crack with the radial crack (related to the relative size  $c^L/c^R$  of the lateral and radial cracks). The observations<sup>26</sup> that the strength increase occurs as  $c^L/c^R$  increases to unity (Fig. 3), and that further growth of both crack systems occurs at  $c^L/c^R = 1$  without further strength increase, suggest that the geometrical interaction dominates.

The differential equation governing the fatigue response of indentation flaws under uniform applied tension is given by combining eqns. 1 and 9<sup>26</sup>

$$dc/dt = v_0 [X_r P / K_c c^{3/2} + \sigma (\pi \Omega c)^{1/2} / K_c]^n \quad (12)$$

In general Eqn. 12 cannot be solved by straightforward separation of variables so numerical solutions are required. However Fuller et al.<sup>29</sup> have obtained analytical solutions for the time to failure for static and dynamic fatigue (Appendix). Their solutions have the same form as the corresponding solutions for stress-free flaws (for  $(c_m/c_f)^{n/2} \ll 1$ )

$$t_f \sigma_f^{n'} = \lambda'_s \quad (\sigma = \text{constant}) \quad (13a)$$

$$\sigma_f = (\lambda'_d \dot{\sigma})^{1/(n'+1)}, \quad (\sigma = \dot{\sigma} t) \quad (13b)$$

but the parameters  $n'$  and  $\lambda'$  differ from the stress-free counterparts

$$n' = (3n+2)/4 \quad (14a)$$

$$\lambda'_s = (2\pi/n')^{1/2} \sigma_m^{n'} c_m/v_0 \quad (14b)$$

$$\lambda'_d = (n'+1)\lambda'_s \quad (14c)$$

Comparative measurements of dynamic fatigue of controlled flaws by Marshall and Lawn<sup>26</sup> have confirmed the predictions of equations 13 and 14. In that study, stress-free controlled flaws were obtained by indentation at fixed load, followed by an annealing treatment which eliminated the residual indentation stress. Figure 4 shows their results for as-indented and annealed flaws. The sloped portion of the curve through the annealed data represents a curve fit according to Eqn. 6b which, in conjunction with the measured inert strength and initial crack length, provides a calibration of the kinetic parameters,  $n = 17.9$  and  $v_0 = 2.4 \text{ mms}^{-1}$ . The curve through the as-indented data was then computed from Eqn. 12 using the calibrated kinetic parameters and measured inert strength ( $\sigma_m = 68 \text{ MPa}$ ). An additional check

on the theory (and direct confirmation that failure in fact occurs by subcritical crack extension) was obtained by monitoring the entire subcritical crack evolution for both flaw types at a particular stress rate. The data are shown in Fig. 5, together with predicted  $c(t)$  curves from Eqn. 12.

The cracks investigated in Figs. 4 and 5 have sizes ( $\sim 65 \mu\text{m}$ ) near the large extreme of the usual strength-controlling flaws in glass. Dynamic fatigue data in the same glass has also been obtained by Dabbs et al.<sup>30</sup> at lower indentation loads, for which the crack sizes extend over most of the size range of natural flaws. For the purpose of comparing data at various indentation loads it is convenient to rewrite Eqn. 12 in terms of reduced variables, based on the reference parameters defined in Eqns. 11a and b:<sup>31</sup>

$$S = \sigma/\sigma_m \quad (15a)$$

$$C = c/c_m \quad (15b)$$

$$T = tv_0/c_m \quad (15c)$$

Thus, Eqn. 12 becomes (for dynamic fatigue)

$$dC/dT = [1/4C^{3/2} + 3\hat{S}TC^{1/2}/4]^n \quad (16)$$

(where  $\hat{S} = S/T$ ), with solution (from Eqn 13b) at sufficiently low stress rates given by

$$S_f = (\Lambda'_d \hat{S})^{1/(n'+1)} \quad (17)$$

where

$$\Lambda_d' = (2\pi/n')^{1/2}(n'+1) \quad (18)$$

With this formulation the indentation load parameter has been incorporated into the normalized variables such that the load does not appear explicitly in Eqn. 16. Hence Eqns. 16 and 17 provide a means of plotting dynamic fatigue data on a universal curve for a given material/environment system.<sup>†</sup> The data of Dabbs et al.<sup>30</sup> for indentation loads in the range 0.05 to 10N are plotted according to this scheme in Fig. 6, along with the prediction of Eqn. 16 (using  $n = 18$ , for soda-lime glass). The data over the entire load range (corresponding to a flaw size range  $\sim 5 \mu\text{m}$  to  $\sim 100 \mu\text{m}$ ) fall on the universal curve, thus supporting the contention that the macroscopic crack growth law governs the response of cracks with sizes approaching a few microns.

### 3. DISCUSSION

#### 3.1 Interpretation of Fatigue Mechanism

The relation between fracture mechanics predictions and the observed fatigue behavior of ceramics and glass will now be reexamined in the light of the indentation analysis. This will involve assessment of two experimental studies from which the apparent discrepancies noted earlier were inferred. In the first study Pletka and Wiederhorn<sup>10</sup> compared macroscopic crack growth observations with dynamic fatigue measurements from machined

<sup>†</sup>

It can be shown that the integration of Eqn. 16 is insensitive to initial crack size in the range  $c_0$  to  $c_m$ . Under such circumstances aging effects which increase the initial crack size do not influence the fatigue strength, and the invariant initial condition  $C_0 = c_0/c_m = 4^{-2/3}$  (see Eqn. 11a and following discussion) may be taken.

surfaces of glass ceramics, and in the second earlier study Mould and Southwick<sup>32,33</sup> investigated the fatigue properties of abraded and scratched glass surfaces. The strength-controlling flaws in both investigations were generated by localized mechanical contact and would be expected to resemble closely the indentation damage; the existence of residual crack-opening stresses has been identified in machining and abrasion damage in independent experiments<sup>16,20</sup>. However there is some evidence that the precise form of residual stress intensity factor (Eqn. 8) can be modified by effects such as partial relaxation of residual stresses due to chipping, and by the modified deformation/fracture geometry in the case of machining damage (which can resemble a linear configuration rather than a "point" damage configuration).

Pletka and Wiederhorn<sup>10</sup> found that, in two glass ceramics, the values of the crack velocity exponent  $n$  deduced from dynamic fatigue measurements (using Eqn. 6b, for Griffith flaws) were  $\sim 25\%$  lower than values determined from direct crack velocity measurements in double cantilever beams. It is immediately apparent from Eqns. 13b and 14a, and from Fig. 4, that differences of this magnitude between  $n$  and  $n'$  (the "apparent" value of  $n$ ) are characteristic of indentation flaws (for the data in Fig. 4,  $n = 18$  and  $n' = 13.7$ ). Moreover Fuller et al.<sup>29</sup> have shown that for indentation flaws with a linear configuration (Appendix) the difference between  $n$  and  $n'$  can be as high as 50%. Therefore, although the interactions between cracks and microstructure that were discussed by Pletka and Wiederhorn as a possible explanation of their results must influence crack growth, the differences in  $n$  values can be fully accounted for by the effect of residual stresses associated with the machining damage.

In a series of carefully controlled experiments Mould and Southwick studied the aging and static fatigue behavior of glass surfaces which had been either abraded with SiC grit or scratched with emery paper. In the aging experiments<sup>33</sup>, an increase in inert strength ( $\sim 30\%$  for abrasion flaws,  $\sim 50\%$  for scratching flaws) was observed when the surfaces were exposed to water during the period between introducing the damage and measuring the strength. The similarity in aging responses of these flaws and the indentation cracks (Section 2.2) suggests that the same mechanism is responsible in both cases. Mould and Southwick concluded that the strength increase was due to rounding of the tips of the strength-controlling flaws. However, the observation of stable growth of indentation cracks during both the aging and the inert strength tests eliminates that mechanism; rather, the strength increase has been attributed to subcritical growth of lateral cracks driven by the residual contact stress.<sup>26,28</sup> The interpretation of the aging affect in terms of residual-stress-driven crack growth is also consistent with the observations of Mould and Southwick that an annealing treatment of the abraded surface increased the strength (due to relaxation of the residual stress), but that no additional strength increase occurred after aging an annealed abraded surface.

In the static fatigue experiments<sup>32</sup>, the fatigue lifetimes of abrasion damage of varying severity and geometrical configurations (point or linear) were compared. Inconsistencies have since been noted with fracture mechanics predictions (based on stress-free flaws) of the absolute failure times<sup>11</sup>, the relative failure times of point and linear flaws<sup>4</sup>, and the variation of failure time with flaw size.<sup>4</sup> These comparisons were based on data that were plotted by Mould and Southwick



in an empirically normalized form: fatigue strength,  $\sigma_f$ , normalized by inert strength,  $\sigma_n$ ; failure time,  $t_f$ , normalized by the failure time,  $t_{0.5}$ , corresponding to  $\sigma_f/\sigma_n = 0.5$ . Unfortunately,  $\sigma_n$  was chosen to be the aged inert strength, whereas the failure times in the fracture mechanics analysis of Section 2.2 are all expressed in terms of the "instantaneous" (i.e. non-aged) inert strength,  $\sigma_m$ . The values of  $t_{0.5}$  calculated from the static fatigue data are very sensitive to the values of  $\sigma_n$ ; a decrease of 20 to 30% in  $\sigma_n$  (typical of the difference between  $\sigma_m$  and  $\sigma_n$ ) alters  $t_{0.5}$  by several orders of magnitude. Because Mould and Southwick did not measure  $\sigma_m$  for all of their surface treatments, and it is not known whether the ratio  $\sigma_n/\sigma_m$  varies with flaw size (they did show that  $\sigma_n/\sigma_m$  is larger for scratches than for abrasions), all of the data cannot be directly compared with the fracture mechanics analysis. However they did measure  $\sigma_m$  for two surface treatments, one abrasion and one scratching. Lifetime measurements from these surfaces are compared with fracture mechanics predictions in Table 1. The predicted failure times for the abrasion flaws in static fatigue were calculated from the expression obtained from Eqns. 13a, 14a, 14b, and 11b;

$$t_f = [9(8\pi/(3n+2))^{1/2} K_C^2 / 16\pi\Omega V_0] \sigma_m^{n'-2} / \sigma_f^{n'} \quad (19)$$

The quantity in square brackets was first calibrated using a lifetime measurement from the indentation data in Fig. 4 ( $\sigma_m = 68$  MPa,  $n=18$ ,  $t_f = 571$ s,  $\sigma_f = 40$ MPa) along with the equivalent expression for dynamic fatigue (right side of Eqn. 19 multiplied by  $(n'+1)$  - see Eqn. 14c). Then the lifetimes in Table 1 were calculated from Eqn. 19 using the instantaneous inert strength,  $\sigma_m = 66$  MPa, measured by Mould and Southwick. The

lifetimes for the scratches were predicted in a similar manner, but using the corresponding expression for linear flaws (Appendix);

$$t_f = [(8\pi/(n+2))^{1/2} K_C^2/4\pi\Omega_L v_0] \sigma_m^{n'-2}/\sigma_m^{n'-2}/\sigma_f^{n'}, \quad (20)$$

along with the measured instantaneous inert strength  $\sigma_m = 63$  MPa, and the relative values of the crack geometry parameter for point and linear flaws,  $\Omega/\Omega_L = 4\pi^2$ , calculated for cracks in an infinite medium (and  $n' = (n+2)/2$  for linear flaws). The predicted lifetimes agree remarkably well with the measured values. It is noted that the large difference in failure times between point and linear flaws, evident in Table 1 and pointed out by Mould and Southwick (a factor of  $\sim 50$  at given  $\sigma_m$  and  $\sigma_f/\sigma_m$ ), is predicted by the fracture mechanics analysis based on indentation flaws, whereas for stress-free flaws the predicted difference is only  $\Omega_L/\Omega = 2.5$ .<sup>4</sup> It is also noted that, although we cannot compare the predicted variations of failure time with flaw size for the data of Mould and Southwick, the fracture mechanics formulation correctly predicts the failure time for abrasion of one size and for indentations of a large range of sizes (see Section 2.2). Therefore it is reasonable to infer that variations of lifetime with abrasion severity will also be predicted by the analysis.

### 3.2 Evaluation of Fatigue Parameters and Prediction of Fatigue Curves

The use of dynamic fatigue testing of indentation cracks, along with Eqns. 13b and 14a-c, provides an attractive alternative to direct velocity measurement of large cracks for calibration of the kinetic parameters  $n$  and  $v_0$ . Part of the attraction of the indentation method lies in its straightforward experimental requirements and the small

experimental scatter which results from the use of cracks of well controlled size (see Fig. 4). But the most important advantage is that measurements are made on cracks of similar size to the strength controlling cracks in real components; any influence on crack response due to crack/microstructure interactions should influence indentation cracks and strength controlling cracks equally, whereas the same may not be true for larger cracks.<sup>10</sup>

Once the kinetic parameters  $n$  and  $v_0$  are known the prediction of a fatigue curve for a given flaw requires determination of  $K_c$ ,  $\Omega$  and  $\sigma_m$  (Eqn. 19). One approach for calibrating these parameters was demonstrated in Sect. 3.1, but the relative values of  $\Omega$  for the strength-controlling flaws and the indentation flaws must be known. (Other calibration schemes are also available.<sup>24</sup>). However, departures from the somewhat idealized flaw configuration which led to Eqn. 19 may be expected in severely damaged surfaces where extensive chipping affords some relief of residual stresses (i.e. reduction of  $X_r$ ). If the resulting reduction of  $c_m$  (Eqn. 11a) is sufficient to make  $c_m < c_0$ , the analytical solutions to Eqn. 12 do not apply and the equation must be integrated numerically. This requires separate calibration of  $X_r P / K_c$  and  $c_0$  (as well as  $K_c$  and  $\Omega$ ). These calibrations can be obtained from inert strength tests on flaws both with and without residual stress (from Eqn. 10), the stress free flaws being obtained, for example, by annealing. The dynamic fatigue curve, predicted in this manner, for abrasion flaws (SiC grit accelerated in gas stream) in the same glass that was used for the data in Fig. 4, is compared with measurements<sup>20</sup> in Fig. 7. The predicted curve was obtained from Eqn. 12, with  $n = 18$ ,  $v_0 = 2.4 \text{ mm} \cdot \text{s}^{-1}$  and  $K_c / (\pi \Omega)^{1/2} = 0.78 \text{ MPa} \cdot \text{m}^{1/2}$  calibrated from the annealed data in Fig. 4,

and  $\chi_r P/K_c = 68 \mu\text{m}^{3/2}$  and  $c_0 = 54 \mu\text{m}$  from inert strength measurements on the actual abrasion flaws. The effect of the residual stress relief on the fatigue curve can be seen by fitting Eqns. 13b to the data; the apparent velocity exponent  $n' = 15.7$  is higher than that for the indentation flaws ( $n' = 13.7$ ) but lower than the value for the stress free flaws ( $n = 17.9$ ).

An alternative approach to prediction of fatigue lifetimes, which avoids the detailed parameter calibration, involves dynamic fatigue testing of the actual flaws to produce a data base; the curve for lifetime in static loading (Eqn. 13a) generates from that of dynamic fatigue (Eqn. 13b) via the simple connecting relation of Eqn. 14c.<sup>29</sup> This approach has already been used extensively, based upon the identical relations for stress free flaws.

#### 4. CONCLUSIONS

The fracture mechanics analysis based on crack growth laws observed for macroscopic cracks, and taking into account the influence of the residual stresses responsible for flaw generation, accurately predicts the fatigue behavior of indentation cracks, abrasion flaws and machining damage. The use of indentation cracks as controlled flaws for characterizing fatigue response offers certain unique advantages; as well as providing a well defined crack system and residual contact stress, the flaws being tested are in the same size range as strength controlling flaws in actual components. Moreover, the ability to predetermine the failure site allows observation of the crack response throughout the failure test. Such

observations provide direct confirmation of the underlying assumption of the fracture mechanics analysis, namely that failure occurs by chemically assisted subcritical crack extension.

The fracture mechanics analysis of fatigue is expected to have certain limitations. The danger of extrapolating crack velocity data due to the ambiguity in fitting analytical equations to the data has already been mentioned.<sup>17</sup> Additional uncertainty in extrapolation arises from the possible existence of regions of the  $v(K)$  curve controlled by different mechanisms; the transport limited region (region II of Fig. 1) which occurs at relatively high velocities can be shown to have negligible effect on fatigue strength<sup>7</sup> (particularly at long failure times), but any change in mechanism at low velocity would have a dominant influence. The existence of a fatigue limit, characterized by crack blunting at low  $K$ , has been demonstrated in some glasses.<sup>34</sup> A second limitation is imposed by the requirement for the existence of a well defined crack; this requirement is satisfied for relatively severe damage modes such as abrasion and machining, but indentation studies have shown that, at contact loads below a threshold, well developed cracks do not form. Although the contact site can still provide a strength-controlling flaw, a distinct difference in the fatigue characteristics of flaws on either side of the threshold has been observed.<sup>35</sup> Subthreshold flaws are ill-defined. If discrete crack nuclei exist within the deformation zone the role of residual stresses must be expected to be even greater than for post-threshold cracks. On the other hand it has been suggested that if the nucleation of cracks from shear processes within the deformation zone is rate controlling, the kinetics of failure would no longer be governed by crack

velocity characteristics.<sup>35</sup> Therefore any attempt to apply the existing fracture mechanics formulation to fatigue of very high strength components such as optical fibers must be regarded with caution.

#### ACKNOWLEDGMENTS

The author is grateful to B. R. Lawn for many helpful discussions.

APPENDIX

Fuller et al.<sup>29</sup> recently obtained analytical solutions to Eqn. 12 for static and dynamic fatigue. They also generalized the analysis to include two extremes of flaw configuration by writing Eqn. 9 as

$$K = X_r P_r / c^{r/2} + \sigma (\pi \Omega_r c)^{1/2}, \quad (A1)$$

where  $r = 3$  for "point" flaws (semicircular crack profile centered about a point-force contact,  $P_r = \text{force}$ ) and  $r = 1$  for "line" flaws (crack of straight front parallel to a line-force contact,  $P_r = \text{force/length}$ ). The inert strengths then become

$$\sigma_m = [r/(r+1)] K_c / (\pi \Omega_r c_m)^{1/2} \quad (A2)$$

where

$$c_m = [(r+1) X_r P_r / K_c]^{2/r} \quad (A3)$$

The solutions to the fatigue equation,

$$dc/dt = v_o [X_r P_r / K_c c^{r/2} + \sigma (\pi \Omega c)^{1/2} / K_c]^n \quad (A4)$$

(obtained from Eqns. 1 and A1), were then given as;

$$t_{f\sigma_f}^{n'} = \lambda_s' \quad (\sigma = \text{constant}) \quad (A5)$$

$$t_{f\sigma_f}^{n'} = \lambda_d' \quad (\sigma = \dot{\sigma} t) \quad (A6)$$

where

$$n' = (rn+2)/(r+1) \quad (A7)$$

$$\lambda'_s = [8\pi/(r+1)n']^{1/2} \sigma_m^{n'} c_m / v_o \quad (A8)$$

$$\lambda'_d = (n'+1)\lambda'_s \quad (A9)$$



REFERENCES

1. S. M. Wiederhorn, J. Amer. Ceram. Soc. 50 407 (1967).
2. S. M. Wiederhorn, pp. 613-46 in Fracture Mechanics of Ceramics, Vol. 2. Edited by R. C. Bradt, D. P. H. Hasselman, and F. F. Lange, Plenum, New York, (1974).
3. A. G. Evans; pp.            in Fracture Mechanics of Ceramics Vol. 2 Edited by R. C. Bradt, D.P. H. Hasselman and F. F. Lange, Plenum, New York (1974).
4. S. M. Wiederhorn and L. H. Boltz, J. Amer. Ceram. Soc. 53 543 (1970).
5. A. G. Evans and S. M. Wiederhorn, Int. J. Frac. 10 379 (1974).
6. J. E. Ritter in Fracture Mechanics of Ceramics, Vol. 4. Edited by R. C. Bradt, D. P. H. Hasselman and F. F. Lange, Plenum, New York, p. 667 (1978).
7. A. G. Evans and H. Johnson, J. Mater. Sci. 10 214 (1975).
8. J. E. Ritter and R. P. LaPorte, J. Amer. Ceram. Soc. 58 265 (1975).
9. S. Mindess and J. S. Naceau, Amer. Ceram. Soc. Bull. 56 429 (1977).
10. B. J. Pletka and S. M. Wiederhorn, p. 745 in Fracture Mechanics of Ceramics, Vol. 4. Edited by R. C. Bradt, D. P. H. Hasselman and F. F. Lange, Plenum, New York (1978).
11. R. H. Doremus, Eng. Frac. Mech. 13 945 (1980).
12. D. B. Marshall and B. R. Lawn, J. Mater. Sci. 14 2001 (1979).
13. D. B. Marshall and B. R. Lawn, J. Mater. Sci. 14 2225 (1979).
14. B. R. Lawn, A. G. Evans and D. B. Marshall, J. Amer. Ceram. Soc. 63 574 (1980).
15. D. B. Marshall, in Nitrogen Ceramics, Sijthoff and Nordhoff, in press.

16. D. B. Marshall, A. G. Evans, B. T. Khuri Yakub, G. S. Kino and J. Tien, Proc. Roy. Soc., in press.
17. S. M. Wiederhorn and J. E. Ritter; p. 202 in Fracture Mechanics Applied to Brittle Materials. Edited by S. W. Freiman. A.S.T.M. Spec. Tech. Publ., 1979, No. 678.
18. G. C. Sih, Handbook of Stress Intensity Factors, Lehigh University, 1973.
19. S. S. Chiang, D. B. Marshall and A. G. Evans, J. Appl. Phys. 53 298 (1982).
20. D. B. Marshall and B. R. Lawn, Comm. Amer. Ceram. Soc. 64 c6 (1981).
21. D. J. Green; in Fracture Mechanics of Ceramics. Edited by R. C. Bradt, A. G. Evans, D. P. H. Hasselman and F. F. Lange, Plenum, New York (1982).
22. D. J. Green, J. Amer. Ceram. Soc. 64 138 (1981).
23. B. R. Lawn, D. B. Marshall and P. Chantikul, J. Mater. Sci. 16 1769 (1981).
24. R. F. Cook, B. R. Lawn and G. R. Anstis, J. Mater. Sci. 17 1108 (1982).
25. D. B. Marshall, J. Amer. Ceram. Soc. in press.
26. D. B. Marshall and B. R. Lawn, J. Amer. Ceram. Soc. 63 532 (1980).
27. P. K. Gupta and N. J. Jubb, Comm. Am. Ceram. Soc. 64 c112 (1981).
28. G. R. Anstis, P. Chantikul, B. R. Lawn and D. B. Marshall, J. Amer. Ceram. Soc. 64 533 (1981).
29. E. R. Fuller, Jr., B. R. Lawn and R. F. Cook, to be published.
30. T. P. Dabbs, B. R. Lawn, and P. L. Kelly, Phys. Chem. Glasses, in press.
31. B. R. Lawn, D. B. Marshall, G. R. Anstis and T. P. Dabbs, J. Mater. Sci. 16 2846 (1981).

AD-A124 025

MICRO AND MACRO MECHANICS OF FRACTURE IN CERAMICS(U)  
CALIFORNIA UNIV BERKELEY DEPT OF MATERIALS SCIENCE AND  
ENGINEERING A G EVANS ET AL. 30 OCT 82

44

UNCLASSIFIED

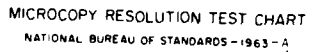
NO0014-81-K-0362

F/G 11/2

NL



END  
DATE  
FILMED  
JMS  
DTIC



MICROCOPY RESOLUTION TEST CHART  
NATIONAL BUREAU OF STANDARDS-1963-A

32. R. E. Mould and R. D. Southwick, J. Amer. Ceram. Soc. 42 582 (1959).
33. R. E. Mould and R. D. Southwick, J. Amer. Ceram. Soc. 43 160 (1960).
34. T. A. Michalske, in Fracture Mechanics of Ceramics, Edited by R. C. Bradt, A. G. Evans, D. P. H. Hasselman and F. F. Lange, Plenum, New York, 1982.
35. T. P. Dabbs and B. R. Lawn, Phys. Chem. Glasses, in press.

Table 1

Fracture Mechanics Predictions of Lifetimes of Abraded and Scratched Glass\*

<u>Flaw Type</u>	<u><math>\sigma_f</math> (MPa)</u>	<u>Failure Times (sec)</u>	
		<u>Measured</u>	<u>Predicted<sup>†</sup></u>
Abrasion (60 grit SiC)	50.3	0.8	1.0
	47.0	4.0	3.0
	37.9	60.0	60.0
Scratch (320 grit emery cloth)	36.8	0.8	1.7
	33.0	4.0	5.0
	26.6	60.0	44.0

\* Data from Mould and Southwick (Ref. 32)

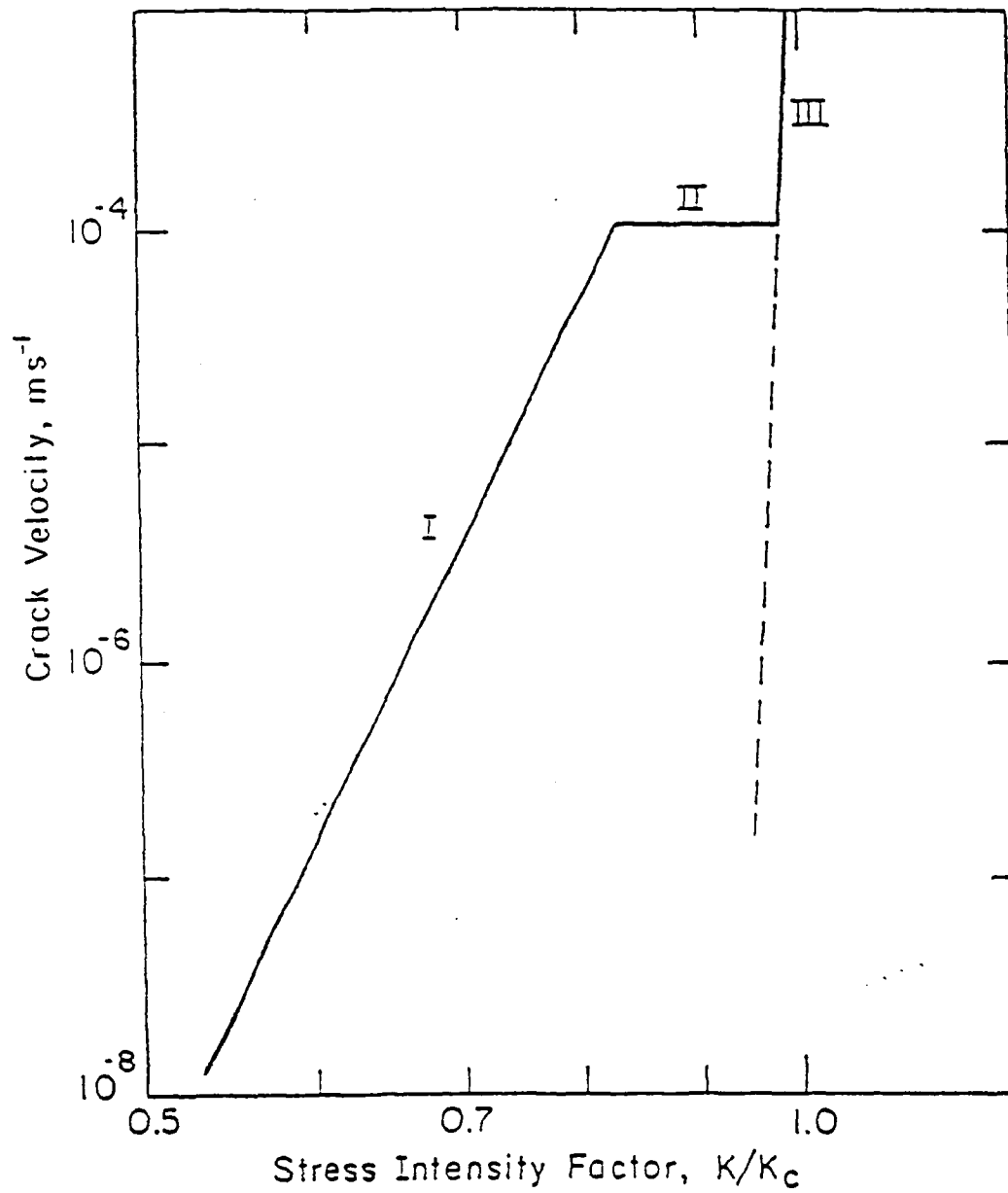
<sup>†</sup> Prediction from Eqns. 19 and 20.

FIGURE CAPTIONS

1. Variation of crack velocity with stress intensity factor for soda-lime glass in water vapour; region I is governed by reaction kinetics, region II by transport rate and region III is independent of environment.
2. (a) Vickers indentation in ZnS.  
(b) Schematic cross section of indentation showing deformation zone (shaded) and fractures; the half-penny radial cracks are oriented normal to the surface and parallel to the indentation diagonals, the penny-shaped lateral cracks are parallel to the surface.
3. Variation of inert strength with lateral/radial crack-size ratio  $c^L/c^R$  for Vickers indentations in soda-lime glass. Ratio  $c^L/c^R$  adjusted by varying interval between indentation and flexure. Dashed line designates scale of indentation impression for  $P = 5N$ . (after Ref. 26).
4. Dynamic fatigue response for indented soda-lime glass disks broken in water. Error bars are standard deviations (10-30 specimens). Solid curve through data for specimens annealed after indentation evaluated from Eqn. 3 in accordance with best fit of Eqn. 6b over the linear region. Solid curve through data for as-indented specimens is prediction of Eqn. 12 using kinetic fracture parameters obtained in the annealed data fit. Shaded regions indicate inert strengths. (after Ref. 26).
5. Evolution of indentation flaws in soda-lime glass/water system at constant applied stress rate,  $\dot{\sigma} = 0.15 \text{ MPa}\cdot\text{s}^{-1}$ . Data for specimens annealed after contact cycle and as-indented. Solid curves are predictions from Eqn. 12. (after Ref. 26).

6. Normalized dynamic fatigue data for soda-lime glass indented at specified loads and broken in water. Shaded band represents inert strength. Solid curve is the prediction of Eqn. 16. (after Ref. 30).
7. Dynamic fatigue of abraded soda-lime discs broken in water. Shaded band represents inert strength; solid curve is evaluation from Eqn. 12. (after Ref. 20).





XBL829-6509

Fig. 1

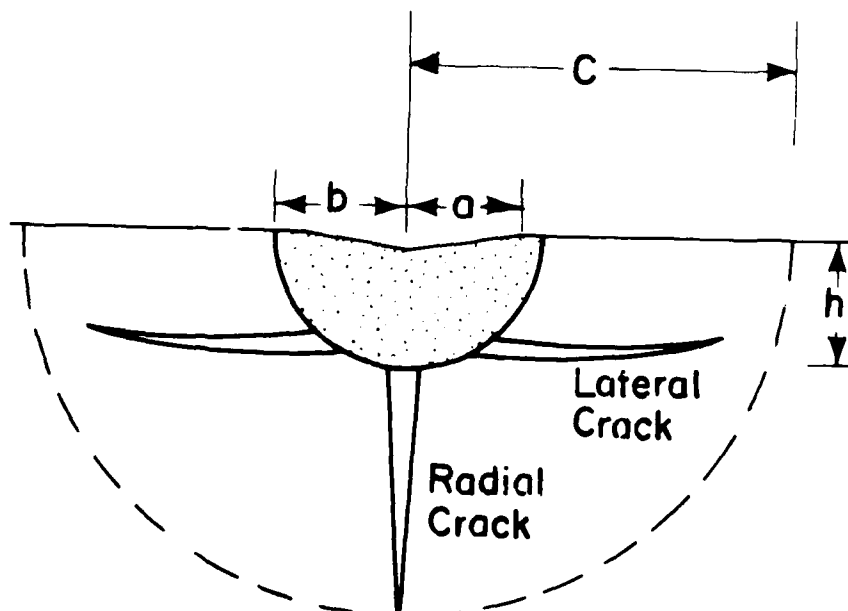
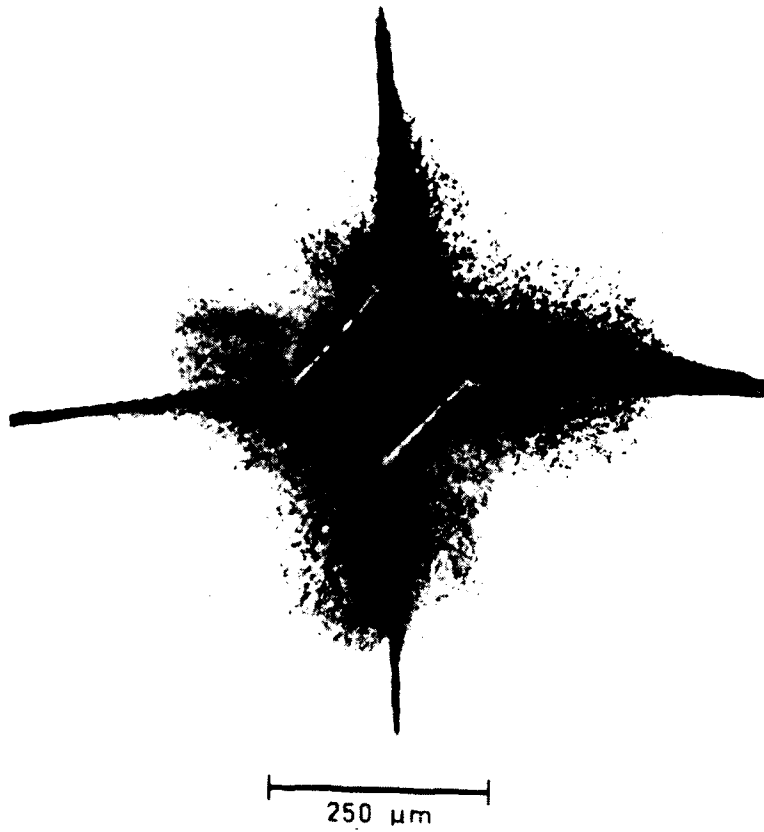


Fig. 2

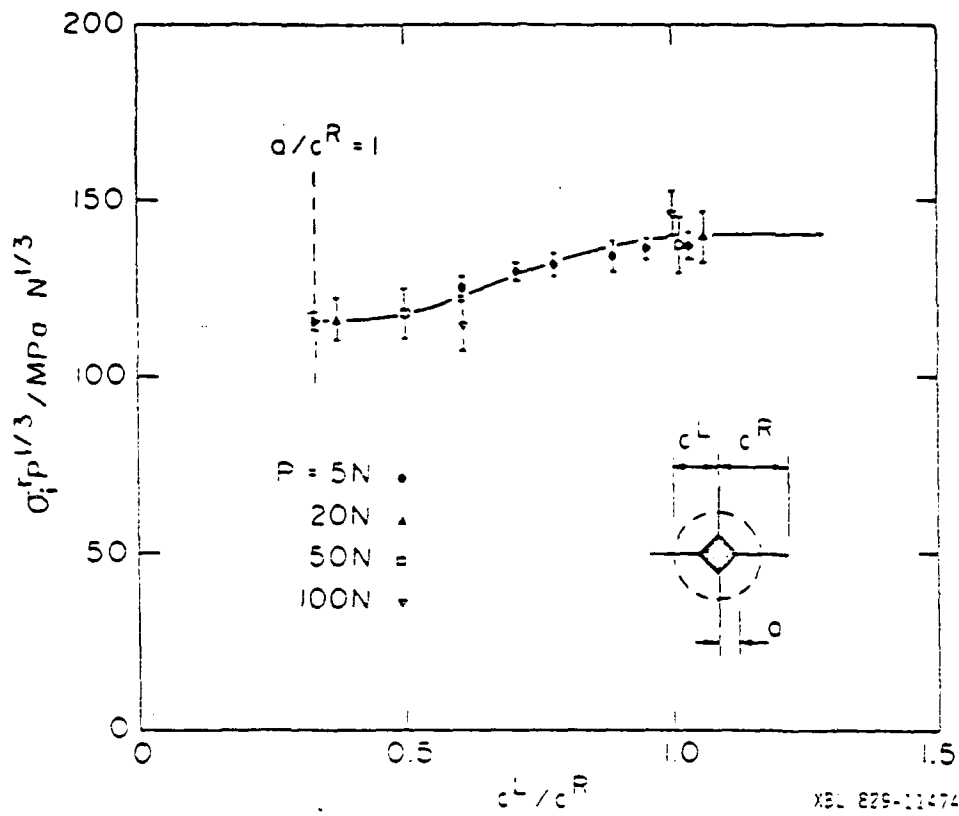
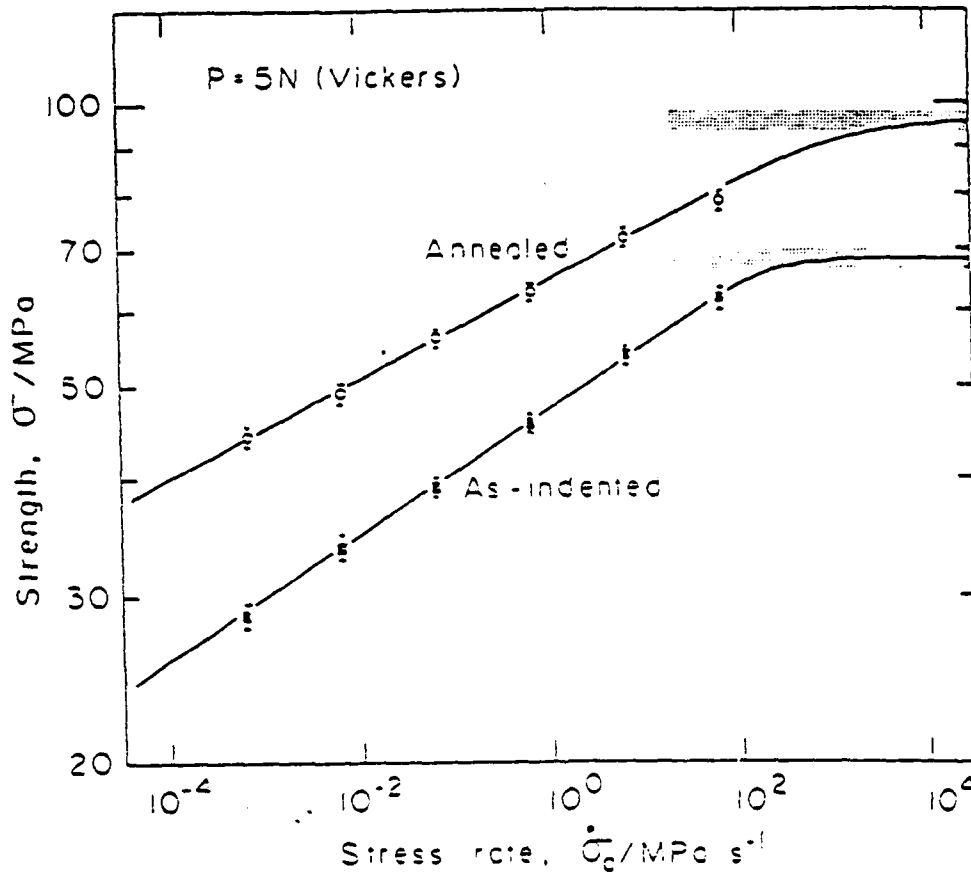
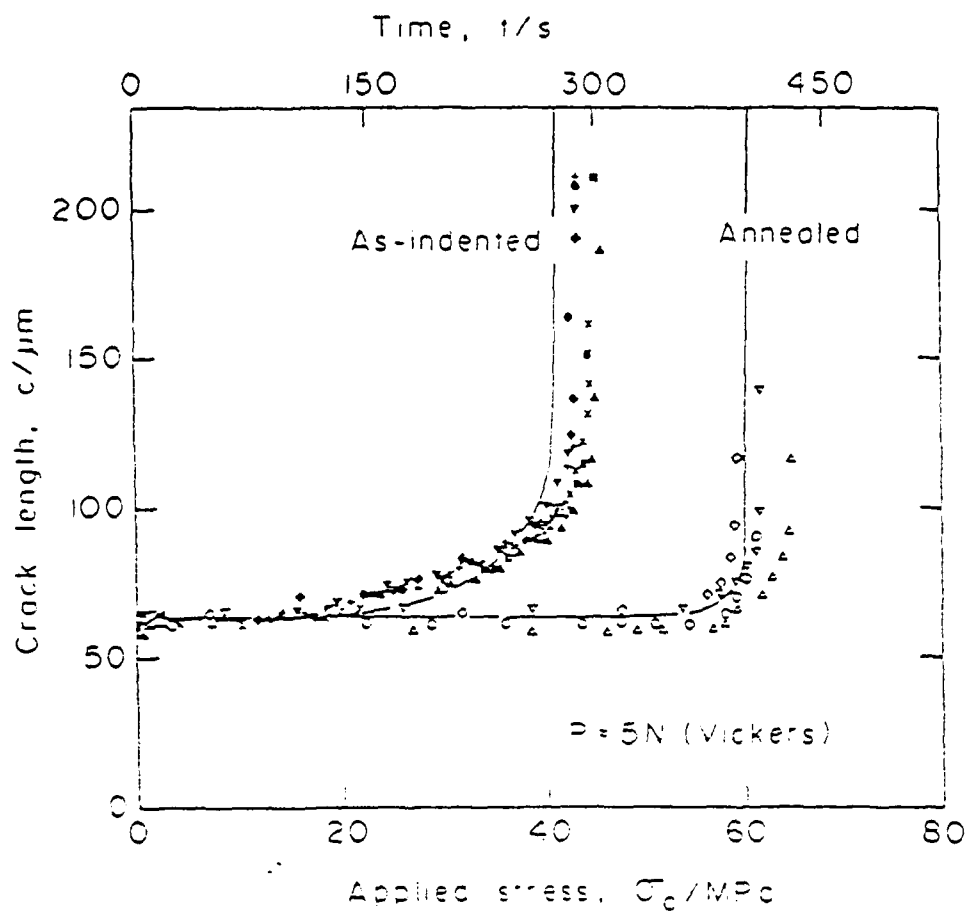


Fig. 3



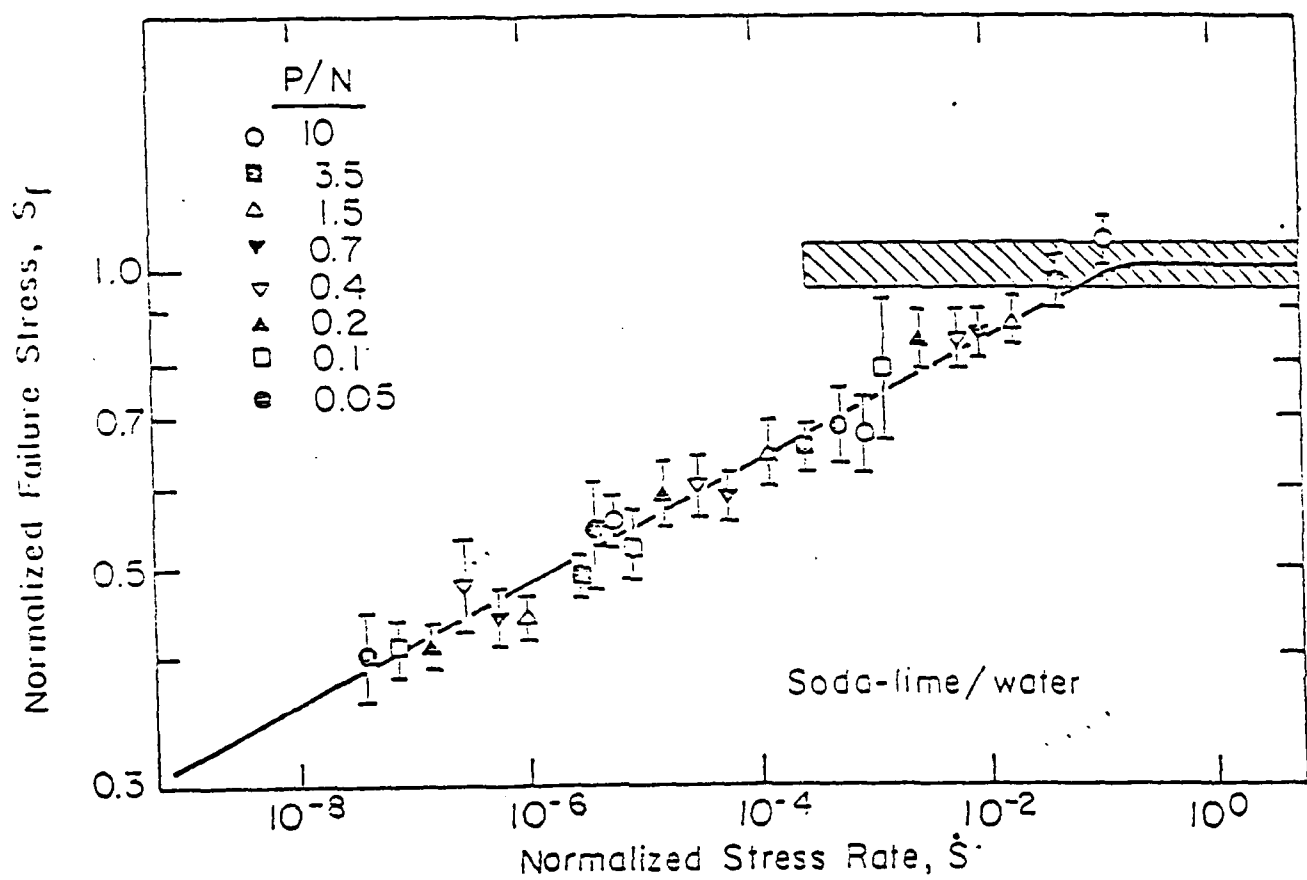
XSL 525-11475

Fig. 4



MSL 829-11473

Fig. 5



XBL 829-6508

Fig. 6

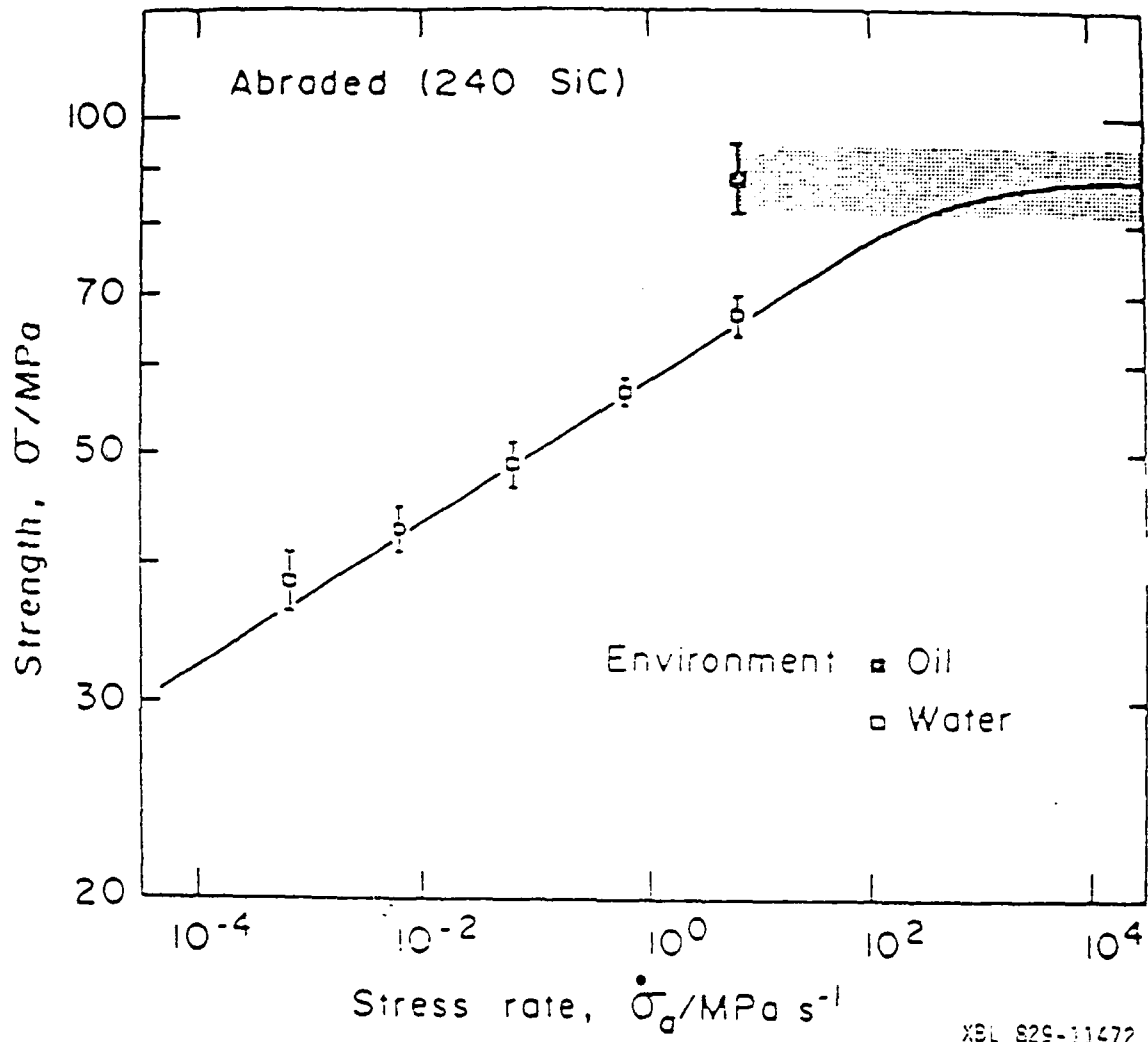


Fig. 7

-300-

RELIABILITY



CHAPTER X

THE STATISTICAL ANALYSIS OF BENDING STRENGTHS FOR BRITTLE SOLIDS:

A MULTIAXIAL FRACTURE PROBLEM

by

J. Lamon and A. G. Evans

Department of Materials Science and Mineral Engineering  
University of California  
Berkeley, CA 94720

THE STATISTICAL ANALYSIS OF BENDING STRENGTHS FOR BRITTLE SOLIDS:  
A MULTIAXIAL FRACTURE PROBLEM

by

J. Lamon and A. G. Evans

Department of Materials Science and Mineral Engineering  
University of California  
Berkeley, CA 94720

ABSTRACT

A general approach for the statistical analysis of brittle fracture under tensile multiaxial stress states has been evaluated for a fracture criterion based upon recent concepts of non-coplanar crack extension. The resultant failure expressions have been applied to bend tests and used to interpret experimental results obtained with porcelain cylinders. Implications for the interpretation of bending tests and some important trends in the failure strength with specimen size are discussed.

## 1. INTRODUCTION

Fracture in brittle solids, that fail by the direct extension of pre-existing flaws, is generally assumed to occur in accord with a weakest link description;<sup>1-4</sup>

$$P_f = 1 - \exp \left[ - \int_V dV \int_0^S g(S) dS \right] \quad (1)$$

where  $P_f$  is the failure probability of a component with volume  $V$ ,  $S$  is the observed fracture strength and  $g(S)dS$  represents the number of flaws in unit volume with a strength between  $S$  and  $S+dS$ . The application of eqn (1) is quite straightforward when the stress-state in the component is homogeneous. However, in many practical situations, the stress state is not homogeneous and proper account must then be taken of the spatial variation in the stress triaxiality. General theories of stress-state effects on the statistics of failure have recently been devised,<sup>5-7</sup> but have not yet been applied to specific test (or component) geometries. The dual intent of the present paper is to provide an experimental demonstration of the practical requirements for a multiaxial analysis (with emphasis upon a simple commonly used mechanical test, such as the bend test), coupled with the development of the related multiaxial weakest link expressions for the failure probability.

The experimental study of bending strengths is conducted on extruded porcelain cylinders, with span lengths selected to encompass both uniaxial tension and an appreciable component of shear. The porcelain material was chosen on the basis that it exhibits negligible acoustic emission activity prior to bending failure, indicative of minimal microcrack coalescence and hence, of the probable pertinence of weakest link concepts.

The statistical analysis of failure is conducted by incorporating recent concepts of non-coplanar crack extension<sup>8</sup>, as a fracture criterion, into a previously derived format for the failure probability.<sup>6</sup> Insertion of the stress distribution pertinent to bending tests (and of a mathematically convenient form of  $g(S)$ ), then permits the failure probability to be derived in terms of the imposed loading, the specimen size and the flaw strength parameters. The resultant failure probability expressions are used to derive flaw population parameters from the experimental results and to discuss implications for the interpretation of bending tests.

## 2. EXPERIMENTAL

### 2.1 Test Configurations

The experiments were conducted in three point bending on extruded porcelain cylinders with three diverse span lengths ( 5 or 7 mm radius). The span lengths used for the testing program were selected on the basis that at least one span be long enough to induce a predominantly uniaxial stress state, whereas the third span be sufficiently short that appreciable shear stresses exist within the test section. A stress analysis of the cylindrical flexure configuration (Appendix I) reveals that the ratio of the maximum shear stress,  $\tau_{\max}$ , to the maximum tensile stress,  $\sigma_{\max}$ , is given by;

$$\frac{\tau_{\max}}{\sigma_{\max}} = \frac{(3+2\nu)}{8(1+\nu)} \frac{R}{\ell} \quad (2)$$

where  $R$  is the cylinder radius,  $2\ell$  is the span length and  $\nu$  is Poisson's ratio. The span lengths selected to obtain an appropriate range in  $R/\ell$ , and hence  $\tau_{\max}/\sigma_{\max}$ , are summarized in Table I.

## 2.2 Test Results

The tests were performed in a dry environment, with short loading times, in order to minimize the influence of slow crack growth. The measured failure loads were expressed in terms of the equivalent maximum tensile stress (Appendix I) and the resultant cumulative failure probabilities obtained, as plotted in fig. 1. Inspection of the failure distributions suggests that a single flaw population dictates failure in the uniaxially stressed, long test specimens; whereas, two separate flaw populations influence the failure of the multiaxially stressed, short test specimens. This influence is substantiated by fractographic observations of flaw origins, which indicate that the failures at the low strength extreme of the multiaxial tests initiate predominantly within the interior of the test specimens; while most other failures originate primarily from surface located defects. The failure results for the short specimens were thus reordered, to conform with the two dominant populations, using the censored data method developed by Johnson.<sup>9</sup> This method provides an approximate initial estimate of the statistical parameters pertinent to both populations (a superior method for deducing these parameters is described in the subsequent section). Comparison of the reranked populations for the multiaxial specimen with the uniaxial population (fig. 2) reveals that the surface dominated populations in the three test geometries exhibit comparable shape parameters ( $\sim 19$ ), suggestive of a unique surface flaw population (a uniqueness that will be quantitatively addressed in a subsequent section); whereas a smaller shape parameter ( $\sim 11$ ) applies to the internal flaw population.

The internally located flaws that dominate the strength of the short specimens at the important, small extreme are subject to a combination of tension and shear (Appendix I). Quantitative statistical analysis of the results thus demands a multiaxial approach. The importance of a multi-axial statistical analysis of fracture is thereby substantiated, even for relatively simple test configurations such as the bending test.

### 3. MULTIAXIAL STATISTICAL ANALYSIS: GENERAL CONCEPTS

#### 3.1 The Equivalent Stress

A multiaxial fracture criterion provides the initial basis for a statistical analysis applicable to a general state of stress. For two-dimensional crack-like defects, several multiaxial crack advance criteria have been proposed.<sup>8,10,11</sup> A number of these criteria yield essentially similar crack advance predictions, and are

in reasonably good accord with experimental measurements. One of these criteria (that has a convenient form for incorporation into the probabilistic multiaxial failure expressions) is based on a maximum in the strain energy release rate,  $\mathcal{G}_{\max}$ , and is given by;<sup>8</sup>

$$\mathcal{G}_{\max} = \frac{(1+\nu)(1+\chi)}{4E} [K_I^4 + 6K_I^2 K_{II}^2 + K_{II}^4]^{1/2} \quad (3)$$

where  $E$  is Young's modulus,  $\chi = 3-4\nu$  under plane strain conditions,  $\chi = (3-\nu)/(1+\nu)$  under plane stress conditions, and  $K_I$  and  $K_{II}$  are the mode I and II stress intensity factors. For a crack subject to a normal tensile stress  $\sigma$  and an in-plane shear stress  $\tau$ , the stress intensity factors are:

$$\begin{aligned} K_I &= \sigma\sqrt{\pi a} \\ K_{II} &= \tau\sqrt{\pi a} \end{aligned} \quad (4)$$

Substituting  $K_I$  and  $K_{II}$  into equation (3) then gives;

$$\frac{E\mathcal{G}_{\max}}{\pi a} = \frac{(1+\nu)(1+\chi)}{4} [\sigma^4 + 6\sigma^2\tau^2 + \tau^4]^{1/2} \quad (5)$$



It is now convenient to define an equivalent stress  $\sigma_E$ , as the uniaxial tensile stress that would induce the same energy release rate  $\mathcal{G}_{\max}$  as the actual stress  $(\sigma, \tau)$ . This stress is simply:

$$\sigma_E = \left[ \frac{E \mathcal{G}_{\max}}{\lambda \pi a} \right]^{1/2} \equiv [\sigma^4 + 6\sigma^2 \tau^2 + \tau^4]^{1/4} \quad (6)$$

where  $\lambda$  is unity for plane stress conditions, and  $(1-\nu^2)$  for plane strain. Crack extension can be considered to occur when the equivalent uniaxial tensile stress  $\sigma_E$  attains the equivalent material strength,  $S_E$ , dictated by the criticality,  $\mathcal{G}_{\max} = \mathcal{G}_c$ . It is assumed in the present study that the equivalent stress applicable to two-dimensional cracks also affords an adequate characterization of the advance of the three-dimensional crack-like defects that typically dictate the strength of ceramic polycrystals.<sup>12</sup> Further study will be needed to investigate this premise.

### 3.2 The Failure Probability

Fracture under multiaxial stress states can be evaluated by determining the flaw density function for each volume element and summing over all volumes. The failure probability of  $\Delta P$  for each element (c.f. eqn 1) is given by:

$$1 - \Delta P = \exp[-\Delta V \int_0^S g(S_{1,2,3}) dS] \quad (7)$$

where  $g(S_{1,2,3})dS$  is the number of flaws per unit volume with a strength between  $S$  and  $S+dS$ ;  $S_1, S_2, S_3$  denote the principal stresses at the fracture criticality and  $\Delta V$  is a volume element within which the principal stresses are essentially uniform.

Fracture initiates from those flaws subject to the critical equivalent stress,  $S_E$ . The flaw density function can consequently be derived from the volume distribution of the critical equivalent stress  $S_E$ . A spherical unit volume (figure 3) is convenient for evaluating the effect of the principal stress field upon the flaw density function in the presence of three-dimensional crack-like defects. The crack-like flaws are then located in planes tangent to the sphere and operated on by tensile and shearing stresses ( $\sigma$ ,  $\tau$ ), induced by the principal stresses ( $\sigma_1$ ,  $\sigma_2$ ,  $\sigma_3$ ) such that;

$$\begin{aligned}\sigma &= \sigma_1 l_1^2 + \sigma_2 l_2^2 + \sigma_3 l_3^2 \\ \tau^2 &= \sigma_1^2 l_1^2 + \sigma_2^2 l_2^2 + \sigma_3^2 l_3^2 - (\sigma_1 l_1^2 + \sigma_2 l_2^2 + \sigma_3 l_3^2)^2\end{aligned}\quad (8)$$

where  $l_1$ ,  $l_2$  and  $l_3$  represent the direction cosines:

$$\begin{aligned}l_1 &= \cos\phi \cos\psi \\ l_2 &= \cos\phi \sin\psi \\ l_3 &= \sin\phi\end{aligned}$$

The magnitude of the principal stress at the crack extension condition can thus be expressed in terms of the equivalent strength by the relation;

$$\begin{aligned}S_E^4 &= \left( \sum_{i=1}^3 S_i l_i^2 \right)^4 + 6 \left( \sum_{i=1}^3 S_i l_i^2 \right)^2 \left[ \sum_{i=1}^3 S_i^2 l_i^2 - \left( \sum_{i=1}^3 S_i l_i^2 \right)^2 \right] + \\ &\quad \left[ \sum_{i=1}^3 S_i^2 l_i^2 - \left( \sum_{i=1}^3 S_i l_i^2 \right)^2 \right]^2\end{aligned}\quad (9a)$$

or, in reduced form;

$$S_E/S_1 = f \left[ \frac{S_2}{S_1}, \frac{S_3}{S_1}, \phi, \psi \right] \quad (9b)$$

The flaw density function  $g(S_{1,2,3})$  can now be related to the flaw density  $g_E(S_E)$  by considering small elements (fig. 3) with a vol/unit sphere given by:  $dV = (1/4\pi)\cos\phi d\phi d\psi$ . Then the flaw density function  $g(S_{1,2,3})$  may be expressed as;

$$g(S_{1,2,3})dS = (1/2\pi) \int_0^{\pi/2} \int_0^{2\pi} g_E(S_E) dS_E \cos\phi d\phi d\psi \quad (10)$$

A functional relation for  $g_E(S_E)$  is needed to proceed with the analysis. One of the commonly observed functional relations is a simple power function.<sup>6,13</sup> Assuming that such a function describes fracture:

$$g_E(S_E) = m S_E^{m-1} S_0^{-m} \quad (11)$$

where  $m$  is the shape parameter and  $S_0$  the scale factor. The flaw density function for specified values of the principal stress ratios  $\sigma_2/\sigma_1$  and  $\sigma_3/\sigma_1$  then becomes:

$$\begin{aligned} g(S_{1,2,3})dS &= m \left( \frac{S_1^{m-1} dS_1}{S_0^m} \right) \left[ \frac{1}{2\pi} \int_0^{\pi/2} \int_0^{2\pi} f^{m+1} \cos\phi d\phi d\psi \right] \\ &= m \left( \frac{S_1^{m-1} dS_1}{S_0^m} \right) I \left( m, \frac{\sigma_2}{\sigma_1}, \frac{\sigma_3}{\sigma_1} \right) \end{aligned} \quad (12)$$

where  $f$  is defined in eqn (9b).

Substituting  $g(S_{1,2,3})$  into equation (7) gives the failure probability for each element as;

$$\Delta P_{ij} = 1 - \exp \left[ -\Delta V_{ij} I_{ij}(m) \left( \frac{S_{ij}}{S_0} \right)^m \right] \quad (13)$$

where  $I_{ij}(m)$  denotes the value of  $I(m, \sigma_2/\sigma_1, \sigma_3/\sigma_1)$  at the specific stress ratios pertinent to the volume element  $\Delta V_{ij}$  and  $S_{ij}$  represents the strengths of the element (expressed in terms of one of the principal stresses).

The total failure probability for the component, evaluated from the product of the individual survival probabilities, is then;

$$P_f = 1 - \exp \left[ - \sum_{ij} \Delta V_{ij} I_{ij}(m) \left( \frac{S_{ij}}{S_0} \right)^m \right] \quad (14)$$

#### 4. STATISTICAL ANALYSIS OF BEND TESTS

##### 4.1 The Failure Probability

For a cylinder subject to three point bending (figure 4) the principal stress field consists of two components, a tensile component  $\sigma_1$  and a compressive component  $\sigma_2$ :

$$\begin{aligned} \sigma_1 &= \frac{\sigma_z}{2} + \sqrt{\frac{\sigma_z^2}{4} + \tau_{xz}^2} \\ \sigma_2 &= -\frac{\sigma_z}{2} + \sqrt{\frac{\sigma_z^2}{4} + \tau_{xz}^2} \end{aligned} \quad (15)$$

where  $\sigma_z$  is the stress normal to the cross section, and  $\tau_{xz}$  the shear stress acting in the vertical longitudinal plane (Appendix 1). The

most highly stressed surface elements are thus essentially subject to uniaxial tension and a simple uniaxial analysis should permit the interpretation of surface flaw induce fracture. Uniaxial analysis yields the failure probability

$$P_s = 1 - \exp \left[ -(\hat{S}/S_0)^m \left[ 4R\ell/(m+1) \right] \int_0^{\theta_0(R/\ell)} \cos^m \theta d\theta \right] \\ \equiv 1 - \exp \left[ -(\hat{S}/S_0)^m K_s(m, R\ell, R/\ell) \right] \quad (16)$$

where  $\theta_0$  is the angular location at which the normal tension  $\rightarrow 0$ .

For  $0.7 > R/\ell > 0$ , as in the present experiments,  $P_s$  is essentially independent of  $R/\ell$ .

Conversely, the internally located flaws are subject to appreciable biaxial stress and hence, a biaxial statistical analysis is needed to adequately characterize failures that initiate from internal flaws. The statistical analysis of such failures can be conveniently performed by subdividing the cylinder into volume elements  $\Delta V_i$  exposed to uniform levels of the principal stress ratio  $\sigma_2/\sigma_1$  (fig. 5). The failure probability deduced from eqn (14) then reduces to:

$$\Delta P_i = 1 - \exp \left[ -\Delta V_i I_i(m) \left( \frac{S_i}{\sigma_0} \right)^m \right] \quad (17)$$

where  $I_i(m) = I(t_i, m)$ , such that  $t_i = \sigma_2/\sigma_1$  in volume element  $\Delta V_i$ .

The analytic expression for  $I_i(m)$ , obtained from the flaw density function  $g(\sigma_{1,2})$ , is given in Appendix II. It is convenient to express  $S_i$  in terms of the peak value,  $\hat{S}$ , of the normal stress  $\sigma_z$

at fracture. This can be achieved by firstly expressing  $\sigma_1$  in terms of the maximum normal stress  $\sigma_{\max}$  (Appendix I);

$$\sigma_1/\sigma_{\max} = \left\{ \frac{x}{2R} \left(1 - \frac{z}{l}\right) + \left[ \frac{x^2}{4R^2} \left(1 - \frac{z}{l}\right)^2 + \frac{(3+2\nu)^2 R^2}{64(1+\nu)^2 l^2} \left(1 - \frac{x^2}{R^2} - \frac{y^2(1-2\nu)}{R^2(3+2\nu)}\right)^2 \right]^{1/2} \right\}$$

$$\equiv h(x/R, y/R, z/l, R/l) \quad (18)$$

The failure probability  $\delta P_i$  of a small volume element  $\delta V_i$  can consequently be expressed in terms of  $\hat{S}$  as

$$\delta P_i = 1 - \exp \left[ - \delta V_i I_i(m) (\hat{S}/S_0)^m h_i^m \right] \quad (19)$$

where  $h_i$  is the uniform value taken by  $h$  in element  $\delta V_i$ . However since  $h$  is not constant over the volume elements  $\Delta V_i$  chosen for analysis of the bend test (i.e. elements subject to a homogeneous stress state, fig. 5), the elemental failure probability becomes;

$$\Delta P_i = 1 - \exp \left[ - I_i(m) (\hat{S}/S_0)^m \int_{\Delta V_i} h^m dV \right] \quad (20)$$

and the total failure probability can be expressed as;

$$P_V = 1 - \exp \left[ - (\hat{S}/S_0)^m \sum_{i=1}^{i=n} I_i(m) \int_{\Delta V_i} h^m dV \right]$$

$$\equiv 1 - \exp \left[ - (\hat{S}/S_0)^m K_V(m, R^2 l, R/l) \right] \quad (21)$$

where  $n$  is the number of elements. The parameter  $K_V$ , obtained by numerical integration, is plotted in figure 6. For the present study the integration of  $\int_{\Delta V_i} h^m dV$  has been carried out over the central region of cylinder ( $n=3$ ) where the volume elements  $\Delta V_i$  are exposed to relatively

high values of the principal stress ratio,  $\sigma_2/\sigma_1$  (0.8, 0.9 and 1). This choice has been made because, as shown by figure 7, the stresses in the central region are very sensitive to changes in the dimensional ratio  $R/\lambda$ ; whereas the stresses in the remainder of the cylinder are essentially invariant with  $R/\lambda$ .

#### 4.2 Comparisons With Experiment: Size Effects

Fractures that occur from a unique surface flaw population (under weakest link conditions) subject to the uniaxial stress state that prevails in the present test configuration, should exhibit fracture strengths that scale directly with the surface area (eqn 16). Specifically, for cylinders with a characteristic radius,  $R$ , the strength at a given failure probability should vary with span length in accord with the proportionality  $S \propto \lambda^{-1/m}$ . This proportionality is approximately satisfied by the results obtained in the porcelain specimens, as demonstrated by comparing the failure strengths of surface initiated failures from the long and short span tests, at constant probability (fig. 8). Furthermore, consistent shape,  $m$ , and scale,  $S_0$ , parameters obtain for both data sets as indicated in Table II and on fig. 2.

It is also possible to derive shape and scale parameters pertinent to the internal flaw population by fitting experimental data, obtained on the short span specimens, to the total failure probability  $P_T$  in the presence of both populations. The total failure probability  $P_T$  may be obtained from equations (16) and (21) as:

$$P_T = 1 - \exp \left[ - \left( \frac{\hat{S}}{S_0} \right)^{m_s} K_s (m_s, R/\ell, R\ell) - \left( \frac{S_v}{S_0} \right)^{m_v} (m_v, R/\ell, R^2\ell) \right] \quad (22)$$

where the subscripts  $s$  and  $v$  refer to the surface and volume populations respectively. Inserting the shape parameter for the surface population determined from long span length tests ( $m=19$ , see Table II) into eqn (22), the appropriate scale factor for the surface population and shape and scale parameters for the internal population can be deduced (corresponding to the minimum difference between experimental and theoretical data). The results, summarized in Table II, indicate smaller values of both the shape and scale parameters for the internal flaw population, consistent with the dominance of this population at the low strength extreme of the short span tests.

The statistical parameters obtained for the surface and internal flaw populations can be used in conjunction with the corresponding probabilistic failure expressions to anticipate some important trends in the failure strength with specimen size. Inserting appropriate scale and shape parameters for both populations from Table II, the strength  $\hat{S}$  at the median failure probability ( $P_T = 0.5$ ) can be deduced from eqn (22), and plotted as a function of span length  $\ell$  for several choices of the radius  $R$  (fig. 9). It is evident that the strength is inversely dependent on the volume and/or the surface area.

An important parameter is the effective probability level  $P^*$  (fig. 10) at which there is a transition from surface flaw failure at high strength levels to failure from internal flaws at the small strength extreme. This probability, obtained by equating failure strengths for the two separate populations and deriving the common probability level, is given by;



$$P^* = 1 - \exp \left\{ - \left( \frac{S_0^V}{S_0^S} \right)^{(m_V m_S / (m_V - m_S))} \frac{K_S^{m_V / (m_V - m_S)}}{K_V^{m_S / (m_V - m_S)}} \right\} \quad (23)$$

The transition probability is plotted as a function of span length for several radii in fig.11 . The effects of dimensions upon the transition probability  $P^*$  indicate that, consistent with intuition, the smaller the stressed volume/surface area ratio (i.e. smaller specimen radii at constant span length) the greater the dominance of the surface flaw population. Specifically, for a 7 mm specimen radius, eqn (23) predicts that fracture at experimentally reasonable probability levels ( $P \sim 10^{-3}$ ) is dominated by the surface flaw population, when the span lengths exceed  $\sim 40$  mm. This is consistent with the fracture origin observations performed on the long span specimens (section 2.2).

Conversely, a high probability of fracture from internal flaws ( $P \geq 0.99$ ) is predicted to obtain in specimens with the same radius (7 mm), but very small span lengths,  $< 5$  mm. However, the acquisition of data on such short specimens has proven prohibitively difficult. Hence, a more rigorous test of the multiaxial model awaits the generation of data on specimens tested in modes that more effectively sample the internal flaw population.

## 5. CONCLUSION

Bending strength distributions obtained at diverse span lengths for porcelain cylinders exhibited an appreciable dependence on the span to radius ratio. Two concurrent flaw populations - internal and surface dominated - were identified from test on specimens with short span lengths, such that the internal flaw population dominated at the low strength extreme.

A general multiaxial approach was developed for quantitative analysis of the results, based upon a non-coplanar strain energy release rate criterion. Insertion of the stress distribution pertinent to bending tests then permitted the failure probability to be derived in terms of the strength, the specimen size and the flaw strength parameters.

Consistent shape and scale parameters were obtained for the surface flaw population at different span lengths. The internal flaw population parameters (determined from the total failure probability) were smaller than those deduced from the surface flaw population, consistent with the dominance of this population at the low strength extreme of the short span tests.

Some important strength trends with specimen size were anticipated. The strength was shown to be inversely related to the volume and/or surface area at given failure probability. The internal flaw population has been shown to dominate at large radii and short span lengths, while the surface flaw population becomes important at small radii and long span lengths.

#### ACKNOWLEDGMENTS

The authors wish to thank the Office of Naval Research for supporting this work under Contract No. N00014-81-K-0362. One of us (J.L.) also thanks the Renault Co. and the 'Centre des Materiaux de l'Ecole des Mines de Paris' for financial assistance.

Appendix 1

Stress Distribution in Cylinders Subjected to 3 Point Bending Conditions

For a cylinder subjected to three point bending conditions (Fig. 4), the stress field consists of a normal tensile component  $\sigma_z$  and two shear components  $\tau_{xz}$  and  $\tau_{yz}$  which can be described by the following relations:<sup>14</sup>

$$\sigma_z = \frac{4F(\ell-z)x}{\pi R^4} \quad (A1)$$

$$\tau_{xz} = \frac{(3+2\nu)F}{2(1+\nu)\pi R^4} [R^2 - x^2 - y^2 \left(\frac{1-2\nu}{3+2\nu}\right)] \quad (A2)$$

$$\tau_{yz} = \frac{(1+2\nu)F_{xy}}{(1+\nu)\pi R^4} \quad (A3)$$

where  $2F$  is the applied load,  $2\ell$  the span length and  $R$  the cylinder radius.<sup>†</sup>

The shear component  $\tau_{yz}$  is negligible, when compared with  $\sigma_z$  and  $\tau_{xz}$  ( $\tau_{yz}$  is orders of magnitude smaller than  $\tau_{xz}$ , except in a subsurface volume where it is considerably smaller than  $\sigma_z$ , figure A1).

The stress components  $\sigma_z$  and  $\tau_{xz}$  expressed in terms of their peak values  $\sigma_{\max}$  and  $\tau_{\max}$  reduce to:

$$\sigma_z = \sigma_{\max} \left(\frac{\ell-z}{\ell}\right) \left(\frac{x}{R}\right) \quad (A4)$$

$$\tau_{xz} = \tau_{\max} \left[ 1 - \frac{x^2}{R^2} - \frac{y^2}{R^2} \left(\frac{1-2\nu}{3+2\nu}\right) \right] \quad (A5)$$

<sup>†</sup>Rounding effects within the vicinity of the peak stress have been neglected.<sup>15</sup> This neglect will result in a relative overestimate of the failure probability for the short specimens, in which the rounding effect is more substantial. However, rounding influences the stress over a small area of surface and its effect is assured to be small.

where

$$\sigma_{\max} = \frac{4F_l}{\pi R^3} \quad \text{and} \quad \tau_{\max} = \frac{(3+2\nu)F}{2(1+\nu)\pi R^2}$$

Appendix II

Determination of the Flaw Density Function in Cylinders

Subjected to 3-Point Bending Conditions

The flaw density function  $g(S_{1,2})$  within small elements (volume/ unit sphere  $dV = (1/4\pi)\cos\phi d\phi d\psi$ ) is derived from the flaw density  $g_E(S_E)$  as;

$$g(S_{1,2})dS = \frac{1}{2\pi} \int_0^{\pi/2} \int_0^{2\pi} g_E(S_E) dS_E \cos\phi d\phi d\psi \quad (A6)$$

The equivalent strength  $S_E$  needed to propagate cracks can be derived from equation (A6) by substituting the following relations for  $\sigma$  and  $\tau$ , expressed in terms of the principal stress  $\sigma_1$  and  $\sigma_2$ :

$$\sigma = \sigma_1 \cos^2\phi \left[ \cos^2\psi - \frac{\sigma_2}{\sigma_1} \sin^2\psi \right] \quad (A7)$$

$$\tau^2 = \sigma_1^2 \cos^2\phi \left[ \cos^2\psi + \frac{\sigma_2^2}{\sigma_1^2} \sin^2\psi \right] - \sigma_1^2 \cos^4\phi \left[ \cos^2\psi - \frac{\sigma_2}{\sigma_1} \sin^2\psi \right]^2 \quad (A8)$$

The expression for  $S_E$  is thus:

$$\begin{aligned} S_E &= S_1 \cos\phi \left[ u_2^2 + 4u_1^2 u_2 \cos^2\phi - 4u_1^4 \cos^4\phi \right]^{1/4} \\ &\equiv S_1 \cos\phi \left[ \beta \left( \frac{\sigma_2}{\sigma_1}, \phi, \psi \right) \right]^{1/4} \end{aligned} \quad (A9)$$

where  $u_1$  and  $u_2$  designate the following expressions:

$$u_1 = \cos^2\psi - \frac{\sigma_2}{\sigma_1} \sin^2\psi \quad (A10)$$

$$u_2 = \cos^2\psi + \frac{\sigma_2^2}{\sigma_1^2} \sin^2\psi \quad (A11)$$

The flaw density function is then given by:

$$\begin{aligned}
 g(S_{1,2})dS &= \left(\frac{S_1}{S_0}\right)^m dS_1 \left[ \frac{1}{2\pi} \int_0^{\pi/2} \int_0^{2\pi} \cos^{m+2} \phi \left[ \beta \left( \frac{\sigma_2}{\sigma_1}, \phi, \psi \right) \right]^{[(m+1)/4]} d\phi d\psi \right] \\
 &\equiv \left(\frac{S_1}{S_0}\right) dS_1 I_i(m)
 \end{aligned} \tag{A12}$$

where  $I_i(m) = I(t_i, m)$ :  $\sigma_2/\sigma_1$  being equal to  $t_i$ .

References

1. A. Freudenthal; pp. 592-621 in Fracture, Vol. II. Edited by Harold Liebowitz, Academic Press, New York, 1969.
2. J. R. Matthews, F. A. McClintock, and W. J. Shack, "Statistical Determination of Surface Flaw Density in Brittle Materials," J. Am. Ceram. Soc. 59 [7-8] 304-308 (1976).
3. A. G. Evans and T. G. Langdon, "Structural Ceramics" Prog. Mater. Sci., 21 [3-4] 171-441 (1976).
4. A. G. Evans and R. L. Jones, "Evaluation of a Fundamental Approach For the Statistical Analysis of Fracture," J. Am. Ceram. Soc., 61 [3-4], 156-60 (1978).
5. S. B. Batdorf and J. G. Crose, "A Statistical Theory for the Fracture of Brittle Structures Subjected to Polyaxial Stress States," J. Appl. Mech., 41 (1974) 459-465.
6. A. G. Evans, "A General Approach for the Statistical Analysis of Multiaxial Fracture," J. Am. Ceram. Soc. 61 [7-8] 302-308 (1978).
7. S. B. Batdorf and M. L. Heinisch, Jr., "Weakest Link Theory Reformulated for Arbitrary Fracture Criterion," J. Am. Ceram. Soc. 61 [7-8], 355-358 (1978).
8. T. K. Hellen and W. S. Blackburn, "The Calculation of Stress Intensity Factors for Combined Tensile and Shear Loading," Int. Journ. Fract. 11 [4] 605-617 (1975).
9. L. G. Johnson, "The Statistical Treatment of Fatigue Experiments," Elsevier Pub. Co., New York, 1964.
10. G. C. Sih, "Strain Energy Density Factor Applied To Mixed Mode Crack Problems," Int. Journ. Fract. 10 [3] 305-321 (1974).

11. B. Cotterell and J. R. Rice, "Slightly Curved or Kinked Cracks," Int. Jnl. Frac. 16 (1980) 155-169.
12. A. G. Evans, "Structural Reliability of Ceramics: A Processing Dependent Phenomenon," Jnl. Amer. Ceram. Soc., in press.
13. W. Weibull, "Phenomenon of Rupture in Solids", Ingenisersvetenskapsakad Handi, 1939, No. 153, pp. 1-55.
14. N. I. Muskhelishvili, "Some Basic Problems of the Mathematical Theory of Elasticity Fundamental Equations, Plane Theory of Elasticity, Torsion and Bending," P. Noordhoff, Groningen, 1953.
15. S. Timoshenko and J. N. Goodier, Theory of Elasticity, (McGraw Hill), N.Y. (1950) p. 100.



Table I.

Test Conditions

Span Length	Radius	$R/\lambda$	$\tau_{\max}/\sigma_{\max}$
190 mm	5 mm	0.053	0.019
140 mm	7 mm	0.1	0.035
20 mm	7 mm	0.7	0.245

Table II  
Shape and Scale Parameters

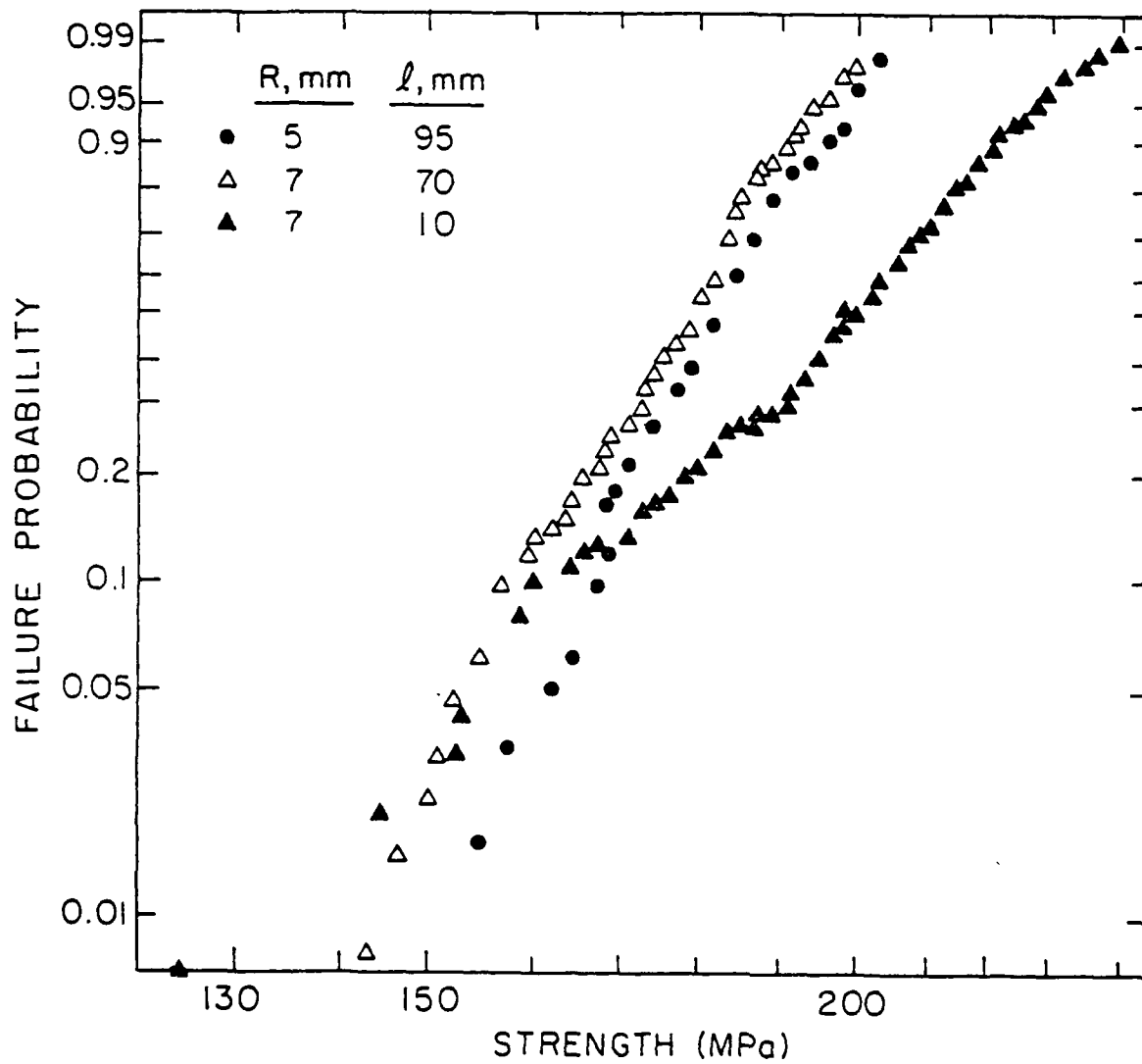
R/ $\lambda$	Shape Parameter $m$	Scale factor $S_0$
0.05	19.3	107.25
0.1	17.6	101.00
0.7	19	115.00
	9.12	9.5

Surface population  
Center population

FIGURE CAPTIONS

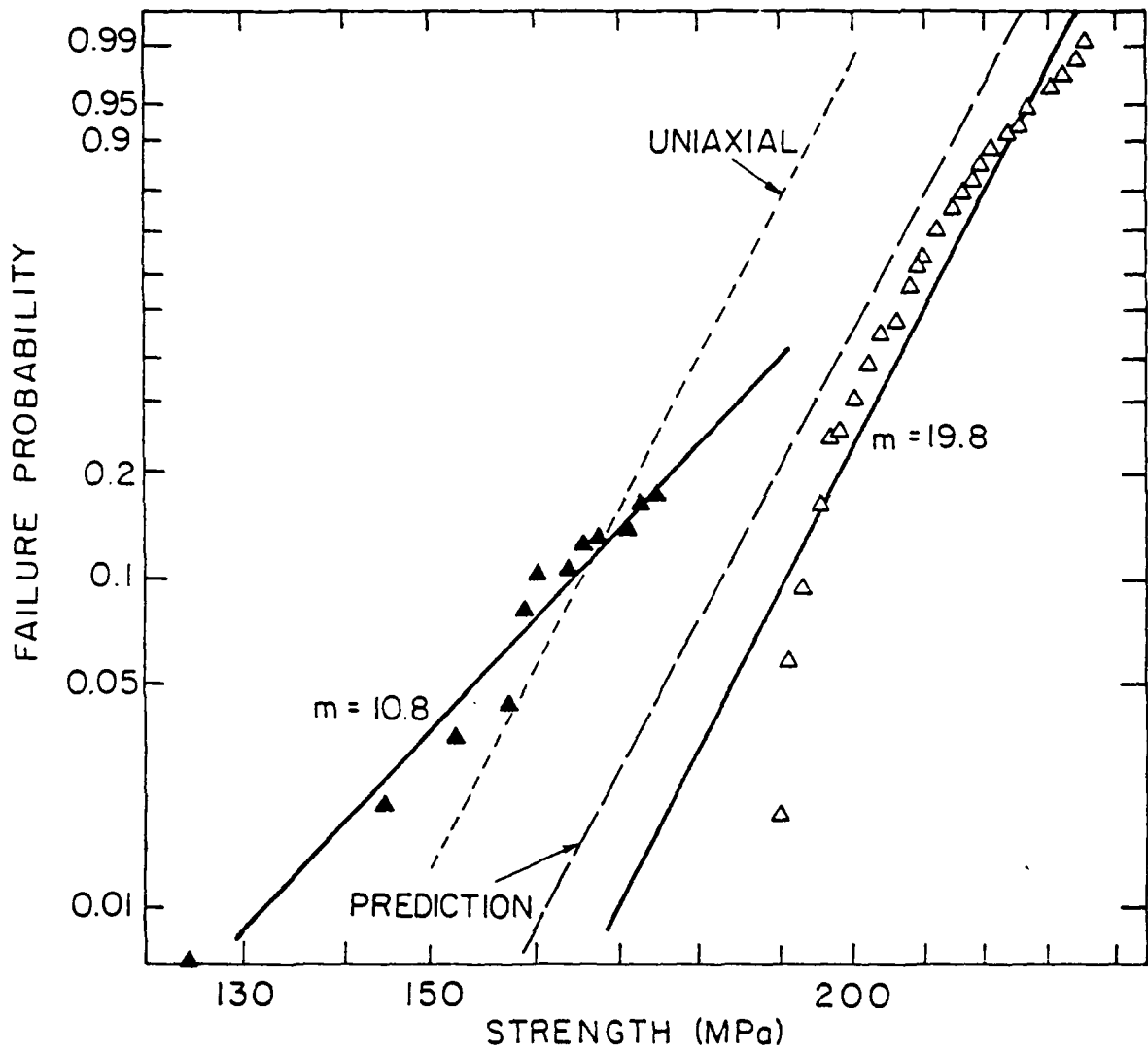
- Figure 1. Strength distributions for porcelain cylinders with various span lengths tested under bending conditions.
- Figure 2. Separated strength distributions for short span specimens obtained after analysis by the censored data method. The uniaxial strength distribution from the long span tests ( $R = 7$  mm,  $\ell = 70$  mm) and the corresponding distributions predicted for the short span tests are also represented.
- Figure 3. Element used to determine fracture condition.
- Figure 4. Diagram of cylinder subject to three point bending.
- Figure 5. Variation of the principal stress ratio  $\sigma_2/\sigma_1$  over (a) the cross-section and (b) a longitudinal section of a cylinder ( $R/\ell = 0.7$ ). Also included is the definition of a volume element  $\Delta V_i$ .
- Figure 6. A plot of the dimensionless parameter  $K_V/R^2\ell$  as a function of the dimensional ratio  $R/\ell$  for  $m = 9$ .
- Figure 7. A plot of the equivalent stress  $\sigma_E$  in the principal stress plane ( $\psi = 0$ ) at the center of cylinder ( $x/R = 0.1$ ,  $z=0$ ) and at the location ( $x/R = 0.5$ ,  $z=0$ ) for several values of the dimensional ratio  $R/\ell$ .
- Figure 8. A comparison of failure strengths of surface initiated failures from long span ( $R/\ell = 0.1$ ) and short span tests ( $R/\ell = 0.7$ ). Also shown is the prediction based upon constancy of flaw populations.

- Figure 9. Plot of the strength  $\hat{S}$  at the median failure probability ( $P_T = 0.5$ ) as a function of half span length for several values of the cylinder radius.
- Figure 10. A schematic of the dependence of transition probability  $P^*$  upon specimen dimensions  $R$  and  $l$ .
- Figure 11. Plot of the transition probability  $P^*$  as a function of half span length for several values of the cylinder radius.
- Figure A1. Distribution of the stress components over the volume of cylinders subject to three point bending.



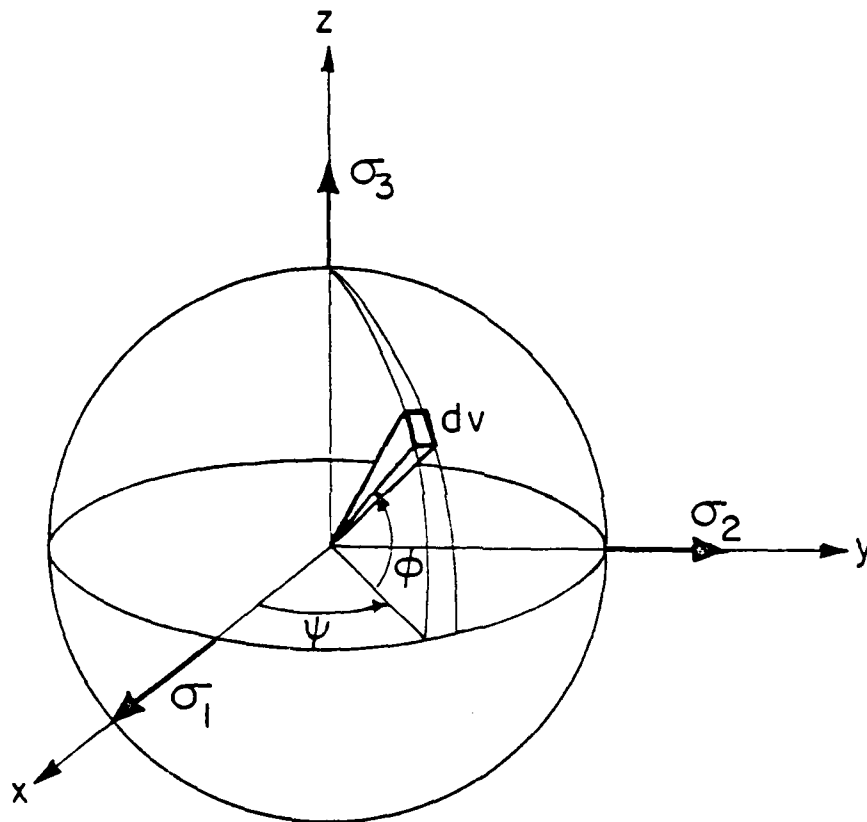
XBL 82I-5055

Fig. 1



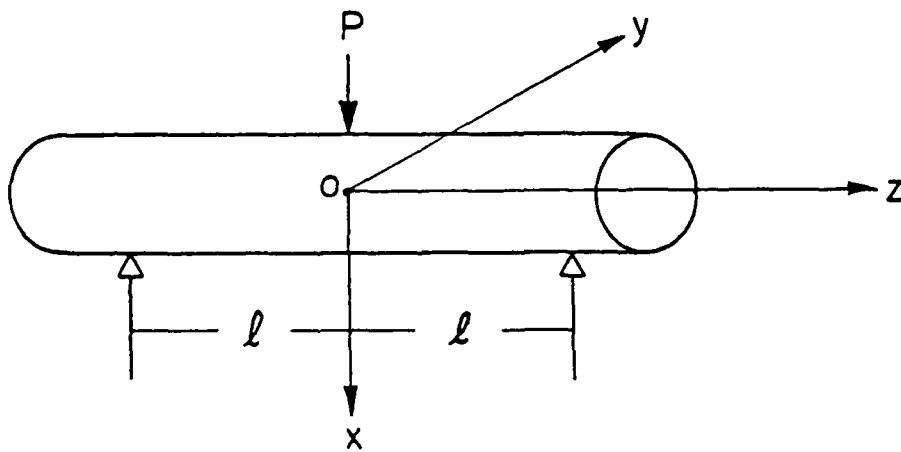
XBL 82! 5056

Fig. 2



XBL 8110-6702

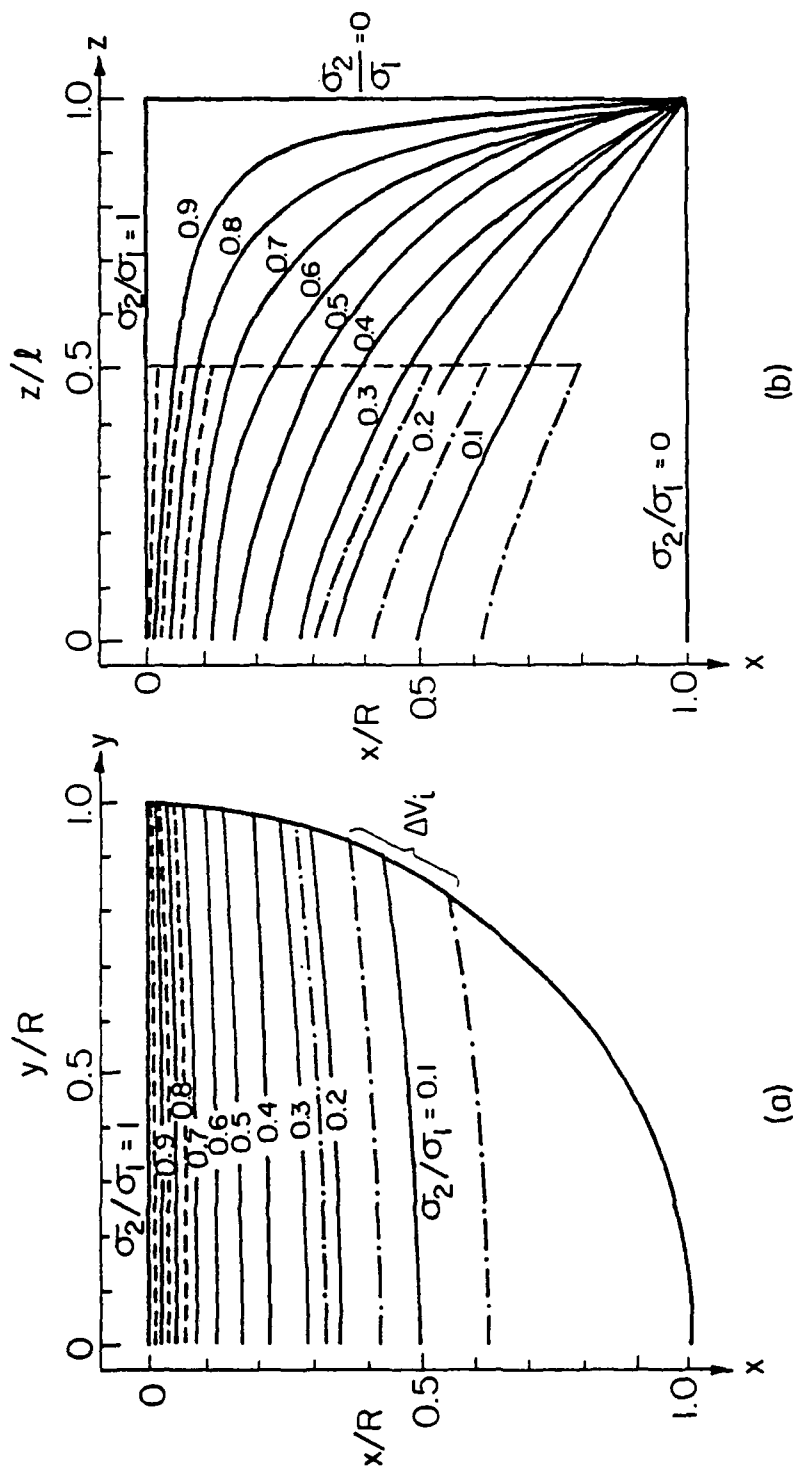
Fig. 3



XBL 8110-6703

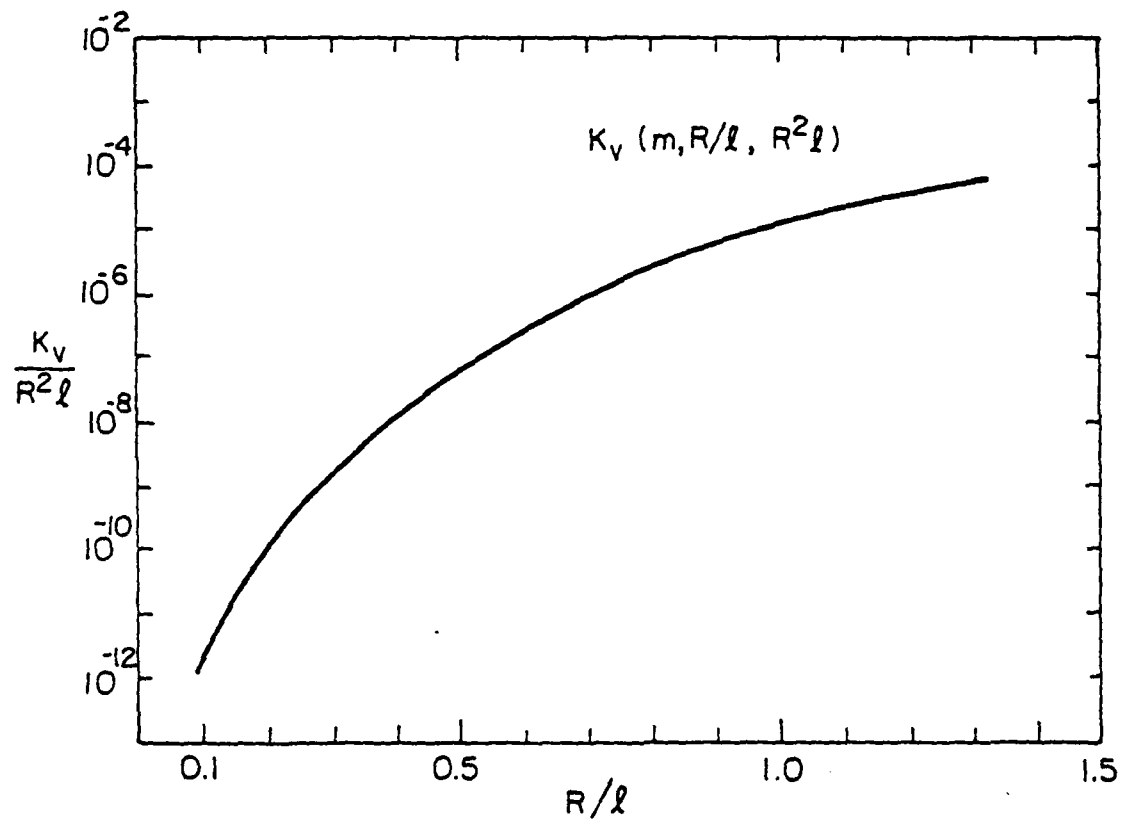
Fig. 4





XBL 821-5057

Fig. 5



XBL 821-5058

Fig. 6

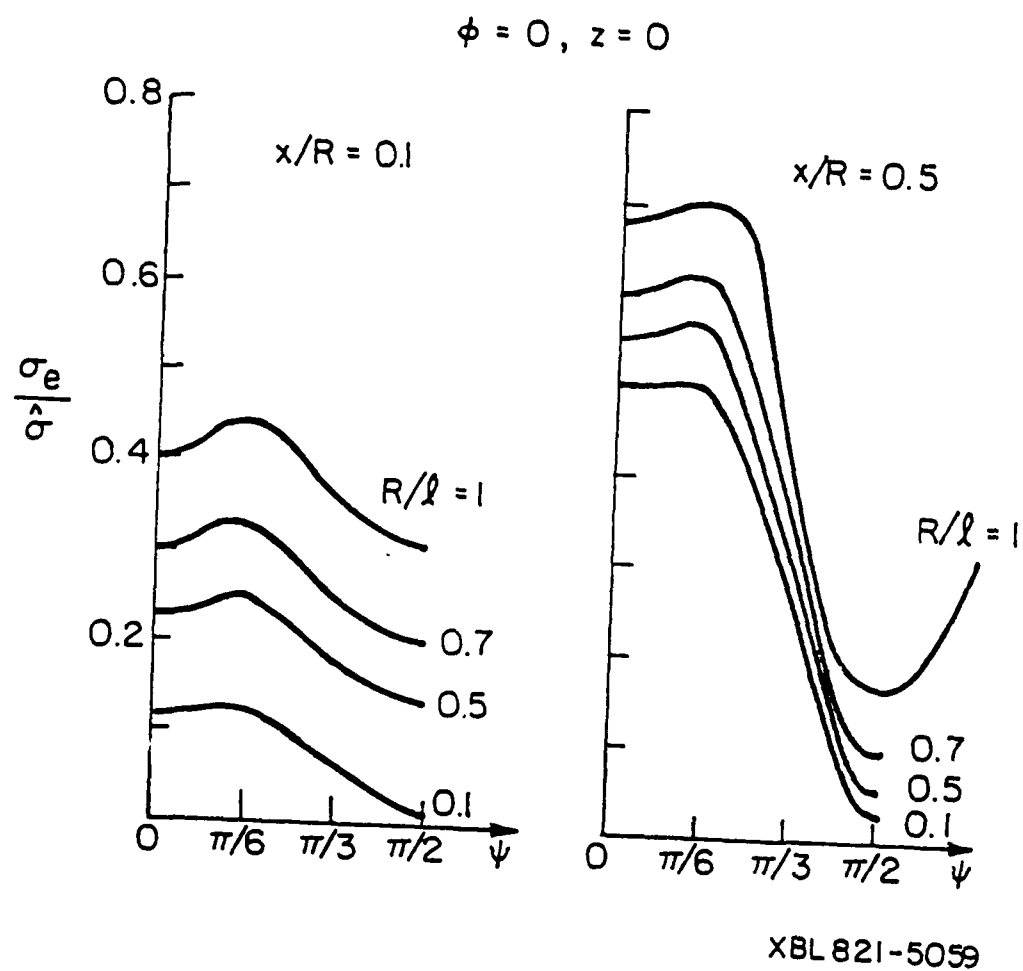


Fig. 7

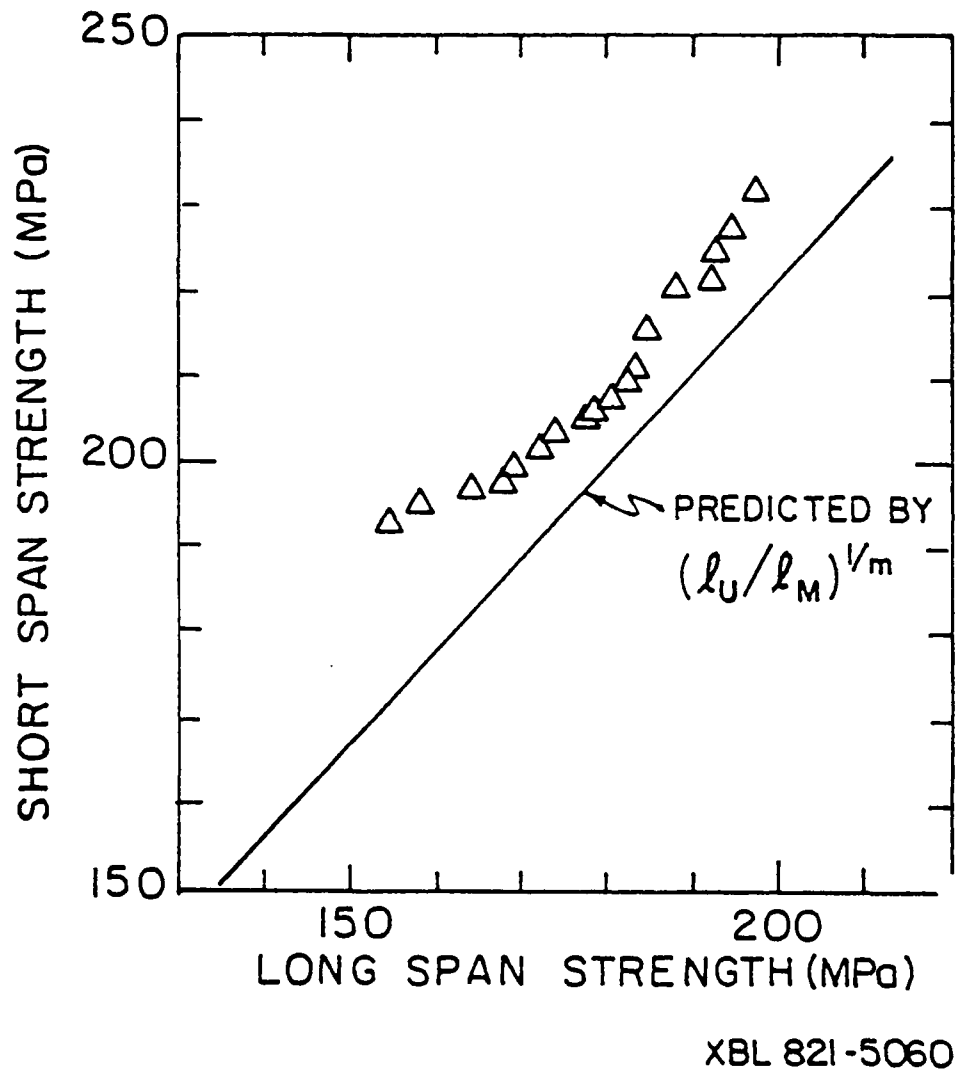
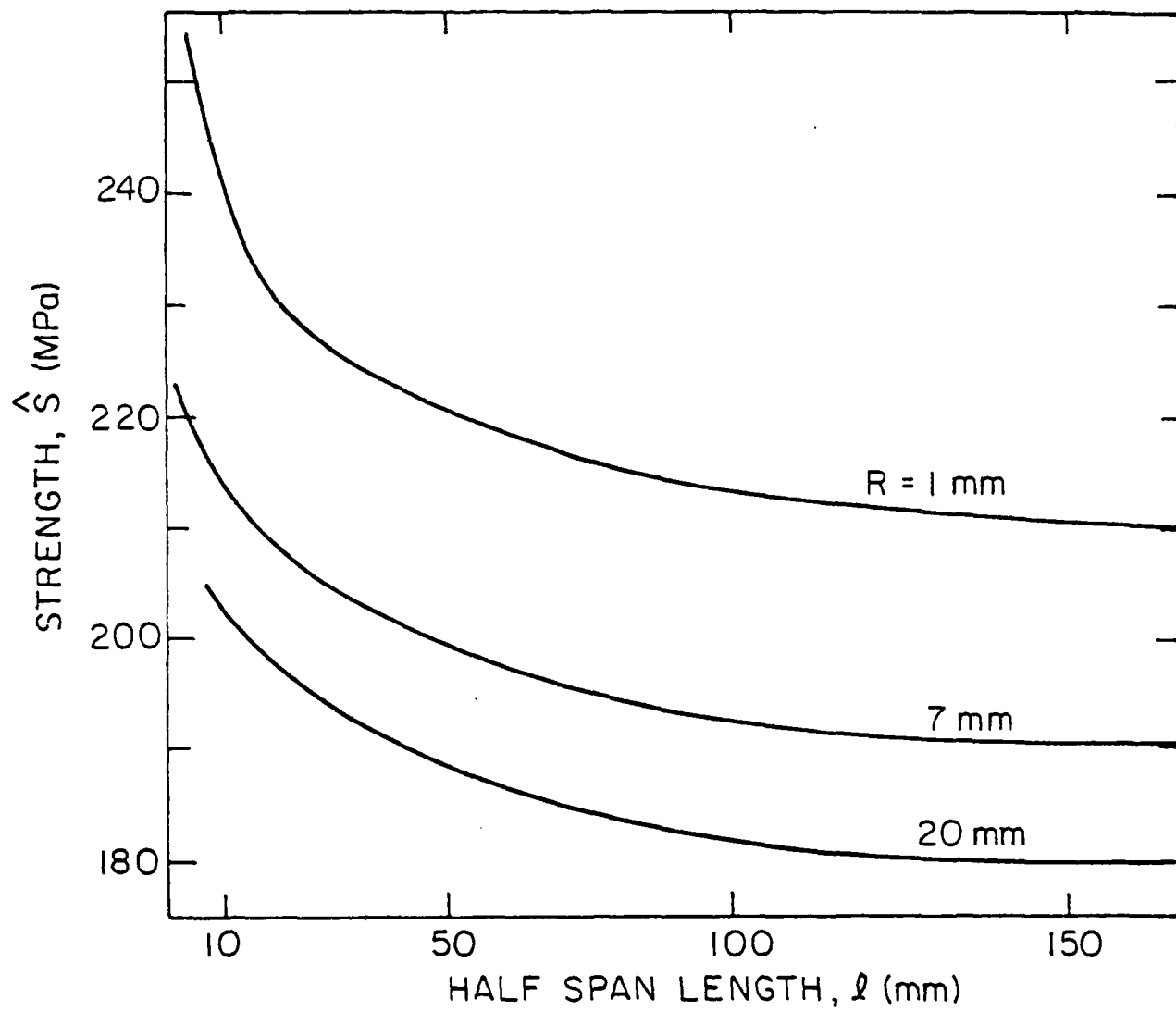
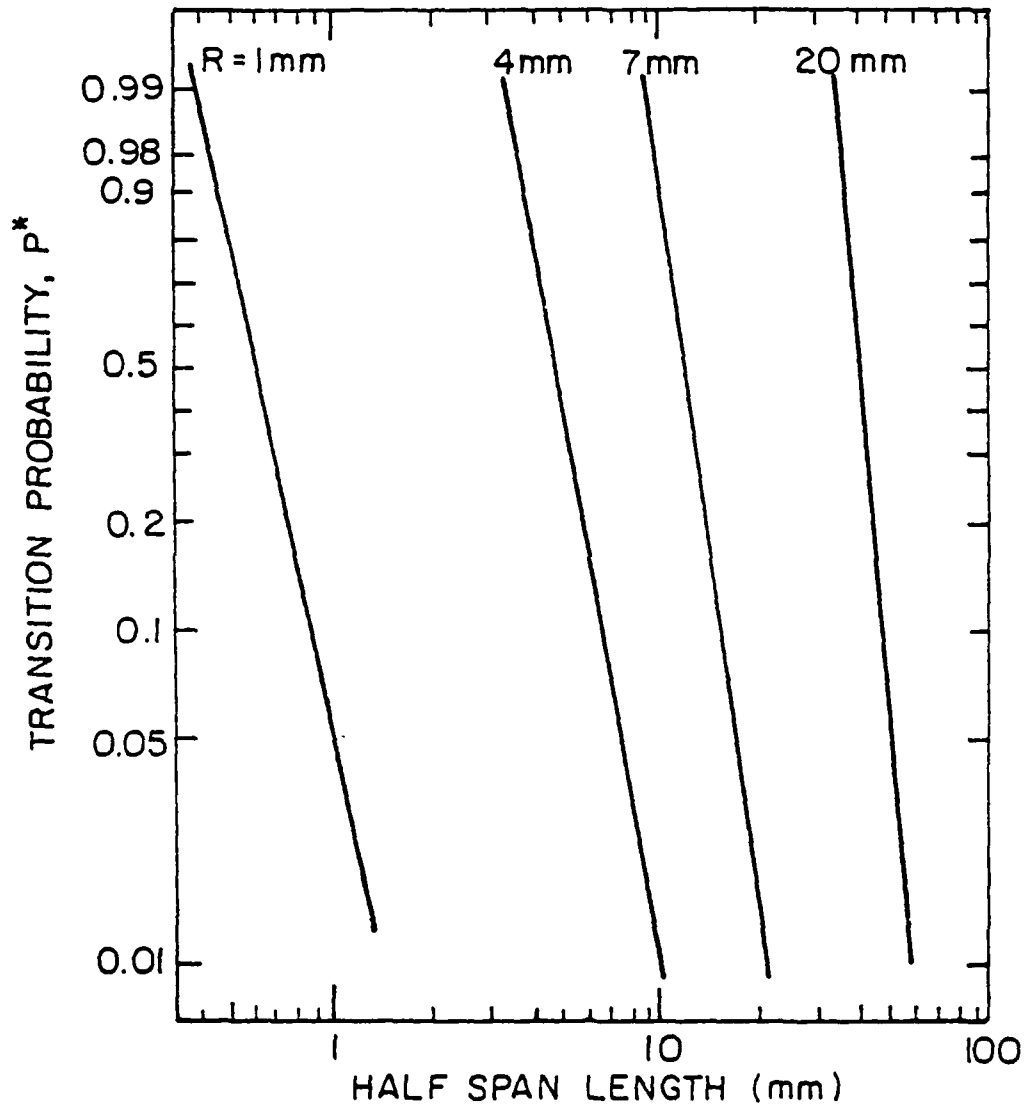


Fig. 8



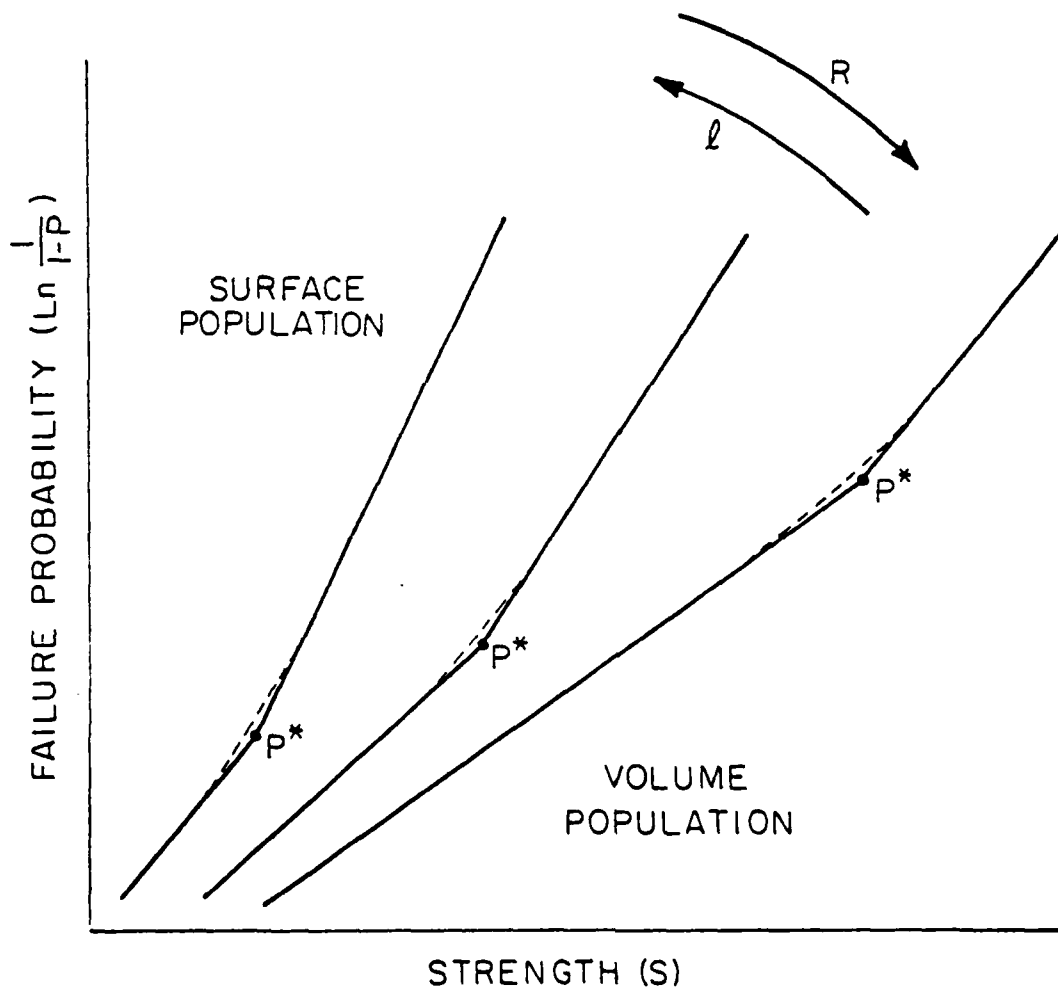
XBL 821-5061

Fig. 9



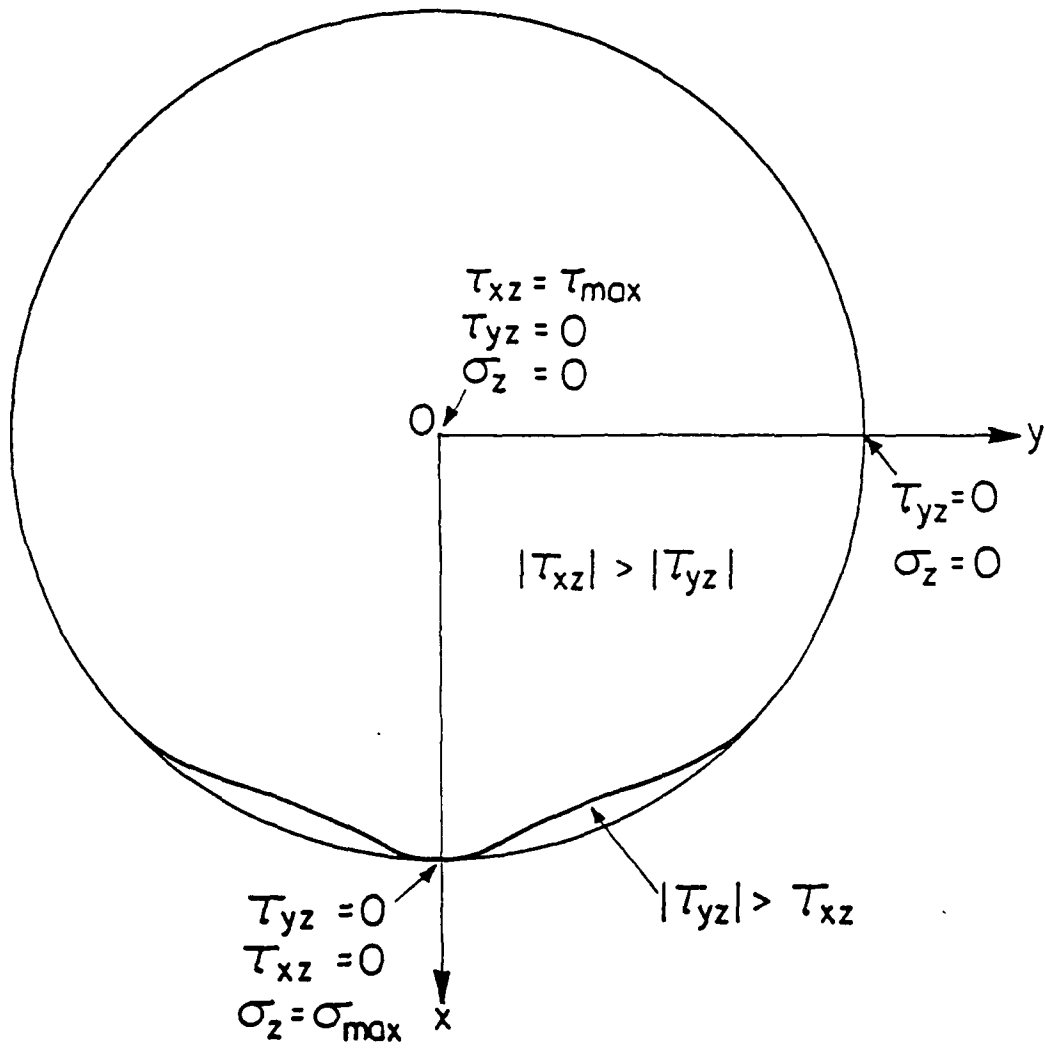
XBL 821-5062

Fig. 10



XBL 821-5103

Fig. 11



XBL8110-6704

Fig. A1



CHAPTER XI

A QUANTITATIVE STUDY OF THERMAL SHOCK  
APPLIED TO SURFACE FLAW POPULATIONS IN ALUMINA

by

J. Lamon, M. Drory and A. G. Evans

Department of Materials Science and Mineral Engineering  
University of California  
Berkeley, CA 94720

A Quantitative Study of Thermal Shock  
Applied to Surface Flaw Populations in Alumina

J. Lamon, M. D. Drory and A. G. Evans

Department of Materials Science and Mineral Engineering  
University of California  
Berkeley, CA 94720

ABSTRACT

The association between the statistical distributions of mechanical strength and thermal shock resistance are quantitatively examined for fracture controlled by a population of surface cracks. The comparison uses gas jet thermal shock tests and coaxial ring mechanical tests (performed on identical alumina discs), in conjunction with finite element analysis. The study demonstrates that the mechanical strength and thermal shock resistance exhibit parity when fracture is dictated by surface cracks. However, associations between strength and thermal shock pertinent to other types of fracture initiating defect await further study.

## I. INTRODUCTION

In many structural applications, ceramic components are subjected to severe thermal shock, which may cause crack propagation and eventual failure. The thermal stress fracture generally occurs from defects (machining flaws or fabrication defects). Quantitative analysis of thermal fracture, which accounts for the distribution of the controlling defects, is thus an important prerequisite for attaining performance reliability in fracture-critical applications.

Thermal shock analysis is generally predicated on a parity between mechanical strength and thermal shock resistance.<sup>1-5</sup> The underlying premise is that thermal fracture results from the macroscopic thermal stresses generated by the temperature transient. Additional stresses that result from thermal inhomogeneities in the material (insulating inclusions, voids) are generally ignored. The validity of the parity premise can only be adequately assessed by the generation of a data base: involving direct, quantitative comparisons between mechanical strength and thermal shock resistance.

Few quantitative comparisons exist in the literature, primarily because the conventional thermal shock tests have not been amenable to stress analysis, by virtue of uncontrolled corner effects and heat transfer variability.<sup>6</sup> The testing of disc specimens, using gas jets<sup>7</sup>, lasers<sup>8</sup> and fluidized beds<sup>2</sup> obviates the stress analysis difficulties. However, the existence of multiple flaw populations<sup>9</sup> (fabrication flaws, surface cracks, edge cracks, etc.) constitutes an additional difficulty. Specifically, it is essential (for purposes of comparison) that the mechanical and thermal tests sample the same flaw population. It is very difficult to create a systematic edge flaw

population; hence, it is desirable to use a test technique that introduces the maximum tensile stress at the disc center. The gas jet method has this advantage.<sup>7</sup> The present study uses the gas jet thermal shock test and the concentric ring biaxial mechanical strength test to examine the thermal shock/mechanical strength parity.

Prior studies<sup>7</sup> have revealed that, for discrete small surface cracks, mechanical strength tests provide a fully quantitative basis for predicting thermal shock failure. It remains, therefore, to examine the comparative fracture behavior exhibited by the range of flaw populations typically encountered in ceramic materials.<sup>9</sup> Surface crack populations are most likely to provide the desirable mechanical strength/thermal shock parity, because such cracks should exert a minimal influence on the heat flux from the surface.<sup>†</sup> Preliminary evidence supporting this contention has been obtained using  $Al_2O_3$ <sup>2</sup> discs tested in fluidized bed apparatus. A fully quantitative surface crack study is presented in the present paper.

## 2. STRESS ANALYSIS

The thermal stress distribution in discs subject to transient thermal stressing by the impingement of a gas jet can be determined using finite element techniques<sup>7</sup>, by adopting the axisymmetric grid depicted in fig. 1. In general, the peak stress,  $\hat{\sigma}$  (fig. 2a) at any location  $(r, z)$  can be expressed in terms of the normalized functions<sup>1,10</sup>

$$\frac{\hat{\sigma}(1-\nu)}{E\alpha\Delta T} = H\left(\frac{r_j h}{k}\right) G\left(\frac{z}{t}, \frac{r}{\ell}, \frac{r_j}{t}\right) \quad (1)$$

---

<sup>†</sup>Populations of fabrication flaws are less likely to exhibit parity because the thermal conduction inhomogeneity at the flaw influences the local heat flux and thus, introduces additional stresses. Studies of fabrication flaws will be reported in subsequent publications.

where  $E$  is Young's modulus,  $\alpha$  is the thermal expansion coefficient,  $\Delta T$  is the imposed temperature differential,  $h$  is the heat transfer coefficient,  $k$  is the thermal conductivity,  $t$  is the disc thickness,  $a$  is the disc radius,  $r_j$  is the jet radius and  $H$  and  $G$  are functions.

Specific variations in the peak stress, for disc specimens exposed to gas jet impingement, determined using finite elements, are plotted in figs. 2b, c. It is noted that conditions of approximate equibiaxial tension exist over a circular surface area (fig. 2b) with diameter  $\approx r_j$ . Outside this region, the tangential stresses decrease very quickly with radial location and become compressive beyond the jet periphery. The stress variation through the thickness (fig. 2c) is approximately linear up to  $\sim t/2$ , whereupon the stress assumes a small, approximately positive invariant value. Cognizance of these stress distributions is essential to the fully quantitative correlation of mechanical and thermal shock data.

### III. MATERIALS AND PROCEDURES

An alumina ceramic was selected for this study.<sup>†</sup> The samples were discs (5 cm. in diameter, 0.25 cm thick), ground and polished on one surface. The concentric ring biaxial tension technique was selected for mechanical tests, as the most convenient for statistical analysis and thermal stress simulation<sup>11,12</sup>. The disc is supported on a concentric ring (radius 16.5 mm) and loaded at the center with a smaller coaxial ring (radius 0.4 mm). The resultant tensile stresses are equibiaxial and uniform over an area dictated by the size of the loaded zone. Specimens

---

<sup>†</sup>AD-998 alumina from Coors Porcelain.

were stressed to failure, at a stress rate of  $\sim 2 \text{ MPa s}^{-1}$  (chosen to give a failure time comparable to that determined<sup>7</sup> for the thermal shock tests), as required to obtain the distribution of mechanical equibiaxial strengths,  $S_b$ .

Identical discs were individually tested in the thermal shock apparatus shown in figure 3. The disc was horizontally supported by fibrous insulation, with a thermocouple placed against the surface of the specimen. The specimen was heated in a resistance furnace until an equilibrium temperature was attained. A rapid temperature change was then imposed onto the disc center using a high velocity helium jet, directed through a 1.5 mm diameter silica tube. The tube diameter was selected such that the equibiaxially stressed area (fig. 2b) was the same as that used for the mechanical tests.<sup>†</sup> After each quench, the test sample was examined for cracks in an optical microscope, using oblique incidence.<sup>13</sup> If no cracking occurred, the temperature differential between the disc and the helium jet was incrementally increased (by  $10^\circ\text{C}$ ) until cracking was obtained. A distribution of critical temperatures,  $\Delta T_c$ , was thereby evaluated.

Associations between the mechanical strength and thermal shock resistance are predicated upon knowledge of the stresses that develop in the thermal shock tests. The specific stresses of interest are the equibiaxial tensile stresses in the vicinity of the jet center ( $r \leq r_j/2$ ,  $z/t \approx 0$ ). These stresses were determined using a calibration procedure<sup>7</sup> which compares the mechanical equibiaxial strength,  $S_b$ , and the critical temperature difference for fracture,  $\Delta T_c$ , for disc samples containing

---

<sup>†</sup>The need for statistical, stressed area corrections in the comparison of the mechanical strength and thermal shock data can then be obviated.

small controlled surface flaws, introduced at the disc center (using indentation procedures). This comparison recognizes that, for a fixed flaw location and test geometry, eqn (1) at the fracture condition reduces to;

$$S_b = [E\alpha\Delta T_c/(1-\nu)] H_0 \quad (2)$$

where  $H_0$  is a constant. Furthermore, when  $H_0$  is determined using surface flaws placed at the disc center,  $H_0$  is position invariant in the range  $r \leq r_j/2$  (i.e. in the region of stress uniformity) and varies with depth (fig. 2c) as

$$H \approx H_0(2z/t) \quad (3)$$

For the specific geometry used in the present study, the test results on preflawed specimens yield the relation;

$$H_0 = r_j h / 4k \quad (4)$$

which, coincidentally, is closely similar to the value for an infinite flat plate<sup>10,14</sup> cooled from one surface, but with the plate thickness replaced by the jet diameter.

#### IV. RESULTS

Typical specimens failed by thermal shock and by biaxial flexure loading are shown in figure 4. In both cases, the modes of fracture are similar. Fracture originates from the central region of the test specimens and progresses as radial cracks which propagate towards the disc periphery.

Statistical analysis of the results was facilitated by identifying the approximate fracture origin in each test specimen, using a combination of optical and scanning electron microscopy. Only specimens that had the fracture origin contained within the zones of equibiaxial tension were selected for analysis. Of these specimens, all of the failure origins in the thermal shock tests appeared to be at the specimen surface; whereas, sub-surface origins were identified in a small proportion of the mechanical tests.

Comparison of the results from mechanical and thermal shock tests is achieved by converting the mechanical strengths into equivalent critical temperatures,  $\Delta T_c$  (using eqn 2) and ranking the data. Using all of the data for specimens that failed in the regions of uniform equibiaxial stress, irrespective of the fracture origin, yields the comparison plotted in fig. 5. The mechanical strength and thermal shock results appear to be essentially coincident, providing preliminary evidence of a parity between mechanical strength and thermal shock resistance.



## 5. DISCUSSION

### 5.1 Statistics of Fracture

Weakest link theories relate the failure probability,  $P_f$ , to the fracture strength, when fracture occurs by direct extension of non-interacting defects.<sup>15,16</sup> For surface cracks, subject to equibiaxial tension,

$$P_f = 1 - \exp \left[ - \int_A dA \int_0^{S_b} g(S_b) dS_b \right] \quad (5)$$

where  $A$  refers to the area of the surface element under stress, and  $g(S_b)dS_b$  is the number of flaws per unit surface with a strength between  $S_b$  and  $S_b + dS_b$ . Alternatively, the failure probability can be expressed in terms of the fracture temperature difference,  $\Delta T_c$ , by simply incorporating eqn (2) (relating the equibiaxial mechanical strength to  $\Delta T_c$ ) into the  $g(S_b)dS_b$  function. For example, an equibiaxial strength distribution given by

$$\int_0^{S_b} g(S_b) dS_b = (S_b/S_0)^m \quad (6)$$

where  $m$  is the shape parameter and  $S_0$  is the scale parameter, yields a thermal stress failure probability, for a uniformly stressed area,  $A$ , given by;

$$P_f = 1 - \exp [-A H_0^m (\Delta T_c / \Delta T_0)^m] \quad (7)$$

Note, however, that connections between  $\Delta T_c(P_f)$  and the uniaxial strength,  $S_u(P_f)$ , must recognize that  $S_b$  and  $S_u$  are connected by a proportionality constant that depends on  $m$ .<sup>17</sup>

Further examination of the present test results, using the preceding statistical description, recognizing that the stressed area is constant and separating the biaxial strength data into the two dominant flaw populations (using sensed statistics<sup>18</sup>), yields the statistical parameters indicated in Table I. Very close agreement between the scale and shape parameter is apparent when the surface flaw population controls both the mechanical strength and thermal shock resistance. The parity between  $S_b$  and  $\Delta T_c$ , for surface flaws, is thus quantitatively confirmed.

## 5.2 Implications

Some effects of test geometry and material properties on the thermal shock resistance of discs subject to gas jets can be deduced by rearranging eqn (7) to give

$$\Delta T_c = \Delta T_0 (A^{-1/m}/H_0) [-\ln(1-P_f)]^{1/m} \quad (8)$$

Assuming that  $H_0$  is given approximately by eqn (4) for a range of geometric conditions<sup>†</sup>, the trends in the median  $\Delta T_c$  ( $P_f = 1/2$ ), for surface flaw control, are illustrated in fig. 6. Specifically, the critical temperature decreases rapidly with increase in jet radius, especially for flaw populations characterized by a small shape parameter; an effect that derives primarily from the effect of jet radius on  $H_0$ .

<sup>†</sup>The absence of a dependence of disc thickness and radius on  $H_0$ , given by eqn (4), suggests a limited range of applicability. Further study will be needed to obtain more general expressions for  $H_0$ .

## 6. CONCLUSIONS

It has been demonstrated, for an alumina ceramic, that a parity between thermal shock resistance and mechanical strength exists, for surface flaw controlled failure. This parity permits the application of weakest link statistics and allows the failure probability to be derived in terms of temperature difference, specific size, the flaw population parameters and thermal shock severity. An analytic approximation for the Biot modulus and the thermal failure probability permits some important trends to be anticipated, such as the strong inverse dependence of the fracture temperature difference on jet size. The equivalent behavior when fracture is controlled by fabrication defects (inclusions or voids) remains to be determined.

References

1. S. S. Manson and R. W. Smith, J. Am. Ceram. Soc., 38 [1] 18-27, (1955).
2. G. G. Trantina, in Thermal Stresses in Severe Environments (Ed. by D. P. H. Hasselman and R. A. Heller) Plenum Press, New York, 1980, pp. 229-244.
3. D. P. H. Hasselman, "Unified Theory Of Thermal Shock," J. Am. Ceram. Soc. 52 (11), 600-604 (1969).
4. D. P. H. Hasselman, J. Am. Ceram. Soc. 54 219 (1971).
5. G. Yagawa and I. Masukazu, ASTM Eleventh National Symposium on Fracture Mechanics, Virginia Polytechnic Institute and State University, June 12-14, 1978.
6. A. F. Emery and A. S. Kobayashi, J. Am. Ceram. Soc. 63 (1980) 410.
7. K. T. Faber, M. D. Huang and A. G. Evans, J. Am. Ceram. Soc. 64 (5) 296 (1981).
8. S. G. Schwillie, R. A. Tanzilli and S. Musikant, "Thermal Stresses in Severe Environments," ibid., p. 553.
9. A. G. Evans, J. Am. Ceram. Soc. 65 (1982) 127.
10. W. D. Kingery, "Factors Affecting Thermal Stress Resistance of Ceramic Materials," J. Am. Ceram. Soc. 38 (1) 3 (1955).
11. D. K. Shetty, A. R. Rosenfield, P. McGuire, G. K. Bansal and W. K. Duckworth, "Biaxial Flexure Tests for Ceramics," Bull. Am. Ceram. Soc. 59 (12), 1193-1197 (1980).
12. M. N. Giovan and G. Sines, "Biaxial and Uniaxial Data for Statistical Comparisons of a Ceramic's Strength," J. Amer. Ceram. Soc. 62 (9-10) 510 (1979).
13. D. B. Marshall, M. D. Drory and A. G. Evans, to be published.

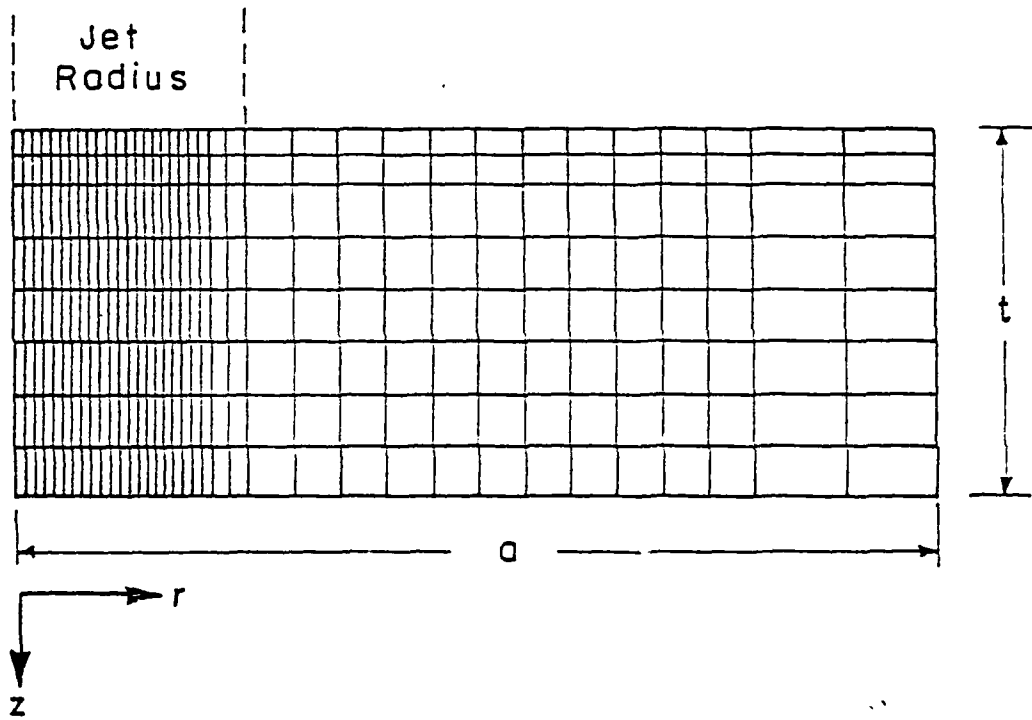
14. F. J. Bradshaw, "Thermal Stresses in Non-Ductile High Temperature Materials," Tech. Note Met. 100, British RAE, February 1949.
15. J. R. Matthews, F. A. McClintock, and W. J. Shack, "Statistical Determination of Surface Flaw Density in Brittle Materials," J. Amer. Ceram. Soc. 59 (7-8) 304-308 (1976).
16. A. G. Evans and R. L. Jones, "Evaluation of a Fundamental Approach For the Statistical Analysis of Fracture," J. Am. Ceram. Soc. 61 (3-4) 156-60 (1978).
17. A. G. Evans, J. Amer. Ceram. Soc. 61 (1978) 302.

Table 1: Shape and scale parameters for surface flaw populations.

	m	$\Delta T_0$
Thermal shock	13.2	16.3
Biaxial flexure	14	17.6

FIGURE CAPTIONS

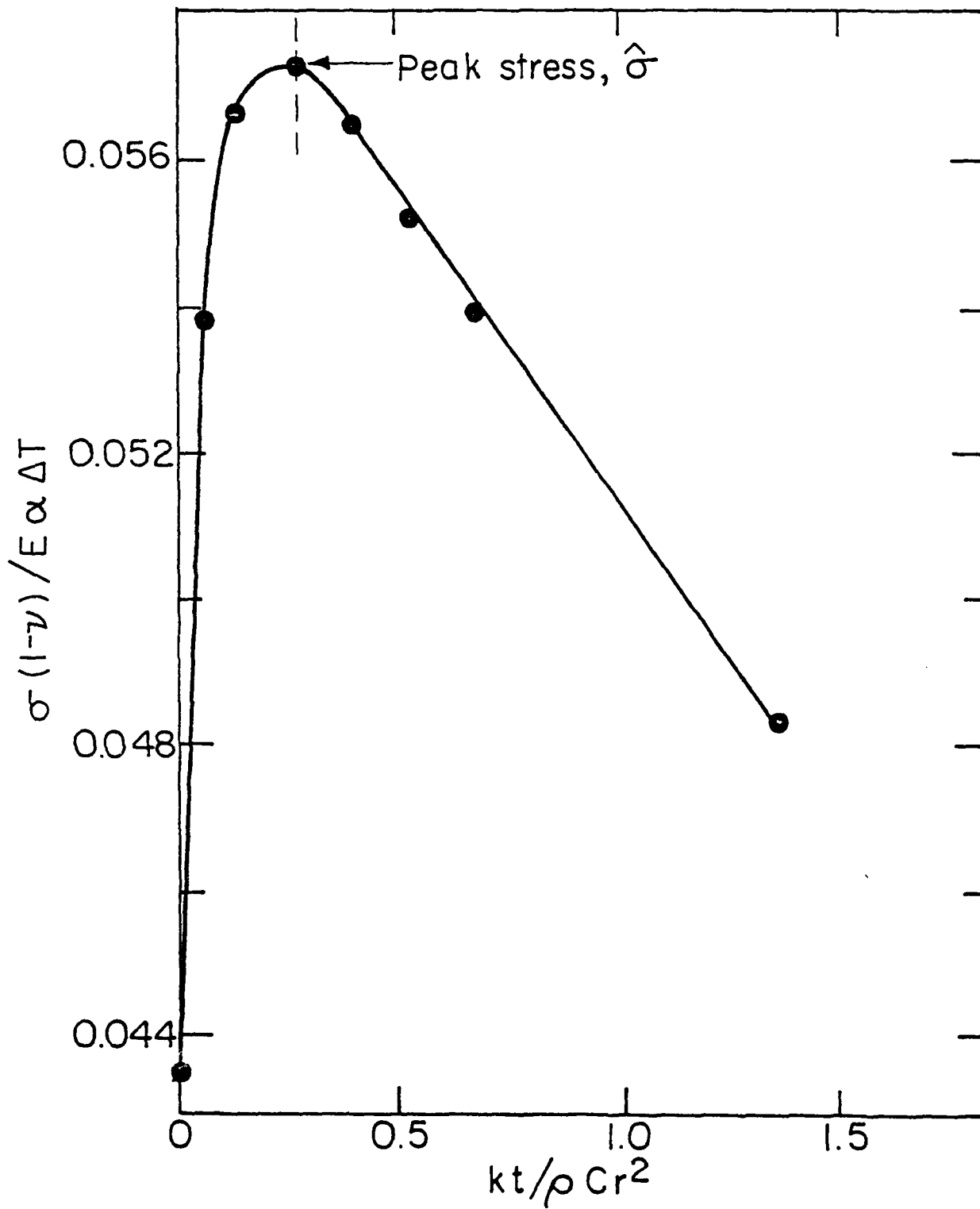
- Fig. 1. The finite element grid used for stress analysis.<sup>7</sup>
- Fig. 2. a. The variation of normalized stress with normalized time at the disc center.  
b. The variation of the peak radial and tangential stresses with radial position, along the surface subject to jet impingement.  
c. The variation in the radial stress at the disc axis with position beneath the cooled surface.
- Fig. 3. A schematic of the thermal shock apparatus.
- Fig. 4. Micrographs of fragmented test specimens:  
a. mechanical tests  
b. thermal shock tests.
- Fig. 5. A comparison of the fracture probabilities derived for the mechanical and thermal shock tests.
- Fig. 6. Predicted effect of jet radius on the fracture temperature, assuming a Biot modulus given by eqn (4).



XBL 822 - 5208

Fig. 1





XBL 822-5214A

Fig. 2a

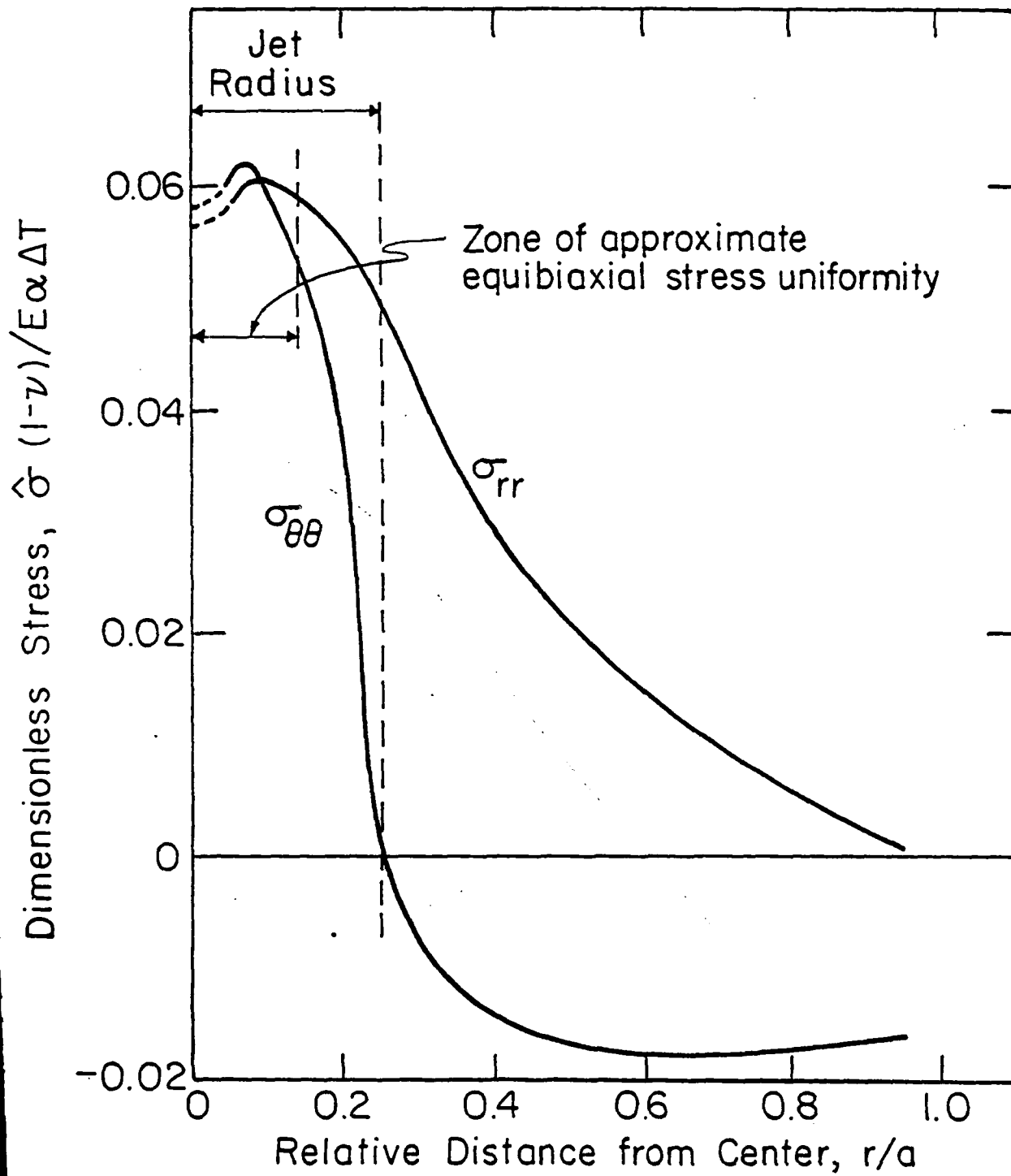
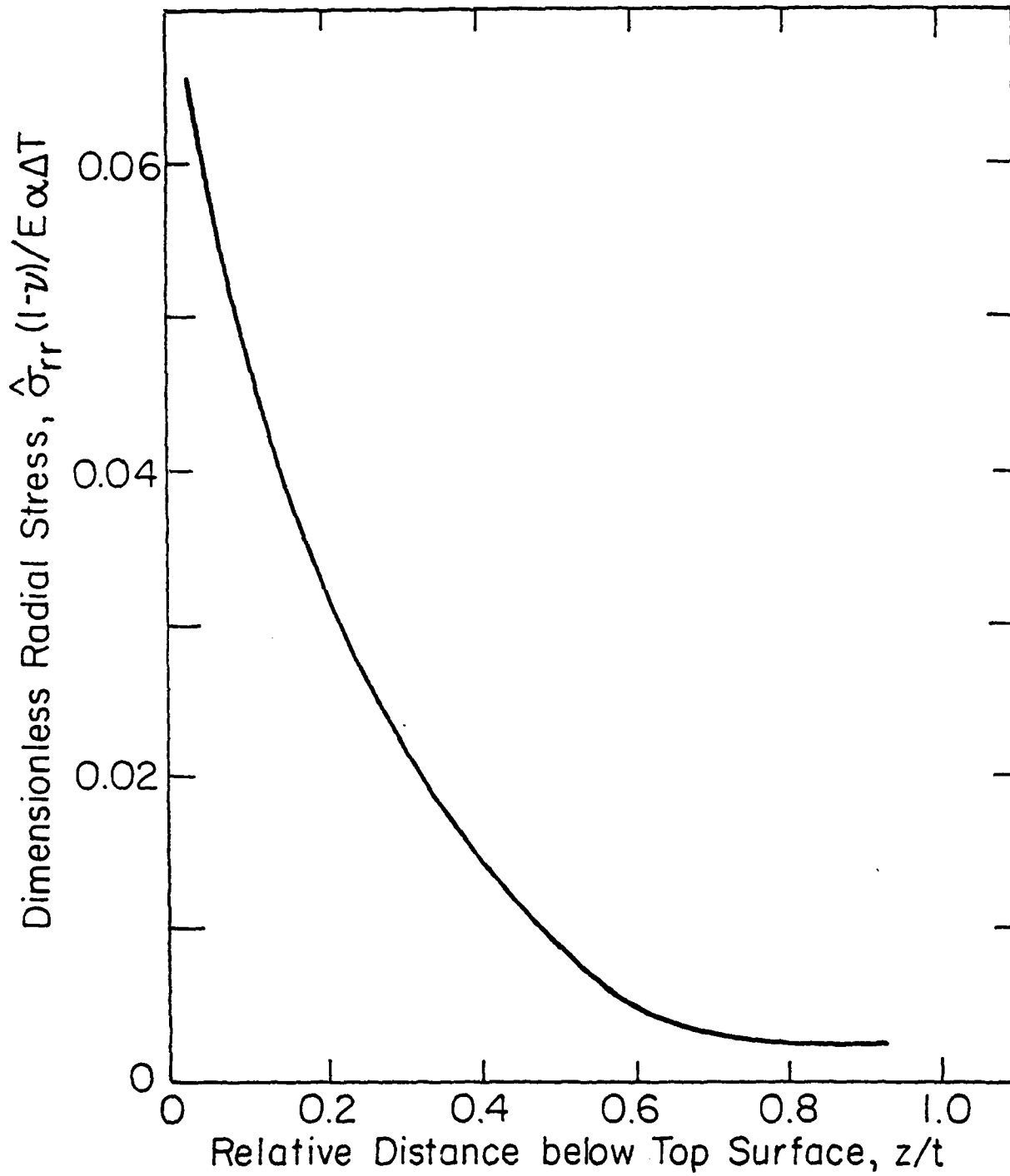


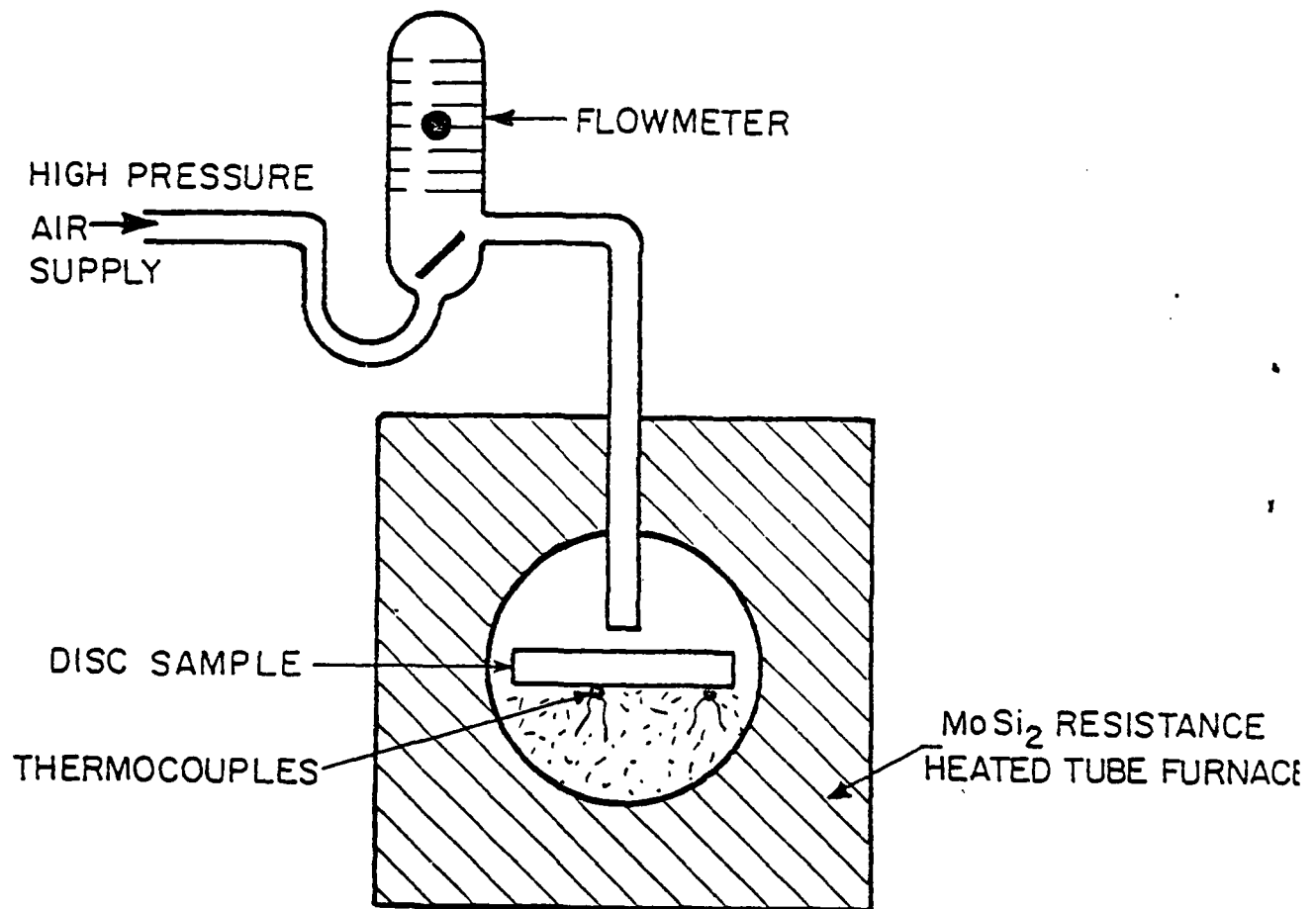
Fig. 2b

XBL 822-5212 A



XBL 822 5213 A

Fig. 2c



XBL 807-556!

Fig. 3

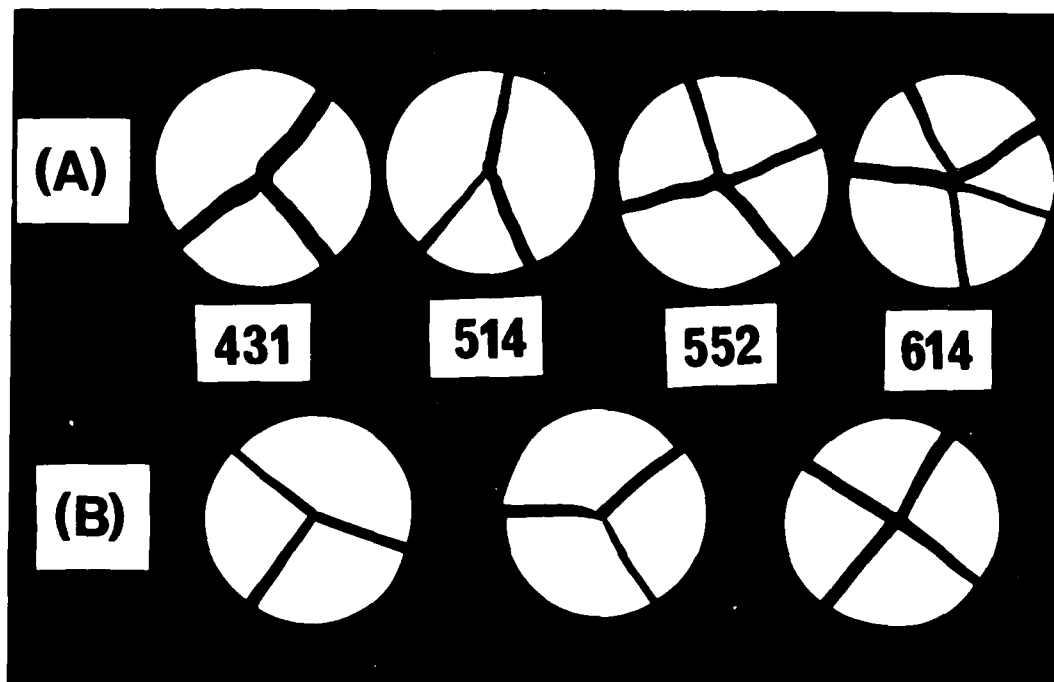


Fig. 4

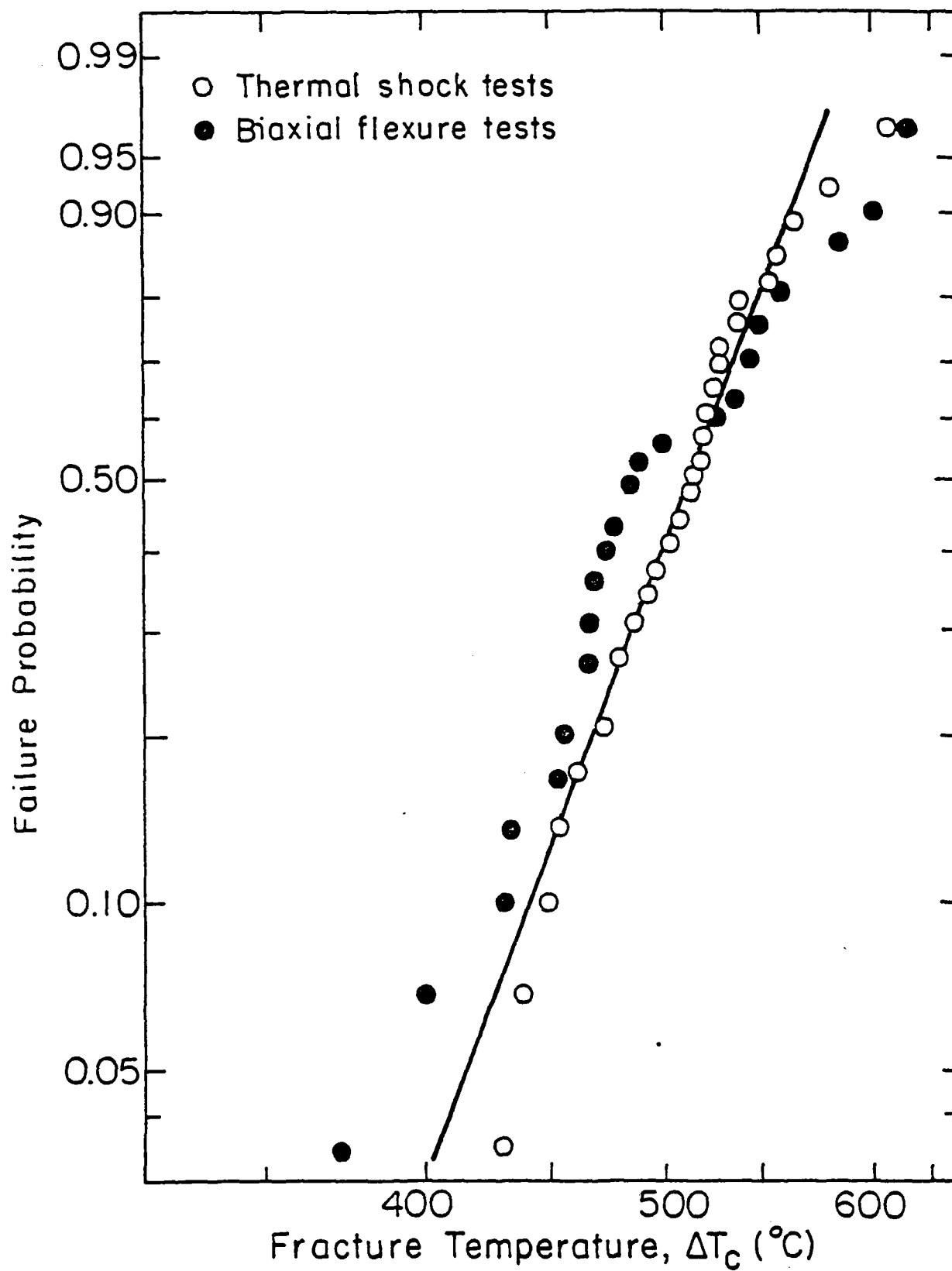
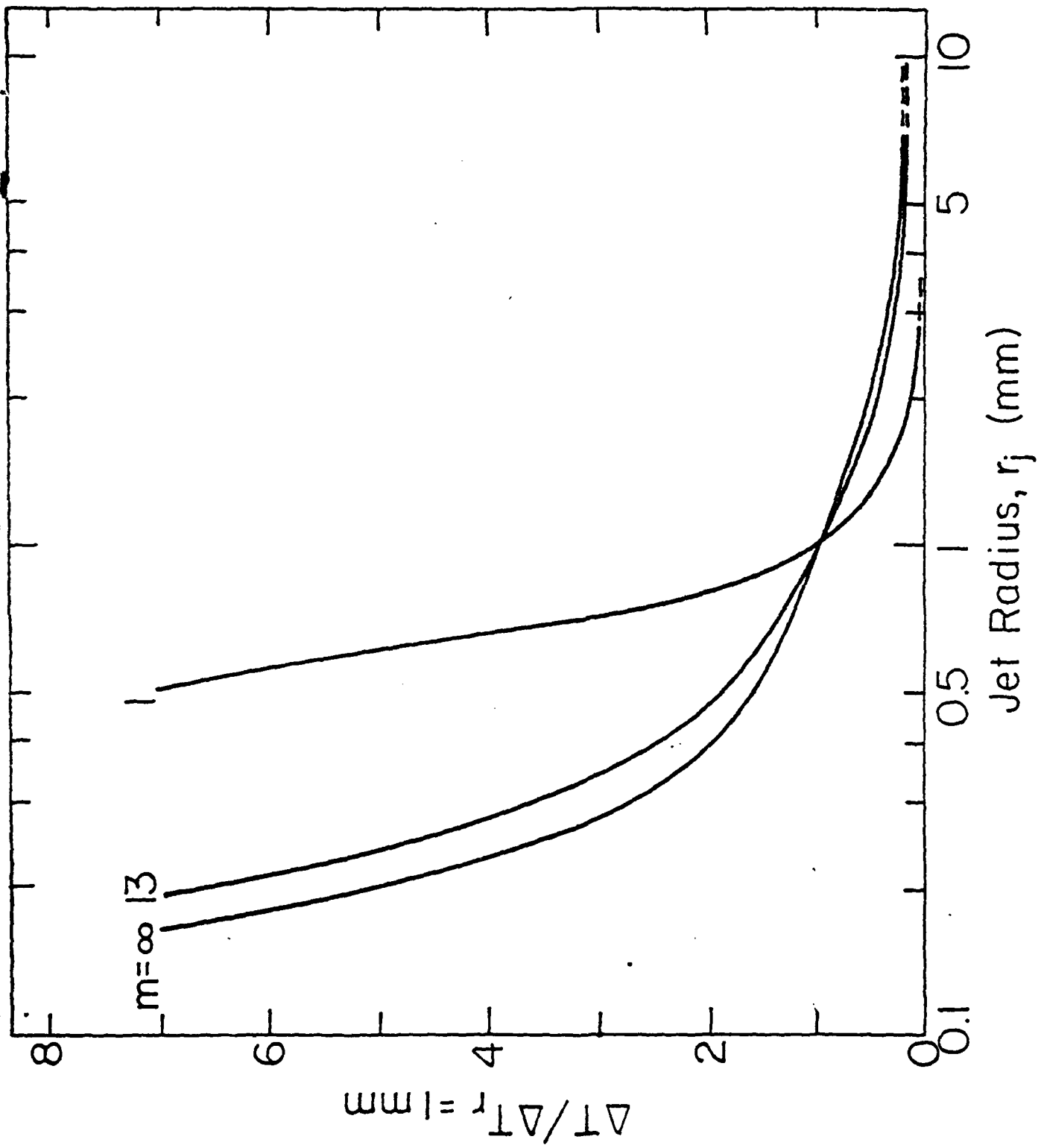


Fig. 5

XBL 829-6584



XBL 829-65R5

Fig. 6

LMET  
- 83